Hans Burchard

Applied Turbulence Modelling in Marine Waters

July 1, 2002

Springer
Berlin Heidelberg NewYork
Barcelona Hong Kong
London Milan Paris
Tokyo

Foreword

The simulation of turbulent mixing processes in marine waters is one of the most pressing tasks in oceanography. It is rendered difficult by the various complex phenomena occurring in these waters like strong stratification, external and internal waves, wind-generated turbulence, Langmuir circulation etc. The need for simulation methods is especially great in this area because the physical processes cannot be investigated in the laboratory. Traditionally, empirical bulk-type models were used in oceanography, which, however, cannot account for many of the complex physical phenomena occurring. In engineering, statistical turbulence models describing locally the turbulence mixing processes were introduced in the early seventies, such as the k-ε model which is still one of the most widely used models in Computational Fluid Dynamics. Soon after, turbulence models were applied more and more also in the atmospheric sciences, and here the k-kL model of Mellor and Yamada became particularly popular. In oceanography, statistical turbulence models were introduced rather late, i.e. in the eighties, and mainly models were taken over from the fields mentioned above, with some adjustments to the problems occurring in marine waters. In the literature on turbulence-model applications to oceanography problems controversial findings and claims are reported about the various models, creating also an uncertainty on how well the models work in marine-water problems. The author and his co-workers have done much clarifying research in this area and have also developed new model versions, and this work is now comprehensively summarised in this book.

The author gives an introduction to the modelling problems and an extensive overview on turbulence models used for applications in oceanography, focusing then on the highest level models in use, namely two-equation models with algebraic-stress relations and on extensions accounting for special problems occurring in marine waters. These models are described in detail and analyses on homogeneous shear flows are presented as well as extensive tests for idealised mixing situations and real-life oceanic and limnic applications, performed with the computer code GOTM (General Ocean Turbulence Model). The interested reader should note that the source code of GOTM containing many of the turbulence models discussed as well as the application examples is available freely on the internet. Of special value for the readers

of the book is the extensive comparative study of the various models and the reconciliation between the different modelling schools which the author has achieved.

In the field of engineering, more advanced, quite complex models were developed since the 70's employing model transport equations for the individual turbulence stresses and heat and mass fluxes. This level of modelling has not received much consideration in oceanography, probably because of the considerable uncertainties about the boundary conditions there. However, also in engineering practice these models were never really accepted; rather the simpler two-equation models (or even one-equation models) are still used whose performance and range of applicability has been increased by non-linear eddy-viscosity and algebraic-stress- model versions. It is therefore interesting to note these are also the types of models on which this book focuses. Engineering turbulence models have been covered well in a number of books, but there was so far no comprehensive treatise on the subject of turbulence modelling in marine waters. The author has filled this gap and has produced a much needed book that provides invaluable information for everybody who sets out to simulate turbulent mixing processes in marine water problems.

W. Rodi

Preface

The original manuscript for this book has been submitted as a Habilitation thesis at the Institute for Oceanography of the University of Hamburg about fifteen months ago. The amount of updates I had to consider now for this published version even after such a short time shows that there is still a lot of research activity going on in the field of marine turbulence. This is motivated to a great extent by the steadily growing available computer power, which allows not only to increase the spatial resolution and temporal coverage, but also the physical resolution of ocean models. Ten years ago, ocean modellers could probably argue that higher-order turbulence closure models were computationally too expensive for consideration in their modelling studies, but nowadays this is only true for climate models simulating several hundreds or thousands of years.

In contrast to that higher-order turbulence closure models have been popular in hydraulic engineering since about thirty years, see the state-of-the-art review by *Rodi* [1980]. Such a model review has however not been written so far for the field of marine turbulence modelling. That might explain why different schools of marine turbulence modelling (basically the European k-ε modellers and the American k-kL modellers) could co-exist more or less peacefully until today, not knowing much of each other. The recently finished concerted action CARTUM (Comparative Analysis and Rationalisation of Second-Moment Turbulence Models, funded by the European Commission) clearly demonstrated persisting misunderstandings between these two schools. The present book tries to fill this gap by presenting applicable turbulence closure models in a general notation.

This book is written not only for all those who work with numerical ocean models. It is also designed for graduate students since it does not require a deep insight into the field of turbulence modelling. It is written as well for observing oceanographers who are interested in the assumptions made for deriving these models and who would like to explain their observational data by means of a water column model. However, a general understanding of applied mathematics and physics is essential for working with this book.

The book is structures as follows: After a general introduction, the full derivation from the Navier-Stokes equations to mathematically complete statistical turbulence closure models is shown. Then the numerical discretisation

of these equations is carried out, followed by a brief overview on the computational implementation into the Public Domain water column model GOTM. Finally, a number of idealised test cases and simulations of in-situ data from field campaigns are discussed. The book is then completed by a list of ten future research perspectives, an appendix with notation rules, transformations between different notations and a list of symbols, a reference list and an index.

Warnemünde, Germany *H. Burchard*
May 2002

Acknowledgement. This study summarises eight years of research I performed in cooperation with many different people. Before acknowledging them for their ideas and contributions, I would like to thank those who funded these years of research:

- The first three years from 1992 to 1995 were paid by the GKSS Research Centre in Geesthacht, Germany in the framework of a cooperation with the University of Hamburg.
- In 1996 my research activities were carried out at the International Centre for Computational Hydrodynamics in Hørsholm, Denmark, funded by the Danish National Research Foundation.
- Three projects within the framework of the European Communities' Program in Marine Science and Technology (MAST) under the contract numbers MAS3-CT96-0053 ('PHASE'), MAS3-CT96-0051 ('MTP II-MATER') and MAS3-CT97-0025 ('PROVESS') supported my studies on turbulence modelling during the years 1997-1998 and 2000.
- The actual compilation of this study was funded by a Habilitation Grant given by the German Research Foundation for the years 1999 and 2001.

There are further two projects which gave me a scientific home during the last years. One of them is a real project, CARTUM (Comparative Analysis and Rationalisation of Second-Moment Turbulence Models) a brainstorming activity funded by the European Community (MAS3-CT98-0172) which brought together turbulence specialists from all over the world. In the framework of this activity, regular meetings were held which gave important impulses to future research in the field of turbulence, also to my personal investigations. The other project is GOTM (General Ocean Turbulence Model, `http://www.gotm.net`), an idealistic software project without any funding initialised by Karsten Bolding (Ispra, Italy) and myself with the aim of constructing a unified computer code for simulating the water column with various turbulence closure schemes. Later, others joined GOTM, Manuel Ruiz Villarreal (Hamburg, Germany), Pierre-Philippe Mathieu (Reading, England), Georg Umgiesser (Venice, Italy), Encho Demirov (Bologna, Italy) and Lars Umlauf (Lausanne, Switzerland). Without the ordering strictness of the GOTM model in the background, the various idealised and real model simulations presented in this study could never have been performed. It is furthermore the scientific discussion with all the GOTM users which broadened my understanding of turbulence modelling.

My scientific understanding of marine turbulence has been strongly influenced by many researchers. Jürgen Sündermann (Hamburg, Germany) opened for me the doors into oceanography and turbulence research. Helmut Baumert (Hamburg, Germany) made me familiar with the basics of turbulence modelling and gave me many useful hints throughout the last years. Eckhard Kleine (Hamburg, Germany) helped me a lot with setting up a working water column model and inspired the idea of Neumann-type boundary conditions for turbulent quantities. I had the pleasure to meet George Mellor (Princeton, New Jersey) occasionally and to discuss problems of k-ε and k-kL models. His statement that he never saw a k-ε model properly reproducing the Monin-Obukhov similarity theory motivated me to start many of these model comparisons. Ole Petersen (Hørsholm, Denmark) opened my eyes for convective turbulence and gave me a lot of insight into modelling details. From Jean-Marie Beckers (Liège, Belgium) I learned a lot about specific numerical problems in oceanography. With Walter Eifler (Ispra, Italy) I had many turbulent

discussions on turbulence and turbulence modelling, especially on the skin effect and non-local transport. Karsten Bolding (Ispra, Italy) introduced me to the miracles of structured programming, UNIX and LINUX operating systems and other such useful features. Encho Demirov (Bologna, Italy) was the person to convince us to separate the GOTM turbulence module from the rest of the model in order to better integrate it into three-dimensional models such as MOM. Eric Deleersnijder (Louvain-la-Neuve, Belgium) was always interested in discussing about the numerical stability of turbulence closure models. Vittorio Canuto (New York, New York) visited me in autumn 1999 with five submitted manuscripts in his suitcase. We found that his new algebraic second-moment closure exactly filled the gap of the missing physically complete, numerically stable and computationally efficient turbulence closure model. Patrick Luyten (Brussels, Belgium) gave me at several occasions insight into his experience and understanding in the theory of oceanic turbulence. With Peter Craig (Hobart, Australia) I had some enlightening discussions about the effect of breaking surface waves on near-surface turbulence. Markus Meier (Norrköping, Sweden) is maybe the scientist with the most experience in embedding the k-ε model into three-dimensional circulation models and I felt during many discussions that we often had the same ideas independently. With Boris Galperin (St. Petersburg, Florida) I had some intense discussions on the basic difference between k-ε models and k-kL models, and we both concluded that there are none. I did not meet Lakshmi Kantha (Boulder, Colorado) before August 2000, but was impressed about the fact that he did some of the essence of my work already 10 years earlier, but never published it. Eric Skyllingstad (Sequim, Washington) gave me some useful hints on parameterisations of Langmuir circulation. Finally, I profited very much from the recent cooperation with Lars Umlauf (Lausanne, Switzerland) on the generic two-equation model.

There are two groups from which I learned all about observing turbulent dissipation rate in the field. One group is the MST team Adolf Stips (Ispra, Italy) and Hartmut Prandke (Petersdorf, Germany) who made their technology surviving the breakdown of the Berlin Wall in 1989. The other group is the FLY team from Bangor in Wales with John Simpson, Tom Rippeth and Neil Fisher. With the latter group, I was happy to have access to fresh first hand data from Liverpool Bay and they were happy to get them numerically reproduced in turn.

The following colleagues made a critical review of the manuscript for this study and gave numerous useful comments: Jean-Marie Beckers (Liège, Belgium), Karsten Bolding (Ispra, Italy), Stefan Heitmann (Hamburg, Germany), Christoph Holz (Hamburg, Germany), Patrick Luyten (Brussels, Belgium), Markus Meier (Norrköping, Sweden), Ole Petersen (Hørsholm, Denmark), Adolf Stips (Ispra, Italy), Lars Umlauf (Darmstadt, Germany), and Manuel Ruiz Villarreal (Hamburg, Germany).

Furthermore, I am grateful to Wolfgang Rodi (Karlsruhe, Germany), from whose publications I profited a lot, for writing the foreword to this book.

Much more than all funding agencies and colleagues, it was my family who gave me the necessary spiritual support and motivation for this study. Therefore, this book is dedicated to my wife Anne who accepted my laptop even on the Sunday breakfast table, my daughter Marie with whom I had to postpone so much Pinocchio reading and to my son Jakob who was born during the compilation of the internal wave section.

Table of Contents

1 Introduction

The pioneering work on statistical turbulence closure schemes performed in the 1970s by many different researchers has been concisely reviewed by *Rodi* [1980]. In those days, complex turbulence schemes were mainly applied in the field of computational fluid dynamics with its well-defined model problems. This restriction to technical and engineering applications can be explained by several arguments: clearly defined model domains and forcing, higher relevance of complex physical features such as non-hydrostatic pressure, bigger computer resources due to better funding e.g. from nuclear research programs, and maybe some more reasons. Apart from technical and engineering applications, higher order turbulence closure schemes were more and more applied in atmospheric sciences as well, see e.g. the famous article by *Mellor and Yamada* [1974]. There, the demand for better turbulence closure models came mainly from meteorological institutes which wanted to improve their weather prediction models. In oceanography however, complex turbulence models were introduced rather late, see e.g. *Rosati and Miyakoda* [1988]. The reason might be that simple bulk models or length scale parametrisations gave reasonable answers and the scientific focus (understanding of general circulation) was not so much related to turbulence closure modelling. The limited computational resources were mainly used for achieving fine spatial resolution and long model runs, see e.g. the recent study by *Demirov and Pinardi* [2001] for the Mediterranean Sea. It has been shown in comparative studies by *Ruddick et al.* [1995] for coastal seas and by *Goosse et al.* [1999] for the global ocean that differential mixing parameterisations should at least consider processes such as production, dissipation and diffusion of turbulence in order obtain qualitatively acceptable results. The trend towards simple and fast turbulence closures is however still ongoing, see e.g. the work of *Large et al.* [1994] who suggested a bulk type empirical model which is wide-spread in oceanography today. In contrast to that, statistical turbulence closure models are believed to mix too inefficiently and exclude important physical processes such as non-local features. This attitude might be explained to a high degree by the work of *Martin* [1985] who compared bulk models with statistical turbulence closure models and found that the mixed layer depth is underpredicted by the latter models. There are many reasons for the failure of statistical models in predicting the depth of the mixed layer.

The main reason seems to be the insufficient consideration of internal waves. The role of these for mixing in the ocean is not fully understood yet and thus parameterisations of their effect on mixing can only be of preliminary character. There is considerable effort in better understanding the complex dynamics of internal waves going on in several international projects, one of them being the CARTUM (Comparative Analysis and Rationalisation of Second-Moment Turbulence Models) project funded by the European Community. Langmuir circulation, caused by the interaction of Stokes drift due to surface waves with mean shear is one other poorly understood mixing mechanism.

Statistical turbulence closure models rather than empirical bulk-type models are the appropriate tool for proper modelling of mixing in the ocean. There are two basic arguments for this. Statistical models do reflect many more physical properties of turbulence than only mixing. Higher statistical moments such as turbulent kinetic energy, its dissipation rate, temperature variance and so on are calculated and can thus be compared to observations. The second argument for statistical turbulence modelling is that bulk-type models cannot account for many processes in estuaries and coastal seas, such as strain-induced periodic stratification (*Simpson et al.* [1990]) or transport of high concentration suspended matter loads (*Winterwerp* [1999]). Since estuarine, shelf sea and ocean modelling studies are often combined, it is desirable that the models for their simulation are equipped with the same turbulence closure model.

Thus, statistical turbulence modelling leads to a better understanding of complex small-scale phenomena in the ocean, although it does not help to understand turbulence itself (*Lesieur* [1997]). Consequently, the focus of this book is put on phenomenological turbulence models rather than fundamental turbulence properties. For better understanding turbulence itself, completely different methods are used, such as Direct Numerical Simulation or Large Eddy Simulation as numerical methods or Particle Image Velocimetry (PIV, see *Bertuccioli et al.* [1999]) or the use of autonomous underwater vehicles (AUV, see *Thorpe et al.* [2002]) equipped with high-resolution sensors as new observational methods. These latter high-resolution methods can be used for finding better parameterisations for statistical turbulence models. However, they are not suitable for investigating macro-scale effects of turbulence such as mixed-layer deepening, tidal straining or the long-term effect of internal wave-mixing.

The aim of this book is to derive statistical turbulence closure models which are fairly general, theoretically well-founded and computationally efficient such that they can be used for a wide range of oceanic applications. This is what the title of this book stands for. It is obvious that these criteria are soft, and that not one only closure scheme will be found which is superior to all others. Furthermore, for each application another closure scheme would be preferable, depending on the complexity of the problem under investiga-

tion. Thus, many different turbulence closures are discussed in this book. The most important steps in the whole spectrum of turbulence closure modelling ranging from the Navier-Stokes equations to a computer executable code for statistically simulating turbulent boundary layer flow is described here. The major focus is put on two-equation turbulence models combined with algebraic second-moment closure schemes. Such models use dynamic equations for the turbulent kinetic energy and a length scale related turbulent quantity which might be the turbulent dissipation rate, the macro length scale, the turbulence frequency or a fully generic length scale equation. Mainly two such models have been competing in oceanography during the last two decades, the k-ε model developed at the Imperial College in London (see *Launder and Spalding* [1972]) and the k-kL model developed at Princeton University, New Jersey by *Mellor and Yamada* [1982]. Here, k stands for turbulent kinetic energy, ε for its dissipation rate and L for the macro length scale. Both models have been applied independently for many years but only recently be compared in detail (*Burchard et al.* [1998], *Burchard et al.* [1999], *Baumert and Peters* [2000]). Both models have been protected by its protagonists like icons. The result of these comparative studies is, that after modifications[1] of the buoyancy production term suggested by *Burchard and Baumert* [1995] for the k-ε model and *Burchard* [2001a] for the k-kL model both models are basically equivalent. It seems to be much more relevant with which second-moment closures these two-equation models are combined, see *Burchard et al.* [1998].

In the same way as numerical models, turbulence measurements in the ocean have become more detailed and reliable in recent years. This is specifically true for dissipation rate observations with micro-structure shear probes as they have been introduced into oceanography by *Osborn* [1974]. Consequently, several comparative model studies have been carried out of which some are discussed in this book. However, such comparative studies can only reach agreement between model results and observations up to a certain degree. This is because turbulence measurements are – due to their statistical character – often based on at least as many idealising assumptions as the numerical models. Furthermore, the forcing data are never complete in a sense that all changes of certain physical parameters in the domain under investigation are explained by fluxes through the boundaries and inner sources or sinks. Therefore, the argument is that turbulence closure models cannot properly be validated with the aid of field observations. The models have to be validated by means of theoretical considerations, and with laboratory experiments or numerical experiments with higher order models such as Large Eddy Simulation.

The final aim of developing practically applicable turbulence closure schemes must be their integration into three-dimensional ocean models. One

[1] These modifications have already been suggested by *Kantha* [1988] but have never been published.

precondition for this is the numerical robustness of these turbulence closure models in the sense that they perform well also for coarse temporal and spatial resolution and numerical noise from the mean flow equations. Another precondition is the availability of a well-tested computer code which can be integrated into three-dimensional models without any further changes, since a complete three-dimensional model is not an appropriate environment for developing turbulence closure models. Development and validation of turbulence models must be performed in the framework of one-dimensional water column models. Therefore, the water column model GOTM (General Ocean Turbulence Model) has been developed and published in the World Wide Web under the address `http://www.gotm.net`, see also the report by *Burchard et al.* [1999]. The model concepts discussed here have been implemented into three-dimensional ocean models and applied to ocean circulation studies. One convincing example is the work of *Meier* [2001] who uses the k-ε model with an algebraic second-moment closure recently presented by *Canuto et al.* [2001] (which is evaluated in the present book as a physically sound and numerically stable closure) for high-resolution simulations of the circulation and heat and salt transport in the Baltic Sea.

This book is structured as follows. After this introduction, the viscous equations of motion are briefly discussed in chapter 2, for a complete mathematical derivation, see e.g. *Chorin and Marsden* [1979]. It is described how turbulence results from these dynamic equations. The problem of multiple scales due to the non-linearity of the Navier-Stokes equations is briefly mentioned. As solution to the problem, the Reynolds decomposition is presented and defined in such a way that the Reynold's averaged equations are derived. The closure problem of turbulence is shown and various parameterisations for the second moments are presented.

In chapter 3, the boundary layer approximation is made such that hydrostatic equations are obtained for which only a few second moments have to be parameterised. The local equilibrium assumption for second moments finally leads to the algebraic second-moment closure schemes for which this book aims for. Non-dimensional stability functions are derived which contain the whole information of the second-moment closure. Four different classes of stability functions are investigated in more detail in terms of the performance of their equilibrium versions for some basic flow situations. Various two-equation turbulence models are then presented, among them the k-ε and the k-kL models, but also a generic two-equation model which has recently been developed by *Umlauf and Burchard* [2001]. The concept of homogeneous shear-layers and the resulting simplifications of the turbulence equations are then used for showing a new perspective of two-equation turbulence models. The steady-state Richardson number is defined which helps better understanding the length scale related equation and calibrating the buoyancy term therein. Finally, modifications are discussed which allow for the consideration of breaking surface waves, internal wave effects and Langmuir circulation.

Numerical discretisation methods are presented in chapter 4. Three problems are discussed in more detail: Positive definite schemes in order to guarantee positivity of turbulent quantities, numerical conservation of energy flux between mean flow and turbulence and numerically stable and accurate discretisations of boundary conditions for turbulent quantities.

The General Ocean Turbulence Model (GOTM) in which most of the physical, mathematical and numerical features discussed here are realised as computer code, is briefly presented in chapter 5.

First model calibrations and validations are performed in chapter 6. These idealistic scenarios are open channel flow, a wind-entrainment study motivated by the *Kato and Phillips* [1969] laboratory experiment and a convective penetration study motivated by the *Willis and Deardorff* [1974] laboratory experiment.

Finally, some one-dimensional water column simulations of field campaign measurements are discussed in chapter 7. The classical scenarios Ocean Weather Station Papa in the Northern Pacific Ocean and the Fladenground Experiment 1976 in the Northern North Sea with only temperature profile observations as validation data are simulated. Four more recent campaigns including turbulence measurements in the Irish Sea, Liverpool Bay, again the Northern North Sea and Lago Maggiore (a lake) are simulated as well.

Ten perspectives for future research resulting from the discussions in this book are listed in section 8.

2 Basic model assumptions

2.1 The viscous equations of motion

In this section, the Navier-Stokes equations which are valid basically for all flow situations are briefly introduced. It is then discussed in detail why realistic environmental problems involving a range of temporal and spatial scales cannot be reproduced on today's (and tomorrow's) computers by means of these equations.

2.1.1 Continuum hypothesis

Seen from almost all viewpoints, fluids are considered as continuous media. The so-called *continuum hypothesis* is based on the fact that the temporal and spatial scales of the underlying molecular structure are clearly separated from the macroscopic scales of e.g. $(1\ \mathrm{mm})^3$. In contrast to this macroscopic scale, the average distance between two water molecules is of the order of 10^{-7} mm.

By making this continuum hypothesis, some of the most relevant properties of a real fluid have to be parameterised such that they are properly represented in the continuous model fluid. The most important properties are the concepts of viscosity and density. In a continuous fluid, the dynamic viscosity μ relates the frictional forces in the fluid, $\mathcal{F}_i$, to the gradients of flow velocity[1], v_i:

$$\mathcal{F}_i = \mu \partial_{jj} v_i. \tag{2.1}$$

The properties of viscosity can most easily be explained by considering a so-called perfect gas, in which the molecules are freely moving without any forces between them, except during mutual collisions. When denoting the root mean square (r.m.s.) speed of one single molecule with $\mathcal{U}$ and the average time between two collisions with $\mathcal{T}$, then the viscosity ν of a perfect gas can be approximated by

[1] Flow velocity is defined as mean velocity of molecules averaged over a volume considerably larger than the free-path length. For an exact statistical definition of flow velocity, see *Batchelor* [1967].

$$\nu = \frac{\mu}{\rho} \approx \mathcal{U}^2\mathcal{T} = \mathcal{L}\mathcal{U} \tag{2.2}$$

with the so-called free-path length $\mathcal{L} = \mathcal{U}\mathcal{T}$, the density ρ and the kinematic viscosity ν. The density ρ is defined as the r.m.s. mass per unit volume and strongly depends on the temperature and the pressure[2] of the fluid. In liquids however, such as water, molecules are packed much more closely such that repulsive and attractive forces between them cannot be neglected any more. Thus the viscosity of water is more complex and cannot be explained by this simple imagination of molecule collisions.

The parameterisation of these inter-molecular forces by the concept of viscosity allows for the accurate description of most macroscopic processes. One important feature which is however not retained any more with this concept is surface tension, which occurs at the interfaces between fluids and gases. Due to inter-molecular forces, there is the tendency to minimise the area of this interface. This has the consequence that gas bubbles mixed into a liquid and liquid drops in gases tend to spherical structures[3]. With this minimisation of the gas-liquid interface area, the transfer of properties and solutes between gas and liquid is minimised as well. This has the consequence that the air-sea interactions between ocean and atmosphere, which are greatly determined by breaking surface waves and subsequent bubble injection into the water and water drops in the air, cannot be directly simulated with this kind of concept. Thus, parameterisations for the air-sea interactions need to be introduced already on this closure level.

For further reading about this topic, the text book of *Batchelor* [1967] is recommended.

2.1.2 Navier-Stokes equations

The equations of motion of a Newtonian fluid[4] have already been derived in the 19$^{\text{th}}$ century by *Navier* [1822] and *Stokes* [1845] and are known as the Navier-Stokes equations. After applying the so-called Boussinesq approximation (vertical density deviations from the mean value are small[5]) the following equations of motion remain (see e.g. *Sander* [1998] or *Haidvogel and Beckmann* [1999]):

$$\partial_j v_j = 0 \tag{2.3}$$

[2] For proper statistical definitions of temperature and pressure, see *Batchelor* [1967].

[3] It also allows insects to move on the water surface without getting wet.

[4] Water behaves to a high degree like a Newtonian fluid, which is characterised by a linear relationship between the non-isotropic parts of the stress and the rate-of-strain tensor, see *Batchelor* [1967].

[5] By means of the Boussinesq approximation, the mass conservation equation simplifies to the incompressibility condition (2.3).

$$\partial_t v_i + v_j \partial_j v_i - \nu \partial_{jj} v_i + 2\varepsilon_{ijl}\Omega_j v_l = -\frac{\partial_i p}{\rho_0} - \frac{g_i}{\rho_0}\rho. \tag{2.4}$$

The equations are given in a Cartesian coordinate system with the first coordinate $x_1 = x$ pointing eastwards, the second coordinate $x_2 = y$ pointing northwards and the third coordinate $x_3 = z$ pointing upwards, i.e. normal to the geopotential. Time is denoted by t. Here, $v_1 = u$, $v_2 = v$ and $v_3 = w$ are the eastward, the northward and the upward velocity components, respectively. Further prognostic variables are potential density ρ and pressure p. A constant reference density is given by ρ_0. The flow is assumed to be influenced by geophysical properties such as gravitation $g_i = (0, 0, g)$ and rotation $\Omega_i = (0, \Omega\cos(\Phi), \Omega\sin(\Phi))$ where $g = 9.81\ \mathrm{m\,s^{-2}}$ is the gravitational acceleration and $\Omega = 7.289 \cdot 10^{-5}\ \mathrm{s^{-1}}$ is the angular velocity of the earth and Φ the latitude. The kinematic viscosity ν has a value of $\nu = 1.3 \cdot 10^{-6}$ $\mathrm{m^2 s^{-1}}$ at 10°C, which strongly varies with temperature such that its value decreases to $\nu = 8.0 \cdot 10^{-7}$ $\mathrm{m^2 s^{-1}}$ at 30°C.

For the alternating tensor ε_{ijk}, see equation (9.5) in section 9.1.

Although the Navier-Stokes equations (2.3) and (2.4) have been known for so long and although they are the basis for treating all kinds of fluid dynamics problems ranging from small-scale technical applications to climate prediction studies, the existence of smooth and physically reasonable solutions could not yet be proven (see *Fefferman* [2000]). This problem is considered by mathematicians as being so severe that it has actually been named as one of seven Millennium Prize Problems by the Clay Mathematics Institute of Cambridge, Massachusetts and its solution will be awarded with one million US Dollar. This dramatic gap in the theoretical understanding of fluid dynamics should always be kept in mind when dealing with systems of partial differential equations derived from the Navier-Stokes equations. However, numerical solutions of the Navier-Stokes can be found such that the hypothesis of existence of smooth and physically reasonable solutions is supported.

2.1.3 Tracer equations

Equations for the active tracers potential temperature T and salinity S are needed in order to calculate the density ρ in marine waters. They can be derived on similar grounds than the Navier-Stokes equations. The potential temperature budget equation has the following form:

$$\partial_t T + v_j \partial_j T - \nu' \partial_{jj} T = \frac{\partial_z I}{c'_p \rho_0}, \tag{2.5}$$

where I is local solar radiation in the water, c'_p the specific heat capacity of water, and ν' the molecular diffusivity of temperature, which has a value

of $\nu' = 1.38 \cdot 10^{-7}$ m^{2}s^{-1}, slightly varying with temperature. The salinity budget equation can be written as:

$$\partial_t S + v_j \partial_j S - \nu'' \partial_{jj} S = 0, \tag{2.6}$$

where ν'' is the molecular diffusivity for salinity, which has a value of $\nu'' = 1.1 \cdot 10^{-9}$ m^{2}s^{-1}.

The potential density ρ of water is determined by the potential temperature T, the salinity S and the pressure p:

$$\rho = \rho(T, S, p). \tag{2.7}$$

For most oceanic applications, the equation of state is approximated by the UNESCO equation of state, see *Gill* [1982]. For lakes however, a slightly modified equation of state should be used in order to account for small salt concentrations (see *Chen and Millero* [1986]). Often, more simple approximations are sufficient:

$$\rho = \rho_0 + \beta_T (T - T_0) + \beta_S (S - S_0). \tag{2.8}$$

with the thermal and haline volume expansion coefficients $\beta_T = \partial_T \rho(T_0, S_0, 0)$ and $\beta_S = \partial_S \rho(T_0, S_0, 0)$, respectively and the reference density $\rho_0 = \rho(T_0, S_0, 0)$.

Together with suitable initial and boundary conditions, the equations (2.3) - (2.7) form a closed system for the seven prognostic quantities v_1, v_2, v_3, p, T, S and ρ. Further dynamic equations for other properties or dissolved substances (e.g. oxygen or carbon dioxide) could easily be added to this system of equations in order to model more complex environmental situations.

2.1.4 Phenomenology of turbulence

The relevant processes in hydrodynamic flows can be described with great accuracy by the set of equations given above. Because of the turbulent dynamics which develop in such flows due to non-linear instabilities, predictions can however only be accurate in a statistical sense. Turbulence is by definition a random and thus unpredictable process (see *Lesieur* [1997] for an in depth discussion). The idealised view for turbulence generated in simple flow geometries is that non-linear instabilities first create large overturns. The kinetic energy contained in these eddies is then transferred to smaller and smaller eddies. Finally, the turbulent eddies are that small that their kinetic energy dissipates into heat due to viscous friction. This so-called energy cascade from larger to smaller scales has been poetically described by *Richardson* [1922] (loc. cit. *Lesieur* [1997], p. 177):

> Big whirls have little whirls,
> which feed on their velocity,

and little whirls have lesser whirls,
and so on to viscosity.

In the ocean of course, the generation of turbulence is much more complex. Due to internal and surface waves and viscous effects near boundaries, turbulence is produced on a whole range of scales.

It was *Kolmogorov* [1941] who predicted for the idealised case of stationary isotropic turbulence at high Reynolds numbers (see definition (2.10)) that the rate of energy dissipation ε at viscous scales controls the whole energy cascade in the so-called inertial subrange. This part of the spectrum lies between the integral wave number (macro-scale) characterising the large energy-containing scales at which turbulence is produced and the dissipative wave number (Kolmogorov micro-scale) characterising the small dissipative scales. Such a typical turbulence energy spectrum is sketched in figure 2.2. According to the famous two-thirds law by *Kolmogorov* [1941], the turbulent energy spectrum for fully developed turbulence scales as follows in the inertial subrange:

$$E(k_w) \propto \varepsilon^{2/3} k_w^{-5/3} \tag{2.9}$$

with the energy spectrum $E(k_w)$ and the wave number k_w.

This means in turn that the energy input to turbulence at the macro-scale determines the dissipation rate ε (see e.g. *Kantha and Clayson* [2000]). This assumption of a spectral equilibrium is the theoretical basis on which all turbulence modelling builds up.

2.1.5 Range of scales

The set of equations (2.3) - (2.7) has been numerically discretised and solved on computers since several years in the field of computational fluid dynamics for solving idealised small-scale problems such as flows around cylinders or between plates. This method of numerically calculating flow problems is known as Direct Numerical Simulation (DNS). However, the applicability of this method to real-world situations is limited by the range of spatial and temporal scales involved. These cover several orders of magnitude, see figure 2.1 for relevant scales in the ocean. The major problem here is that processes on all scales interact with each other due to the non-linear character of the Navier-Stokes equations such that a consideration of only the scales of interest is not sufficient.

One quantity which characterises the intensity of turbulence is the dimensionless integral-scale Reynolds number

$$R_e = \frac{qL}{\nu} \tag{2.10}$$

with the r.m.s. velocity of the turbulent fluctuations, q, and the integral length scale of the turbulent motions, L. The latter length scale can also be

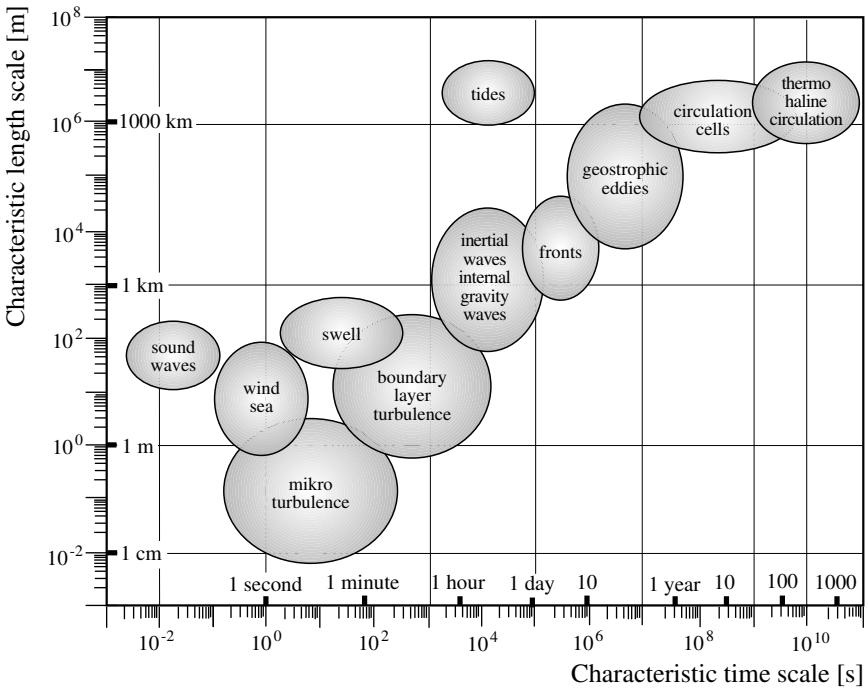

Fig. 2.1. Temporal and spatial scales of various typical processes in the ocean from *von Storch and Zwiers* [1999]. Courtesy to Hans von Storch, Geesthacht, Germany.

interpreted as the macro length scale of turbulence representing the size of the energy-containing eddies (see *Kantha and Clayson* [2000]). The Reynolds number can be interpreted as the ratio of the non-linear terms (advection) and the linear terms (diffusion) in the Navier-Stokes equations. With typical sizes of $q = 0.1$ ms^{-1} and $L = 1$ m like in the oceanic mixed layer values of $R_e \approx 10^5$ can easily be reached. According to *Frisch* [1995] the number of grid points to fully resolve this flow up to the smallest eddies grows with $R_e^{9/4}$. With a time step proportional to the grid size, the numerical effort for the calculation of such a problem for a certain number of eddy turnovers behaves like R_e^3. Since with todays computers only problems with integral-scale Reynolds numbers up to $R_e \approx 10^4$ can be solved, we are even far away from fully resolving a few large (i.e. energy-containing) eddies. Since real-world problems itself are some orders of magnitudes larger than such large eddies, it is for now and for the near and far future impossible to entirely solve them by applying DNS (see *Lesieur* [1997]). Only small details such as turbulence caused by Kelvin-Helmholtz instability in the thermocline could be so far investigated by means of DNS, see *Smyth et al.* [2001].

One attempt to solve this problem is Large Eddy Simulation (LES). With this method, the large energy-containing eddies are resolved. The smaller scales into which the kinetic energy is transferred are parameterised with a sub-scale turbulence closure model. Such a division of the flow is justified since it is the large eddies which most efficiently transport properties of the fluid (see *Ferziger and Perić* [1999]). This division of the flow in resolved and unresolved parts is obtained by a spatial filtering of the Navier-Stokes equations. The filter length is determined by the grid size of the numerical model. This filter length should idealistically be inside the inertial subrange replacing the Kolmogorov micro-scale by the filter scale without significantly changing the dynamics of the large eddies. LES models are by definition three-dimensional and non-hydrostatic. Thus, LES models are in principle based on the same set of equations as DNS with the only difference that now the viscosity ν and the diffusivities ν' and ν'' are replaced by eddy viscosities and diffusivities obtained from a turbulence closure model (see e.g. *Ferziger* [1995]). Depending on the sub-grid scale model, these eddy viscosities and diffusivities might be different for horizontal and vertical directions leading to a tensorial formulation for the turbulent mixing. A hierarchy of subgrid scale models of various complexities is given by *Canuto* [1994].

LES has been applied to a variety of oceanic problems in recent years. Deep convection in the ocean has been studied by *Jones and Marshall* [1993], *Send and Marshall* [1995] and *Denbo and Skyllingstad* [1996]. Processes in the equatorial Pacific have been investigated by *Large and Gent* [1999] and *Skyllingstad et al.* [1999], ice-ocean interactions have been simulated by *Kämpf and Backhaus* [1999], and the phenomenon of Langmuir circulation as consequence of wave-current interaction has been studied by *Skyllingstad and Denbo* [1995] and *McWilliams et al.* [1997]. The deep diurnal cycle of turbulence in the surface mixed layer of the equatorial Pacific Ocean has been studied by *Wang et al.* [1998]. LES has been extensively used for validating one-dimensional turbulence closure models, see e.g. *Ayotte et al.* [1996] and *Large and Gent* [1999]. For some idealised scenarios LES has been frequently applied for statistical properties of turbulence which cannot easily be quantified in laboratory experiments or field studies. For a recent study of the effect of rotation on statistical properties of convective turbulence, see *Mironov et al.* [2000]. Most of these studies deal with convective turbulence in which the size of the large eddies is relatively large with respect to the relevant mean flow scales processes such as the mixed layer depth. For stably stratified flows, where the energy-containing eddies are limited in size, LES is in principle computationally too costly for resolving the turbulent motion down into the inertial subrange. Sometimes, nesting techniques coupling models for larger scales to models for smaller scales are used for overcoming these problems, see *Sullivan et al.* [1998].

All these applications are however in principle used for studying processes which are macroscopically homogeneous in the horizontal direction. This is

obtained by using periodic or solid wall boundary conditions at the lateral boundaries and spatially homogeneous (often slightly disturbed by noise) surface forcing. Due to limited computer resources, the application of LES models to more complex three-dimensional situations is still in the far future.

The method suitable for such more complex flow situations is the so-called ensemble averaging resulting in the so-called Reynold's-averaged Navier-Stokes equations (RANS), from which various classes of turbulence closure models can be derived, see section 2.2.3. It is characteristic for RANS that they do not contain any random turbulent motion. These are all parameterised by the sub-scale turbulence model in a statistical sense. Thus, we have a hierarchy of methods at hand, ranging from DNS for resolving the entire turbulence over LES resolving large eddies and parameterising smaller structures to RANS where all turbulent motion is parameterised (see *Ferziger* [1995]). The range of resolved and parameterised scales are shown in figure 2.2.

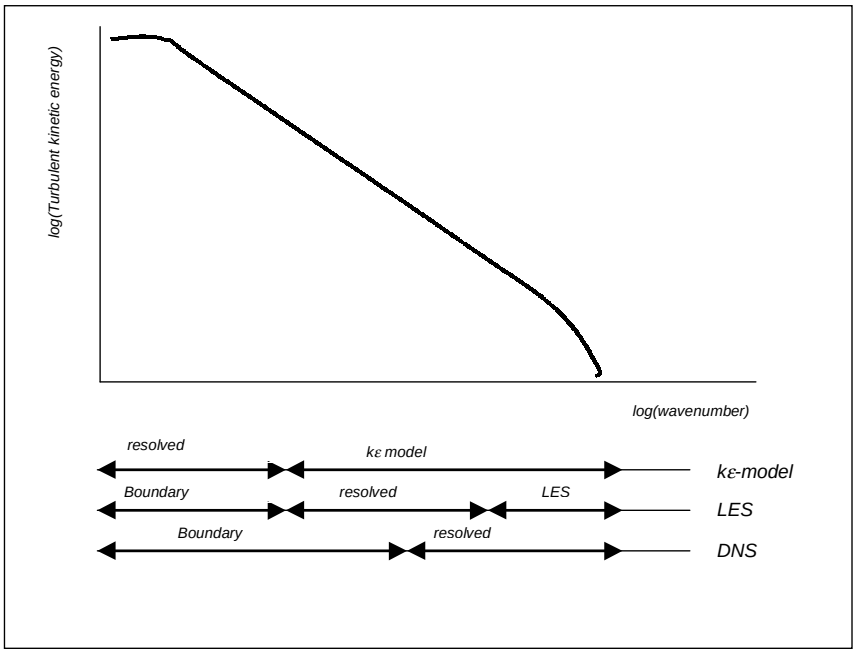

Fig. 2.2. Range of resolved and parameterised scales for Reynold's averaged models (here: k-ε model), Large Eddy Simulation (LES) and Direct Numerical Simulation (DNS). The curve shown above is an idealised turbulence energy spectrum ranging from low wave numbers (left, large eddies) to high wave numbers (right, dissipative Kolmogorov scale). Courtesy to Ole Petersen, Hørsholm, Denmark.

In the following, methods based on RANS are discussed in further detail.

2.2 The Reynold's decomposition

Here, the dynamic equations are derived which result from the Reynold's decomposition. It is discussed, how transport equations for unknown higher moments can be constructed which in turn contain new unknown moments of one order higher. This leads to the well-known Friedmann-Keller series (see *Keller and Friedmann* [1924]) and the turbulence closure problem.

2.2.1 One-point closures

The method derived in the following and used throughout this work is often referred to as one-point closure modelling. Statistical properties of a flow are considered for each single point in the physical space, allowing for correlations between different physical quantities or autocorrelations in this point. By doing so, characteristics such as mean flow, fluctuations, variances etc. are defined, which have certain significant physical meanings for the flow under consideration. This method of one-point closure modelling is suitable for complex geophysical flows, since it is economic in terms of computational costs and has a certain degree of realism in modelling these statistical flow properties of interest. It should however be noted that this method does not contribute to a deeper understanding of the underlying turbulence itself. It is therefore necessary to extensively validate models within the class of one-point closure modelling against results of DNS and LES, and also against laboratory and field data.

In contrast to this, two-point closure models deal with the correlations of physical properties between various scales of motion, in the physical as well as in the Fourier space. This theory has been described in detail by *Orszak* [1977]. It is very promising for investigating various properties of turbulence, since it is much faster than DNS such that high Reynolds numbers can be reached. However, similarly to LES, it is still too costly for solving complex geophysical fluid problems. Two-point closure models can however be exploited in the framework of renormalisation group theory for the determination of empirical parameters for one-point closure models, see e.g. *Canuto et al.* [2001] and the work of Semion Sukoriansky and Boris Galperin carried out in the framework of the CARTUM project (pers. comm., see section 5.6).

2.2.2 Ensemble averages

For any prognostic variable U, a decomposition into a mean field $\bar{U} = \langle U \rangle$ and a fluctuating field $\tilde{U}$ is formally carried out:

$$U = \bar{U} + \tilde{U}. \tag{2.11}$$

The fluctuating part of the flow is defined such that the mean of it vanishes:

$$\langle \tilde{U} \rangle = 0 \tag{2.12}$$

This decomposition is named after *Reynolds* [1895] who observed turbulent motion in pipe flows. Generally, such a decomposition is only well-defined when a clear separation between small and large scales, a so-called spectral gap, exists. For the phenomenon of turbulence a spectral gap is generally not present in contrast to the separation between molecular motions from flow motions which leads to the continuum hypothesis discussed above. However, with a suitable averaging technique, the decomposition can be formally carried out.

Various averaging procedures have been proposed. For example, the averaging by means of a temporal filter is quite an arbitrary procedure, see *Hinze* [1975]. Here, the theoretical concept of ensemble averaging is a way around this problem: Assume that a certain realisation of a flow situation is repeated n times on the same domain with the same macroscopic initial conditions and external forcing. At a certain time t_0 and at a certain position (x_0, y_0, z_0) the property U_i is observed for the experiment i. The ensemble average is then defined as the mean value of all $U_i(t_0, x_0, y_0, z_0)$ for the limit of infinitely many realisations:

$$\bar{U}(t_0, x_0, y_0, z_0) = \lim_{n \to \infty} \frac{1}{n} \sum_{i=1}^{n} U_i(t_0, x_0, y_0, z_0). \tag{2.13}$$

The following four properties of the averaging process are needed for the derivation of the Reynold's equations, see section 2.2.3:

1. Linearity:
$$\langle U + \lambda V \rangle = \langle U \rangle + \lambda \langle V \rangle. \tag{2.14}$$
2. Derivatives and averages commute:
$$\langle \partial_x U \rangle = \partial_x \langle U \rangle \tag{2.15}$$
3. Double averages:
$$\langle \langle U \rangle \rangle = \langle U \rangle \tag{2.16}$$
4. Product average:
$$\langle U \langle V \rangle \rangle = \langle U \rangle \langle V \rangle \tag{2.17}$$

It can be shown that only the ensemble averaging procedure (2.13) fulfils the properties (2.14) - (2.17), see *Mohammadi and Pironneau* [1994]. However, other than temporal or spatial filters, this cannot be applied to the analysis of real world phenomena. According to the ergodic assumption however, it is assumed that for stationary and homogeneous turbulence the

ensemble average can be identically replaced by temporal and spatial filters, see *Hinze* [1975]. For those who observe turbulence in the ocean, this has the important consequence that temporal and spatial averaging intervals have to be chosen such that turbulence within these intervals can be regarded as stationary and homogeneous in principle.

2.2.3 The Reynold's equations

By applying the ensemble average operation (2.13) to the system of equations (2.3) - (2.6) and applying the rules (2.14) - (2.17), the following budget equations for velocities and tracers result:

$$\partial_t \bar{v}_i + \bar{v}_j \partial_j \bar{v}_i - \partial_j(\nu \partial_j \bar{v}_i - \langle \tilde{v}_j \tilde{v}_i \rangle) + 2\varepsilon_{ijl}\Omega_j \bar{v}_l = -\frac{\partial_i \bar{p}}{\rho_0} - g_i \frac{\bar{\rho}}{\rho_0} \tag{2.18}$$

$$\partial_j \bar{v}_j = 0 \tag{2.19}$$

$$\partial_t \bar{T} + v_j \partial_j \bar{T} - \partial_j(\nu' \partial_j \bar{T} - \langle \tilde{v}_j \tilde{T} \rangle) = \frac{\partial_z I}{c'_p \rho_0}, \tag{2.20}$$

$$\partial_t \bar{S} + v_j \partial_j \bar{S} - \partial_j(\nu'' \partial_j \bar{S} - \langle \tilde{v}_j \tilde{S} \rangle) = 0. \tag{2.21}$$

For the density, it is assumed that the Taylor expansion around $(\bar{T}, \bar{S}, \bar{p})$ converges fast such that the higher order terms can be neglected (see *Burchard* [1995]):

$$\bar{\rho} = \langle \rho(\bar{T} + \tilde{T}, \bar{S} + \tilde{S}, \bar{p} + \tilde{p}) \rangle \approx \rho(\bar{T}, \bar{S}, \bar{p}). \tag{2.22}$$

Some new terms appear in the equations (2.18) - (2.22) such that the system is no longer closed. These second moments (statistical correlations between two flow properties in the same location) are the Reynolds stresses $\langle \tilde{v}_i \tilde{v}_j \rangle$, turbulent heat fluxes[6] $\langle \tilde{v}_i \tilde{T} \rangle$ and the turbulent salinity fluxes $\langle \tilde{v}_i \tilde{S} \rangle$, i.e. in total 12 new terms for which closure assumptions have to be made.

The Reynold's equations (2.18) may be transformed into a transport equation for the mean kinetic energy per unit mass, defined as

$$e = \frac{1}{2} \bar{v}_i^2. \tag{2.23}$$

After multiplying (2.18) by $\bar{v}_i$, the following energy equation is obtained:

[6] Heat flux and temperature flux are used here synonymously, assuming basically constant density and specific heat content.

$$\begin{aligned}&\partial_t e + \partial_j \left(\bar{v}_j e + \bar{v}_i \langle \tilde{v}_i \tilde{v}_j \rangle - \nu \partial_j e + \frac{\bar{v}_j \bar{p}}{\rho_0} \right) \\ &= \langle \tilde{v}_i \tilde{v}_j \rangle \partial_j \bar{v}_i - \frac{g \bar{v}_3 \bar{\rho}}{\rho_0} - \nu (\partial_j \bar{v}_i)^2 .\end{aligned} \tag{2.24}$$

On the left hand side, only gradient terms appear which redistribute the energy due to advective or diffusive processes whilst on the right hand side appear fluxes between mean kinetic energy and turbulence (see the equation for turbulent kinetic energy, (2.31)), fluxes between mean kinetic and potential energy and direct viscous dissipation into heat.

2.2.4 The Reynolds stress and turbulent flux equations

For the so-called second moments, transport equations can be derived from the viscous equations and the Reynold's averaged equations. In order to obtain equation for the Reynolds stresses $\langle \tilde{v}_i \tilde{v}_j \rangle$, equation (2.4) is subtracted from equation (2.18) which gives an equation for $\tilde{v}_i$. This will then be formally multiplied by $\tilde{v}_j$ and added to the same equation but with exchanged indices. After ensemble averaging the resulting equation and applying the rules (2.14) - (2.17), transport equations for the Reynolds stresses are obtained:

$$\begin{aligned}&\partial_t \langle \tilde{v}_i \tilde{v}_j \rangle + \partial_l \left(\bar{v}_l \langle \tilde{v}_i \tilde{v}_j \rangle + \langle \tilde{v}_l \tilde{v}_i \tilde{v}_j \rangle - \nu \partial_l \langle \tilde{v}_i \tilde{v}_j \rangle \right) \\ &= \underbrace{-\partial_l \bar{v}_i \langle \tilde{v}_l \tilde{v}_j \rangle - \partial_l \bar{v}_j \langle \tilde{v}_l \tilde{v}_i \rangle}_{P_{ij}} \underbrace{- 2\Omega_l (\varepsilon_{ilm} \langle \tilde{v}_j \tilde{v}_m \rangle + \varepsilon_{jlm} \langle \tilde{v}_i \tilde{v}_m \rangle)}_{\Omega_{ij}} \\ &\quad \underbrace{- \frac{1}{\rho_0} \{ g_i \langle \tilde{v}_j \tilde{\rho} \rangle + g_j \langle \tilde{v}_i \tilde{\rho} \rangle \}}_{B_{ij}} \underbrace{- \frac{1}{\rho_0} (\langle \tilde{v}_i \partial_j \tilde{p} + \tilde{v}_j \partial_i \tilde{p} \rangle)}_{\Pi_{ij}} \\ &\quad \underbrace{- 2\nu \langle (\partial_l \tilde{v}_j)(\partial_l \tilde{v}_i) \rangle}_{\varepsilon_{ij}} .\end{aligned} \tag{2.25}$$

It was *Chou* [1940] who first derived such a transport equation for the Reynolds stresses, see also *Chou* [1945]. The terms on the right hand side are grouped together such that P_{ij} is the shear production, Ω_{ij} redistribution due to rotation, B_{ij} the buoyancy production, Π_{ij} the pressure-strain correlator and ε_{ij} the dissipation of the Reynolds stress $\langle \tilde{v}_i \tilde{v}_j \rangle$.

After an analogous procedure, transport equations for the turbulent heat and salinity fluxes are obtained as well:

$$\begin{aligned}
&\partial_t\langle\tilde{v}_i\tilde{T}\rangle + \partial_j\Big(\bar{v}_j\langle\tilde{v}_i\tilde{T}\rangle + \langle\tilde{v}_i\tilde{v}_j\tilde{T}\rangle - (\nu+\nu')\partial_j\langle\tilde{v}_i\tilde{T}\rangle\Big) \\
&\quad + \nu'\langle\tilde{T}\partial_{jj}\tilde{v}_i\rangle + \nu\langle\tilde{v}_i\partial_{jj}\tilde{T}\rangle \\
&\quad = \underbrace{-\langle\tilde{v}_i\tilde{v}_j\rangle\partial_j\bar{T} - \langle\tilde{v}_j\tilde{T}\rangle\partial_j\bar{v}_i}_{P_{iT}} - \underbrace{2\varepsilon_{ijl}\Omega_j\langle\tilde{v}_l\tilde{T}\rangle}_{\Omega_{iT}} \\
&\quad - \underbrace{\frac{g_i}{\rho_0}\langle\tilde{T}\tilde{\rho}\rangle}_{B_{iT}} - \underbrace{\frac{1}{\rho_0}\langle\tilde{T}\partial_i\tilde{p}\rangle}_{\Pi_{iT}} - \underbrace{2(\nu+\nu')\langle(\partial_j\tilde{v}_i)(\partial_j\tilde{T})\rangle}_{\varepsilon_{iT}}
\end{aligned} \tag{2.26}$$

Here, P_{iT} is the mean gradient production, Ω_{iT} redistribution due to rotation, B_{iT} the buoyancy production, Π_{iT} the pressure-strain correlator and ε_{iT} the dissipation of the turbulent heat flux $\langle\tilde{v}_i\tilde{T}\rangle$. The solar radiation is here considered to be non-fluctuating. This is indeed a crude assumption since radiation in the water column should be expected to be fluctuating due to differential refraction at surface waves and organic and anorganic suspended matter. To the knowledge of the author of this book, this phenomenon has not yet been investigated in detail. The transport equation for the turbulent salinity flux $\langle\tilde{v}_i\tilde{S}\rangle$ is analogue and is therefore not shown here.

Since the density fluctuations $\tilde{\rho}$ are usually approximated by the linear term of its Taylor series (see *Burchard* [1995]),

$$\tilde{\rho} \approx \tilde{T}\partial_{\bar{T}}\rho(\bar{T},\bar{S}) + \tilde{S}\partial_{\bar{S}}\rho(\bar{T},\bar{S}), \tag{2.27}$$

transport equations are also needed for the second moments $\langle\tilde{T}^2\rangle$, $\langle\tilde{S}^2\rangle$ and $\langle\tilde{T}\tilde{S}\rangle$ in order to calculate the B_{iT} term in the $\langle\tilde{v}_i\tilde{T}\rangle$ equation. Exact transport equations for those can be derived as well, examples are given here for $\langle\tilde{T}^2\rangle$:

$$\begin{aligned}
&\partial_t\langle\tilde{T}^2\rangle + \partial_j\Big(\bar{v}_j\langle\tilde{T}^2\rangle + \langle\tilde{v}_j\tilde{T}^2\rangle + \nu'\partial_j\langle\tilde{T}^2\rangle\Big) = \\
&\quad \underbrace{-2\langle\tilde{v}_j\tilde{T}\rangle\partial_j\bar{T}}_{P_T} \underbrace{-2\nu'\langle(\partial_j\tilde{T})^2\rangle}_{\varepsilon_T}
\end{aligned} \tag{2.28}$$

and $\langle\tilde{T}\tilde{S}\rangle$:

$$\begin{aligned}
&\partial_t\langle\tilde{T}\tilde{S}\rangle + \partial_j\Big(\bar{v}_j\langle\tilde{T}\tilde{S}\rangle + \langle\tilde{v}_i\tilde{T}\tilde{S}\rangle - (\nu'+\nu'')\partial_j\langle\tilde{T}\tilde{S}\rangle\Big) \\
&\quad = \underbrace{-\langle\tilde{v}_j\tilde{S}\rangle\partial_j\bar{T} - \langle\tilde{v}_j\tilde{T}\rangle\partial_j\bar{S}}_{P_{TS}} \\
&\quad\quad \underbrace{-\Big(2(\nu'+\nu'')\langle(\partial_j\tilde{T})(\partial_j\tilde{S})\rangle + \nu'\langle\tilde{T}\partial_{jj}\tilde{S}\rangle + \nu''\langle\tilde{S}\partial_{jj}\tilde{T}\rangle\Big)}_{\varepsilon_{TS}}
\end{aligned} \tag{2.29}$$

In (2.28) and (2.29), P_T and P_{TS} are production due to mean gradients and ε_T and ε_{TS} dissipation of $\langle\tilde{T}^2\rangle$ and $\langle\tilde{T}\tilde{S}\rangle$, respectively.

New unknown quantities appear now in the equations, namely the third moments $\langle\tilde{v}_i\tilde{v}_j\tilde{v}_k\rangle$, $\langle\tilde{v}_i\tilde{v}_j\tilde{T}\rangle$, $\langle\tilde{v}_i\tilde{T}^2\rangle$ and $\langle\tilde{v}_i\tilde{T}\tilde{S}\rangle$ and the pressure-strain correlators Π_{ij} and Π_{iT}.

Also for these correlators, transport equations could be derived from the sets of equations (2.4) - (2.6) and (2.18) - (2.21). However, this would create unknown fourth order terms. This so-called Friedmann-Keller series (see *Keller and Friedmann* [1924]) could be continued until infinity, but by doing so, a closed system of equations will never be obtained. This is the well-known closure problem of statistical turbulence.

The solution is to make closure assumptions for the unknown terms based on empirical considerations. This procedure is motivated by the hypothesis that the importance of the higher order terms deceases with their order in relevant flow situations.

So-called second-moment closures are discussed in section 2.3.

2.2.5 The exact equations for turbulent kinetic energy and its dissipation rate

The turbulent kinetic energy k, defined as the kinetic energy per unit mass of the velocity fluctuations is defined as

$$k = \frac{1}{2}\langle\tilde{v}_i^2\rangle = \frac{1}{2}q^2, \tag{2.30}$$

the unit is usually $\mathrm{J\,kg^{-1}}$. A transport equation for k can be derived directly from (2.25) by setting $i = j$:

$$\begin{aligned}
&\partial_t k + \partial_j\Big(\bar{v}_j k + \langle\tilde{v}_j\tfrac{1}{2}\tilde{v}_i^2\rangle - \nu\partial_j k + \tfrac{1}{\rho_0}\langle\tilde{v}_j\tilde{p}\rangle\Big) \\
&\quad = \underbrace{-\langle\tilde{v}_j\tilde{v}_i\rangle\partial_i\bar{v}_j}_{P}\ \underbrace{-\tfrac{g}{\rho_0}\langle\tilde{v}_3\tilde{\rho}\rangle}_{B} - \underbrace{\nu\langle(\partial_j\tilde{v}_i)^2\rangle}_{\varepsilon},
\end{aligned} \tag{2.31}$$

Here, P is the shear production, B the buoyancy production and ε the dissipation rate of turbulent kinetic energy. It should be noted that the shear production term P equals the energy loss of mean kinetic energy due to internal friction into turbulent kinetic energy, see equation (2.24). This conservation principle will be considered for the discretisation of the shear production term, see section 4.3. For the dissipation rate,

$$\varepsilon = \nu\langle(\partial_j \tilde{v}_i)^2\rangle \tag{2.32}$$

(the unit is usually $\mathrm{W\,kg^{-1}}$), which appears as a sink on the left hand side of the k-equation, an exact equation can be derived as well, see e.g. *Wilcox* [1998]:

$$\begin{aligned}
&\partial_t \varepsilon + \partial_j \Big(\bar{v}_j \varepsilon + \langle \tilde{v}_j \nu (\partial_j \tilde{v}_i)^2 \rangle - \nu \partial_j \varepsilon + 2\tfrac{\nu}{\rho_0} \langle \partial_i \tilde{v}_j \partial_i \tilde{p} \rangle \Big) \\
&\quad = \underbrace{-2\nu \partial_j \bar{v}_i \Big(\langle \partial_i \tilde{v}_k \partial_j \tilde{v}_k \rangle + \langle \partial_k \tilde{v}_i \partial_k \tilde{v}_j \rangle \Big) - 2\nu \partial_{jk} \bar{v}_i \langle \tilde{v}_k \partial_j \tilde{v}_i \rangle}_{P_\varepsilon} \\
&\quad \underbrace{-2\nu \tfrac{g}{\rho_0} \partial_j \langle \tilde{v}_3 \partial_j \tilde{\rho} \rangle}_{B_\varepsilon} \underbrace{- 2\nu \left(\langle \partial_j \tilde{v}_i \partial_k \tilde{v}_i \partial_j \tilde{v}_k \rangle + \nu \langle (\partial_{ij} \tilde{v}_k)^2 \rangle \right)}_{\varepsilon_\varepsilon}
\end{aligned} \tag{2.33}$$

In (2.33), the terms on the right hand side have been ordered such that those containing mean flow shear or curvature are denoted by shear production of dissipation, P_ε, those containing density fluctuations are denoted by buoyancy production, B_ε, and those containing only gradients of fluctuations are denoted by dissipation of dissipation, ε_ε. The gradient terms are all put onto the left hand side.

It is evident that for both equations (2.31) and (2.33), the effect of the Coriolis rotation is vanished and that pressure fluctuations do not act as sources or sinks for k and ε, but do only transport these quantities such as advective or diffusive transports.

2.3 Second-moment closures

The aim of second-moment closures is to derive a closed system of equations based on the second-moment equations for $\langle \tilde{v}_i \tilde{v}_j \rangle$ and $\langle \tilde{v}_i \tilde{T} \rangle$, (2.25) and (2.26). Other second moments which have to be closed are the temperature variance $\langle \tilde{T}^2 \rangle$ as part of the B_{iT} term in equation (2.26), and - if salinity is considered as well - terms containing salinity fluctuations such as $\langle \tilde{v}_i \tilde{S} \rangle$, $\langle \tilde{S}^2 \rangle$ and $\langle \tilde{T} \tilde{S} \rangle$. The closure is achieved by relating the pressure-strain correlators Π_{ij} and Π_{iT} to the known second moments and mean flow quantities, see section

2.3.1. Some assumptions have to be made for the viscous dissipation terms ε_{ij} and ε_{iT}, see section 2.3.2. In the case of more than one active tracer, further assumptions have to be made for the tracer cross-correlations, which is briefly discussed in section 2.3.4.

Since the full consideration of equations (2.25) and (2.26) requires the solution of nine (plus one for the tracer invariance and eventually four more if salinity is included plus one more for $\langle \tilde{T}\tilde{S} \rangle$), often some assumptions are made which lead to an algebraic system for the second moments, see section 3.1.2. Together with this, the rotational terms which mean an enormous complication for obtaining this algebraic system of equations are often neglected. The class of closure schemes which finally results are the so-called algebraic second-moment one-point closure schemes, which are good compromise between high accuracy and low computational costs for many environmental flow situations. The problem will then still depend on two parameters for which dynamical transport equations have been derived in section 2.2.5, the turbulent kinetic energy (TKE), k, and the turbulent dissipation rate of the TKE, ε. For these two quantities, various closures will be presented in section 3.2. The basic results which are summarised in sections 2.3.1 - 3.1.2 have been taken from the recent publication by *Burchard and Bolding* [2001].

2.3.1 Pressure-strain correlators

Here, three different approaches for closing the pressure-strain correlators Π_{ij} and Π_{iT} will be presented. They have been published by

- *Kantha and Clayson* [1994] (henceforth denoted by KC). This model is an extension of the theory which has been developed by *Mellor and Yamada* [1974] and *Mellor and Yamada* [1982], two publications which play a fundamental role in geophysical fluid dynamics since that time. A hierarchy of models has been presented in these papers of which the level 2.5 model defines the algebraic second-moment one-point closure schemes on which the focus is put here.
- *Burchard and Baumert* [1995] (based on the work of *Rodi* [1980] and *Hossain* [1980], henceforth denoted by RH). In his famous review publication, *Rodi* [1980] summarised the work of *Daly and Harlow* [1970], *Hanjalic and Launder* [1972], *Launder and Spalding* [1972], *Launder* [1975a], *Launder et al.* [1975], *Rodi* [1976], *Gibson and Launder* [1978] and many others on the field of second-moment closures. After simplifying the pressure-strain correlator according to *Rodi* [1980], *Hossain* [1980] extended this theory towards a complete algebraic closure. *Burchard* [1995] and *Burchard and Baumert* [1995] derived implicit so-called stability functions from this theory.
- *Canuto et al.* [2001] (henceforth CA). In this recent publication, the work of the 80's and 90's is exploited for deriving state-of-the-art algebraic second-moment closures. Important contributions to this theory are from *Shih and*

Shabbir [1992], *Canuto* [1994], *Canuto et al.* [1994], *Canuto and Dubovikov* [1997a] and *Canuto and Dubovikov* [1997b]. For the determination of empirical parameters, extensive use of two-point closure modelling has been made.

The theories developed in KC, RH and CA can be summarised in the following general expression for the pressure-strain correlator Π_{ij} which appears on the right hand side of (2.25):

$$\Pi_{ij} = \underbrace{c_1 \frac{\varepsilon}{k}\left(\langle\tilde{v}_i\tilde{v}_j\rangle - \frac{2}{3}\delta_{ij}k\right)}_{\text{(R1)}} + \underbrace{c_2\left(P_{ij} - \frac{2}{3}\delta_{ij}P\right)}_{\text{(R2)}} + \underbrace{c_3\left(B_{ij} - \frac{2}{3}\delta_{ij}B\right)}_{\text{(R3)}}$$
$$+ \underbrace{c_4\left(D_{ij} - \frac{2}{3}\delta_{ij}P\right)}_{\text{(R4)}} + \underbrace{c_5 k S_{ij}}_{\text{(R5)}} \tag{2.34}$$

with P_{ij} and B_{ij} from (2.25) and P and B from (2.31), respectively. For the Kronecker symbol δ_{ij}, see section 9.1. The basic form of (2.34) can be derived by applying the divergence operator to the exact transport equation for velocity fluctuations and solving the resulting Poisson equation for the pressure fluctuations by means of the Green's function, see *Rotta* [1951].

Further definitions are mean shear

$$S_{ij} = \frac{1}{2}(\partial_i\bar{v}_j + \partial_j\bar{v}_i) \tag{2.35}$$

and the anisotropic shear production

$$D_{ij} = -\langle\tilde{v}_i\tilde{v}_l\rangle\partial_j\bar{v}_l - \langle\tilde{v}_j\tilde{v}_l\rangle\partial_i\bar{v}_l. \tag{2.36}$$

The parameters $c_1, \ldots, c_5$ have been introduced for parameterisation of the pressure-strain correlators. Setting them all to zero would result in the neglect of these terms. The single terms have the following meaning: Return to isotropy (R1), see *Rotta* [1951], shear production (R2), buoyancy production (R3), and anisotropic contribution due to shear, (R4) and (R5). It has been found by *Launder et al.* [1975] that the isotropic shear production term (R2) clearly dominates the anisotropic shear terms (R4) and (R5). These terms are therefore neglected in the closure RH by *Rodi* [1980], *Hossain* [1980] and *Burchard and Baumert* [1995]. A consideration of these terms would have led to serious problems in solving the resulting non-linear system of equations, see section 3.1.3. The empirical parameters $c_1, \ldots, c_5$ are given in table 2.1 for the closures KC, RH and CA. It can be seen that the model KC neglects pressure-strain effects due to shear and buoyancy production, the model RH neglects effects of terms (R4) and (R5), and only the model CA considers all terms.

It is shown in detail by *Umlauf* [2001][7] that the CA model is isomorphic to the model by *Launder et al.* [1975], see also *Zeman and Tennekes* [1975]. The calibration of these empirical parameters is referenced in the respective publications of the KC, the RH, and the CA model. It should be noted that in the original version of the RH model, wall proximity functions have been included in the parameters (see *Hossain* [1980]). These are neglected here.

Model	c_1	c_2	c_3	c_4	c_5	c_{1T}	c_{2T}	c_{3T}	c_{4T}	c_T
KC	2.98	0.0	0.0	0.0	0.32	3.70	0.7	0.2	0.0	1.23
RH	1.8	0.6	0.5	0.0	0.0	3.0	0.33	0.33	0.0	1.6
CA	2.5	0.776	0.5	0.208	0.512	5.97	0.6	0.33	0.4	1.44

Table 2.1. Parameters for the Reynolds stress closure models.

Similarly to (2.34), the theories KC, RH and CA for parameterising the pressure-strain term Π_{iT} appearing on the right hand side of (2.26) can be generally written as (see *Launder* [1975b]:

$$\begin{aligned}\Pi_{iT} = & \underbrace{c_{1T}\frac{\varepsilon}{k}\langle\tilde{v}_i\tilde{T}\rangle}_{\text{(H1)}} \\ & + \underbrace{c_{2T}\langle\tilde{v}_j\tilde{T}\rangle\partial_j\bar{u}_i}_{\text{(H2)}} - \underbrace{c_{3T}\frac{g_i}{\rho_0}\partial_T\rho\langle\tilde{T}^2\rangle}_{\text{(H3)}} - \underbrace{c_{4T}\langle\tilde{v}_i\tilde{T}\rangle V_{ij}}_{\text{(H4)}}\end{aligned} \tag{2.37}$$

with mean vorticity

$$V_{ij} = \frac{1}{2}(\partial_j\bar{v}_i - \partial_i\bar{v}_j). \tag{2.38}$$

In (2.37), the terms have the following physical meaning: return to isotropy (H1), production by mean gradients (H2), production by buoyancy (H3), and contribution due to vorticity (H4). Here, the KC and the RH model neglect the (H4) term whereas CA considers all terms (see table 2.1). The closure by *Mellor and Yamada* [1982] chose the same value for c_{1T} than KC did, but used $c_{2T} = c_{3T} = 0$.

2.3.2 Dissipation terms

Following the theory of *Kolmogorov* [1941], the statistical properties of turbulent flow at high Reynolds numbers are invariant in terms of rotation, see also the discussion by *Frisch* [1995]. This so-called local isotropy assumption

[7] The author of this book is grateful to Lars Umlauf for providing a manuscript with the conversion of the *Canuto et al.* [2001] closure to the present notation.

leads to the following simplification of the dissipation term ε_{ij} appearing on the right hand side of the Reynolds stress equation (2.25):

$$\varepsilon_{ij} = \frac{2}{3}\delta_{ij}\varepsilon. \tag{2.39}$$

According to *Rotta* [1951], this local isotropy principle can be further exploited such that the dissipation term ε_{iT} in the heat flux equation (2.26) vanishes:

$$\varepsilon_{iT} = 0. \tag{2.40}$$

For the dissipation of $\langle\tilde{T}^2\rangle$, see equation (2.28), the following parameterisation is used (see *Launder* [1975a]):

$$\varepsilon_T = \frac{2}{c_T}\frac{\varepsilon}{k}\langle\tilde{T}^2\rangle \tag{2.41}$$

with the empirical parameter c_T from table 2.1.

The assumption of high Reynolds number seems to be very restrictive for the application of oceanic turbulence models. However, only a few low Reynolds number models have so far been applied in the marine environment, see e.g. *Svensson and Omstedt* [1990] for an application of the k-ε model to flow under melting sea-ice, which establishes a stably stratified near-wall flow with low flow velocities. In most other applications, the Reynolds number is assumed to be high, i.e. of the order of at least 10^6, which is theoretically justified when the water is deep or flow velocities are high.

2.3.3 Third moments

Further closure assumptions have to be made for the third moments $\langle\tilde{v}_l\tilde{v}_i\tilde{v}_j\rangle$, $\langle\tilde{v}_i\tilde{v}_j\tilde{T}\rangle$ and $\langle\tilde{v}_i\tilde{T}^2\rangle$, which occur on the left hand sides of equations (2.25), (2.26) and (2.28), respectively. By following the same principle as applied to derive equations for the second moments (see section 2.2.4), equations for the third moments can be derived as well, see *Andre et al.* [1982], *Canuto* [1992]. Based on this and by assuming stationarity and locality, *Canuto et al.* [1994] derived a closed set of algebraic equations for the shear-free third moments. The extensive use of symbolic algebra is however inevitable on this level of sophistication. Recently, *Canuto et al.* [2001] extended this third-moment closure to flow with shear.

An alternative approach has been suggested by *Zilitinkevich et al.* [1999]. They related the third moment $\langle\tilde{w}^2\tilde{T}\rangle$ (vertical flux of vertical turbulent temperature flux) to the vertical temperature flux $\langle\tilde{w}\tilde{T}\rangle$ by means of the vertical velocity skewness $\langle\tilde{w}^3\rangle/\langle\tilde{w}^2\rangle^{3/2}$. With similar arguments, *Mironov et al.* [1999] suggested to parameterise the vertical flux of temperature variance, $\langle\tilde{w}\tilde{T}^2\rangle$, by the product of the temperature skewness $\langle\tilde{T}^3\rangle/\langle\tilde{T}^2\rangle^{3/2}$ and the

vertical turbulent temperature flux. By doing so, they remove an inconsistent non-symmetric behaviour of a similar parameterisation suggested earlier by *Abdella and McFarlane* [1997]. However, since these parameterisations depend on the skewnesses of velocity and temperature, closures for the third moments $\langle\tilde{w}^3\rangle$ and $\langle\tilde{T}^3\rangle$ are still required.

In a different approach, *D'Alessio et al.* [1998] use non-local informations provided by the surface fluxes for the parameterisation of third moments. These are used for obtaining non-local algebraic expressions for the second moments.

In the so-called down-gradient approach, which is most widespread due to its simplicity, third moments are related to the gradients of second moments by using an eddy diffusivity:

$$\langle\tilde{v}_i\tilde{x}\tilde{y}\rangle = -\nu_{xy}\partial_i\langle\tilde{x}\tilde{y}\rangle \tag{2.42}$$

with the eddy viscosity ν_{xy} for any fluctuations $\tilde{x}$ and $\tilde{y}$. It has however been shown by many investigations (see, e.g. *Moeng and Wyngaard* [1989]) that the down-gradient approximation (2.42) seriously underestimates third moments due to the neglect of non-local characteristics.

In the turbulence closure models on which focus is made in the present investigation, the closure of third moment in the budget equations of the second moments is however made in a much simpler way: they are neglected since local equilibrium is assumed such that consequently the left hand sides of (2.25), (2.26) and (2.28) and (2.29), vanish, see section 3.1.2.

Third moments also appear in the transport equations for turbulent kinetic energy and its dissipation rate, see equations (2.31) and (2.33), respectively. Also for the third moment for k, *Canuto et al.* [1994] and *Canuto et al.* [2001] suggest complex algebraic closures. The flux of dissipation rate could then be related to the TKE flux by scaling the latter with the turbulent time scale, k/ε, see *Canuto* [1992]. However, in most applications, the down-gradient approach is used for the parameterisation of the third moments of the TKE and its dissipation rate, see e.g. *Rodi* [1980]. The eddy diffusivities for these quantities are then usually related to the eddy viscosity for momentum by turbulent Schmidt numbers, see section 3.2.5. Also with the down-gradient approximation for these fluxes of turbulent kinetic energy and dissipation rate, observed values seem to be significantly underestimated, see figure 6.11. In the convective boundary layer for example, $\langle\tilde{w}^3\rangle$ which is one of the components of the vertical TKE flux is positive throughout the boundary layer (see *Canuto et al.* [1994], *Mironov et al.* [2000]) whilst $\partial_z\langle\tilde{w}^2\rangle$ changes sign at about half of the depth of the convective boundary layer, see figure 6.10. Therefore *Canuto et al.* [2001] postulate:

> ... Due to these reasons we shall abandon the DGA and solve [the third-moment transport equations]. The only approximation is that we consider the stationary case.

However, in the present investigation the down-gradient approximation is used for the turbulent transports of turbulent kinetic energy k and its dissipation rate ε. There is one simple reason for this: computational costs. In a one-dimensional model environment these costs are of course irrelevant. But since it is the intention to suggest improved turbulence closure models for three-dimensional models, computational costs are an issue. However, the influence of better parameterisations for third moments of k and ε should be investigated in the future for the framework presented here.

2.3.4 Tracer cross-correlations

Most publications in which turbulence models are derived deal with only one active tracer which is usually potential temperature, see e.g. *Mellor and Yamada* [1974], *Mellor and Yamada* [1982], *Rodi* [1980], and *Canuto et al.* [2001]. However, in most geophysical flow applications a second active tracer is relevant as well, which is usually salinity for the ocean and moisture for the atmosphere. After carrying out the Reynold's decomposition and averaging, one additional term has to be considered, which is the tracer cross-correlation term representing the turbulent interaction between the two tracers. In the ocean, this term is $\langle \tilde{T}\tilde{S} \rangle$, for which an exact transport equation can be derived, see equation (2.29). What is in principle done here, is assuming that the dissipation rate of $\langle \tilde{T}\tilde{S} \rangle$ is zero, as already done for the dissipation term in the heat flux equation (2.28). After neglecting the transport terms, see section 3.1.2, the production term consequently vanishes as well. It is thus assumed that temperature and salinity fluctuations are not correlated, i.e. $\langle \tilde{T}\tilde{S} \rangle = 0$.

Experience shows that this simplifying assumption does not always hold. Typical examples are double-diffusive processes such as salt fingering (warm and salty over fresh and cold water) or diffusive convection (cold and fresh over warm and salty water). Such processes are driven by the different molecular diffusivities of heat and salt which differ by two orders of magnitude, see section 2.1.3. Parameterisations for such processes have been proposed for example by *Large et al.* [1994] in order to overcome the problem of neglected tracer cross-correlations. Recently, *Canuto et al.* [2002] suggested to carry out a complete derivation of algebraic second moments including such cross-correlations. In order to do so, they had to apply the mass average rather than the Reynold's average, see *Canuto* [1997]. The consequences of this new closure however need further investigation.

3 Boundary layer models

3.1 Boundary layers

In this section the basic assumption is made that the aspect ratio of the flow is small, i.e. that horizontal scales are much larger than vertical scales. This leads to considerable simplifications of the dynamic equations. For the mean flow this has the main consequence that now prognostic equations only for the horizontal velocity components are needed. For the turbulence modelling, the number of terms to be parameterised decreases significantly.

3.1.1 Boundary-layer approximation

In environmental flow situations, not all terms in the Reynold's averaged equations (2.18) are relevant for the determination of the flow characteristics. In order to investigate which terms could be neglected, a scale analysis is usually performed. Here, we look at a typical ocean mixed layer or estuarine scenario. For the latter, processes near the bottom are considered as well. Typical scales would be:

Horizontal velocity	$\mathcal{U}$	$\approx \mathcal{O}(1)\ \mathrm{m\,s^{-1}}$
Horizontal length scale	$\mathcal{L}$	$\approx \mathcal{O}(10^5)\ \mathrm{m}$
Vertical length scale	$\mathcal{H}$	$\approx \mathcal{O}(10)\ \mathrm{m}$
Molecular viscosity	ν	$\approx \mathcal{O}(10^{-6})\ \mathrm{m^2 s^{-1}}$
Turbulent velocity scale	$\mathcal{U}_*$	$\approx \mathcal{O}(10^{-2})\ \mathrm{m\,s^{-1}}$
Angular velocity	Ω	$\approx \mathcal{O}(10^{-4})\ \mathrm{s^{-1}}$
Reference density	ρ_0	$\approx \mathcal{O}(10^3)\ \mathrm{kg\,m^{-3}}$
Reference density difference	$\Delta\rho_0$	$\approx \mathcal{O}(1)\ \mathrm{kg\,m^{-3}}$
Reference pressure difference	ΔP_0	$\approx \mathcal{O}(10^2)\ \mathrm{N\,m^{-2}}$
Gravitational acceleration	g	$\approx \mathcal{O}(10)\ \mathrm{m\,s^{-2}}$

It should be noted that the scalings are somehow arbitrary and that the boundary layer equations could also be derived with other combinations of scales. In contrast to the other scalings, the scaling of the reference pressure difference ΔP_0 is not easy to determine and is more an experience value than an observation. A value of $10^2\ \mathrm{N\,m^{-2}}$ is equivalent to a surface elevation difference of 0.1 m, a scale which is actually typical in the open ocean over distances of the order of $\mathcal{L} = 10^5$ m.

The turbulent velocity scale could be either surface or bottom friction velocity or the convective Deardorff scale, see equation (6.5). The range of values for the ratio of vertical to horizontal velocity fluctuations is about $0.522 \leq \langle\tilde{w}^2\rangle^{1/2}/\langle\tilde{u}^2\rangle^{1/2} \leq 1.58$, see e.g. *Galperin et al.* [1988]. Thus, the same scaling for vertical and horizontal velocity fluctuations, $\mathcal{U}_*$ will be used here. From the scales defined above, a typical aspect ratio $\alpha = \mathcal{H}/\mathcal{L} \approx 10^{-4}$ and a typical time scale $\mathcal{L}/\mathcal{U} \approx 10^5 s = \mathcal{O}(1\text{day})$ can be derived. The scaling of the mean vertical velocity $\bar{w}$ is obtained by using the mass conservation (2.19) as $\mathcal{U}\mathcal{H}/\mathcal{L} \approx \mathcal{O}(10^{-4})\ \mathrm{m\,s^{-1}}$.

For estimating the order of magnitude of individual terms, the equations for $\bar{u} = \bar{v}_1$ and $\bar{w} = \bar{v}_3$, see (2.18), are rewritten in explicit form:

$$\begin{aligned}
&\underbrace{\partial_t \bar{u}}_{\mathcal{U}^2/\mathcal{L}} + \underbrace{\partial_x(\bar{u}^2)}_{\mathcal{U}^2/\mathcal{L}} + \underbrace{\partial_y(\bar{u}\bar{v})}_{\mathcal{U}^2/\mathcal{L}} + \underbrace{\partial_z(\bar{u}\bar{w})}_{\mathcal{U}^2/\mathcal{L}} + \underbrace{\nu\partial_{xx}\bar{u}}_{\nu\mathcal{U}/\mathcal{L}^2} + \underbrace{\nu\partial_{yy}\bar{u}}_{\nu\mathcal{U}/\mathcal{L}^2} + \underbrace{\nu\partial_{zz}\bar{u}}_{\nu\mathcal{U}/\mathcal{H}^2} \\
&\quad + \underbrace{\partial_x\langle\tilde{u}^2\rangle}_{\mathcal{U}_*^2/\mathcal{L}} + \underbrace{\partial_y\langle\tilde{u}\tilde{v}\rangle}_{\mathcal{U}_*^2/\mathcal{L}} + \underbrace{\partial_z\langle\tilde{u}\tilde{w}\rangle}_{\mathcal{U}_*^2/\mathcal{H}} + \underbrace{2\Omega\cos(\Phi)\bar{w}}_{\Omega\mathcal{U}\mathcal{H}/\mathcal{L}} - \underbrace{2\Omega\sin(\Phi)\bar{v}}_{\Omega\mathcal{U}} = \\
&\quad - \underbrace{\rho_0^{-1}\partial_x\bar{p}}_{\Delta P_0/(\rho_0\mathcal{L})},
\end{aligned} \tag{3.1}$$

$$\begin{aligned}
&\underbrace{\partial_t \bar{w}}_{\mathcal{U}^2\mathcal{H}/\mathcal{L}^2} + \underbrace{\partial_x(\bar{u}\bar{w})}_{\mathcal{U}^2\mathcal{H}/\mathcal{L}^2} + \underbrace{\partial_y(\bar{v}\bar{w})}_{\mathcal{U}^2\mathcal{H}/\mathcal{L}^2} + \underbrace{\partial_z(\bar{w}^2)}_{\mathcal{U}^2\mathcal{H}/\mathcal{L}^2} + \underbrace{\nu\partial_{xx}\bar{w}}_{\nu\mathcal{H}\mathcal{U}/\mathcal{L}^3} + \underbrace{\nu\partial_{yy}\bar{w}}_{\nu\mathcal{H}\mathcal{U}/\mathcal{L}^3} + \underbrace{\nu\partial_{zz}\bar{w}}_{\nu\mathcal{U}/(\mathcal{H}\mathcal{L})} \\
&\quad + \underbrace{\partial_x\langle\tilde{u}\tilde{w}\rangle}_{\mathcal{U}_*^2/\mathcal{L}} + \underbrace{\partial_y\langle\tilde{v}\tilde{w}\rangle}_{\mathcal{U}_*^2/\mathcal{L}} + \underbrace{\partial_z\langle\tilde{w}^2\rangle}_{\mathcal{U}_*^2/\mathcal{H}} - \underbrace{2\Omega\cos(\Phi)\bar{u}}_{\Omega\mathcal{U}} = \\
&\quad - \underbrace{\rho_0^{-1}\partial_z(\bar{p}-p_0)}_{\Delta P_0/(\rho_0\mathcal{H})} - \underbrace{\rho_0^{-1}g(\rho-\rho_0)}_{g\Delta\rho_0/\rho_0},
\end{aligned} \tag{3.2}$$

where

$$p_0 = z' g \rho_0 \tag{3.3}$$

with the distance from the surface, z', is the hydrostatic reference pressure.

The resulting orders of magnitude for the single terms in equations (3.1) and (3.2) are shown in table 3.1. According to this, the major balance in the $\bar{u}$ equation is established by the horizontal component of the Coriolis term and the pressure gradient term. This balance is known as geostrophy. Terms with one order of magnitude lower are the substantial derivative (containing change in time and advection terms) and the turbulent vertical transport. All other terms are at least three orders of magnitude smaller, and can thus

$\bar{u}$ equation (3.1)							
$\Omega\mathcal{U}$	$\frac{\Delta P_0}{\rho_0 \mathcal{L}}$	$\frac{\mathcal{U}^2}{\mathcal{L}}$	$\frac{\mathcal{U}_*^2}{\mathcal{H}}$	$\frac{\nu\mathcal{U}}{\mathcal{H}^2}$	$\frac{\Omega\mathcal{U}\mathcal{H}}{\mathcal{L}}$	$\frac{\mathcal{U}_*^2}{\mathcal{L}}$	$\frac{\nu\mathcal{U}}{\mathcal{L}^2}$
$\mathcal{O}(10^{-4})$	$\mathcal{O}(10^{-4})$	$\mathcal{O}(10^{-5})$	$\mathcal{O}(10^{-5})$	$\mathcal{O}(10^{-8})$	$\mathcal{O}(10^{-8})$	$\mathcal{O}(10^{-9})$	$\mathcal{O}(10^{-16})$
$\bar{w}$ equation (3.2)							
$\frac{\Delta P_0}{\rho_0 \mathcal{H}}$	$\frac{g\Delta\rho_0}{\rho_0}$	$\Omega\mathcal{U}$	$\frac{\mathcal{U}_*^2}{\mathcal{H}}$	$\frac{\mathcal{U}_*^2}{\mathcal{L}}$	$\frac{\mathcal{U}^2\mathcal{H}}{\mathcal{L}^2}$	$\frac{\nu\mathcal{U}}{\mathcal{H}\mathcal{L}}$	$\frac{\nu\mathcal{U}\mathcal{H}}{\mathcal{L}^3}$
$\mathcal{O}(10^{-2})$	$\mathcal{O}(10^{-2})$	$\mathcal{O}(10^{-4})$	$\mathcal{O}(10^{-5})$	$\mathcal{O}(10^{-9})$	$\mathcal{O}(10^{-9})$	$\mathcal{O}(10^{-12})$	$\mathcal{O}(10^{-20})$

Table 3.1. Typical scales for ocean mixed layers and estuarine flow for the $\bar{u}$ equation (3.1) and for the $\bar{w}$ equation (3.2). All terms have the unit $\mathrm{m\,s^{-2}}$.

be neglected in flow situations to which the scales given above fit. For the $\bar{v}$ equation all terms scale in accordance to the $\bar{u}$ equation. For the vertical velocity equation (3.2), the major balance is given by the vertical pressure gradient and the gravitational acceleration terms, which is the so-called hydrostatic equilibrium. All other terms are at least two orders of magnitude smaller, and could thus be neglected in the flow situations scaled above. A similar scaling can be carried out with the $\bar{T}$ and the $\bar{S}$ equation (2.20) and (2.21), respectively.

All horizontal mixing terms, i.e. the horizontal gradients of the turbulent fluxes, are of the order of four orders of magnitude smaller than the substantial derivative of the horizontal velocity components or tracers. This has the consequence that the retention of these terms in the horizontal velocity and tracer equations is generally irrelevant. In ocean circulation models however, the so-called meso-scale activity is generally not resolved by the numerical discretisation due to relatively coarse horizontal grid spacing. In order to account for this efficient physical transport process nevertheless, various parameterisations have been proposed, ranging from linear or bi-linear diffusion with constant meso-scale eddy diffusivity over diffusion with grid-size depending eddy diffusivity (see *Smagorinsky* [1963]) to the method of thickness diffusion suggested by *Gent and McWilliams* [1990]. In the latter scheme, eddy-induced transport velocities are added to the tracer advection velocities. For a review of such meso-scale parameterisations, see *Haidvogel and Beckmann* [1999]. For numerical problems associated with lateral mixing schemes, see *Griffies et al.* [1998] and *Beckers et al.* [1998]. It should be kept in mind that such meso-scale transport parameterisations are basically needed for numerical reasons. Some of the meso-scale activity could however also be suppressed due to the scaling with a horizontal length scale $\mathcal{L} \approx \mathcal{O}(100)$ km (pers. comm. Jean-Marie Beckers).

The scales given above are quite arbitrary and should be regarded as an empirical argument rather than a mathematical derivation. For each new application of models, the validity of the underlying scaling assumptions should in principle be tested. This could strictly only be done by first applying the complete model and then evaluating the relevance of the single terms. The

experience shows for example that the vertical turbulent fluxes are sometimes only of the order of the viscous fluxes, such as near the surface or bottom or in the areas of strong vertical density stratification, the so-called pycnocline. These terms are thus often retained in the Reynold's averaged equations for $\bar{u}$, $\bar{v}$, $\bar{T}$ and $\bar{S}$ when focus is set on investigating turbulent mixing, although they are three orders of magnitude smaller than the other terms in the scaling above. This is of course inconsistent with the fact that the vertical components of the Coriolis vector are still neglected in the horizontal velocity equations. Inclusion of this rotational term would on the other hand be inconsistent with energy conservation laws since vertical velocity does not contribute to kinetic energy after this scaling analysis, see *Haidvogel and Beckmann* [1999]. However, as said before, the scaling is arbitrary and can only serve as a guideline for simplifying the set of equations.

More rigorous mathematical tools such as asymptotic analysis (see e.g. *Kevorkian and Cole* [1996]) could be a perspective for more systematically analysing the Reynolds averaged equations. Such methods have already successfully been applied to low Mach number compressible flows with the aim of constructing more efficient numerical schemes (see *Klein* [1995]). *Meister* [1999] recently presented a rigorous mathematical justification of this method of asymptotic expansions. However, the incompressible hydrostatic primitive equations which are used here have so far not been derived with such advanced methods (pers. comm. Rupert Klein).

After this scale analysis, the Reynold's averaged equations now form the following set of primitive equations equations:

$$\begin{aligned}\partial_t\bar{u} + \partial_x(\bar{u}^2) + \partial_y(\bar{u}\bar{v}) + \partial_z(\bar{u}\bar{w}) - \nu\partial_{zz}\bar{u} + \partial_z\langle\tilde{u}\tilde{w}\rangle - f\bar{v} = \\ -g\frac{\bar{\rho}(\zeta)}{\rho_0}\partial_x\zeta + \int_z^\zeta \partial_x b\, dz',\end{aligned} \tag{3.4}$$

$$\begin{aligned}\partial_t\bar{v} + \partial_x(\bar{u}\bar{v}) + \partial_y(\bar{v}^2) + \partial_z(\bar{v}\bar{w}) - \nu\partial_{zz}\bar{v} + \partial_z\langle\tilde{v}\tilde{w}\rangle + f\bar{u} = \\ -g\frac{\bar{\rho}(\zeta)}{\rho_0}\partial_y\zeta + \int_z^\zeta \partial_y b\, dz',\end{aligned} \tag{3.5}$$

$$\partial_x\bar{u} + \partial_y\bar{v} + \partial_z\bar{w} = 0, \tag{3.6}$$

$$\partial_t\bar{T} + \partial_x(\bar{u}\bar{T}) + \partial_y(\bar{v}\bar{T}) + \partial_z(\bar{w}\bar{T}) - \nu'\partial_{zz}\bar{T} + \partial_z\langle\tilde{w}\tilde{T}\rangle = \frac{\partial_z I}{c_p'\rho_0}, \tag{3.7}$$

$$\partial_t\bar{S} + \partial_x(\bar{u}\bar{S}) + \partial_y(\bar{v}\bar{S}) + \partial_z(\bar{w}\bar{S}) - \nu''\partial_{zz}\bar{S} + \partial_z\langle\tilde{w}\tilde{S}\rangle = 0, \tag{3.8}$$

$$\bar{\rho} = \rho(\bar{T}, \bar{S}, p_0) \tag{3.9}$$

In (3.4) and (3.5), the hydrostatic equilibrium has been used for reformulating the pressure gradient term into an external pressure gradient and an internal pressure gradient, see *Burchard and Petersen* [1997]. Here, ζ is the surface elevation and b the buoyancy

$$b = -g\frac{\bar{\rho} - \rho_0}{\rho_0}. \tag{3.10}$$

The Coriolis parameter is now defined as $f = 2\Omega\sin(\Phi)$. The surface elevation ζ is calculated prognostically by vertically integrating the mass conservation condition (3.6) and applying kinematic boundary conditions which basically prescribe that fluid particles at the boundaries move parallel to these boundaries:

$$\partial_t\zeta = -\partial_x\int_{-H}^{\zeta} u(z)\,dz - \partial_y\int_{-H}^{\zeta} v(z)\,dz. \tag{3.11}$$

The matrices P_{ij}, B_{ij}, S_{ij}, and V_{ij} (see section 2.3.1) resulting from the application of the boundary layer approximation to equation (2.25) are now of the following form:

$$P_{ij} = \begin{pmatrix} -2\partial_z\bar{u}\langle\tilde{u}\tilde{w}\rangle & -\partial_z\bar{u}\langle\tilde{v}\tilde{w}\rangle - \partial_z\bar{v}\langle\tilde{u}\tilde{w}\rangle & -\partial_z\bar{u}\langle\tilde{w}^2\rangle \\ -\partial_z\bar{u}\langle\tilde{v}\tilde{w}\rangle - \partial_z\bar{v}\langle\tilde{u}\tilde{w}\rangle & -2\partial_z\bar{v}\langle\tilde{v}\tilde{w}\rangle & -\partial_z\bar{v}\langle\tilde{w}^2\rangle \\ -\partial_z\bar{u}\langle\tilde{w}^2\rangle & -\partial_z\bar{v}\langle\tilde{w}^2\rangle & 0 \end{pmatrix} \tag{3.12}$$

$$B_{ij} = \frac{g}{\rho_0}\begin{pmatrix} 0 & 0 & \langle\tilde{u}\tilde{\rho}\rangle \\ 0 & 0 & \langle\tilde{v}\tilde{\rho}\rangle \\ \langle\tilde{u}\tilde{\rho}\rangle & \langle\tilde{v}\tilde{\rho}\rangle & 2\langle\tilde{w}\tilde{\rho}\rangle \end{pmatrix} \tag{3.13}$$

$$S_{ij} = \frac{1}{2}\begin{pmatrix} 0 & 0 & \partial_z\bar{u} \\ 0 & 0 & \partial_z\bar{v} \\ \partial_z\bar{u} & \partial_z\bar{v} & 0 \end{pmatrix}, \qquad V_{ij} = \frac{1}{2}\begin{pmatrix} 0 & 0 & \partial_z\bar{u} \\ 0 & 0 & \partial_z\bar{v} \\ -\partial_z\bar{u} & -\partial_z\bar{v} & 0 \end{pmatrix} \tag{3.14}$$

The calculation of density gradients is simplified by assuming that the speed of sound, $c = \sqrt{\partial_\rho p}$ is infinite, which is consistent with the assumption of incompressibility. Thus, density gradients can be calculated as follows:

$$\partial_i\bar{\rho} = \partial_T\rho\,\partial_i\bar{T} + \partial_S\rho\,\partial_i\bar{S} \tag{3.15}$$

with the thermal and haline volume expansion coefficients $\partial_T\rho$ and $\partial_S\rho$, respectively, which still depend on the hydrostatic reference pressure p_0.

The equations (3.4) - (3.9) are often referred to as the hydrostatic primitive equations. Here, the further assumption has implicitly be made that $\mathcal{L}$ is small compared to the radius of the earth, which avoids the transformation

of these equations into spherical coordinates, see *Haidvogel and Beckmann* [1999].

In terms of turbulence modelling, the main consequence of these scaling assumptions is that the system of equations (3.4) - (3.9) now only contains four turbulent transport terms for which closure assumptions have to be made: $\langle\tilde{u}\tilde{w}\rangle$, $\langle\tilde{v}\tilde{w}\rangle$, $\langle\tilde{w}\tilde{T}\rangle$ and $\langle\tilde{w}\tilde{S}\rangle$. This closure will be completed in section 3.1.2.

3.1.2 Algebraisation of second moments

With the assumptions made so far, the system of hydrostatic primitive equations (3.4) - (3.9) together with the transport equations for the second moments (2.25), (2.26) and (2.28) form a closed system of model equations. However, this still requires the calculations of fourteen prognostic equations for the second moments

$$\begin{aligned}&\langle\tilde{u}^2\rangle,\ \langle\tilde{u}\tilde{v}\rangle,\ \langle\tilde{u}\tilde{w}\rangle,\ \langle\tilde{v}^2\rangle,\ \langle\tilde{v}\tilde{w}\rangle,\ \langle\tilde{w}^2\rangle,\ \langle\tilde{u}\tilde{T}\rangle,\\ &\langle\tilde{v}\tilde{T}\rangle,\ \langle\tilde{w}\tilde{T}\rangle,\ \langle\tilde{u}\tilde{S}\rangle,\ \langle\tilde{v}\tilde{S}\rangle,\ \langle\tilde{w}\tilde{S}\rangle,\ \langle\tilde{T}^2\rangle,\ \langle\tilde{S}^2\rangle.\end{aligned} \tag{3.16}$$

Additionally, the dissipation rate of the turbulent kinetic energy, ε has to be calculated, see e.g. equation (2.41).

In order to reduce the large amount of computational effort for solving these equations, further simplifications have to be made. One method which is often applied is the local equilibrium assumption for these dynamic equations, which leads to algebraic expressions for the second moments. The algebraic second-moment closures presented here are derived from the dynamic equations (2.25), (2.26) and (2.28) by means of two different approaches. The basic approach is to neglect time variation and advective and turbulent transports of Reynolds stresses $\langle\tilde{v}_i\tilde{v}_j\rangle$, the fluxes of temperature and salinity, $\langle\tilde{v}_i\tilde{T}\rangle$ and $\langle\tilde{v}_i\tilde{T}\rangle$, respectively and the variances of temperature and salinity, $\langle\tilde{T}^2\rangle$ and $\langle\tilde{S}^2\rangle$, respectively. In order to retain the transport of turbulent kinetic energy k, the TKE equation multiplied with $\frac{2}{3}\delta_{ij}$ has to be subtracted from the Reynolds stress equation (2.25) first, and then the left hand side of the resulting transport equation for $\langle\tilde{u}_i\tilde{u}_j\rangle - \frac{2}{3}\delta_{ij}k$ is set to zero. Furthermore, the left hand sides of the temperature and salinity flux equations and the equations for $\langle\tilde{T}^2\rangle$ and $\langle\tilde{S}^2\rangle$ are set to zero as well.

Mellor and Yamada [1974] and *Mellor and Yamada* [1982] used this approach for their so-called level $2\frac{1}{2}$ model. They justify the neglect of transports for $\langle\tilde{v}_i\tilde{v}_j\rangle$, $\langle\tilde{v}_i\tilde{T}\rangle$ and $\langle\tilde{v}_i\tilde{S}\rangle$ by a scaling procedure where terms are ordered by their degree of deviation from isotropy. This results in their level 3 model. The additional neglect of transport terms in the $\langle\tilde{T}^2\rangle$ and $\langle\tilde{S}^2\rangle$ equations then allows for a complete algebraisation.

Here, a non-equilibrium version of the model suggested by *Kantha and Clayson* [1994] is derived by applying the above discussed algebraisation procedure to the equations (2.25), (2.26) and (2.28). This is an extension of the

Mellor and Yamada [1974] and *Mellor and Yamada* [1982] level $2\frac{1}{2}$ model in which the parameterisation of the pressure correlations in the heat flux equation are simpler, because of $c_{2T} = c_{3T} = 0$. The quasi-equilibrium model by *Kantha and Clayson* [1994] is achieved from the non-equilibrium model by applying the equilibrium condition $P + B = \varepsilon$ to the resulting equations, see section 3.1.6.

The same approach for algebraisation is used by *Canuto et al.* [2001].

After this procedure, a linear system of algebraic equations for the 14 second moments listed in (3.16) is obtained for the non-equilibrium version of the model by *Kantha and Clayson* [1994] and the model by *Canuto et al.* [2001].

A different, less rigorous procedure for the algebraisation of the Reynolds stress equation has been suggested by *Rodi* [1976]. The basic assumption is that the ratio of transport of Reynolds stresses to the transport of TKE (see equation (2.31)) is equal to the ratio of Reynolds stresses to TKE:

$$\frac{\partial_t \langle \tilde{v}_i \tilde{v}_j \rangle + \partial_l (\bar{v}_l \langle \tilde{v}_i \tilde{v}_j \rangle + \langle \tilde{v}_i \tilde{v}_j \tilde{v}_l \rangle)}{P + B - \varepsilon} = \frac{\langle \tilde{v}_i \tilde{v}_j \rangle}{k}. \tag{3.17}$$

A similar approach is then used for the temperature flux equation:

$$\frac{\partial_t \langle \tilde{v}_i \tilde{T} \rangle + \partial_l (\bar{v}_l \langle \tilde{v}_i \tilde{T} \rangle + \langle \tilde{v}_l \tilde{v}_i \tilde{T} \rangle)}{P + B - \varepsilon} = \frac{1}{2} \frac{\langle \tilde{v}_i \tilde{T} \rangle}{k}, \tag{3.18}$$

and, analogously, for the salinity flux equation.

This alternative approach has been first applied by *Rodi* [1980] to the Reynolds stress equation and by *Hossain* [1980] to the heat flux equation.

The transport equations for the temperature and salinity variances $\langle \tilde{T}^2 \rangle$ and $\langle \tilde{S}^2 \rangle$ are algebraised in the same manner as for the previously discussed models simply by setting the transport to zero.

Application of this method for algebraisation to the transport equations (2.25), (2.26) and (2.28) and the analogous equations for salinity flux and salinity variance leads to a non-linear system of algebraic equations for the 14 second moments listed in (3.16).

However, already when solving for the linear system of equations for the 14 second moments, the resulting algebraic expressions are expected to be extremely complex[1] due to the rotational terms. For some simplified cases, so-called stability functions which contain the algebraic second-moment closures have been explicitly calculated by *Galperin et al.* [1989], *Galperin and Kantha* [1989], *Hassid and Galperin* [1994] and *Canuto et al.* [2001]. These simplified cases are flows without stratification, i.e. $\partial_z b = 0$, limitation to axial rotation, i.e. at the poles ($\Phi = \pm 90°$) and limitation to spanwise rotation, i.e. at the equator ($\Phi = 0°$). *Canuto et al.* [2001] conclude in their recent publication that

[1] For the non-linear system, it is even not sure whether a solution exists.

Rotation affects the closure problem through the pressure correlations and the equation for the dissipation ε.

Since rotational terms are not explicitly included in the exact equation for ε, (2.33), rotation should be considered indirectly for the parameterisation of the vertical fluxes due to third-order moments and pressure gradients.

For stable stratification, the effect of rotation on the flow seems to be small, see *Galperin et al.* [1989]. For instable stratification however, there is numerous evidence mainly from Large Eddy Simulation studies that rotation can significantly reduce turbulent convective mixing when the turbulent Rossby number $R_o = w_*/(fD)$ is sufficiently large, see *Jones and Marshall* [1993], *Sander et al.* [1995] and *Mironov et al.* [2000]. Such strongly convective situations with deep mixing and subsequent deep water formation occur however only in limited areas during limited periods. Such specific areas are mainly located in the Gulf of Lions (Western Mediterranean Sea) and the Greenland Sea, see *Schott et al.* [1994] and *Marshall and Schott* [1999] for an overview.

Due to the problems associated with the consideration of rotation for the derivation of algebraic turbulence closures and to the comparably limited relevance for marine flows, the rotational effect in the Reynolds stress equations (2.25) will be neglected in the following.

After all the assumptions made above, i.e.

- parameterisation of pressure-strain correlators,
- parameterisation of dissipation terms,
- neglect of tracer cross-correlations,
- boundary layer approximation,
- neglect or simplification of transport of second moments,
- neglect of rotational terms in the second-moment equations,

closed systems of equations are obtained for the second moments listed in (3.16). The empirical parameters for the correlators including salinity fluctuations are simply set to the same values than in the corresponding correlators including temperature fluctuations. This resulting system of equations is linear for the models KC and CA, and non-linear for the model RH. Despite the different structures of the systems of equations, they all result in the simple, well known relations of the eddy viscosity and the eddy diffusivity principle:

$$\langle \tilde{u}\tilde{w} \rangle = -c_\mu \frac{k^2}{\varepsilon} \partial_z \bar{u}, \tag{3.19}$$

$$\langle \tilde{v}\tilde{w} \rangle = -c_\mu \frac{k^2}{\varepsilon} \partial_z \bar{v}, \tag{3.20}$$

$$\langle \tilde{w}\tilde{T} \rangle = -c'_\mu \frac{k^2}{\varepsilon} \partial_z \bar{T} \tag{3.21}$$

$$\langle \tilde{w}\tilde{S} \rangle = -c'_\mu \frac{k^2}{\varepsilon} \partial_z \bar{S} \tag{3.22}$$

With (2.27), an adequate eddy viscosity assumption for the vertical density flux results:

$$\langle \tilde{w}\tilde{\rho} \rangle = -c'_\mu \frac{k^2}{\varepsilon} \partial_z \bar{\rho}. \tag{3.23}$$

The eddy viscosity ν_t and diffusivity ν'_t resulting from this closure are of the following form:

$$\nu_t = c_\mu \frac{k^2}{\varepsilon}, \qquad \nu'_t = c'_\mu \frac{k^2}{\varepsilon}. \tag{3.24}$$

This reflects the relation of *Kolmogorov* [1942] and *Prandtl* [1945] which assumes that eddy viscosity and diffusivity are proportional to a velocity scale and a macro length scale of turbulence. Here, $k^{1/2} = q/\sqrt{2}$ is the velocity scale and

$$L = c_L \frac{k^{3/2}}{\varepsilon} \tag{3.25}$$

with $c_L = (c^0_\mu)^{3/4}$ a macro length scale for energy-containing eddies, which is calculated by means of the *Taylor* [1935] scaling. In (3.25) c^0_μ is the value for c_μ resulting from $B = 0$ and $P = \varepsilon$, see table 6.1 on page 120.

The relation of *Kolmogorov* [1942] and *Prandtl* [1945], equation (3.24), resembles the derivation of kinematic viscosity for a perfect gas, see equation (2.2), where also proportionality of viscosity to a length scale and a velocity scale has been assumed. At this point it should be briefly discussed, why turbulence mixes. Due to the small-scale shear generated by turbulence during the energy cascade, the instantaneous curvature of all flow properties is increased significantly. Since viscous forces, see e.g. equation (2.1), are proportional to the second derivative of the transported flow property, mixing is increased. This leads to an apparent viscosity (for momentum) or diffusivity (for tracers), the so-called eddy viscosity or diffusivity.

All the information on second moments is now contained in the rather complex, non-dimensional stability functions c_μ and c'_μ. Despite their differences, these stability functions depend for all models only on two non-dimensional parameters, the shear number and the buoyancy number, respectively:

$$\alpha_M = \frac{k^2}{\varepsilon^2} M^2, \qquad \alpha_N = \frac{k^2}{\varepsilon^2} N^2 \tag{3.26}$$

with the shear frequency squared, $M^2 = (\partial_z \bar{u})^2 + (\partial_z \bar{v})^2$ and the Brunt-Väisälä frequency squared, $N^2 = \partial_z b$ with buoyancy b from (3.10).

The fact that the eddy viscosity assumption is re-introduced by the algebraic formulations of the second moments, (3.19) - (3.22), might be considered

as a step backwards. *Launder* [1990] has a clearly negative attitude versus the eddy viscosity assumption:

> If one had to pick an animal whose character most resembled turbulence my choice would be an irritable, unpredictable old goat, liable to react violently when prodded. Modelling turbulence by an eddy viscosity scheme is roughly like replacing it by an inoffensive, docile sheep.

He however continues saying:

> For the Nineties one needs a model that retains something of the old goat in turbulence. One class of closure that does that - indeed the simplest class - is second-moment closure.

The way how the turbulence closure is treated here seems thus to be a good compromise between the efficiency of eddy viscosity schemes and the complexity of complete second-moment closures.

The different stability functions are given in the section 3.1.3. It should be noted that up to this point no assumption about the calculation of the turbulent dissipation rate ε has been made.

3.1.3 Non-equilibrium stability functions

Here, the sets of stability functions are given for the models of KC (*Kantha and Clayson* [1994]), HR (*Rodi* [1980], *Hossain* [1980], *Burchard and Baumert* [1995]) and CA (*Canuto et al.* [2001]). An alternative set of stability functions also proposed by *Canuto et al.* [2001] (from here on denoted by CB) is given as well. They are displayed as functions of α_M and α_N in figures 3.1-3.4.

At this stage, the closure of the second moments is practically finished. It should be noted however that all these sets of stability functions should be limited by certain constraints (see section 3.1.5) in order to assure positivity of the eddy viscosity ν_t and diffusivity ν_t' and of the velocity variances $\langle\tilde{u}^2\rangle$, $\langle\tilde{v}^2\rangle$ and $\langle\tilde{w}^2\rangle$, see equations (3.30)-(3.32).

Model of *Kantha and Clayson* [1994]. In the paper of *Kantha and Clayson* [1994], only the quasi-equilibrium version of the stability functions is given. However, also full versions can be derived which are then of the same form as the stability functions originally suggested by *Mellor and Yamada* [1982] with the exception that c_2 and c_3 in equation (2.34) are non-zero now.

In our notation (3.19) - (3.22), this set of stability functions may be formulated as:

$$\begin{aligned} c_\mu &= \frac{0.1682 + 0.03269\alpha_N}{A}, \\ c_\mu' &= \frac{0.1783 + 0.01586\alpha_N + 0.003173\alpha_M}{A}, \end{aligned} \tag{3.27}$$

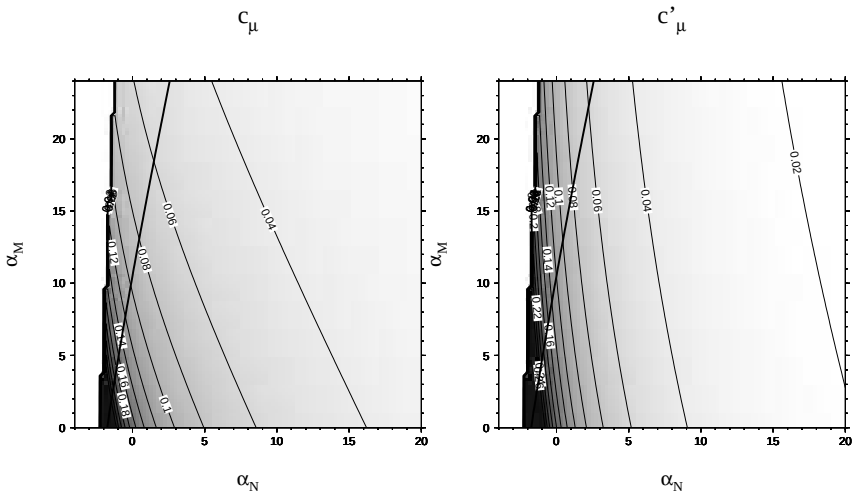

Fig. 3.1. Complete version of stability functions c_μ and c'_μ displayed as functions of the non-dimensional buoyancy number α_N and shear number α_M according to *Kantha and Clayson* [1994]. The white area indicates that the functions are not defined there. The bold line marks the equilibrium state $P + B = \varepsilon$.

with $A = 1 + 0.4679\alpha_N + 0.07372\alpha_M + 0.01761\alpha_N\alpha_M + 0.03371\alpha_N^2$.

The exact form of (3.27) in terms of the empirical parameters (see table 2.1) contained in equations (2.34), (2.37) and (2.41) is given in *Burchard and Bolding* [2001].

It can be seen from figure 3.1 that both stability functions decrease with increasing stratification and shear. For strongly instable stratification with $\alpha_N < 0$ the stability functions are not partially defined such that realisability constraints are necessary, see section 3.1.5.

Model of *Rodi* [1980], *Hossain* [1980], *Burchard and Baumert* [1995]. In contrast to the models of *Kantha and Clayson* [1994] and *Canuto et al.* [2001], the model of *Rodi* [1980] and *Hossain* [1980] in the version of *Burchard and Baumert* [1995] results in stability functions c_μ and c'_μ which not only depend on α_M and α_N, but additionally depend on the non-dimensional term $(P+B)/\varepsilon-1$, i.e. on the degree of deviation from local turbulence equilibrium. This is a consequence of the specific closure concept used in that model, see equation (3.17) and (3.18). Traditionally, these stability functions have been solved in numerical models by using the value for $(P + B)/\varepsilon - 1$ on an old time level. In this form, the stability functions have been presented first by *Rodi* [1980] and *Hossain* [1980].

However, because of $(P + B)/\varepsilon = c_\mu\alpha_M - c'_\mu\alpha_N$, these equations for c_μ and c'_μ can be expressed as implicit functions of α_M and α_N. The evaluation procedure which has been suggested by *Burchard and Baumert* [1995] is first

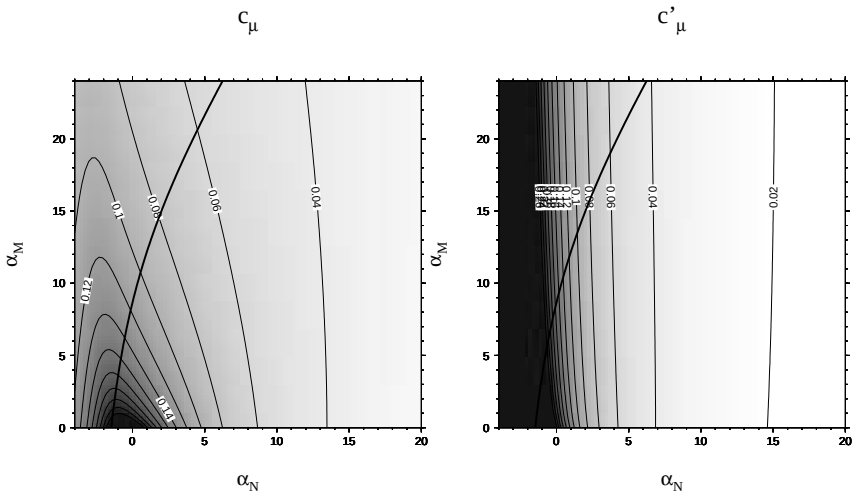

Fig. 3.2. Same as figure 3.1 but for the *Rodi* [1980] and *Hossain* [1980] (version of *Burchard and Baumert* [1995]) stability functions.

solving for $(P+B)/\varepsilon - 1$ by means of a Newton iteration and then inserting that value into the formulations for c_μ and c'_μ. This procedure is discussed in detail in *Burchard and Bolding* [2001].

These numerically solved implicit stability functions are displayed in figure 3.2. In contrast to the *Kantha and Clayson* [1994] and also the *Canuto et al.* [2001] stability functions, they are defined over the whole domain $-\infty < \alpha_N < +\infty$ and $0 \leq \alpha_M < +\infty$. This cannot be proved mathematically, but negative values have not been found for arbitrary values of α_N and α_M. This does of course not imply that these stability functions are physically sound even for extreme values of α_N and α_M. Indeed, the strong decrease of c_μ for instable stratification suggests that the algebraic assumptions made are not valid for such strongly convective regimes.

Model of *Canuto et al.* [2001]. The stability functions as they result from the closure assumptions carried out by *Canuto et al.* [2001] are as follows:

$$\begin{aligned} c_\mu &= \frac{0.1070 + 0.01741\alpha_N - 0.00012\alpha_M}{A}, \\ c'_\mu &= \frac{0.1120 + 0.004519\alpha_N + 0.00088\alpha_M}{A}, \end{aligned} \tag{3.28}$$

with $A = 1 + 0.26\alpha_N + 0.029\alpha_M + 0.0087\alpha_N^2 + 0.005\alpha_N\alpha_M - 0.000034\alpha_M^2$.

Despite the higher complexity of the transport equations for Reynolds stresses and heat fluxes due to consideration of more terms for the pressure-strain correlators, these stability functions are structurally similar to those of *Kantha and Clayson* [1994].

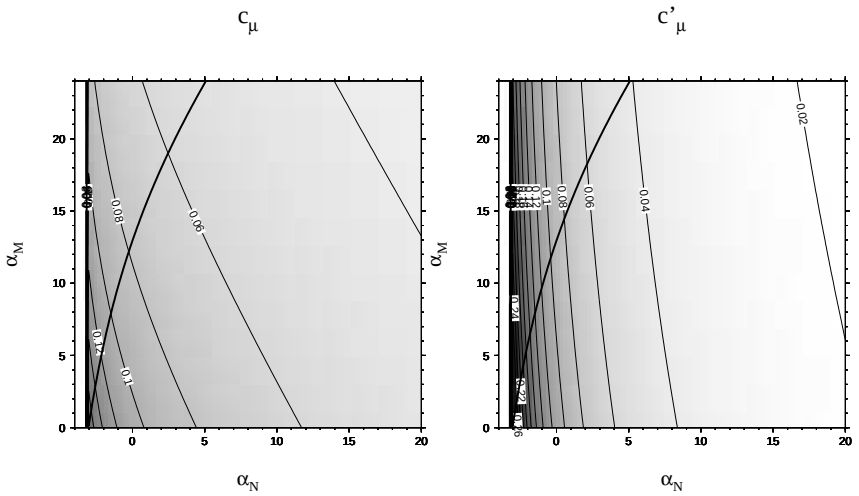

Fig. 3.3. Same as figure 3.1 but for the *Canuto et al.* [2001] (version A) stability functions.

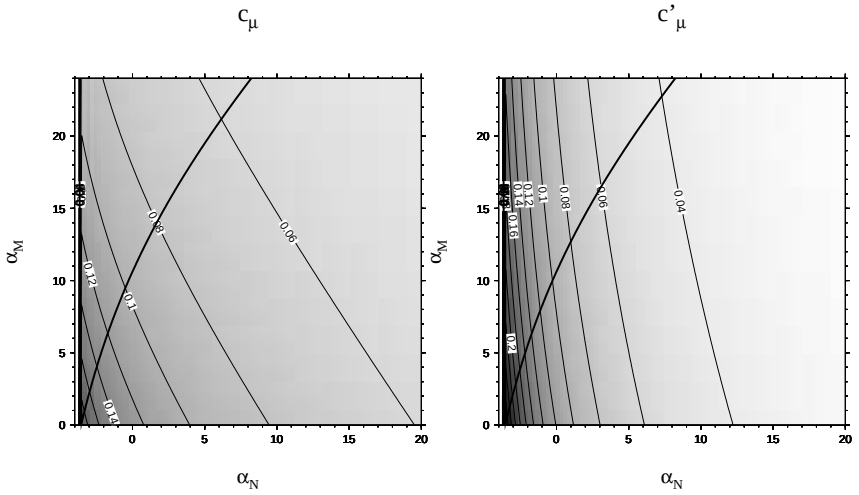

Fig. 3.4. Same as figure 3.1 but for the *Canuto et al.* [2001] (version B) stability functions.

These stability functions will be denoted by CA. The exact form can be found in *Burchard and Bolding* [2001]. In their paper, *Canuto et al.* [2001] give another set of stability functions derived on the ground of different assumptions. They will be denoted by CB and are of the following form:

$$\begin{aligned} c_\mu &= \frac{0.1270 + 0.01526\alpha_N - 0.00016\alpha_M}{A}, \\ c'_\mu &= \frac{0.1190 + 0.004294\alpha_N + 0.00066\alpha_M}{A}, \end{aligned} \tag{3.29}$$

with $A = 1 + 0.2\alpha_N + 0.0315\alpha_M + 0.0058\alpha_N^2 + 0.004\alpha_N\alpha_M - 0.00004\alpha_M^2$.

Both sets of stability functions are displayed in figures 3.3 and 3.4. They look basically both similar to the *Kantha and Clayson* [1994] stability functions displayed in figure 3.1. However, a closer inspection reveals that the convective limit seems to be weaker and the line of local equilibrium is not that close to the line of neutral stratification. This could be the reason why the *Canuto et al.* [2001] version A set of stability functions allows for numerically stable simulations of idealised boundary layers, in contrast to the *Kantha and Clayson* [1994] scheme, see section 6.2.3 and *Burchard and Deleersnijder* [2001].

It should be noted that the way how the stability functions (3.27) – (3.29) are displayed here is physically not very appealing. However, it gives a feeling about their general structure. For a deeper physical understanding of the differences, one would have to step back to the derivation of these functions, see equations (2.34) and (2.37), or even better to the original papers.

3.1.4 Velocity and tracer variances

Although not needed for the closure of the turbulent transport terms for momentum and heat, it is possible to compute the auto-correlations (or variances) of velocity and temperature. They can be used for model validation, see section 6.3. The auto-correlation terms are often measured in the field or obtained in idealistic situations by LES or DNS. For four closure procedures KC, RH, CA and CB, these auto-correlators can be written as:

$$\langle \tilde{u}^2 \rangle = \frac{2}{3}k + e_1\frac{k}{\varepsilon}\frac{e_2\nu_t(\partial_z\bar{u})^2 - e_3\nu_t(\partial_z\bar{v})^2 - B}{1 + e_4(\frac{P}{\varepsilon} + \frac{B}{\varepsilon} - 1)}, \tag{3.30}$$

$$\langle \tilde{v}^2 \rangle = \frac{2}{3}k + e_1\frac{k}{\varepsilon}\frac{-e_3\nu_t(\partial_z\bar{u})^2 + e_2\nu_t(\partial_z\bar{v})^2 - B}{1 + e_4(\frac{P}{\varepsilon} + \frac{B}{\varepsilon} - 1)}, \tag{3.31}$$

$$\langle \tilde{w}^2 \rangle = \frac{2}{3}k - e_1\frac{k}{\varepsilon}\frac{(e_2 - e_3)\nu_t(\partial_z\bar{u})^2 + (e_2 - e_3)\nu_t(\partial_z\bar{v})^2 - 2B}{1 + e_4(\frac{P}{\varepsilon} + \frac{B}{\varepsilon} - 1)}, \tag{3.32}$$

$$\langle \tilde{T}^2 \rangle = c_T\frac{k}{\varepsilon}\nu'_t(\partial_z\bar{T})^2, \tag{3.33}$$

where the empirical parameters $e_1, \ldots, e_4$ are given in table 3.2. For c_T, see table 2.1. Exact expressions for these parameters are given in the *Burchard and Bolding* [2001].

Model	e_1	e_2	e_3	e_4
KC	0.224	2.0	1.0	0.0
RH	0.185	1.6	0.8	0.556
CA	0.160	1.093	0.027	0.0
CB	0.135	1.362	0.033	0.0

Table 3.2. Parameters for calculating the variances $\langle\tilde{u}^2\rangle$, $\langle\tilde{v}^2\rangle$, $\langle\tilde{w}^2\rangle$ and $\langle\tilde{T}^2\rangle$.

It can be easily seen that (3.30) - (3.32) are consistent with the definition of turbulent kinetic energy k, see equation (2.30). It should be noted that the well-known stability functions suggested by *Galperin et al.* [1988] are included in the analysis of section 3.1.2 as well. They are obtained from the KC model by assuming quasi-equilibrium and setting $c_2 = c_3 = 0$. In the paper by *Galperin et al.* [1988], (2.30) does apparently not hold, because a residual term remains. However, it can be shown that this residual term is proportional to $P + B - \varepsilon$ which vanishes with the quasi-equilibrium assumption.

3.1.5 Realisability constraints

Due to the simplifying model assumptions which lead to the formulation of stability functions, these are not valid over the whole domain $0 \leq \alpha_M < \infty$ and $-\infty < \alpha_N < \infty$. There are restrictions for (i) convective regimes due to instable stratification (large negative α_N), (ii) strong shear (large α_M), and (iii) strongly stable stratification (large positive α_N).

The restrictions due to convection are the most obvious. It is known that third moments such as $\langle\tilde{w}^3\rangle$, $\langle\tilde{w}^2\tilde{T}\rangle$,and $\langle\tilde{w}\tilde{T}^2\rangle$ which have been set to zero here, play an important role in such situations (see *Canuto et al.* [1994], *Mironov et al.* [2000]). The stability functions KC, CA and CB predict negative values here which would turn the dynamical equations for momentum and heat to ill-posed problems. Here we would suggest as a practical solution to avoid negative stability functions and set upper limits for c_μ and c'_μ. In accordance with *Galperin et al.* [1988] these could be 0.46 for c_μ and 0.61 for c'_μ. For avoiding numerical instabilities, the smoothing procedure suggested by *Burchard and Petersen* [1999] might be useful. The RH stability function for c_μ is decreasing with increasing instability, a feature physically at least difficult to interpret. Here, a lower limit for α_N should be derived from the criterium that the gradient of c_μ with respect to α_N should be negative.

Since strongly stable stratification could as well lead to negative vertical velocity variance, an upper limit for α_N should be introduced as well. *Kantha*

and Clayson [1994] suggest for example $\alpha_N < 9.6$ for their quasi-equilibrium model.

Another physical constraint on the realisability of the stability functions is the positivity of the velocity variances. It can be seen from the definition of $\langle\tilde{w}^2\rangle$, equation (3.32), that high shear as well as strongly stable stratification might lead to negative values of $\langle\tilde{w}^2\rangle$. Demanding positivity of $\langle\tilde{w}^2\rangle$ leads after application of equation (3.32) to a further (implicit and therefore difficult to use) constraint on α_M and α_N. In order to guarantee that the normalised vertical velocity variance $\langle\tilde{w}^2\rangle/k$ is not smaller than 0.24 which seems to be the physical limit, *Mellor and Yamada* [1982] suggest the condition

$$\alpha_M < 16.5 + 517\alpha_N, \tag{3.34}$$

which also defines a lower limit for α_N. Others (*Hassid and Galperin* [1983] and *Canuto et al.* [2001]) suggest to derive upper limits for α_M by demanding that the shear stress should not decrease for increasing shear. *Burchard and Deleersnijder* [2001] found however, that such a constraint is not needed for the *Canuto et al.* [2001] stability functions when used together with a k-ε model.

The reason for this can be understood by inspecting figure 3.5 where the dimensionless shear stress $S_M G_M^{1/2} \propto u_*^2/k$ is displayed as function of $G_M \propto \alpha_M$ and $G_H \propto -\alpha_N$. Following *Burchard and Deleersnijder* [2001], the notation by *Mellor and Yamada* [1982] is used here, for an exact conversion, see section 9.1.2. Shown are stresses computed from non-equilibrium stability functions by *Mellor and Yamada* [1982] (similar to *Kantha and Clayson* [1994]) and *Canuto et al.* [2001], version A, see section 3.1.3. For both cases, $G_M \propto \alpha_M$ is limited in the stress calculation such that the stress, u_*^2/k, increases for increasing shear, $G_M \propto \alpha_M$, which is often used as realisability constraint for stability functions:

$$\partial_{G_M}\left(\frac{u_*^2}{k}\right) \propto \partial_{\alpha_M}\left(\frac{u_*^2}{k}\right) > 0. \tag{3.35}$$

The most striking difference between the two stress calculations in figure 3.5 is now, that for the *Mellor and Yamada* [1982] model, the local equilibrium line $P+B=\varepsilon$ is above constraint (3.35) and for the *Canuto et al.* [2001] model below this constraint. This has the consequence that for the former model without (3.35) (the constraint by *Mellor and Yamada* [1982], (3.34), is much weaker) that the quasi-equilibrium state, which is a good approximation for shear flows, is in the area where the shear stress decreases with increasing shear. It has been shown by *Burchard and Deleersnijder* [2001] that this might be the mechanism for the instabilities usually caused by this model, since the instabilities vanish when limiting G_M by (3.35). These instabilities can also be avoided by using so-called quasi-equilibrium versions of the stability function from the beginning on, see section 3.1.6. For a detailed investigation of these instabilities, see section 6.2.3.

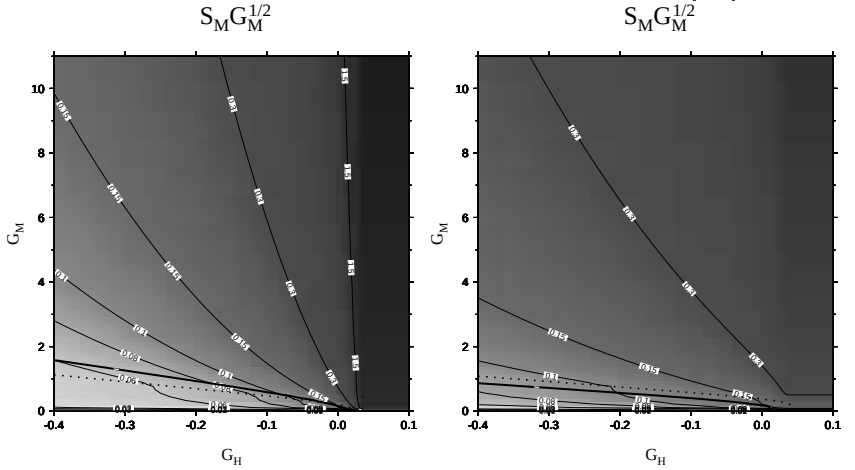

Fig. 3.5. The normalised shear stress $S_M G_M^{1/2} \propto u_*^2/k$ as functions of $G_M \propto \alpha_M$ and $G_H \propto -\alpha_N$ computed by using the *Mellor and Yamada* [1982] (left) and the *Canuto et al.* [2001], version A (right) stability functions. The bold line shows the condition $P + B = \varepsilon$, the dotted line the constraint (3.35) in the sense that (3.35) is fulfilled for all points below the dotted line.

3.1.6 Quasi-equilibrium stability functions

The quasi-equilibrium state is defined as the state where production and dissipation of turbulent kinetic energy are balanced, i.e. $P + B = \varepsilon$. This can be transformed to the relation

$$c_\mu \alpha_M - c'_\mu \alpha_N = 1. \tag{3.36}$$

This quasi-equilibrium state has often been used for simplifying stability functions depending on both, α_M and α_N. The most well-known example is the work of *Galperin et al.* [1988] where relation (3.36) has been used for improving the performance of the stability functions proposed by *Mellor and Yamada* [1982], which have been proven to be numerically unstable (see *Deleersnijder and Luyten* [1994]). *Galperin et al.* [1988] found by applying the scale analysis introduced by *Mellor and Yamada* [1974] that it is not a model inconsistency to prescribe $P + B = \varepsilon$ only for the stability functions but still retain the full dynamic TKE equation, see also section 3.1.4.

The bold lines in figures (3.1) - (3.4) indicate the quasi-equilibrium states for the four sets of stability functions discussed in this paper. The stability functions suggested by *Galperin et al.* [1988] are expressed as functions of α_N. Relation (3.36) allows also to express the stability functions depending on the gradient Richardson number $R_i = \alpha_N/\alpha_M$, which has often been done for further analysing the stability functions as shown in figure 3.6 for the four sets of stability functions. The maximum value of R_i which can be reached

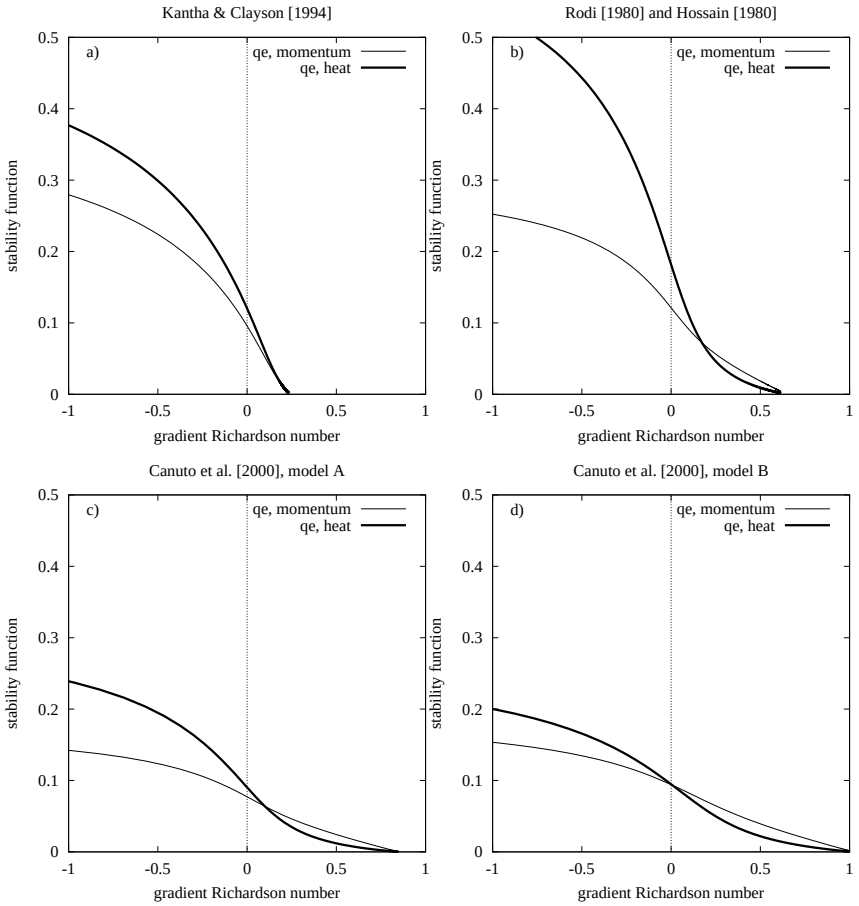

Fig. 3.6. Quasi-equilibrium versions of stability functions c_μ and c'_μ displayed as functions of the gradient Richardson number R_i. a) Model of *Kantha and Clayson* [1994] [1994], b) Model of *Rodi* [1980] and *Hossain* [1980], c) Model A of *Canuto et al.* [2001], d) Model B of *Canuto et al.* [2001].

in the quasi-equilibrium is called the 'critical' Richardson number R_i^c. For the models discussed here, they have the values shown in table 6.1 on page 120. It can be seen that the model of *Kantha and Clayson* [1994] already suppresses turbulence for stratifications around $R_i = 0.2$, whereas the other models allow for mixing at Richardson numbers significantly higher.

For stable stratification, laboratory and LES data for the turbulent Prandtl number $P_r = c_\mu / c'_\mu$ are compared to the turbulent Prandtl number computed by the quasi-equilibrium stability functions (see figure 3.7). All the functions are within the uncertainty of the data. Only the KC quasi-

equilibrium stability functions do not reach high turbulent Prandtl numbers due to their relatively small critical gradient Richardson number.

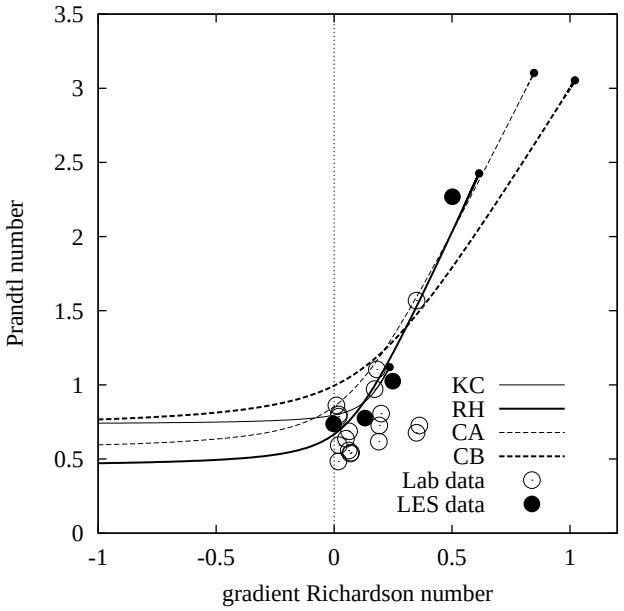

Fig. 3.7. Turbulent Prandtl number, calculated from the quasi-equilibrium version of stability function displayed as function of the gradient Richardson number R_i. KC: Model of *Kantha and Clayson* [1994], RH: Model of *Rodi* [1980] and *Hossain* [1980], CA: Model A of *Canuto et al.* [2001], CB Model B of *Canuto et al.* [2001]. The laboratory data are from *Rohr* [1985], the LES data are from *Schumann and Gerz* [1995]. The small bullets mark the maximum values of the turbulent Prandtl numbers due to the critical Richardson number R_i^c.

Another way of displaying the quasi-equilibrium stability functions is to transform them into the Monin-Obukhov similarity form. This has already been suggested by various authors, see *Mellor and Yamada* [1982] and *Kantha and Clayson* [1994]. *Monin and Obukhov* [1954] found for the atmospheric boundary layer non-dimensional relations between fluxes of momentum and heat and gradients of velocity and density, respectively. Based on the Monin-Obukhov length, $L_M = -u_*^3/(\kappa B)$, gradients of momentum and buoyancy can be expressed as follows:

$$\partial_z \bar{u} = \frac{u_*}{\kappa z'} \Phi_M \left(\frac{z'}{L_M} \right), \qquad \partial_z b = -\frac{B}{\kappa z' u_*} \Phi_H \left(\frac{z'}{L_M} \right) \tag{3.37}$$

with the distance from the boundary, z' and the von Kármán constant $\kappa = 0.4$. With the friction velocity $u_*^2 = c_\mu \frac{k^2}{\varepsilon}|\partial_z u|$, the buoyancy flux $B = -c'_\mu \frac{k^2}{\varepsilon}\partial_z b$ and the macro length scale $L = \kappa z'$, the variables $\xi = z'/L_M$, Φ_M and Φ_H can be expressed as

$$\xi = (c_\mu^0)^{3/4} \frac{c'_\mu}{c_\mu^{3/2}} \cdot \frac{\alpha_N}{\alpha_M^{3/4}}, \tag{3.38}$$

and

$$\Phi_M = (c_\mu^0)^{3/4} \frac{\alpha_M^{1/4}}{c_\mu^{1/2}}, \quad \Phi_H = (c_\mu^0)^{3/4} \frac{c_\mu^{1/2} \alpha_M^{1/4}}{c'_\mu}, \tag{3.39}$$

where the turbulent Prandtl number can be expressed as $P_r = \Phi_M/\Phi_H = c_\mu/c'_\mu$.

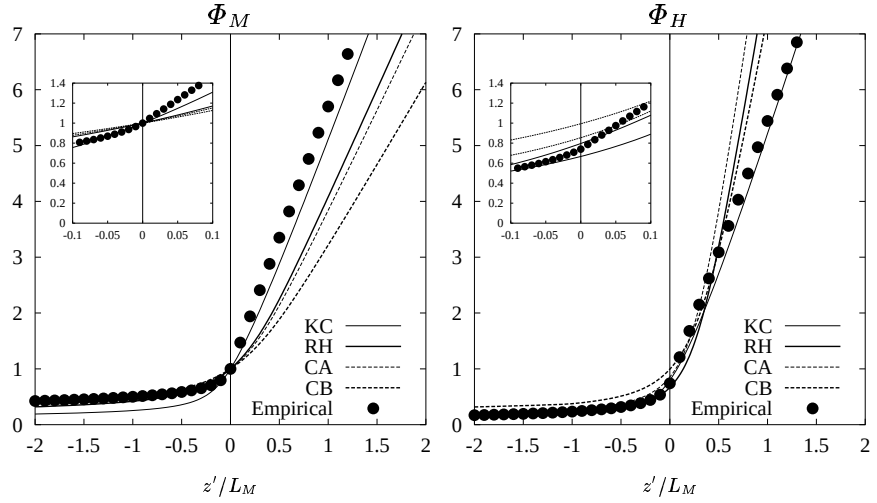

Fig. 3.8. Monin-Obukhov similarity functions Φ_M and Φ_H as calculated from the quasi-equilibrium stability functions of *Kantha and Clayson* [1994] (KC), *Rodi* [1980] and *Hossain* [1980] (RH), *Canuto et al.* [2001] (CA,CB). The empirical curves are taken from *Businger et al.* [1971].

Figure 3.8 shows the Monin-Obukhov similarity functions Φ_M and Φ_H as functions of ξ in comparison to empirical curves by *Businger et al.* [1971]. The stability functions by *Kantha and Clayson* [1994] are clearly the closest to the empirical curves which are based on measurements in the atmospheric boundary layer. It should be noted that this is due to a tuning of the parameters c_2 and c_3. *Mellor and Yamada* [1982] achieved a good agreement with the *Businger et al.* [1971] data with their relatively simple closure by

setting $c_2 = c_3 = 0$. It is difficult to explain why more complex parameterisations of the pressure-strain correlations cause worse agreement with the Monin-Obukhov theory. But it might be due to the fact that this theory is valid only close to boundaries where some of the closure assumptions could be wrong. Another reason could be that the *Businger et al.* [1971] measurements are taken at the atmosphere where in comparison to water different molecular viscosities and diffusivities are present. This could be particularly significant at strongly stable stratification with large positive values of ξ.

3.2 Two-equation models

In the second-moment closure presented here as formulations for the eddy viscosity and eddy diffusivity, see equation (3.24), the turbulent kinetic energy k and its dissipation rate ε still occur as unknows. They are contained in the stability functions as a ratio, defining a time scale $\tau = k/\varepsilon$ and in the relations of Prandtl and Kolmogorov as ratio k^2/ε. Thus, either algebraic relations or prognostic equations have to be calculated for k and ε. In principle, three methods for this are found in the literature, see e.g. *Luyten et al.* [1996a]:

- Zero-equation models: here, the TKE is calculated from the local equilibrium condition of turbulence, $P + B = \varepsilon$ and the dissipation rate is calculated by means of an algebraic relation for the macro length scale L from which the dissipation rate ε is then recalculated by means of equation (3.25).
- One-equation models: here, the TKE is calculated from a transport equation derived from equation (2.31) and the macro length scale is treated algebraically as in zero-equation models.
- Two-equation models: here, both the TKE and the macro length scale are calculated from transport equations. This book is concentrating mainly on such two-equation models.

There are many suggestions for the algebraic calculation of the macro length scale. Rather simple forms are based on the work of *Blackadar* [1962], where L is basically a function of the distance from surface and bottom. Others follow a suggestion of *Kochergin* [1987] and choose a constant macro length in the surface and bottom mixed layer plus a background value in strongly stratified regions (see *Pohlmann* [1991], *Pohlmann* [1996b]). The latter method has however two disadvantages: the law of the wall is not reproduced near boundaries and the length scale has discontinuities in time and space. Complex algebraic relations have for example been suggested by *Therry and Lacarrère* [1983] and *Gaspar et al.* [1990] and built into an Ocean General Circulation Model by *Blanke and Delecluse* [1993]. In this approach, the macro length scale is calculated as the distance which a fluid particle has to move such that the change of potential energy equals the turbulent

kinetic energy. Other approaches by *Eifler and Schrimpf* [1992] and *Demirov et al.* [1998] or by *Beckers* [1995] and *Delhez et al.* [1999] or by *Axell and Liungman* [2001] combine several macro length scales such as the law of the wall scaling, see equation (3.56), and the scaling according to the buoyancy length scale, see equation (3.73) and also *Meier* [2000].

However, the focus of this book is on two-equation models. For the macro length scale related transport equation, many options are possible. Through equation (3.25) which defines a non-linear relation between k, ε and the macro length scale L, a second transport equation for any quantity $k^m\varepsilon^n$ with $n \neq 0$ would in principle be sufficient for calculating the dissipation rate ε, see *Rodi* [1987]. Such a generic model will be investigated in detail in section 3.2.13. Furthermore well-known specialised cases of this generic model will be discussed, namely the k-ε model (section 3.2.5) and the k-kL model (section 3.2.6). The k-ω model with $\omega = \varepsilon/k$ will be briefly discussed in section 3.2.7.

The ε and the kL equation are the two prognostic transport equations for a length scale related variable which are mainly in use in oceanography. The structural similarity of these two equations has been discussed recently by *Burchard et al.* [1998], *Burchard and Petersen* [1999], *Baumert and Peters* [2000] and *Burchard and Bolding* [2001], see also section 3.2.9.

Since the late seventies, a controversial discussion about the higher physical relevance of each of the two length scale equations has been carried out. The arguments of the main protagonists of this discussion are cited here:

Mellor and Yamada [1982]:

> While one cannot assert great confidence in [the kL equation], we prefer it rather than the differential equation for dissipation ...
> ... it seems fundamentally wrong to us to use an equation which describes the small scale turbulence to determine the turbulent macroscale. Operationally, however, after some terms are modelled, the dissipation transport equation is a special case of a more general length scale equation ...

Rodi [1987]:

> The arguments for the relative merits of the ε and the kL equations are rather academic because both equations are fairly empirical and, with the constants suitable adjusted, perform in a similar manner. One difference is that the kL equation requires an additional near-wall term ... while the ε equation does not.

In the concept of one-point closures, the macro length scale L is to be defined via the *Taylor* [1935] scaling (3.25), since L cannot be directly defined in terms of one-point correlators. This makes it difficult to construct a transport equation for L. In the terminology of two-point closures however,

the macro length scale L "is defined as the integral of the two-point, longitudinal correlation function, integrated with respect to the distance separating the two points" (*Mellor* [1985]). *Mellor* [1985] adds to his criticism of the k-ε model that the ε-equation cannot properly be extended into two-point correlations. Thus, a transport equation for a macro length scale should be preferred. However, both authors, *Mellor and Yamada* [1982] and *Rodi* [1987], seem to express some kind of acceptance of the respective other model, since both are subject to severe empirical assumptions. This pragmatic viewpoint also holds here in this book, when the two models are discussed.

One appealing feature of the k-ε model however is that it has one prognostic equation for the macro scale of turbulence, which is the k-equation (k is mainly contained in the large eddies), and one for the Kolmogorov micro scale λ which is defined by means of the dissipation rate ε:

$$\lambda = \left(\frac{\nu^3}{\varepsilon}\right)^{1/4}. \tag{3.40}$$

It should be noted that the viscous dissipation has been observed for the ocean to be dominant at eddy sizes 30 to 60 times the Kolmogorov scale λ by *Gargett and Holloway* [1984] and *Moum* [1990]. Any instrument for measuring turbulent dissipation such as shear probes is therefore limited in size since the smallest dissipative eddies with diameters of about $2\pi\lambda$ have to be resolved, which is often difficult near the surface and the bottom, see *Prandke and Stips* [1998].

3.2.1 The TKE-equation

The TKE equation is basically the same for all types of these models. It can be derived from the exact Reynold's averaged equation (2.31) by applying the boundary layer approximation discussed in section 3.1.1, applying the down-gradient approximation for the third moment and neglecting advective terms:

$$\partial_t k - \partial_z \left(\left(\nu + \frac{\nu_t}{\sigma_k} \right) \partial_z k \right) = P + B - \varepsilon, \tag{3.41}$$

σ_k denotes here the turbulent Schmidt number for vertical flux of TKE. For the shear production P and the buoyancy production B application of (3.19) and (3.23) results in:

$$P = \nu_t \left((\partial_z \bar{u})^2 + (\partial_z \bar{v})^2 \right), \qquad B = -\nu_t' \partial_z b \tag{3.42}$$

with the buoyancy b from equation (3.10). It should be noted that the k-kL model by *Mellor and Yamada* [1982] uses a slightly different parameterisation of the third moment of the TKE, see section 3.2.6.

Before discussing in detail the possibilities for deriving length scale related equations for the calculation of ε, the concept of roughness (section 3.2.2), the law of the wall (section 3.2.3) and boundary conditions derived from that (section 3.2.4) are presented.

3.2.2 Roughness

The coordinates for bottom and surface are located at the edge of the validity of the model equations, which is excluding the unresolved zones near the boundaries (see figure 3.9).

Roughness lengths at bottom and surface, z_0^b and z_0^s have to be defined. For the bottom, this is done here as follows (see e.g. *Kagan* [1995]):

$$z_0^b = 0.1\frac{\nu}{u_*^b} + 0.03h_0^b. \tag{3.43}$$

with the molecular viscosity ν, the friction velocity u_*^b and the height of the bottom roughness elements, h_0^b. The formula (3.43) interpolates between the limits of completely smooth ($h_0^b = 0$) and completely rough bottom ($h_0^b \gg \nu/u_*^b$). In tidal flow, e.g., the roughness can periodically change between smooth and rough bed. It should be noted that the bed roughness z_0^b may be a complex function of bed forms (see e.g. *Ke et al.* [1994]), sediment dynamics (see e.g. *Smith and McLean* [1977] or *Sheng and Villaret* [1989]) and surface waves (see *Grant and Madsen* [1979] and also *Mellor* [2001b]).

For estimating the sea surface roughness z_0^s, an adaptation of the *Charnok* [1955] formula to the sea surface is often used:

$$z_0^s = \alpha_C \frac{(u_*^s)^2}{g} \tag{3.44}$$

with the dimensionless parameter $\alpha_C = 1400$ (see *Craig and Banner* [1994]). Just to give a feeling for this formula: By using the *Kondo* [1975] bulk formulae for estimating the air-sea fluxes, under the assumption of no temperature difference between sea and air, a wind speed at 10 m above the sea surface of $U_{10} = 5\ \mathrm{m\,s^{-1}}$ results in $z_0^s = 0.005$ m and a wind speed of $U_{10} = 25\ \mathrm{m\,s^{-1}}$ results in $z_0^s = 0.19$ m. This seems to slightly underestimate realistic conditions, since *Gemmrich and Farmer* [1999] measured $z_0^s = 0.2$ at wind speeds of only $U_{10} = 15\ \mathrm{m\,s^{-1}}$. For a discussion of the problems associated with the determination of z_0^s, see page 90. For the interpretion of the surface roughness as the virtual origin , see also *Thompson and Turner* [1975] and section 3.3.1.

It should be noted that this definition of a surface roughness excludes the so-called surface skin effect. Near the air-sea interface, strong gradients are observed which develop due to the absence of turbulence in the viscous sublayer, see e.g. *Grassl* [1976].

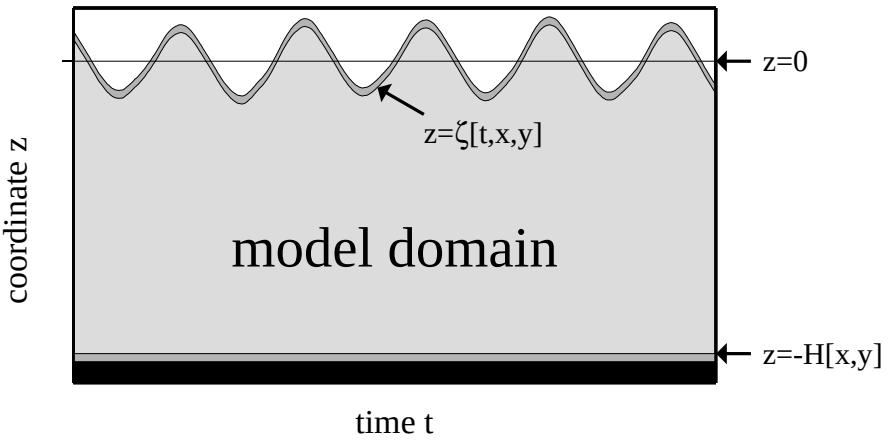

Fig. 3.9. Sketch showing the definition of the model domain, which is only the light grey area in the (t, z)-space. The dark grey areas are the viscous sublayers, which are not described by the model equations and the effect of which has to be parameterised. The thicknesses of these sublayers are z_0^b for the bottom layer and z_0^s for the surface layer.

3.2.3 The law of the wall

The law of the wall is an idealisation of the equations of motions which reproduces flow profiles near walls with high accuracy. In order to obtain these equations, the stationary, unstratified and non-rotational equations for one horizontal velocity component $\bar{u}$ is considered:

$$\partial_z(\nu_t \partial_z \bar{u}) = g\partial_x \zeta \tag{3.45}$$

Vertical integration and the assumption a zero surface momentum flux results in:

$$\nu_t \partial_z \bar{u} = (u_*)^2 \left(1 - \frac{z'}{D}\right) \tag{3.46}$$

with $z = -H$ being the bottom coordinate, $D = \zeta + H$ being the water depth, $(u_*)^2 = -gD\partial_x\zeta$ (for $\partial_x\zeta < 0$) being the bottom friction velocity squared and $z' = z + H$ being the distance from the bottom. Furthermore, local turbulence equilibrium is assumed,

$$P = \varepsilon, \tag{3.47}$$

and the macro length scale being

$$L = \kappa(z + z_0)\left(1 - \frac{z'}{D}\right)^{1/2}, \tag{3.48}$$

with the von Kármán constant $\kappa = 0.4$. This asymmetric formulation considers the smaller dampening of turbulent eddies by the stress-free surface in comparison to the bottom. With the eddy viscosity

$$\nu_t = c_\mu^0 \frac{k^2}{\varepsilon}, \tag{3.49}$$

the shear production

$$P = \nu_t(\partial_z \bar{u})^2, \tag{3.50}$$

the dissipation rate from (3.25) and the bottom boundary condition $\bar{u}(-H) = 0$, the following solution for $\bar{u}$, k, ε and ν_t is obtained:

$$\frac{\bar{u}(z')}{u_*} = \frac{1}{\kappa}\ln\left(\frac{z' + z_0}{z_0}\right), \tag{3.51}$$

$$k(z') = \frac{u_*^2}{\sqrt{c_\mu^0}}\left(1 - \frac{z'}{D}\right), \tag{3.52}$$

$$\varepsilon(z') = \frac{(u_*)^3\left(1 - \frac{z'}{D}\right)}{\kappa(z' + z_0)} \tag{3.53}$$

and

$$\nu_t = \kappa u_*(z' + z_0)\left(1 - \frac{z'}{D}\right). \tag{3.54}$$

For positions close to the wall with $z'/D \ll 1$, the classical law of the wall results. For further details, see *Nezu and Nakagawa* [1993].

It should be noted that usually constant stress near walls is associated with the law of the wall, which is expressed by

$$\partial_z(\nu_t \partial_z \bar{u}) = (u_*^s)^2 \tag{3.55}$$

instead of equation (3.46) and

$$L = \kappa(z + z_0) \tag{3.56}$$

instead of equation (3.48). Both concepts lead to the logarithmic profile of velocity, equation (3.51), anyway, see *Burchard et al.* [1999]. However, since this situation is untypical for the ocean the alternative approach of linearly decreasing shear stress has been chosen here.

3.2.4 Boundary conditions

For the horizontal velocity components $\bar{u}$ and $\bar{v}$, no-slip boundary conditions are applied at the bed:

$$\bar{u} = \bar{v} = 0, \qquad \text{for } z = -H. \tag{3.57}$$

By exploiting the law of the wall, this is transformed to a quadratic friction boundary condition for the numerical discretisation, see section 4.4. The bottom boundary conditions for temperature and salinity are usually formulated as no-flux conditions unless specific thermal or freshwater sources at the bed are considered:

$$\nu_t' \partial_z \bar{T} = \nu_t' \partial_z \bar{S} = 0, \qquad \text{for } z = -H. \tag{3.58}$$

At the surface, fluxes of momentum and temperature are calculated by means of bulk formulae which relate atmospheric parameters to these fluxes:

$$\nu_t \partial_z \bar{u} = \frac{\tau_s^x}{\rho_0}, \qquad \nu_t \partial_z \bar{v} = \frac{\tau_s^y}{\rho_0}, \qquad \text{for } z = \zeta \tag{3.59}$$

with the surface stress components $\tau_s^x = u_*^{sx} u_*^s$ and $\tau_s^y = u_*^{sy} u_*^s$ with $u_*^s = \sqrt{(u_*^{sx})^2 + (u_*^{sy})^2}$ and

$$\nu_t' \partial_z \bar{T} = \frac{Q_s + Q_l + Q_b}{c_p' \rho_0}, \qquad \text{for } z = \zeta, \tag{3.60}$$

with the sensible heat flux, Q_s, the latent heat flux, Q_l and the long wave back radiation, Q_b. For the studies presented in chapter 7, the *Kondo* [1975] bulk formulae have been used for calculating the momentum and temperature surface fluxes due to air-sea interactions. For the surface freshwater flux, which defines the salinity flux, the difference between evaporation Q_E (from bulk formulae) and precipitation Q_P (from observations or atmospheric models) is calculated:

$$\nu_t' \partial_z \bar{S} = \frac{\bar{S}(Q_E - Q_P)}{\rho_0(0)}, \qquad \text{for } z = \zeta, \tag{3.61}$$

where $\rho_0(0)$ is the density of freshwater at sea surface temperature. In the presence of sea-ice, the calculation of freshwater flux is more complex, see e.g. *Large et al.* [1994]. For water column simulations with significant imbalance between Q_E and Q_P, the freshwater flux is of great importance for the near surface stratification, see e.g. *Clayson and Kantha* [1999] for the tropical Pacific Ocean. However, for many short term calculations, the freshwater flux can often be neglected compared to the surface heat flux.

The law of the wall, see section 3.2.3, is usually exploited for deriving boundary conditions for turbulent quantities. For standard situations, no difference is made for the bottom and for the surface. During strong wind

periods when breaking surface waves are present, surface boundary conditions have to be however modified, see section 3.3.2. It is therefore assumed that the boundaries under consideration lie inside the wall region with $z'/D \ll 1$. For marine applications, Dirichlet-type (prescription of value) or Neumann-type (prescription of turbulent flux) are common, but also mixed types could easily be derived from the law of the wall. With the notation shown in figure 3.9, which locates the bottom boundary $z = -H$ at the upper edge of the unresolved bottom layer and the surface boundary $z = \zeta$ at the lower edge of the unresolved surface layer, the Dirichlet-type boundary conditions for k and ε are of the following form:

$$k(z') = \frac{u_*^2}{\sqrt{c_\mu^0}} \tag{3.62}$$

and

$$\varepsilon(z') = \frac{|u_*|^3}{\kappa(z' + z_0)}. \tag{3.63}$$

The distance from the boundary, z', is retained in the boundary condition (3.63), in order to allow to locate the boundary condition at an arbitrary position within the wall layer. This is specifically useful for numerical schemes with staggered grid organisation.

It has been shown by *Burchard et al.* [1998] that the Dirichlet-type boundary conditions may lead to poor numerical accuracy. The reason is the difficulty of accurately discretising the fluxes of ε between the two first discrete ε-values. *Stelling* [1995] had therefore suggested to exploit the law of the wall for the discretisation of this term by setting

$$\nu_t = \frac{u_*^4}{\varepsilon}. \tag{3.64}$$

Another possibility had been successfully tested by *Burchard and Petersen* [1999], following a suggestion Eckard Kleine, Hamburg (pers. comm.): The use of Neumann-type boundary conditions for k and ε (see also *Meier* [1997]). For the logarithmic boundary layer, they are of the following form:

$$\frac{\nu_t}{\sigma_k}\partial_z k = 0 \tag{3.65}$$

and

$$\frac{\nu_t}{\sigma_\varepsilon}\partial_z \varepsilon = -\left(c_\mu^0\right)^{3/4} \frac{\nu_t}{\sigma_\varepsilon} \frac{k^{3/2}}{\kappa(z' + z_0)^2}. \tag{3.66}$$

In (3.66), the down-gradient approximation for the third moment of ε with the turbulent Schmidt number σ_ε has been used. It has been avoided to use u_* in this Neumann-type boundary condition for ε in order to obtain

non-zero dissipation rate values near a stress-free surface. This is important for reproducing pressure-gradient driven open channel flow, in which bottom-generated turbulence penetrates up to the surface, see *Nezu and Nakagawa* [1993] and also section 6.1, figure 6.1. An alternative Dirichlet-type boundary condition containing one extra empirical parameter had been introduced by *Rodi* [1980], which has been successfully used for example by *Baumert and Radach* [1992] for simulating pressure-gradient driven channel flow. For the numerical performance of the flux boundary conditions for the k-ε model, see section 4.4.

3.2.5 The k-ε model

For ε, an exact transport equation (2.33) has been derived from the Navier-Stokes equations. In contrast to the equivalent equation for the turbulent kinetic energy k, that equation needs a number of closure assumptions. The most common approach is to model the right hand side of the ε-equation as scaled linear combinations of the three terms on the right hand side of the TKE-equation, see (2.31) for the exact form and (3.41) for the modelled form. The new empirical parameters which occur by applying this approach have then to be determined by theoretical assumptions, observations or laboratory or numerical experiments.

c_μ	σ_k	$c_{1\varepsilon}$	$c_{2\varepsilon}$
0.09	1.0	1.44	1.92

Table 3.3. Empirical constants for the standard k-ε model.

This modelling strategy leads to the following closed form of the ε-equation:

$$\partial_t \varepsilon - \partial_z \left(\left(\nu + \frac{\nu_t}{\sigma_\varepsilon} \right) \partial_z \varepsilon \right) = \frac{\varepsilon}{k} (c_{1\varepsilon} P + c_{3\varepsilon} B - c_{2\varepsilon} \varepsilon), \tag{3.67}$$

which contains four adjustable parameters. These can be calibrated by considering idealised flow situations in which most of the terms are negligible. $c_{2\varepsilon}$ had been calibrated by observing freely decaying homogeneous turbulence behind a grid. In this situation, the k-ε model degenerates to a balance of time derivatives and dissipation terms. It can be shown that for long integration times, the solution for k follows a power law of the following type:

$$\frac{k}{k_0} = A \left(\frac{t}{\tau_0} \right)^d \tag{3.68}$$

with the decay rate, d, with the constant parameter A and the initial values for turbulent kinetic energy, k_0 and the turbulent time scale, τ_0. This gives the following relation between d and $c_{2\varepsilon}$:

$$d = \frac{1}{1 - c_{2\varepsilon}}. \tag{3.69}$$

The decay rates, d, have been estimated by a number of laboratory experiments, see *Bradshaw* [1975], *Townsend* [1976], *Domaradzki and Mellor* [1984], *Mohamed and Laure* [1990]. The range of these experiments is $-1.3 < d < -1$. The value from table 3.3, $c_{2\varepsilon} = 1.92$ corresponds thus with $d = -1.09$ which is well inside the experimental range.

$c_{1\varepsilon}$ can be determined by wind tunnel experiments with homogeneously sheared grid turbulence. An alternative, theoretical approach has been presented by *Tennekes* [1989], who analyses a transport equation for the macro length scale L, see equation (3.86). The value resulting from this theoretical consideration, $c_{1\varepsilon} = 1.5$ deviates only slightly from the value give in table 3.3, see also *Baumert and Peters* [2000].

The buoyancy related parameter $c_{3\varepsilon}$ has been subject to controversial debate since years. By pragmatic arguments, *Rodi* [1987] suggests a value of $0 \leq c_{3\varepsilon} \leq 0.29$ for stable stratification and $c_{3\varepsilon} = 1.44$ for unstable stratification[2]. *Baum and Caponi* [1992] suggest $c_{3\varepsilon} = 1.14$ for stable and unstable stratification, and *Kochergin and Sklyar* [1992] support this by arguing that $c_{3\varepsilon} \geq 1$ should hold. *Burchard and Baumert* [1995] were the first who published arguments for negative $c_{3\varepsilon}$ (for stable stratification) based on the consideration of stationary solutions of homogeneous shear layers. However, *Kantha* [1988] has used such arguments several years earlier, but never published them. The unpublished report by *Kantha* [1988] had been made available to the author of this book by Lakshmi L. Kantha not before August 2000. In later publications such as *Kantha and Clayson* [1994] and *Kantha and Clayson* [2000], these arguments had never been repeated. For an in depth discussion of the determination of $c_{3\varepsilon}$ under stable stratification, see section 3.2.11.

The turbulent Schmidt number σ_ε can be determined by the requirement that the solution of the ε-equation fulfils the law of the wall. After assuming stationarity, neglecting density gradients and inserting (3.47), (3.52), (3.53) and (3.54) with $z' \ll D$ into (3.67), the following expression results for σ_ε:

$$\sigma_\varepsilon = \sigma_{\varepsilon 1} = \frac{\kappa^2}{c_\mu^{1/2}(c_{2\varepsilon} - c_{1\varepsilon})} \approx 1.111, \tag{3.70}$$

where the empirical parameters from table 3.3 have been used. It should be noted that σ_ε needs a different scaling when the law of the wall does not apply. This is typically the case under breaking surface waves, see *Burchard*

[2] It should be noted that *Rodi* [1987] uses a different notation for $c_{3\varepsilon}$ than the author of this book. This lead to an erroneous reference to the *Rodi* [1987] values for $c_{3\varepsilon}$ in *Burchard et al.* [1999] and other related publications. The author of this book is grateful to Lars Axell, Norrköping, for pointing this out.

[2001b] and figure 3.17, when σ_ε is a function of the shear production to dissipation ratio, P/ε, with σ_ε from (3.70) being a special case for $P/\varepsilon = 1$.

With these parameters, the so-called standard k-ε model is defined. It should be noted that a major simplification has been carried out for this model type concerning the stability functions. c_μ is a constant in the standard k-ε model. In order to properly reproduce the dependence of the turbulent Prandtl number, see figure 3.7, c'_μ is usually modelled as c_μ divided by the turbulent Prandtl number. This turbulent Prandtl number could be taken from *Munk and Anderson* [1948] (see *Burchard and Baumert* [1995]), a simple linear relation (see *Baumert and Peters* [2000]) or a non-linear relation as suggested by *Schumann and Gerz* [1995] (see section 3.2.12, equation (3.108)). Applications of the standard k-ε model to marine and limnic flows have been made by various authors such as *Marchuk et al.* [1977], *Svensson* [1978], *Svensson* [1979], *Omstedt et al.* [1983], *Rodi* [1987], *Omstedt* [1990], *Burchard and Baumert* [1995], *Burchard and Baumert* [1998], *Burchard et al.* [1998] and *Burchard et al.* [1999].

Within a three-dimensional ocean model, *Nihoul et al.* [1989] slightly modified the k-ε model for simulating currents in the Northern Bering Sea. *Baumert* [1992] used a standard k-ε model for simulating three-dimensional baroclinic flow around Heligoland Island (German Bight) and *Pietrzak et al.* [2002] recently applied a three-dimensional baroclinic model with the standard k-ε model and general vertical coordinates to simulate drift of suspended matter with the Jutland coastal current (Eastern North Sea) and the Odden ice tongue formation in the Greenland Sea.

The use of k-ε models in connection to second-moment closure modelling is not that widespread. *Rodi* [1980] and *Hossain* [1980] developed such advanced k-ε models and applied them to flows typical to engineering problems such as open channel flow. *Burchard and Baumert* [1995] and *Burchard and Bolding* [2001] calibrated and applied such models successfully to mixed layers in shelf seas and the open ocean. *Luyten et al.* [1996a] reproduced the complex dynamics of the Rhine outflow region with a k-ε model in combination with a quasi-equilibrium second-moment closure scheme. Recently *Meier* [2001] (see also *Meier* [2000]) applied k-ε models with various second-moment closures inside a three-dimensional model for the Baltic Sea.

The fact that the k-ε model in connection with second-moment closures has only recently been more extensively applied to geophysical flows, might be the reason for the misunderstanding among many scientists that the concept of the k-ε model always means the standard k-ε model. When the author of this book gave a seminar to George L. Mellor in 1998 about such advanced k-ε models, the latter stated

> Then, the k-ε model is a Mellor-Yamada type model as well.

This is fully acceptable, as long as the second-moment closures by *Mellor and Yamada* [1974] and *Mellor and Yamada* [1982] or closures built up them

such as *Galperin et al.* [1988], *Mellor* [1989], *Kantha and Clayson* [1994] or *Mellor* [2001a] are considered. The main difference is that the kL-equation is substituted by the ε-equation in such advanced k-ε models, see *Burchard et al.* [1998].

3.2.6 The k-kL model

In their classical paper on systematising turbulence closure models, *Mellor and Yamada* [1974] applied a simple algebraic equation for calculating the macro length scale, suggested by *Blackadar* [1962] for the atmospheric boundary layer. Some years later, *Mellor and Yamada* [1982] developed an alternative equation for kL, which is a prognostic transport equation motivated by the two-point correlation function, see *Rotta* [1951]. A similar equation for kL had already been constructed by *Rotta* [1968] by means of dimensional analysis. A wall correction term has first been introduced by *Ng and Spalding* [1972] in order to properly reproduce near-wall flow. Similarly to the ε-equation, this equation is based on various, not well-founded assumptions. *Mellor and Yamada* [1982] write about this equation:

> The closure assumptions are complicated, and we consider the result less convincing than the previous assumptions and more likely to be amended in the future.

However, this equation has been unchanged since today, see *Mellor* [2001a]:

$$\partial_t (kL) - \partial_z \left(S_l \sqrt{2k} L \partial_z (kL) \right) = \frac{L}{2} \left[E_1 P + E_3 B - \left(1 + E_2 \left(\frac{L}{L_z} \right)^2 \right) \varepsilon \right]. \tag{3.71}$$

Here, the same notation as for the k-ε model is used. For the conversion formulae to the *Mellor and Yamada* [1974] notation, see section 9.1.2. The relation between L and ε is defined by equation (3.25) with $c_L = 2^{3/2}/B_1 \approx 0.17$.

It should be noted that a slightly modified TKE equation is generally used in the k-kL models:

$$\partial_t k - \partial_z \left(S_q \sqrt{2k} L \partial_z k \right) = P + B - \varepsilon. \tag{3.72}$$

The only difference in comparison to the TKE equation (3.41) is the constant stability function S_q which leads to higher entrainment through density interfaces, see *Simpson et al.* [1996]. Furthermore, in contrast to the k-ε and the k-ω model, the viscous mixing term is neglected in the *Mellor and Yamada* [1982] model.

The empirical parameters occurring in equations (3.71) and (3.72), see table 3.4, are calibrated by the same means as for the k-ε model. Thus, it is not surprising, that they well correspond to each other, see *Baumert and Peters* [2000] and section 3.2.9.

B_1	E_1	E_2	E_3	S_q
16.6	1.8	1.33	1.8	0.2

Table 3.4. Empirical model parameters for the k-kL model.

Only for the buoyancy production related parameter E_3 which corresponds to $c_{3\varepsilon}$ for the k-ε model, the same problem arises as already for the k-ε model. Like *Rodi* [1980] for the k-ε model, *Mellor and Yamada* [1982] chose the same empirical coefficient for the buoyancy production and for the shear production, arguing that it "might be preceded by another constant if data can be found to unambiguously support a value other than unity", where "unity" is here related to the ratio of E_1/E_3. It was again *Kantha* [1988] in his unpublished manuscript who first suggested a completely different value for E_3, based on limitations of the macro length scale for stably stratified flow. In the same year, *Galperin et al.* [1988], suggested to apply an algebraic length scale limitation proportional to the buoyancy length scale (3.99) ,

$$L^2 \leq L_{lim}^2 = \frac{0.56k}{N^2} \qquad \text{for } N^2 > 0, \tag{3.73}$$

when using the k-kL with $E_3 = E_1$, in order "to reflect the limiting effects of stable stratification on the size of turbulent eddies". In combination with (3.25), this limitation is is equivalent to

$$L \leq \frac{0.65}{(c_\mu^0)^{3/8}} \left(\frac{\varepsilon}{N^3}\right)^{1/2} \tag{3.74}$$

with the Ozmidov length scale $L_O = \left(\varepsilon/N^3\right)^{1/2}$, see equation (3.98) and the discussion by *Luyten et al.* [1996a].

Burchard [2001a] could recently show that the consequence of not using the limitation (3.73) leads to a pronounced, unphysical maximum of the macro length scale L in the entrainment region below a stably stratified boundary layer. However, after calibrating E_3 in the same way as done before with $c_{3\varepsilon}$, *Burchard* [2001a] could show that the model performs properly also without the length scale limitation (3.73), see section 6.2.2. Recently, *Mellor* [2001a] suggested to modify the *Taylor* [1935] scaling, (3.25), such that the proportionality factor c_L is a function of stratification rather than being constant. By doing so, he could much better than before reproduce the *Dickey and Mellor* [1980] experiment. In this experiment the decay of

turbulence in stably stratified flow without shear into internal waves is simulated in a tank. This new choice for c_L could possibly compensate for the physically unmotivated choice of $E_3 = 1.8$.

Inserting the log-law solution from section 3.2.3, into (3.71) leads to

$$S_l = \frac{1 + E_2 - E_1}{\kappa^2 B_1} \approx 0.2, \tag{3.75}$$

see *Mellor and Yamada* [1982]. Furthermore, $S_q = S_l$ is used for the TKE equation.

The diagnostic length scale L_z which has to be prescribed for the kL-equation should follow the law of the wall near boundaries. For matching the surface and the bottom boundary layer, various profiles are possible, such as a parabola shaped one,

$$L_z = \kappa \frac{(d_b + z_0^b)(d_s + z_0^s)}{(d_b + z_0^b) + (d_s + z_0^s)}, \tag{3.76}$$

and a triangle shaped one,

$$L_z = \kappa \min(d_b + z_0^b, d_s + z_0^b), \tag{3.77}$$

see *Burchard et al.* [1998].

Here, d_s is the distance from the surface and d_b the distance from the bottom. The choice for L_z plays an important role in open channel flow, see section 6.1.

Since the publication of *Mellor and Yamada* [1982], turbulence closure models using the kL equation have been extensively used in geophysical fluid dynamics. Most oceanic applications have been carried out with the Princeton Ocean Model (POM) introduced by *Blumberg and Mellor* [1987], such as *Ezer and Mellor* [1992], *Aikman et al.* [1996], *Ezer and Mellor* [1997], *Ezer* [1999], *Ezer* [2000], *Jungclaus and Vanicek* [1999] and *Jungclaus and Mellor* [2000]. The Modular Ocean Model (MOM, see *Bryan* [1969] and *Cox* [1984]) optionally works with the k-kL model, see *Rosati and Miyakoda* [1988]. A sensitivity study comparing the k-kL model with simpler turbulence parameterisations in the coastal zone has been carried out by *Ruddick et al.* [1995]. *Yamada* [1983] is one of the few applications of this model in the atmosphere.

3.2.7 Other approaches

The k-ε and the k-kL model are the only two-equation models which have been extensively applied to geophysical flows. However, due to the relation between k, ε and L given by equation (3.25), any other variable $k^n \varepsilon^m$ with $m \neq 0$ could be used for the calculation of the macro length scale, see section 3.2.13.

In engineering flow applications, some of such alternative length scale equations have been developed. Extensions to geophysical flow situations

should pose in principle no additional problems, the main additions would be buoyancy effects which are mostly ignored in engineering applications. The most well-known alternative model is the k-ω model, where $\omega = \varepsilon/k$ is the turbulence frequency with the unit [s^{-1}]. *Kolmogorov* [1942] already suggested the use of the k-ω model, but the present form of this model has mainly been developed by *Wilcox* [1988] and *Wilcox* [1998]. When adding buoyancy effects (see *Umlauf et al.* [2001]) in analogy to the ε and the kL equation, see (3.67) and (3.71), respectively, the ω equation is of the following form:

$$\partial_t \omega - \partial_z \left(\left(\nu + \frac{\nu_t}{\sigma_\omega} \right) \partial_z \omega \right) = \frac{\varepsilon}{k^2} \left(c_{\omega 1} P + c_{\omega 3} B - c_{\omega 2} \varepsilon \right) . \tag{3.78}$$

Baumert and Peters [2000] found that the parameters for neutral flow, $c_{\omega 1}$ and $c_{\omega 2}$, are in good agreement with those for the k-ε and the k-kL model. In the latest version of the k-ω model, the coefficients for the dissipation terms, c_L (see equation (3.25)) and $c_{\omega 2}$ depend on the flow state itself, in order to better account for free shear flows (see *Wilcox* [1998]).

Two other types of model which should be mentioned here, are the k-τ (*Speziale et al.* [1990]) and k-$k\tau$ models (*Zeierman and Wolfshtein* [1986]), where $\tau = k/\varepsilon = \omega^{-1}$ is the turbulent time scale. However, according to the findings of section 3.2.13, these two models should have problems with properly reproducing the law of the wall unless extra wall-terms are included as in the kL equation (3.71).

3.2.8 Homogeneous shear layers

For some basic investigations of turbulence models it is instructive to consider idealised flows far away from boundaries with constant shear and stratification. This leads to the concept of homogeneous shear layers. Such flows have been approximated in laboratory flumes (see *Rohr et al.* [1988] and *Piccorillo and van Atta* [1997]) and numerically by means of Direct Numerical Simulation (see *Gerz et al.* [1989], *Holt et al.* [1992], *Shih et al.* [2000]). In the real ocean, such homogeneous shear layers might be present for short times only, although usually disturbed by internal waves. However, situations in which the time scales of the mean flow are much larger than those for the turbulence are typical for the ocean. Therefore, homogeneous shear layers seem to be a basic flow situation and turbulence closure models should thus be able to properly reproduce them.

3.2.9 Two-equation models as dynamic systems

Mathematically formulated, this concept leads to vanishing diffusion terms in all turbulent equations such that they become ordinary differential equations

only depending on time t. For homogeneous shear layers, the idealised dynamical system for k and ε can be formulated in the following way (*Burchard* [1995], *Baumert and Peters* [2000]):

$$d_t k = \frac{k}{\tau}\left(\frac{\tau^2}{\tau_k^2} - 1\right), \tag{3.79}$$

$$d_t \varepsilon = \frac{\varepsilon}{\tau}\left(\frac{\tau^2}{\tau_\varepsilon^2} - c_{2\varepsilon}\right) \tag{3.80}$$

with the time scales:

$$\tau = \frac{k}{\varepsilon}, \tag{3.81}$$

$$\tau_k = (c_\mu M^2 - c'_\mu N^2)^{-1/2} \tag{3.82}$$

and

$$\tau_\varepsilon = (c_{1\varepsilon} c_\mu M^2 - c_{3\varepsilon} c'_\mu N^2)^{-1/2}. \tag{3.83}$$

A dynamic equation may be derived for τ as well:

$$\dot{\tau} = (c_{2\varepsilon} - 1)\left(1 - \frac{\tau^2}{\tau_\infty^2}\right) \tag{3.84}$$

with the asymptotic time scale

$$\tau_\infty = \left(\frac{c_{2\varepsilon} - 1}{\tau_\varepsilon^{-2} - \tau_k^{-2}}\right)^{1/2}. \tag{3.85}$$

The mathematical properties of the dynamic system (3.79) - (3.85) with special consideration of steady-state solutions and asymptotic behaviour will be studied in more detail in sections 3.2.10 - 3.2.12.

In this context of ordinary differential equations, transport equations for any property $k^n \varepsilon^m$ can be derived from (3.79) and (3.80). It is for example interesting to inspect the transport equation for the macro length scale $L \propto k^{3/2}\varepsilon^{-1}$ in homogeneous shear layers:

$$\dot{L} = \frac{k^{1/2}}{\varepsilon}\left(\left(\frac{3}{2} - c_{1\varepsilon}\right)P + \left(\frac{3}{2} - c_{3\varepsilon}\right)B + \left(\frac{3}{2} - c_{2\varepsilon}\right)\varepsilon\right). \tag{3.86}$$

For this situation of homogeneous shear layers, *Tennekes* [1989] argues:

> On dimensional grounds, L cannot depend upon the shear because the shear is homogeneous and cannot impose a *length* scale. This requires that $c_{1\varepsilon} = 3/2$. [Notation adjusted to this book.]

This argument is an a posteriori confirmation of the empirical value of $c_{1\varepsilon} = 1.44 \approx 3/2$ given in table 3.3, see also *Baumert and Peters* [2000].

It is also the transport equation for kL which can now be derived in the same way:

$$d_t(kL) = \frac{L}{2}\left(\left\{E_1 c_\mu M^2 - E_3 c'_\mu N^2\right\}\frac{k^2}{\varepsilon} - E_2\varepsilon\right). \tag{3.87}$$

This formulation allows for a quantitative comparison of the empirical parameters on the right hand sides of the ε and the kL equation, see *Baumert and Peters* [2000]:

$$E_1 = 5 - 2c_{1\varepsilon},\ E_2 = 5 - 2c_{2\varepsilon},\ E_3 = 5 - 2c_{3\varepsilon} \tag{3.88}$$

With (3.88), $E_1 = 2.12$ and $E_2 = 1.16$ would result from table 3.3 containing the empirical parameters for the k-ε model, $c_{1\varepsilon}$ and $c_{2\varepsilon}$. With $E_1 = 1.8$ and $E_2 = 1.0$ (see *Mellor and Yamada* [1982]), these values are indeed similar to each other.

Here, the question for appropriate values for $c_{\varepsilon 3}$ and E_3 has been left open, for a discussion see *Burchard and Bolding* [2001] for $c_{\varepsilon 3}$ and *Burchard* [2001a] for E_3 and section 3.2.11. The calibration of $c_{\varepsilon 3}$ and E_3 will be performed in sections 6.2.1 and 6.2.2, respectively.

3.2.10 Analytical solution of idealised system

For constant values of τ_k and τ_ε, an analytical solution of the system (3.79) and (3.80) exists[3] for each pair of positive initial values k_0 and ε_0:

$$\tau(t) = \frac{1 - Ce^{-\frac{t}{\tau_1}}}{1 + Ce^{-\frac{t}{\tau_1}}}\tau_\infty, \tag{3.89}$$

$$k(t) = k_0 e^{-\frac{t}{\tau_m}}\left[\frac{1 + Ce^{-\frac{t}{\tau_1}}}{1 + C}\right]^{\frac{\tau_\infty^2}{(c_{2\varepsilon}-1)\tau_k^2}}\left[\frac{1 - Ce^{-\frac{t}{\tau_1}}}{1 - C}\right]^{-\frac{1}{c_{2\varepsilon}-1}}, \tag{3.90}$$

and

$$\varepsilon(t) = \varepsilon_0 e^{-\frac{t}{\tau_m}}\left[\frac{1 + Ce^{-\frac{t}{\tau_1}}}{1 + C}\right]^{\frac{\tau_\infty^2}{(c_{2\varepsilon}-1)\tau_\varepsilon^2}}\left[\frac{1 - Ce^{-\frac{t}{\tau_1}}}{1 - C}\right]^{-\frac{c_{2\varepsilon}}{c_{2\varepsilon}-1}} \tag{3.91}$$

[3] For the algebraic second-moment closure schemes presented in sections 3.1.3 and 3.1.6, this assumption of constant time scales τ_k and τ_ε is not correct, since the stability functions still depend on the variable time scale τ. Constant stability functions would be obtained in this idealised situation with homogeneous shear layers for the standard k-ε model, see section 3.2.5.

with

$$C = \frac{\tau_\infty - \frac{k_0}{\varepsilon_0}}{\tau_\infty + \frac{k_0}{\varepsilon_0}}, \tag{3.92}$$

and the time scales

$$\tau_m = \tau_\infty \frac{\tau_k^2}{\tau_\infty^2 - \tau_k^2} \tag{3.93}$$

and

$$\tau_1 = \frac{1}{2} \frac{\tau_\infty}{c_{2\varepsilon} - 1}. \tag{3.94}$$

This solution has been already been presented by *Burchard* [1995] and *Burchard and Baumert* [1995] with different notation.

Figures 3.10 and 3.11 display analytical solutions for k, ε and τ with $c_{\varepsilon 1} = 1.5$, $c_{\varepsilon 2} = 2$, $c_{\varepsilon 3} = -1.06$, $c_\mu = 0.09$, $c'_\mu = 0.073$ and $N^2 = 10^{-4}\mathrm{s}^{-2}$. Three cases are studied in which the shear M is adjusted such that the gradient Richardson number $R_i = N^2/M^2$ has the values $R_i = 0.15$, $R_i = 0.2$ and $R_i = 0.25$, resulting in $\tau_k < \tau_\infty$, $\tau_k = \tau_\infty$ and $\tau_k > \tau_\infty$, respectively. For the three cases, $\tau_k = 138$ s, $\tau_k = 163$ s and $\tau_k = 187$ s, respectively, and $\tau_\infty = 149$ s, $\tau_\infty = 163$ s and $\tau_\infty = 174$ s, respectively, holds. The choice for $c_{\varepsilon 3}$ leads to a steady-state Richardson number of $R_i^{st} = 0.2$, for the definition see section 3.2.11. For k and ε, a variety of different initial values k_0 and ε_0 has been used.

The analytical solution of this idealised k-ε model allows for studying some aspects of the general behaviour of such two-equation models. First of all, the positivity of k and ε for all positive initial values k_0 and ε_0 and all times t is obvious[4]. It can be furthermore immediately seen from the solution for the time scale τ, (3.89), that for all M^2 and N^2, τ converges towards a steady state, i.e. $\tau \to \tau_\infty$. The time scale of this asymptotic process is of the order of τ_∞ itself. This is graphically demonstrated in figures 3.10 and 3.11 for three different values of M^2. The steady state of (3.89), $\tau = \tau_\infty$ is called *structural equilibrium* and has some interesting physical implications, see *Baumert and Peters* [2000] and section 3.2.12. The analytical solutions for k and ε, (3.90) and (3.91), respectively, contain an exponential factor with the time scale τ_m which can be, depending on M^2 and N^2, positive, negative or infinity. In the latter case, which is a consequence of $\tau_\infty = \tau_k$, k and ε converge towards a steady state depending on the initial values. This physically interesting situation will be discussed in more detail in section 3.2.11.

[4] For a positivity proof for the complete k-ε model, see *Mohammadi and Pironneau* [1994].

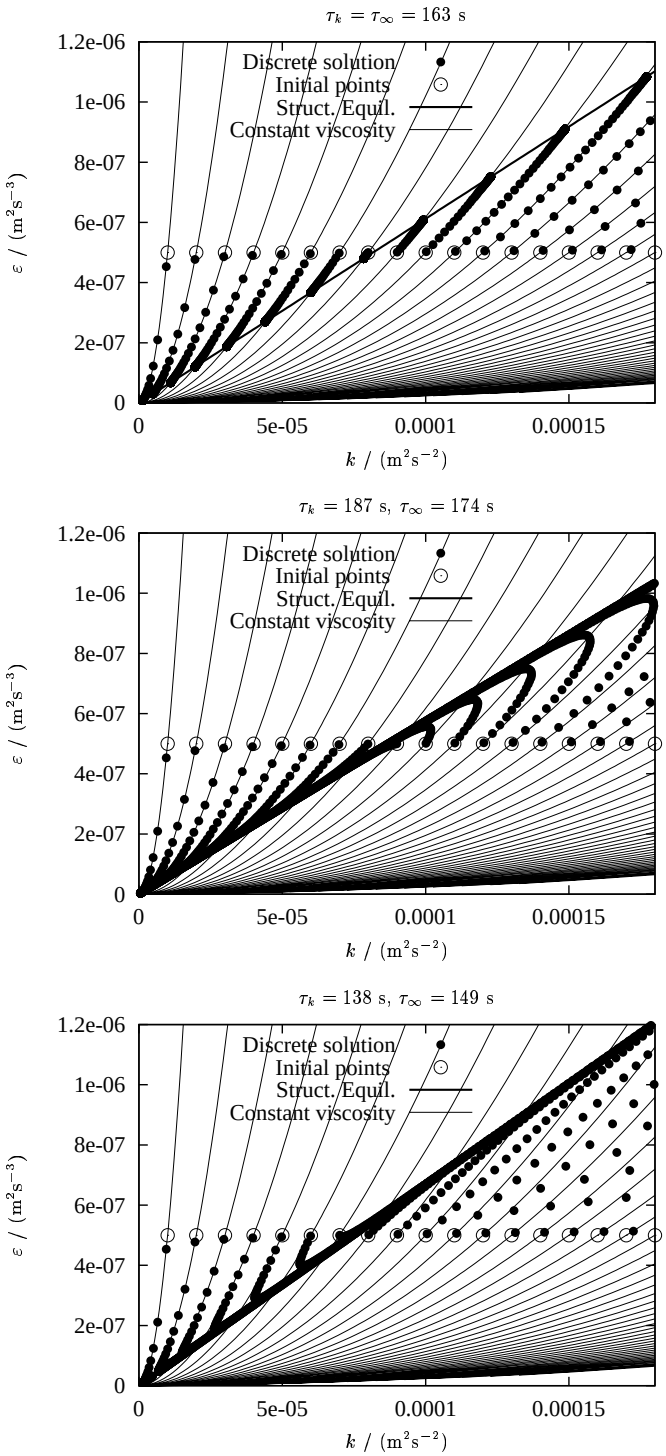

Fig. 3.10. Analytical solution of k-ε model in k-ε space with a steady-state Richardson number of $R_i^{st} = 0.2$, see section 3.2.11. Shown are the solution with steady-state (upper panel, $R_i = 0.2$), a decaying solution (middle panel, $R_i = 0.25$) and a solution with unlimited growth (lower panel, $R_i = 0.15$).

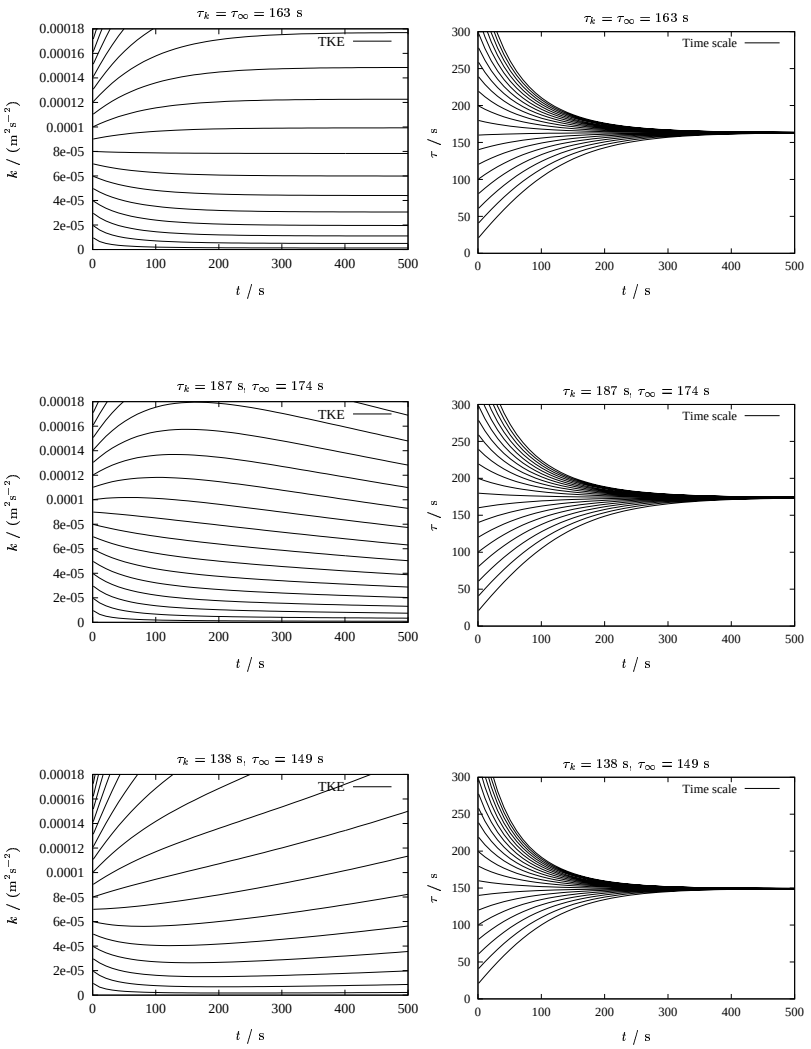

Fig. 3.11. Analytical solution of k-ε model as time series with a steady-state Richardson number of $R_i^{st} = 0.2$, see section 3.2.11. Shown are the solution with steady-state (upper panel, $R_i = 0.2$), a decaying solution (middle panel, $R_i = 0.25$) and a solution with unlimited growth (lower panel, $R_i = 0.15$).

Finally one other physically interesting feature of this idealised k-ε model should be discussed. From, (3.79) and (3.80), an ordinary differential equation for the eddy viscosity ν_t can be derived:

$$\dot{\nu}_t = \frac{\nu_t}{\tau}\left[\tau^2\left\{(\tau_k^{-2} - \tau_\infty^{-2})(c_{2\varepsilon} - 1) - \tau_k^{-2}(c_{2\varepsilon} - 2)\right\}\right] \tag{3.95}$$

With $\tau_k = \tau_\infty$ and $c_{2\varepsilon} = 2$, (3.95) would lead to stationary eddy viscosity ν_t. Since the empirical value for $c_{2\varepsilon} = 1.92$ is very close to this, it can be assumed that the eddy viscosity is more or less invariant in situations in which the homogeneous k-ε model has stationary solutions. It can be clearly seen in figure 3.10 that the trajectories of k and ε are basically parallel to the lines of constant eddy viscosity even when $\tau_k = \tau_\infty$ does not hold.

It is not known to the author of this book whether this invariance of the eddy viscosity has ever been investigated in more detail. One could possibly find arguments similar to those by *Tennekes* [1989], see equation (3.86), saying that for freely decaying turbulence the eddy viscosity should not depend on the dissipation rate, and thus arguing $c_{2\varepsilon} = 2$. However, this idea is very speculative, but should probably be further discussed in the turbulence modelling community.

3.2.11 The steady-state Richardson number

If in equations (3.79) and (3.80), $\dot{k}$ and $\dot{\varepsilon}$ are set to zero, then the total equilibrium of the k-ε model is reached and the following relation, which is a precondition for the steady state can be derived:

$$R_i = R_i^{st} = \frac{c_\mu}{c_\mu'} \cdot \frac{c_{2\varepsilon} - c_{1\varepsilon}}{c_{2\varepsilon} - c_{3\varepsilon}}. \tag{3.96}$$

The steady-state Richardson number R_i^{st} thus depends on the empirical parameters $c_{1\varepsilon}$, $c_{2\varepsilon}$ and $c_{3\varepsilon}$ in the ε-equation and on the actual stability function chosen. In contrast to $c_{1\varepsilon}$ and $c_{2\varepsilon}$, the buoyancy flux related parameter $c_{3\varepsilon}$ has never directly been determined by laboratory experiments. Figure 3.12 shows how $c_{3\varepsilon}$ and R_i^{st} are related to each others for the various stability functions discussed in section 3.1.3. This figure may be compared to figure 3 by *Burchard and Baumert* [1995] where the flux Richardson number was considered instead.

For all four second-moment closure models, realistic steady-state Richardson numbers with $R_i^{st} \leq 0.25$ require $c_{3\varepsilon} < -0.4$, such that on physical grounds, $c_{3\varepsilon}$ should be negative in any case. This means that the value of $c_{3\varepsilon} \geq 0$ as used in most investigations is physically unsound. Furthermore, all graphs in figure 3.12 are monotonically increasing such it can be stated for all four closures that smaller $c_{3\varepsilon}$ cause smaller steady-state Richardson numbers.

The concept of the steady-state Richardson number has recently been applied to the *Mellor and Yamada* [1982] two-equation model by *Burchard*

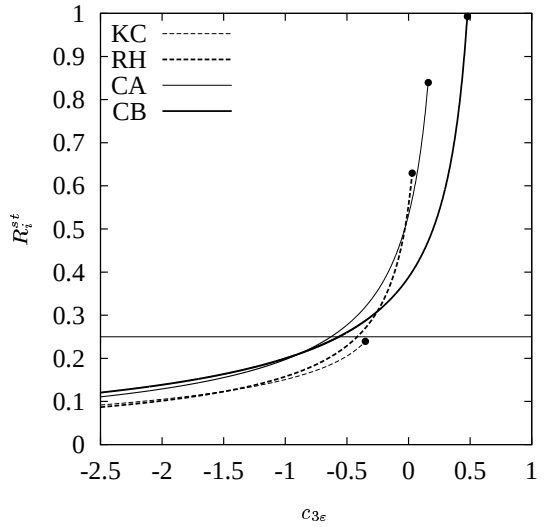

Fig. 3.12. Steady-state gradient Richardson number R_i^{st} as function of $c_{3\varepsilon}$ for the different sets of stability functions: Models of *Kantha and Clayson* [1994] (KC), *Rodi* [1980] and *Hossain* [1980] (RH), version A of *Canuto et al.* [2001] (CA), and version B of *Canuto et al.* [2001] (CB).

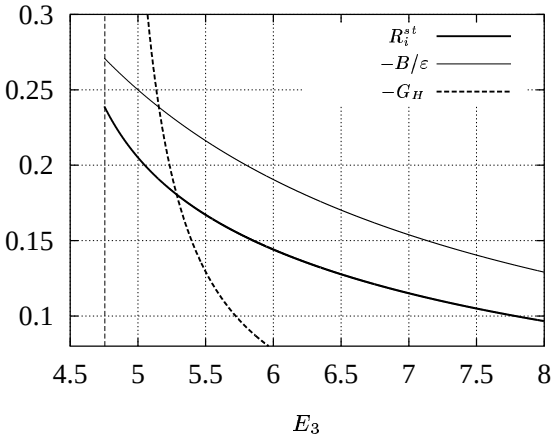

Fig. 3.13. The steady-state Richardson number R_i^{st}, normalised buoyancy production $-B/\varepsilon$ and the parameter $-G_H \propto \alpha_N$ for steady-state as functions of E_3.

[2001a] as well. The result is shown in figure 3.13 for the quasi-equilibrium second-moment closure by *Kantha and Clayson* [1994]. Physically sound results are obtained for $E_3 > 4.752$ only. This means that the original value of $E_3 = 1.8$ by *Mellor and Yamada* [1982] has no proper physical meaning. Two other buoyancy related quantities are shown as function of E_3 in figure 3.13 as well, B/ε and $-G_H \propto \alpha_N$ (for the exact relation see equation (9.11)), the latter quantity being an important parameter in the *Mellor and Yamada* [1974] and *Mellor and Yamada* [1982] second-moment closures.

The steady-state Richardson number for homogeneous shear layers can be estimated by means of Direct Numerical Simulation (DNS, see section 2.1.5) and physical experiments in laboratory flumes. *Gerz et al.* [1989] and *Holt et al.* [1992] were the first who used Direct Numerical Simulation of sheared, stratified flow. They demonstrated the existence of a stationary (or steady-state) Richardson number R_i^{st} and showed its dependence on the Reynolds number R_e. According to *Schumann and Gerz* [1995], $R_i^{st} < R_i^{\infty}$ with the asymptotic Richardson number $R_i^{\infty} = 0.25$ should hold. By analysing laboratory data from *Rohr* [1985] obtained from homogeneously shear-layered saltwater flow, they conclude that $R_i^{st} = 0.16 \pm 0.06$. In a recent publication, *Shih et al.* [2000] could quantify the dependence of the steady-state Richardson number R_i^{st} on the Reynolds number R_e. They suggest the following empirical relationship between these two non-dimensional numbers:

$$R_i^{st} \approx \frac{0.25}{1 + \frac{103}{R_e}} \underset{R_e \to \infty}{\longrightarrow} > 0.25. \tag{3.97}$$

For proper implementation of the concept of the steady-state Richardson number into numerical models, an exact calibration of R_i^{st} is needed, such that $c_{3\varepsilon}$ and E_3 can be determined for each set of stability functions. Such calibrations will be carried out in sections 6.2.1 and 6.2.2 with the aid of a simple wind-entrainment experiment.

3.2.12 Structural equilibrium

The so-called structural equilibrium has been first defined by *Schumann* [1994]. It is reached when the time scale $\tau = k/\varepsilon$ is in steady state and the total equilibrium is obviously a special case of it. It can be shown that – other than the total equilibrium discussed in section 3.2.11 – the solution for (3.79) and (3.80) tends to the structural equilibrium for all Richardson numbers. *Baumert and Peters* [2000] recently showed how a k-ε model equipped with an empirical closure for the stability functions could reproduce data found for ratios of relevant turbulent length scales. This is here repeated for the four algebraic second-moment closures presented in section 3.1.3.

Various length scales have been defined for turbulent flow. Among them are the Ozmidov scale

$$L_O = \left(\frac{\varepsilon}{N^3}\right)^{1/2} \tag{3.98}$$

and the buoyancy scale

$$L_b = \frac{k^{1/2}}{N}, \tag{3.99}$$

of specific interest (see *Baumert and Peters* [2000]). The Ozmidov scale corresponds to a balance between inertial and buoyant effects (*Lesieur* [1997]). The buoyancy scale is often used as a measure for an upper limit of L in stably stratified flow, see *Galperin et al.* [1988] and equation (3.73). However, with the macro length scale L, the Ozmidov and the buoyancy scale are closely related to each other:

$$L_O = (c_\mu^0)^{3/8} \frac{L_b^{3/2}}{L^{1/2}} \tag{3.100}$$

and

$$\frac{L_b}{L_O} = \alpha_N^{1/4} \tag{3.101}$$

Another important length scale is the Ellison scale, defined as:

$$L_E = \frac{-\langle \tilde{\rho}^2 \rangle^{1/2}}{\partial_z \bar{\rho}} \tag{3.102}$$

(with the density fluctuation $\tilde{\rho}$), which is often set equal to the Thorpe scale L_{Th}. The latter has been introduced by *Thorpe* [1977] as the distance over which fluid parcels have to be vertically reordered in order to obtain a monotone density profile. The Ellison and the Thorpe scale are related to the macro length scale L through the following relation (see *Baumert and Peters* [2000]):

$$L_E = L_{Th} = \frac{L}{2C_t(c_\mu^0)^{3/4}} \tag{3.103}$$

with $C_t = 1.4$. When assuming structural equilibrium for the k-ε model in the homogeneous shear layer approximation, then the ratios L_E/L_O and L_E/L_b can be transformed as follows:

$$\frac{L_E}{L_O} = \frac{1}{2C_t}\alpha_N^{3/4} \tag{3.104}$$

$$\frac{L_E}{L_b} = \frac{1}{2C_t}\alpha_N^{1/2} \tag{3.105}$$

For a different view of the Thorpe to Ozmidov length scale ratio shown in equation (3.104), see *Luyten et al.* [1996a] and equation (27) therein. Furthermore, the two ratios (3.104) and (3.105) can be expressed as implicit

functions of the gradient Richardson number R_i. These implicit functions can be numerically solved by a one-dimensional Newton iteration. The results are shown in figure 3.14 for five different sets of stability functions in comparison to the empirical curves, resulting from fits to data by *Rohr* [1985] and *Schumann and Gerz* [1995], see *Baumert and Peters* [2000]:

$$\frac{L_E}{L_O} \approx 4.2 R_i^{3/4} \tag{3.106}$$

and

$$\frac{L_E}{L_b} \approx 1.6 R_i^{1/2}. \tag{3.107}$$

Four of these stability functions tested are those resulting from second-moment closures as introduced in section 3.1.3. The fifth is a semi-algebraic closure where c_μ is a constant and c'_μ a function of the turbulent Prandtl number P_r:

$$c_\mu = c_\mu^0, \qquad c'_\mu = \frac{c_\mu^0}{P_r} \tag{3.108}$$

with $c_\mu^0 = 0.09$. We choose here for the turbulent Prandtl number P_r a formulation suggested by *Schumann and Gerz* [1995]:

$$P_r = P_r^0 \exp\left(-\frac{R_i}{P_r^0 R_i^\infty}\right) + \frac{R_i}{R_i^\infty} \tag{3.109}$$

with the neutral turbulent Prandtl number $P_r^0 = 0.74$ and $R_i^\infty = 0.25$. Simple models like this are for example the standard k-ε model, see section 3.2.5.

Figure 3.14 reveals that all tested stability functions reproduce the increase of the L_E/L_O and L_E/L_b ratios with increasing gradient Richardson number. However, the *Kantha and Clayson* [1994] stability functions do significantly deviate from the empirical curves which are quantitatively well approximated by the other stability functions. It is visible that the simple stability functions from the standard k-ε model show the best agreement with the empirical curve. This has already been shown by *Baumert and Peters* [2000] for a similar set of simple stability functions. The larger deviations of the more complex second-moment closures (RH, CA and CB) for the L_E/L_b ratio are not surprising, since they have been developed fully independently from these data. Their performance could probably be improved by slightly adjusting some empirical parameters.

This detailed investigation of idealised flow in structural equilibrium adds some confidence to the use of second-moment closure schemes since it shows that basic flow relations are well reproduced.

Recently, *Shih et al.* [2000] presented some new results from Direct Numerical Simulations of homogeneous shear layers. They could confirm a hypothesis by *Rogallo* [1981] who postulated that the non-dimensional shear rate

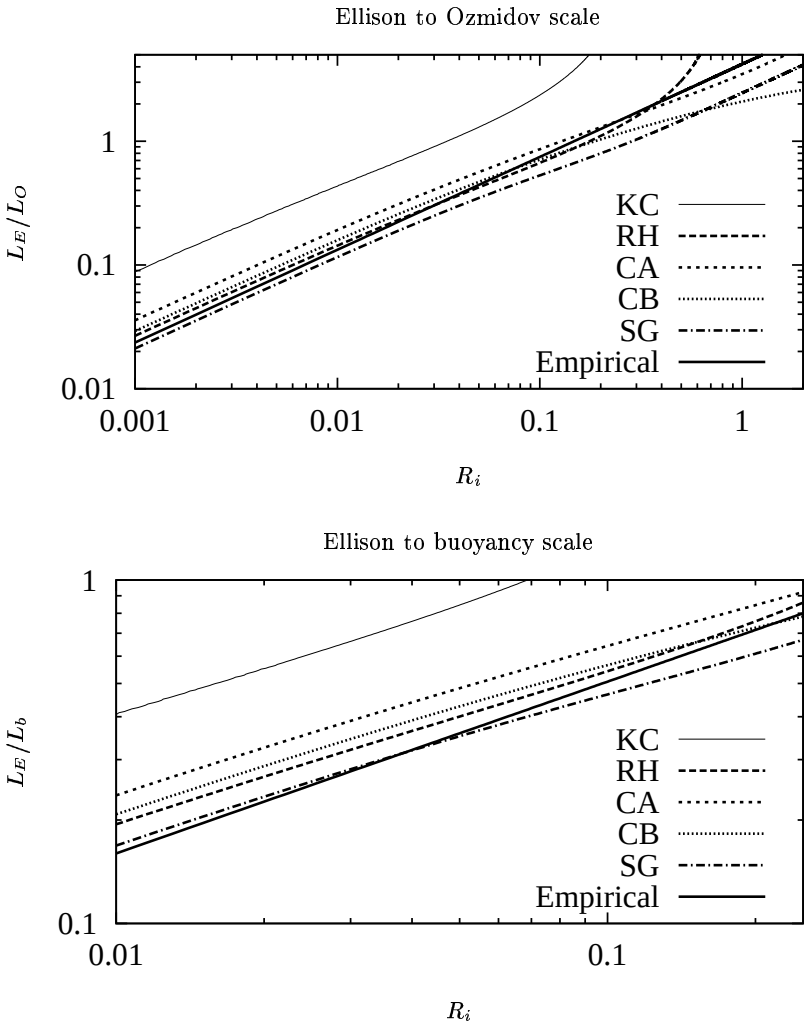

Fig. 3.14. The ratios L_E/L_O and L_E/L_b as functions of the gradient Richardson number R_i, where L_E is the Ellison, L_O the Ozmidov and L_b the buoyancy scale. Shown are curves resulting from the *Kantha and Clayson* [1994] (KC), the *Rodi* [1980] and *Hossain* [1980] (RH), the *Canuto et al.* [2001] (CA, CB), and a semi-empirical set of stability functions using a turbulent Prandtl number parameterisation as suggested by *Schumann and Gerz* [1995] (SG), see equation (3.108). These are compared to the empirical estimates from equations (3.106) and (3.107).

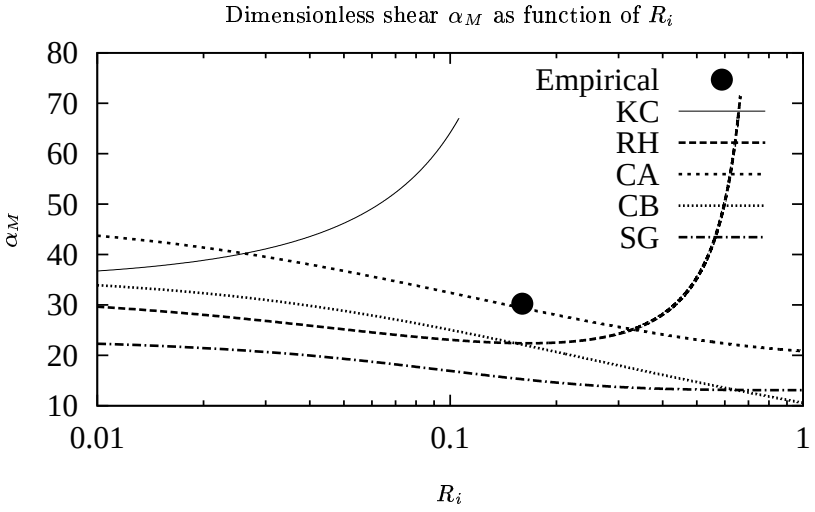

Fig. 3.15. The dimensionless shear α_M as functions of the gradient Richardson number R_i. Shown are curves resulting from the *Kantha and Clayson* [1994] (KC), the *Rodi* [1980] and *Hossain* [1980] (RH), the *Canuto et al.* [2001] (CA, CB), and a semi-empirical set of stability functions using a turbulent Prandtl number parameterisation as suggested by *Schumann and Gerz* [1995] (SG), see equation (3.108). For all stability functions, a steady-state Richardson number of $R_i^{st} = 0.25$ has been used. The results are compared to a Direct Numerical Simulation result by *Shih et al.* [2000] for $R_i = 0.16$.

$\alpha_M = M^2\tau^2$ must approach a finite non-zero constant for large Reynolds numbers. For a Richardson number of $R_i = 0.16$ they found $\alpha_M \to 30$ for large times, independently from the initial value of α_M. If one interprets the approach towards this constant as the arrival at the structural equilibrium, then this can be simulated by the sets of stability functions discussed before. This structural equilibrium is described for two-equation models by $\tau = \tau_\infty$, see equation (3.84). For the k-ε model, this can be transformed to the following relation for α_M:

$$\alpha_M = \frac{c_{2\varepsilon} - 1}{(c_{1\varepsilon} - 1)c_\mu - (c_{3\varepsilon} - 1)c'_\mu R_i}. \tag{3.110}$$

The relation (3.110) is implicit for non-equilibrium stability functions, since c_μ and c'_μ do still depend on α_M and has to be solved by a non-linear Newton iteration. Figure 3.15 shows the results for five sets of stability functions as function of the gradient Richardson number R_i. For the *Kantha and Clayson* [1994] stability functions no solution could be found for $R_i > 0.11$ and for the *Rodi* [1980] and *Hossain* [1980] scheme no solution was found for

$R_i > 0.66$. The two sets of stability functions by *Canuto et al.* [2001] and the empirical set suggested by *Schumann and Gerz* [1995] do both weakly decrease with R_i. The version A by *Canuto et al.* [2001] predicts the result of *Shih et al.* [2000] with great accuracy. The empirical stability functions with a constant c_μ are much too low although they well predicted estimates for the length scale ratios, see figure 3.14. It would be interesting to investigate the performance of the quasi-equilibrium versions of the stability functions in this framework. It would also be interesting to see whether the decrease of the non-dimensional shear with increasing Richardson number can be confirmed by means of DNS studies.

3.2.13 Generic two-equation model

If one accepts the *Taylor* [1935] scaling, see equation (3.25), which relates k, ε and the macro length scale L, then the approach for modelling the right hand side of the ε-equation could be generalised to a transport equation for any quantity $k^n\varepsilon^m$ with $m \neq 0$. This could then be used for calculating ε. This approach will be presented and tested here. For a more in depth discussion, see also *Umlauf and Burchard* [2001]. Together with the down-gradient approximation of the third moment, a transport equation for $k^n\varepsilon^m$ could be of the following form[5]:

$$\partial_t\left(k^n\varepsilon^m\right) - \partial_z\left(\nu + \frac{\nu_t}{\sigma_{nm}}\partial_z\left(k^n\varepsilon^m\right)\right) = k^{n-1}\varepsilon^m\left(c_{1nm}P + c_{3nm}B - c_{2nm}\varepsilon\right). \tag{3.111}$$

Here, σ_{nm} is a turbulent Schmidt number relating the vertical flux of $k^n\varepsilon^m$ to the Reynolds stress. Together with the turbulent Schmidt number σ_k for the turbulent kinetic energy equation, (3.41), c_{1nm}, c_{2nm}, c_{3nm}, σ_{nm}, n and m, sum up to a total of seven adjustable parameters for the generic two-equation model. It should be recalled here, that the parameters $c_{1\varepsilon}$, $c_{2\varepsilon}$ and $c_{3\varepsilon}$ for the dissipation rate equation (3.67) have been calibrated for the vertically homogeneous transport equation, i.e. by neglecting vertical diffusion of turbulent quantities, see section 3.2.5.

When neglecting the turbulent fluxes of ε and $k^n\varepsilon^m$, then (3.111) is equivalent with (3.67) such that

$$c_{inm} = mc_{i\varepsilon} + n, \qquad \text{for } i = 1,\ldots,3. \tag{3.112}$$

The turbulent Schmidt number σ_{nm} is determined by insertion of the law of the wall into equation (3.111), as already done for the k-ε model

[5] It should be noted that *Umlauf and Burchard* [2001] use a different notation, there m is the exponent for k and n the exponent for the macro length scale L. For converting their notation into the present notation, the following transformations would be needed: $m = -\bar{n}$ and $n = \bar{m} + \frac{3}{2}\bar{n}$ with the overbars denoting the *Umlauf and Burchard* [2001] exponents.

(see equation (3.70)) and for the k-kL model (see equation (3.75)), see also *Launder and Spalding* [1974]. The result for σ_{nm} is:

$$\sigma_{nm} = \frac{m\kappa^2}{(c_{2\varepsilon} - c_{1\varepsilon})c_\mu^{1/2}}, \tag{3.113}$$

which is a generalisation of equation (3.70). Thus, σ_{nm} does not depend on n. Much more interesting, though, is the fact that σ_{nm} is positive only for positive m. This has the consequence that all models with $m < 0$ do not fit into this concept since the diffusivity ν_t/σ_{nm} should be positive by definition. The k-kL model for example has the exponents $n = 5/2$ and $m = -1$. That is the reason why that model needs an extra wall term for stabilising the model near walls. The estimate (3.75) does therefore only work after considering this extra term. The same problems are expected for the k-τ model with $n = 1$ and $m = -1$ and the k-$k\tau$ model with $n = 2$ and $m = -1$, see section 3.2.7. In contrast to this the k-ω model with $n = -1$ and $m = 1$ (see section 3.2.7) does fit into this concept of a generic two-equation model.

Thus, the four empirical parameters c_{1nm}, c_{2nm}, c_{3nm} and σ_{nm} are fixed for the generic two-equation model, for m and σ_k all positive values are admissible and for n so far no restrictions have been found. The calibration of two of these three empirical parameters will be discussed in section 3.3.1 for the case of grid-generated shear-free turbulence, see also *Umlauf and Burchard* [2001].

Boundary conditions for this generic model can easily be derived from the law of the wall, see section 3.2.3. The adequate Dirichlet-type boundary condition for $k^n\varepsilon^m$ is

$$k^n\varepsilon^m = \frac{u_*^{2n+3m}}{\left(c_\mu^0\right)^{n/2}\kappa^m(z' + z_0)^m}. \tag{3.114}$$

The flux condition for $k^n\varepsilon^m$ can be formulated as:

$$\frac{\nu_t}{\sigma_{nm}}\partial_z\left(k^n\varepsilon^m\right) = -\left(c_\mu^0\right)^{3/4}\frac{k^{3/2m+n}}{\kappa^m(z' + z_0)^{m+1}}, \tag{3.115}$$

which is a generalisation of the flux condition for ε, (3.66).

3.3 Surface and internal wave effects

There are various processes in the ocean which cannot sharply be separated from turbulence. These are specifically non-linear waves which interact with turbulence in ways which are not yet fully understood. Short surface waves create turbulence when they break. They are also responsible for Langmuir circulation, a near-surface process well understood only in recent years. For both processes, dissipation of internal waves into turbulence and Langmuir

circulation, theories exist which can be partially exploited for their parameterisation in boundary layer models. Consideration of such processes in ocean models is however still far from being a standard procedure.

The same is true for internal waves which interact with turbulence in various ways. Also here a clear separation between internal wave kinetic energy and turbulent kinetic energy is difficult.

These three processes are discussed in this section from the viewpoint of turbulence modelling. The modelling of turbulence production by breaking surface waves with two-equation models has recently been investigated in detail by *Burchard* [2001b] and *Umlauf and Burchard* [2001], the results presented here in section 3.3.2 are mainly taken from those publications. An important key to understand parameterisations of surface wave breaking is the numerical simulation of shear-free turbulent flows which are typically generated by oscillating grids. The simulation of such idealised flows as carried out by *Umlauf and Burchard* [2001] is discussed in section 3.3.1. Production of turbulence by internal wave energy is discussed in section 3.3.3 and the perspectives of parameterising the interaction between turbulence and Langmuir circulation are outlined in section 3.3.4.

3.3.1 Shear-free turbulence

The first step in understanding the behaviour of two-equation models in the wave-enhanced layer is the investigation of a special case, in which turbulence decays spatially away from a source without mean shear. Turbulence generated by an oscillating grid in a water tank has been used in various laboratory experiments to study the spatial decay of velocity fluctuations in this basic turbulent flow, where turbulent transport and dissipation balance. Having the influence of grid generated turbulence on interfacial mixing in stratified fluids in mind, pioneering works of this type were conducted by *Thompson and Turner* [1975] and *Hopfinger and Toly* [1976]. Since their results were not entirely conclusive, a large number of similar experiments followed until very recently (*Hannoun et al.* [1988], *Nokes* [1988], *deSilva and Fernando* [1992], *Cheng and Law* [2001]). A DNS study of the transport-dissipation balance at low Reynolds numbers was performed by *Briggs et al.* [1996].

All grid stirring experiments cited in table 3.5 confirm a power law for the decay of k and a linear increase of the length scale L according to

$$k = K(z' + z_0^s)^{\alpha_k}, \qquad L = \tilde{\kappa}(z' + z_0^s), \tag{3.116}$$

where K, $\tilde{\kappa}$, and z_0^s are constants, and the source of turbulence has been assumed to be at $z' = 0$. Note, that in these experiments, z_0^s is not related to any kind of surface roughness length. Rather, it is connected to the length scale of injected turbulence which is determined uniquely by the spectral properties of turbulence at the source. As already pointed out by *Thompson and Turner* [1975], the decay of k occurs with respect to the so-called virtual

origin $z' = -z_0^s$ which never coincides with the position of the source. In agreement with *Hopfinger and Toly* [1976], we define the virtual origin as the point, where the turbulent length-scale, L, becomes zero. It has been remarked by almost all authors that the decay coefficients are very sensitive with respect to small uncertainties in position of the virtual origin.

The values in table 3.5 suggest that the decay rate for the turbulent kinetic energy is likely to be between $-3 < \alpha_k < -2$. The values of $\tilde{\kappa}$, i.e. the slope of the turbulent length scale, L, indicate that in all cases $\tilde{\kappa} < \kappa \approx 0.4$, in contrast to $\tilde{\kappa} = \kappa$ predicted by the models of *Craig and Banner* [1994] and *Craig* [1996] and its adaptation to the k-ε model by *Burchard* [2001b].

Measured decay rates:	α_k	$\tilde{\kappa}$
Thompson and Turner [1975]	-(3.0)	0.1
Hopfinger and Toly [1976]	- 2.0	0.17-0.33
Nokes [1988]	-(1.7-3.0)	—
Hannoun et al. [1988]	-(2.0)	0.1
Briggs et al. [1996], DNS	- 2.45	—
Cheng and Law [2001]	- (2.0)	0.06-0.2

Table 3.5. Decay exponent for the turbulent kinetic energy, α_k, and the constants of proportionality for the length-scale, $\tilde{\kappa}$, in grid stirring experiments and DNS. The values in brackets have been calculated by assuming that the decay exponent for the horizontal velocity fluctuations is half of that for k. This table has been adapted from *Umlauf and Burchard* [2001].

For parameterising the effect of an oscillating grid or breaking surface waves, which has the consequence of injecting TKE into the water column, *Craig and Banner* [1994] have suggested an alternative surface boundary condition for TKE:

$$-\nu_t \partial_z k = c_w (u_*^s)^3, \qquad \text{for } z = 0. \tag{3.117}$$

For breaking surface waves, the empirical parameter c_w should depend on the wave age and has been estimated to be $c_w = 100$ for fully developed waves. For $c_w = 0$, the classical boundary condition for no wave breaking, see equation (3.65) is retained.

For achieving a problem for which an analytical solution can be found, lower a boundary condition has to be fixed at infinite depth:

$$-\nu_t \partial_z k = 0, \qquad \text{for } z = -\infty. \tag{3.118}$$

With these boundary conditions and without mean shear and stratification ($P = B = 0$), the analytical solution for the TKE equation is of the form:

$$k = \frac{(u_*^s)^2}{c_\mu^{1/2}} \left[\left(\frac{3\sigma_k}{2} \right)^{1/2} c_\mu^{1/4} c_w \left(\frac{z' + z_0^s}{z_0^s} \right)^{-\alpha_m} \right]^{2/3} \tag{3.119}$$

with

$$\alpha_m^2 = \frac{3}{2} \frac{c_\mu^{1/2} \sigma_k}{\tilde{\kappa}^2}, \tag{3.120}$$

such that the effective decay rate

$$\alpha_k = - \left(\frac{\frac{2}{3} c_\mu^{1/2} \sigma_k}{\tilde{\kappa}^2} \right)^{1/2} \tag{3.121}$$

depends on the choices for c_μ, σ_k and $\tilde{\kappa}$.

With (3.25) and the second equation from (3.116), the following equation for the dissipation rate ε is obtained:

$$\varepsilon = \frac{(u_*^s)^3}{\tilde{\kappa}(z' + z_0^s)} \left[\left(\frac{3\sigma_k}{2} \right)^{1/2} c_\mu^{1/4} c_w \left(\frac{z' + z_0^s}{z_0^s} \right)^{-\alpha_m} \right]. \tag{3.122}$$

Generally, none of the existing two-equation models would yield the solution (3.119) and (3.122), since they have not been adapted to this situation (see, e.g. *Baumert et al.* [2000]). Only recently, two different strategies, by *Burchard* [2001b] and by *Umlauf and Burchard* [2001], respectively, have been developed for extending two-equation models accordingly.

Approach of *Burchard* [2001b] For adapting the k-ε model for this situation, *Burchard* [2001b] suggested to use the classical values $c_\mu = 0.09$, $\sigma_k = 1.0$ and $\tilde{\kappa} = \kappa = 0.4$ and to modify the turbulent Schmidt number in the ε equation, σ_ε. In the case of a wall layer, σ_ε has been determined in section 3.2.5 by exploiting the law of the wall. Also for the shear-free case, an exact value for σ_ε can be found by inserting the analytical solution for k and ε (3.119) and (3.122), respectively, into the dissipation rate equation (3.67):

$$\sigma_\varepsilon = \sigma_{\varepsilon 0} = \left(\frac{4}{3} \alpha_m + 1 \right) (\alpha_m + 1) \frac{\tilde{\kappa}^2}{c_{2\varepsilon} c_\mu^{1/2}}. \tag{3.123}$$

For $\tilde{\kappa} = 0.4$, as assumed in the models of *Craig and Banner* [1994] and *Burchard* [2001b], the resulting turbulent Schmidt number is $\sigma_\varepsilon \approx 2.4$.

It should be noted, that equation (3.120) predicts spatial decay rates of $\alpha_k = -1.12$ for $\tilde{\kappa} = 0.4$. A comparison with table 3.5 shows that this value strongly underestimates the results of the laboratory experiments. A more realistic value of $\tilde{\kappa} = 0.2$ would lead to a TKE decay rate of $\alpha_k \approx 2.24$ which is well in the range of the experiments.

In the latter case however, the law of the wall with $\kappa = 0.4$ would have been violated. It seems thus, that the k-ε model does not contain enough

free parameters for properly considering the law of the wall and shear free turbulence at the same time (see also *Umlauf* [2001]). Recently, *Umlauf et al.* [2001] could show that the k-ω model (see section 3.2.7) accidentally performs reasonably well in both, shear-dominated and shear-free flow.

Approach of *Umlauf and Burchard* [2001] Because of this failure of the k-ε model, a more radical approach for extending two-equation models to flows with shear-free turbulence has been suggested by *Umlauf and Burchard* [2001]. They calibrated the generic length scale equation (3.111) to a number of unstratified flow situations. The remaining six model parameters σ_k, σ_{nm}, c_{mn1}, c_{nm2}, n and m are considered as completely free parameters. With the following assumptions, most of these parameters could be fixed:

- In shear-dominated turbulence, the law of the wall with $\kappa = 0.4$ and $c_\mu = 0.09$ has to be retained, see section 3.2.3.
- The decay rate of homogeneous turbulence is $d = -1.2$ which is well in the range of the laboratory experiments, see section 3.2.5.
- The *Tennekes* [1989] argument on the macro length scale is used for determining c_{nm1}, see section 3.2.8 and equation (3.86) therein.
- In shear-free turbulence, the spatial decay rate of turbulence is $\alpha_k = -2.0$ and the slope of the macro length scale is $\tilde{\kappa} = 0.2$. Alternatively, $\alpha_k = -2.5$ and $\tilde{\kappa} = 0.2$ are considered.

With these five conditions for the 6 unknown parameters, four of the parameters could be fixed and a functional dependence between the exponents n and m defined. The four resulting parameters and the exponent n for two different values of the exponent m are listed in table 3.6 for two different values of α_k. It should be noted that the physical values chosen for determining these parameters are arbitrary choices of values lying well in the range of the experimental values. However, for any other choice, empirical model parameters could be calculated as well.

α_k	$\tilde{\kappa}$	n	m	σ_k	σ_{nm}	c_{nm1}	c_{nm2}
-2.0	0.2	0.00	0.67	0.80	1.07	1.0	1.22
-2.0	0.2	0.37	1.09	0.80	1.75	2.0	2.36
-2.5	0.2	-0.58	1.05	1.25	1.68	1.0	1.35
-2.5	0.2	-0.61	1.74	1.25	2.78	2.0	2.58

Table 3.6. Empirical values of some model parameters for the generic model as function of the spatial decay rate of TKE, σ_k, the slope of the macro length scale, $\tilde{\kappa}$, and the choice for n. This table is adapted from table 11 by *Umlauf and Burchard* [2001]. For the different notations, see footnote 5 on page 76.

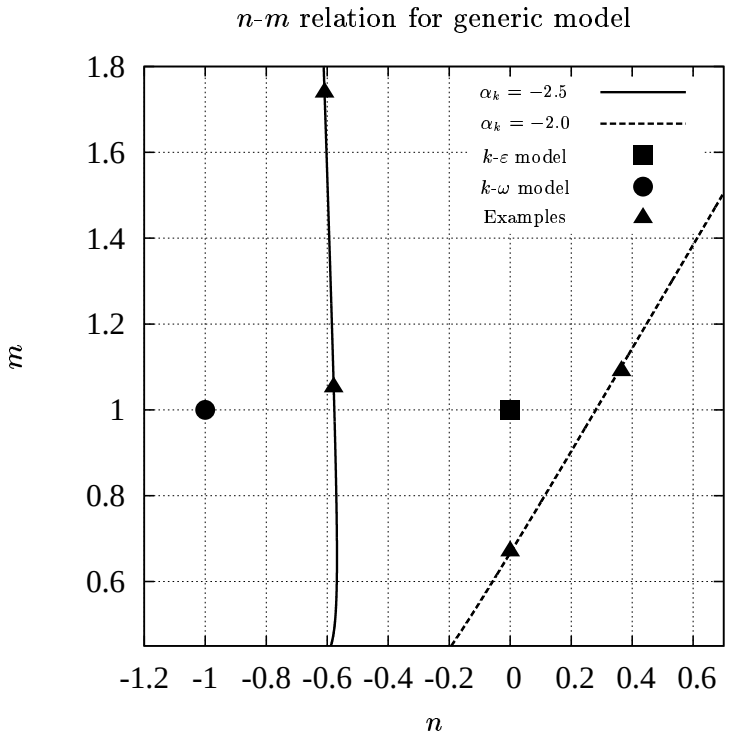

Fig. 3.16. Functional dependence of the exponents n and m for the generic two-equation model. The curves are shown for two different values of σ_k. Furthermore, the positions of the k-ε and the k-ω models as special cases of the generic model and the four examples from table 3.6 are shown. This figure is adapted from figure 2 by *Umlauf and Burchard* [2001]. For the different notations, see footnote 5 on page 76.

3.3.2 Wave-enhanced surface layer

Measurements of various investigators proved the existence of a layer of enhanced (with respect to the log-law) turbulence below breaking surface waves, see e.g. *Kitaigorodskii et al.* [1983], *Thorpe* [1984a] and *Osborn et al.* [1992]. More detailed measurements showed that the turbulent dissipation rate has logarithmic slopes between -2.7 and -1.9 in this wave-enhanced layer in contrast to -1 for the logarithmic law, see e.g. *Terray et al.* [1996], *Drennan et al.* [1996] and *Anis and Moum* [1995]. The present view is now, that below a near surface layer of thickness z_0^s in which all properties including the turbulent dissipation rate are well mixed, a wave-enhanced layer with a thickness of about 10 times the so-called surface roughness length is situated. Below that, the "classical" law-of-the-wall boundary layer scaling is established. Between

these three layers, intermediate states can be found. The wave-enhanced layer is characterised by a shear production which is orders of magnitudes smaller than the turbulent dissipation rate, whereas turbulence production and dissipation are assumed to be of equal size in the log-layer below.

In their famous paper, *Craig and Banner* [1994] suggested to model the flux of turbulent kinetic energy due to breaking waves into the water column as proportional to the cube of the surface friction velocity. Additionally, they found an analytical solution for an idealised model problem for the wave-enhanced layer by simply neglecting shear production of turbulence. Two years later, *Craig* [1996] published an analytical solution for an idealised model problem which combines both, the wave-enhanced layer, and the log-layer below including the transition zone between both of them. Since then, several authors have included this new approach into their models, see e.g. *Stacey and Pond* [1997], *D'Alessio et al.* [1998], *Noh and Kim* [1999] and *Canuto et al.* [2001]. These models have however all in common that they are one-equation models which diagnostically prescribe the macro length scale of turbulence near the surface as proportional to the distance from the surface.

Here, the two two-equation approaches discussed in the previous section 3.3.1 will be applied to the case of surface wave breaking including shear. However, before doing so, the shear-free analytical solutions for k and ε, (3.119) and (3.122), respectively, will be generalised to shear flow.

Analytical solution In order to account for shear, a prognostic equation for the horizontal velocity has to be included. For this idealised situation, rotation is neglected and the wind is assumed to be parallel to the x-direction such that only one velocity component $\bar{u}$ is considered. In this contexts, the surface momentum flux has the usual form, see equation (3.59):

$$-\nu_t \partial_z \bar{u} = (u_*^s)^2, \qquad \text{for } z = 0. \tag{3.124}$$

Assuming constant stress over the whole water column, the lower boundary condition for $\bar{u}$ is formulated as follows:

$$-\nu_t \partial_z \bar{u} = (u_*^s)^2, \qquad \text{for } z = -\infty, \tag{3.125}$$

For the turbulent kinetic energy, k, the same boundary conditions as in the shear-free case, (3.117) and (3.118), respectively, are used.

Craig [1996] suggested an analytical function which approximates the solution of the system of equations (3.25), (3.47), (3.49), (3.50), (3.55) and (3.56) together with boundary conditions (3.117), (3.118), (3.124) and (3.125). In contrast to that, the system of equations is here slightly modified such that a problem is formulated which exactly has the analytical solution of *Craig* [1996]. In order to achieve this, the turbulence production (3.50) has to be slightly modified:

$$P = a\frac{(u_*^s)^3}{\kappa(z' + z_0^s)}, \tag{3.126}$$

where a may be zero or unity, depending whether the shear-free case is considered ($a = 0$, see section 3.3.1 and *Craig and Banner* [1994]) or the general case of combining the wave-enhanced and the 'wall-of-the-law-layer' ($a = 1$, see *Craig* [1996]). For $a = 1$, the production for (3.126) is taken from the analytical solution for the law of the wall without wave breaking, see section 3.2.3.

With this modified turbulence production, the analytical solution can be generalised as follows:

$$k = \frac{(u_*^s)^2}{c_\mu^{1/2}}\left[a + \left(\frac{3\sigma_k}{2}\right)^{1/2} c_\mu^{1/4} c_w \left(\frac{z' + z_0^s}{z_0^s}\right)^{-\alpha_m}\right]^{2/3} \tag{3.127}$$

$$\varepsilon = \frac{(u_*^s)^3}{\kappa(z' + z_0^s)}\left[a + \left(\frac{3\sigma_k}{2}\right)^{1/2} c_\mu^{1/4} c_w \left(\frac{z' + z_0^s}{z_0^s}\right)^{-\alpha_m}\right] \tag{3.128}$$

with α_m from (3.120).

For $a = 0$ and $c_w > 0$, this is identical with the analytical solution presented by *Craig and Banner* [1994], for $a = 1$ and $c_w = 0$, the law of the wall is obtained. For the general case, $a = 1$ and $c_w > 0$, the wave-enhanced upper layer and the log-layer below can be identified from this solution for k and ε: for $z' \gg z_0^s$, the first term in the square brackets and thus the log-law dominates. For $z' \to 0$, the second term and thus enhanced turbulence is dominant, if the standard values in table 3.3 are used.

Approach of *Burchard* [2001b] It has been shown in the previous section 3.3.1, that for the shear-free case a modified Schmidt number for the dissipation rate, $\sigma_\varepsilon \approx 2.4$ must be used instead of the wall-law value of $\sigma_\varepsilon \approx 1.1$. For the general case of shear strongly varying with depth, *Burchard* [2001b] suggested an interpolation of σ_ε between these two cases characterised by $P/\varepsilon = 0$ (shear-free) and $P/\varepsilon = 1$ (shear-dominated). In order to obtain this dependency on P/ε, the fact that the expression in the square brackets of equation (3.128) equals ε/P with P from equation (3.126) has been exploited. The result is shown in figure 3.17 for $\sigma_k = 1$. It can be seen that the curve for σ_ε is close to a linear interpolation between $P/\varepsilon = 1$ and $P/\varepsilon = 0$.

In order to carry out numerical simulations of the wave enhanced layer with the k-ε model, a surface boundary condition for the dissipation rate ε has to be derived. By using the analytical solutions for k and ε, (3.119) and (3.122), a Neumann-type boundary condition for ε is of the following form:

$$-\frac{\nu_t}{\sigma_\varepsilon}\partial_z\varepsilon = -(c_\mu^0)^{3/4}\frac{\nu_t}{\sigma_\varepsilon}\frac{\frac{3}{2}\frac{\sigma_k (c_\mu^0)^{3/4}}{c_\mu} c_w (u_*^s)^3 + \kappa k^{3/2}}{\kappa^2 (z' + z_0^s)^2}. \tag{3.129}$$

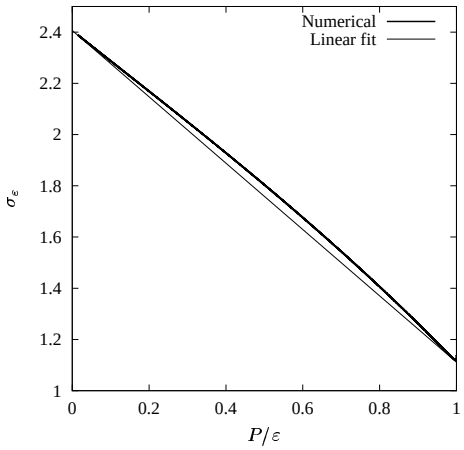

Fig. 3.17. The turbulent Schmidt number σ_ε as it occurs in the dissipation rate equation for $\sigma_k = 1$. Shown are numerical solution of the idealised analytical problem and a linear fit.

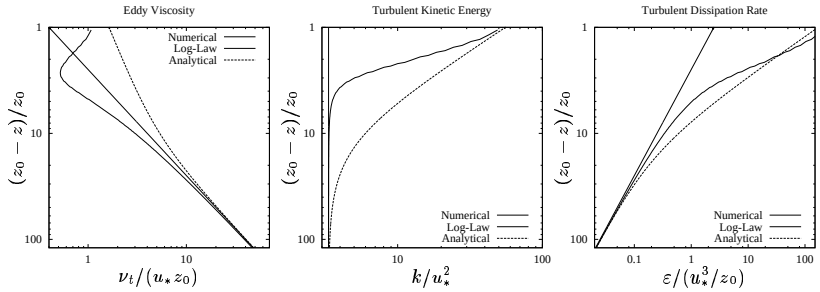

Fig. 3.18. Results of a numerical simulation of the wave-enhanced layer obtained by the non-modified k-ε model compared to analytical solutions for the log-law and the wave-enhanced layer. Shown are profiles of non-dimensional eddy viscosity, turbulent kinetic energy, and turbulent dissipation rate.

This is a generalisation of the Neumann-type boundary condition (3.66) suggested by *Burchard and Petersen* [1999] (see also the discussion by *Meier* [1997]) which is obtained by setting $c_w = 0$.

Since indefinite depth is not realisable in a numerical model, a water depth D of 3000 times larger than the roughness length z_0 (here $D = 50$ m and $z_0 = 0.0166$ m^{-s}) is applied for the idealised model simulations. It is such assumed that near-bed processes play a negligible role for the wave-enhanced layer. In this section, the standard value for the turbulent Schmidt number for TKE, $\sigma_k = 1$ is used.

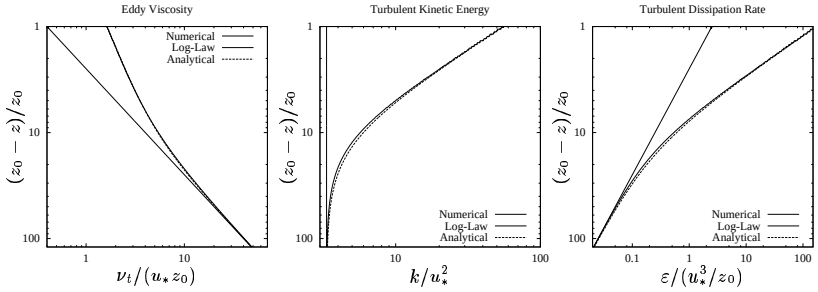

Fig. 3.19. Results of a numerical simulation of the wave-enhanced layer obtained by the modified k-ε model with constant c_μ compared to analytical solutions for the log-law and the wave-enhanced layer. Shown are profiles of non-dimensional eddy viscosity, turbulent kinetic energy, and turbulent dissipation rate.

The model is driven with a constant surface friction velocity which in this case was $u_*^s = 0.01\ \mathrm{m\,s^{-1}}$. After initialising the velocity with $u = 0$, it took about 5 days of simulation in order to reach a steady-state solution with a constant shear stress over the whole water column.

The simulations in this section were carried out with high numerical resolution with $\Delta z/z_0 < 0.1$ at the surface which was obtained by choosing adequate values for the number of layers N_i and the grid zooming parameter d_u with $N_i = 1000$ and $d_u = 3$, see equation (4.2).

The need for adapting σ_ε in order to reproduce surface wave breaking is shown in figure 3.18, where the analytical solution is compared to the application of the k-ε model with unmodified turbulent Schmidt number $\sigma_\varepsilon = \sigma_{\varepsilon 1}$ from equation (3.70). It can be seen that the results for k and ε significantly deviate from the analytical solution in the wave-enhanced layer.

In contrast to that, when using the modified k-ε model, the analytical and the numerical solution are almost identical, if the spatial resolution of the numerical model is sufficiently fine (not shown here). Small deviations between numerical result and analytical solution are mainly due to the fact that the linear fit to σ_ε has been used instead of the more exact numerical solution, see figure 3.17.

Furthermore, numerical solutions of the complete problem with shear production from (3.50) instead of (3.126) are shown in figure 3.19. It should be noted again that an analytical solution for this problem could not be found. It can be clearly seen here that the numerical solution is now sufficiently close to the idealised analytical solution given as equations (3.119) and (3.122).

Approach of *Umlauf and Burchard* [2001] The approach suggested by *Umlauf and Burchard* [2001] can directly be applied to the shear flow with injection of turbulence kinetic energy at the surface. From the calibration carried out in the previous section 3.3.2, it would be expected that the slope

of the macro length scale would be $\tilde{\kappa} = 0.2$ near the surface where the shear production to dissipation ratio is small and $\kappa = 0.4$ in deeper layers where turbulence is near local equilibrium. The profiles of the macro length scale shown in figure 3.20 in linear scale do indeed exactly fulfil this: near the surface, the profiles for shear-flow converge to those for shear-free flow. For the case with shear, small differences in slope occur between different choices of the exponent n in the transition zone between shear-free ($P/\varepsilon \ll 1$) and shear-dominated ($P/\varepsilon \approx 1$) flow. However, deeper down in the water column the two slopes are identical again. The profiles for the turbulent kinetic energy are shown in figure 3.20 with double-logarithmic scaling. From this, it can be clearly seen that the surface slope is exactly $\alpha_k = -2$, as prescribed by means of the calibration procedure discussed in the previous section 3.3.2.

The depth of the wave-enhanced layer calculated by the generic two-equation model with the present specifications seems to be slightly shallower than the one predicted by the modified k-ε model, see figure 3.19.

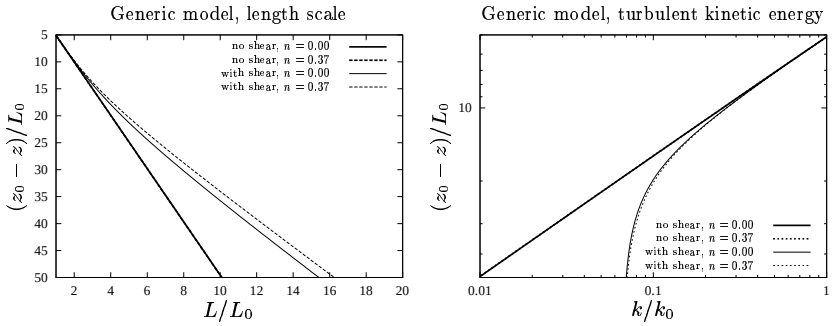

Fig. 3.20. Profiles of macro length scale L (left panel) and turbulent kinetic energy k (right panel) computed by the approach of *Umlauf and Burchard* [2001] for the wave-enhanced layer. The profiles have been normalised by the surface values of k and L, k_0 and $L_0 = 0.2 * z_0$, respectively. The spatial decay rate of turbulent kinetic energy was set here to $\alpha_k = -2.0$, see also table 3.6.

Reproducing near-surface dissipation rate measurements *Terray et al.* [1999] scaled three different sets of near surface dissipation rate measurements under breaking waves such that they more or less collapse into one curve. The scaling of depth was made by using the significant wave height H_s. By comparing the *Craig and Banner* [1994] model to these data, they found a z_0^s/H_s ratio of 0.85. In figures 3.21 and 3.22, this comparison is reproduced with the k-ε model equipped with the *Canuto et al.* [2001] shear-dependent stability function c_μ and the generic model approach by *Umlauf and Burchard* [2001] with $\alpha_k = -2.0$, respectively. The profiles for the dissipation

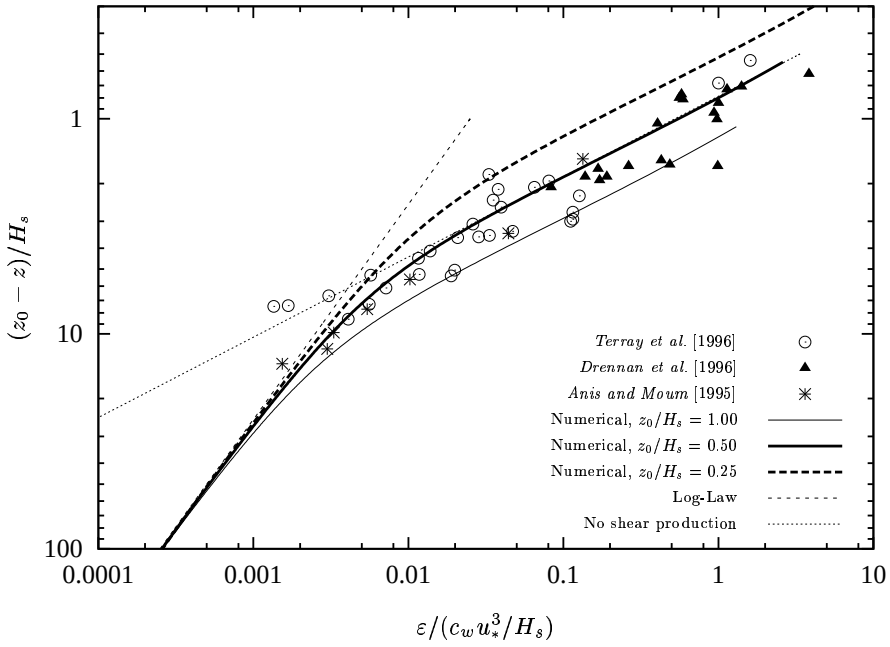

Fig. 3.21. Observations and simulations of turbulent dissipation rate in the wave-enhanced layer. The observations of *Terray et al.* [1996], *Drennan et al.* [1996] and *Anis and Moum* [1995] are normalised by surface TKE flux and significant wave height, see *Terray et al.* [1999]. The simulations have been carried out with the k-ε model by *Burchard et al.* [2001] using the modified turbulent Schmidt number σ_ε with surface roughness length to wave height ratios of 1, 0.5 and 0.25. The shear-dependent stability function c_μ by *Canuto et al.* [2001] has been used here. As comparison, the log-law with $\sigma_\varepsilon = \sigma_{\varepsilon 1}$ and the pure wave breaking case (no shear production) with $\sigma_\varepsilon = \sigma_{\varepsilon 0}$ are shown as well.

rates have here been calculated from profiles made non-dimensional with the friction velocity u_* and the surface roughness length z_0 (as in figures 3.18 and 3.19) which have then been shifted by the factor z_0/H_s in z-direction and by the factor of $c_w * z_0/H_s$ in ε-direction. For the modified k-ε model, most of the data fall within the two simulated curves given by $z_0^s/H_s = 0.25$ and $z_0^s/H_s = 1$. Similarly, for the generic two-equation model approach by *Umlauf and Burchard* [2001] (see figure 3.22), most of the data lie between the simulated curves for $z_0^s/H_s = 0.5$ and $z_0^s/H_s = 2$.

Although the two models calculate considerably different slopes for the near-surface dissipations rates (-2.68 for the *Burchard* [2001b] model and -4.0 for the *Umlauf and Burchard* [2001] model), both models seem to fit the data quite well. However, the data do not allow to give preference for one or the other model approach.

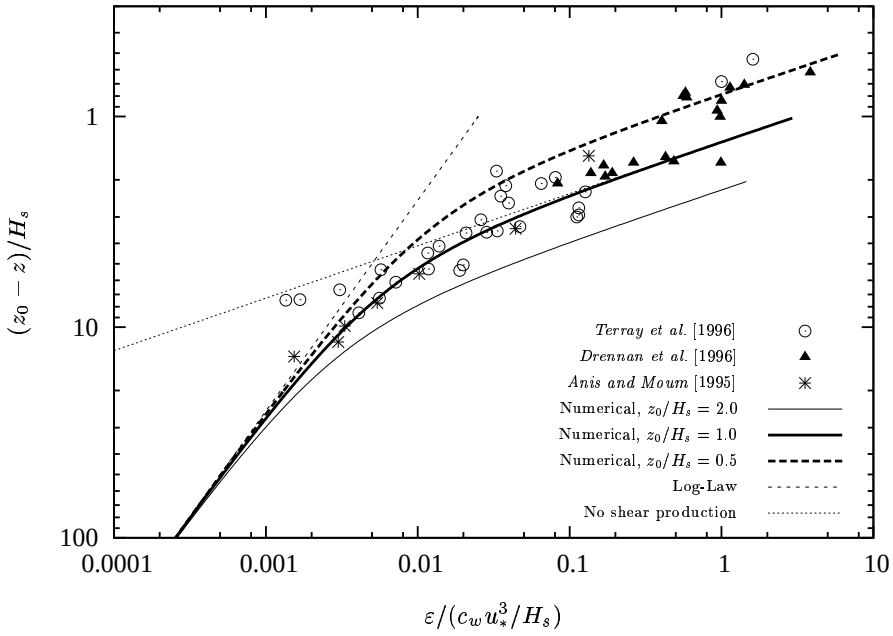

Fig. 3.22. As figure 3.21, but simulations have been carried out with the generic two-equation model by *Umlauf and Burchard* [2001] with surface length scale $z_0 = L_0/0.2$ to wave height H_s ratios of 2.0, 1.0 and 0.5. As comparison, the log-law and the shear-free case are shown as well. The empirical constant $c_w = 100$ is the coefficient of proportionality for relating the surface flux of turbulent kinetic energy to the cubed friction velocity. The spatial decay rate of turbulent kinetic energy was set here to $\alpha_k = -2.0$, see also table 3.6.

It should be noted that recent results of *Gemmrich and Farmer* [1999] contradict the assumption of a fixed z_0^s/H_s ratio, as there a ratio of less than 0.05 had been measured in the open ocean. Since z_0^s is the significant height of air-bubble entrainment into the water due to wave breaking, it is not necessarily related to the significant wave height. However, this discussion will not be continued here, because the surface roughness length is the relevant model parameter which has to be calculated outside the model and then used as model input. It is unfortunately the significant wave height which is part of standard oceanic measurements and not the surface roughness length, so the question how to calculate z_0^s remains open.

The upper model boundary is here located at the bottom of the unresolved surface layer of height z_0^s, the air-bubble entrainment zone, in which the turbulent dissipation rate is assumed to be constant. At this location, where the vertical coordinate z of the model is set to zero, the macro length of turbulence is fixed to $L = \kappa z_0^s$. This is in accordance to the arguments of

Terray et al. [1999] that the macro length scale should increase proportionally to the distance from the surface.

Remaining problems The determination of the surface roughness length z_0^s is still an open scientific question. Several authors have related this quantity directly to the significant wave height, see *Terray et al.* [1996], *Drennan et al.* [1996] and *Terray et al.* [1999]. However, recent field measurements in the open ocean by *Gemmrich and Farmer* [1999] showed a completely different relation between roughness length and significant wave height, such that obviously more complex parameterisations for the surface roughness length are needed. *Stacey* [1999] found that the *Charnok* [1955] formula, see equation (3.44) actually is consistent with a scaling of z_0^s with the significant wave height H_s. Until better parameterisations are found, the *Charnok* [1955] formula relating surface roughness length to surface friction velocity seems thus to be a good compromise. The empirical parameter α_C used within (3.44) however seems to underestimate actual roughness lengths. *Craig* [1996] concludes that the determination of the surface roughness length will be a major challenge in the future. This is motivated even more after the *Gemmrich and Farmer* [1999] paper.

3.3.3 Internal waves

Compared to surface waves, internal waves are a much more complex phenomenon. They are guided by stratification varying with time in the three-dimensional space. They are three-dimensional themselves with horizontal and vertical modes in contrast to surface waves which are essentially two-dimensional. And, moreover, they interact non-linearly with their wave guide, the stratification of the flow. Various models have been developed for simulating and understanding oceanic internal waves, for a review, see e.g. *Olbers* [1983].

From a turbulence modellers point of view, internal wave dynamics must not be neglected, since dissipation of internal waves creates mixing, which is a priori not considered by classical turbulence closure models. There are two main mechanisms for dissipation of internal waves: Kelvin-Helmholtz instabilities and breaking of internal waves.

Kelvin-Helmholtz (or shear) instabilities occur when mean shear locally increases such that the local Richardson number is below the asymptotic gradient Richardson number of $R_i^\infty = 0.25$ such that turbulent patches are produced at the crest of the internal wave. By means of Direct Numerical Simulation of single Kelvin-Helmholtz billows, the creation of mixing due to Kelvin-Helmholtz instabilities has been investigated in detail by *Smyth* [1999], *Smyth and Moum* [2000a] and *Smyth and Moum* [2000b]. One of the surprising features which have been found in these investigations is the fact that mixing is extraordinary efficient during preturbulent overturns when turbulence is not yet fully developed. The future aim of such small scale DNS

studies of internal wave dynamics must be to improve internal wave parameterisations for large scale oceanic models, since DNS is computationally much too expensive for use on larger scales, see the reasoning in section 2.1.5.

Similarly to surface waves, breaking of internal waves occurs when the particle speed of the wave crest exceeds the wave speed and a statically unstable stratification is created. This phenomenon has been investigated in detail by *Thorpe* [1979]. In contrast to Kelvin-Helmholtz instabilities, mean shear is not needed for this process.

According to *D'Asaro and Lien* [2000], dissipation of internal waves into turbulence mainly takes place in high energy (i.e. high shear) regions with gradient Richardson numbers of $R_i \leq 1$. At about $R_i \approx 1$, a so-called wave-turbulence transition exists, above which the internal wave dynamics is dominated by interactions between internal waves. In their recent paper, *D'Asaro and Lien* [2000] discussed that the dissipation rate depends in this low energy regime above the wave-turbulence transition on the internal wave energy squared. For models of such wave-wave interaction regimes in the ocean, see *Müller et al.* [1986]. For internal waves dynamics in estuarine flow, see e.g. *Uittenbogaard* [1995].

For both, Kelvin-Helmholtz instabilities and breaking of internal waves, simple parameterisations have been suggested in the past. They are simple because they do not use any explicit information on the internal wave state in the model.

Following *Gill* [1982], *Mellor* [1989] suggested to add internal wave shear (related to the Brunt-Väisälä frequency N^2) to the mean shear M^2 in the shear production term such that it is of form

$$P = \nu_t (M^2 + 0.7N^2). \tag{3.130}$$

In (3.130), the square of the internal wave shear has been parameterised by $0.7N^2$, see *Gill* [1982]. With inserting this modified shear production term into the TKE equation (3.72) and the length scale equation (3.71), *Mellor* [1989] was able to significantly improve the surface temperature results for the 1977 Mixed Layer Experiment (MILE, see *Martin* [1986]). *Burchard et al.* [1999] and *Villarreal* [2000] could however show in an application to the Ocean Weather Station Papa data that internal mixing is greatly underestimated with this scheme, when integrated into a k-ε model. This could be due to the fact that diffusion of TKE is treated differently by the k-ε and the k-kL model. In the k-ε model application, internal mixing could only be raised to realistic levels by additionally imposing a lower limit for the turbulent kinetic energy, see *Villarreal* [2000]. For a one-dimensional application of the k-ε model to the Southern Baltic Sea, *Axell* [2002] added an internal wave shear production term (and a Langmuir circulation term, see section 3.3.4) to the k and the ε equation. The internal wave shear production is assumed to be proportional to the vertically integrated internal wave energy and the Brunt-Väisälä frequency. The internal wave energy pool is filled by an energy

flux proportional to the wind energy input. After properly calibrating this model, *Axell* [2002] could well reproduce the Baltic Sea deep water mixing over 10 years.

Large et al. [1994] suggest separate simple parameterisations for shear instabilities (SI) and internal wave breaking (IW). The shear instability induced viscosities and diffusivities are modelled as a strongly decreasing function of the gradient Richardson number R_i,

$$(\nu_t)^{SI} = (\nu_t')^{SI} = \begin{cases} 0, & \text{for } R_i > 0.7, \\ 5 \cdot 10^{-3} \left(1 - \left(\frac{R_i}{0.7}\right)^2\right)^3 \ \mathrm{m^2 s^{-1}}, & \text{for } 0 < R_i < 0.7, \\ 5 \cdot 10^{-3} \ \mathrm{m^2 s^{-1}}, & \text{for } R_i < 0. \end{cases} \tag{3.131}$$

In contrast to that, it is assumed that internal wave induced viscosities and diffusivities are constant:

$$\begin{aligned} (\nu_t)^{IW} &= 10^{-4} \ \mathrm{m^2 s^{-1}}, \\ (\nu_t')^{IW} &= 10^{-5} \ \mathrm{m^2 s^{-1}}. \end{aligned} \tag{3.132}$$

Thus, when the turbulent kinetic energy is small (extinction of turbulence, diagnosed by the turbulent kinetic energy k being smaller than a certain value, usually 10^{-6} J kg^{-1}), the sum of shear induced and internal wave induced viscosities and diffusivities $(\nu_t)^{SI} + (\nu_t)^{IW}$ is imposed instead of using the diffusivities ν_t and ν_t' given by the model. This model was applied by *Kantha and Clayson* [1994] to different situations and appeared to promote increased mixing in stably stratified situations. For achieving satisfying results for the Ocean Weather Station Papa data in the Northern Pacific Ocean with a k-kL model, they needed however to increase $(\nu_t')^{IW}$ from (3.132) by a factor of 5.

Another method has been proposed by *Luyten et al.* [1996b] in order to realistically reproduce dissipation rate measurements in the Irish Sea inside the pycnocline. According to a suggestion by *Galperin et al.* [1988], they used the length scale limiting condition (3.73) as lower limit for the turbulent dissipation rate ε:

$$\varepsilon^2 \geq \varepsilon_{\min} = 0.045 k^2 N^2 \qquad \text{for } N^2 > 0. \tag{3.133}$$

Luyten et al. [1996b] however found that condition (3.133) is not sufficient for avoiding an unlimited extinction of the turbulence level in strongly stratified regions since a decrease of the turbulent kinetic energy k significantly weakens (3.133). Based on observations of oceanic turbulence by *Gregg* [1987], *Luyten et al.* [1996b] motivate a lower limit of the turbulent kinetic energy k, which turns out to be a tuning parameter:

$$k \geq k_{\min}. \tag{3.134}$$

For their Irish Sea simulation, they use $k_{\min} = 3 \cdot 10^{-6}$ J kg^{-1}. In a numerical simulation of the same Irish Sea measurements with different k-ε model than *Luyten et al.* [1996b], *Burchard et al.* [1998] used a slightly higher value of $k_{\min} = 7.6 \cdot 10^{-6}$ J kg^{-1}, see also section 7.4.1. In a more recent study, *Bolding et al.* [2000] however needed to reduce the minimum value to $k_{\min} = 1.0 \cdot 10^{-6}$ J kg^{-1} in order to reproduce internal mixing coefficients in the Northern North Sea of about $5 \cdot 10^{-5}$ m^{2}s^{-1}. It was found by *van Haren* [2000] that this seems to be a quite constant background diffusivity in the thermocline which changes only insignificantly when the shear regime switches from inertial oscillations to semi-diurnal tides. This difference to the Irish Sea study by *Burchard et al.* [1998] could be motivated by the fact that here the new stability functions by *Canuto et al.* [2001] have been used and not the older functions by *Galperin et al.* [1988], which have been shown by *Burchard and Bolding* [2001] to mix less efficiently.

One could actually try to extend the suggestion by *Luyten et al.* [1996b] by using an estimate for the turbulent dissipation rate made by *Gregg and Sanford* [1988] inside the thermocline:

$$\varepsilon = 13\nu N^2. \tag{3.135}$$

According to *D'Asaro and Lien* [2000], such models do however only hold for the high energy regime below the wave-turbulence transition at about $R_i \approx 1$. After presenting their model for the low energy regime above the wave-turbulence regime, they argue:

> The observation that both the high energy limit of the model presented here and the low energy limit of *Burchard et al.* [1998] yield similar parameterisations (eq. 3.74, 3.133, 6.2) suggests that a hybrid model, combining appropriate aspects of each, may be possible.

Thus, it seems that some perspectives are given for improving the parameterisation of internal mixing dynamics. The problems related to the modelling of internal mixing near the wave-turbulence transition is clearly underlined by *Baumert and Peters* [2000] when discussing micro-structure data analysed by *Peters et al.* [1995] in the equatorial undercurrent:

> The underlying problem is that the turbulent kinetic energy, ..., is not uniquely defined in stratified flows with a broadband energy spectrum dominated by internal waves.

Motivated by this work, *Baumert and Peters* [2002] recently suggested that

> there is an extra buoyancy-related loss term to TKE that does not contribute to mixing. Physically, this is thought of as energy transfer from turbulence to internal waves and other non-turbulent processes.

With a zero-dimensional version of such a heuristic type of model, they could well simulate the laboratory experiment by *Dickey and Mellor* [1980] and other observational studies of turbulence. It will be interesting to see, how this model performs in comparison to complete one-dimensional water column models as discussed in this book.

A great portion of the ocean abyssal mixing below the thermocline is believed to be caused by internal wave dynamics as well. It is known from tracer release experiments by *Ledwell et al.* [1993] and many other studies that the mixing coefficients are of the order of 10^{-5} m^2s^{-1} almost everywhere in the deep ocean. There are attempts to account for this abyssal mixing in turbulence closure modelling by using the universal Garrett-Munk spectrum (see *Garrett and Munk* [1972], *Garrett and Munk* [1975]) for estimating the shear induced by internal waves in order to insert it into the shear production term P, see *Canuto et al.* [2002]. However, at certain locations such as near seamounts or mid-ocean ridges, mixing can be up to the order of 10^{-2} m^2s^{-1} due to interaction of internal tides with bathymetry and other processes (see *Polzin et al.* [1996]). It is almost impossible to account for these mixing effects in turbulence closure models, although they might be be of great importance on larger time scales.

3.3.4 Langmuir circulation

As a characteristic phenomenon on the sea surface of lakes, estuaries, coastal seas or the open ocean, Langmuir circulation is well-known to many sailors, even when they have no theoretical understanding of fluid dynamics. The streaky patterns on the sea surface roughly aligned to the wind direction have been first qualitatively been described and interpreted by *Langmuir* [1938] as convergence zones caused by vortices counter-rotating around horizontally oriented axes. More recently, bubble clouds concentrated in the Langmuir cell convergence zones have been investigated in detail by *Thorpe* [1984b], *Thorpe* [1992] and *Osborn et al.* [1992].

Although the phenomenon is obvious even to laymen, convincing theories for the dynamics of Langmuir circulation have only been developed in recent years. The mechanism with which Langmuir circulation could successfully be simulated by means of Large Eddy Simulation (LES) studies has first been proposed by *Craik and Leibovich* [1976]. According to their model, Langmuir circulation arises from the nonlinear interaction between the Stokes drift due to surface waves and the vertical shear of wind-induced currents. *Leibovich* [1977] models this instability as a vortex force

$$-\boldsymbol{V}_s \times \boldsymbol{\omega} \tag{3.136}$$

entering the left hand side of the Reynold's averaged momentum equations (2.18). Here,

$$\boldsymbol{V}_s = (U_s, V_s, 0) = 0.016 \exp(z'/L_w)(U_{10}, V_{10}, 0) \tag{3.137}$$

is the Stokes drift vector, where $L_w = 0.12(U_{10}^2 + V_{10}^2)/g$ is the wave length for a fully developed sea (see *Li and Garrett* [1993]), U_{10} and V_{10} are the 10 m wind speed components, and $\boldsymbol{\omega} = (\omega_1, \omega_2, \omega_3)$ is the absolute vorticity with

$$\omega_i = \varepsilon_{imn} \partial_m \bar{u}_n + \Omega_i. \tag{3.138}$$

McWilliams et al. [1997] show that this vortex force reduces for boundary layers with horizontally averaged equations to simply modifying the Coriolis terms. When considering the vortex force, they are of form $-f(\bar{v} + V_s)$ and $f(\bar{u} + U_s)$ as on the left hand sides of the hydrostatic primitive equations (3.4) and (3.5), respectively. In order to consider Langmuir circulation for the budget of turbulent kinetic energy as well, *Skyllingstad and Denbo* [1995] derive modified shear production and vertical flux terms for the TKE equation (3.41). When accepting the down-gradient approximation for the Reynolds stresses and vertical TKE flux, these terms are of the form

$$P = \nu_t \left\{ \partial_z \bar{u} \left(\partial_z \bar{u} + \partial_z U_s \right) + \partial_z \bar{v} \left(\partial_z \bar{v} + \partial_z V_s \right) \right\} \tag{3.139}$$

for the shear production and

$$F(k) = -\nu_t \left(\partial_z k - U_s \partial_z \bar{u} - V_s \partial_z \bar{v} \right) \tag{3.140}$$

for the vertical flux of TKE. Furthermore, for their non-local mixed-layer model, *D'Alessio et al.* [1998] suggest to add the maximum downwelling velocity

$$w_*^{LC} = c^{LC} \sqrt{U_{10}^2 + V_{10}^2} \tag{3.141}$$

with $0.0025 \leq c^{LC} \leq 0.0085$ (see *Leibovich* [1983]) to the Deardorff velocity scale w_*, see equation (6.5), which is used for parameterising the third moments. With all these modifications, *D'Alessio et al.* [1998] could improve the performance of their water column model when applied to the OWS Papa data set which is described in section 7.2. The mixed layer depth was significantly deeper during autumn and winter when high wind speeds dominated the surface forcing. However, the overall changes in sea surface temperature were relatively small, since the thermal stratification is weak during these high wind speed seasons. The significant additional deepening during autumn and winter might be caused by the non-local formulation of the parameterisation by *D'Alessio et al.* [1998]. Due to the exponential decrease of the Stokes drift velocity with depth, it would however be expected that only shallow diurnal mixed layers would be rapidly eroded by Langmuir circulation, see *Weller and Price* [1988].

A somewhat simpler parameterisation of Langmuir circulation has recently been suggested by *Axell* [2002] who assumed a sine profile of the

downwelling velocity w_*^{LC} in the mixed layer and an additional shear production term P_{LC} due to Langmuir circulation with

$$P_{LC} = \frac{w_*^{LC}}{D_m} \tag{3.142}$$

with the mixed layer depth D_m. However, also *Axell* [2002] concludes that the effect of this parameterisation on the mixed layer depth is small.

This limited impact on the depth of the ocean mixed layer has been similarly discussed for the direct effect of breaking surface waves on turbulence, see the work of *Craig and Banner* [1994] and *Craig* [1996] and also section 3.3.2. What seems to be missing up to now is a unified theory for the turbulence dynamics under breaking surface waves combining the theories of *Craig and Banner* [1994] for the TKE surface flux due to wave breaking and *Craik and Leibovich* [1976] for the Langmuir circulation due to Stokes drift.

It is evident from Large Eddy Simulation studies (see *Skyllingstad and Denbo* [1995]) that Langmuir circulation is a multi-scale phenomenon, in contrast to the idealistic, theoretical view as given for example by *Pollard* [1977]. Similarly to internal wave-turbulence interaction (see section 3.3.3), there is a definition problem also for separating turbulence from Langmuir circulation. That might be the reason why models for Langmuir circulation are still only rarely included in ocean circulation models, see e.g. *Large et al.* [1994]. According to Eric Skyllingstad (pers. comm.), there has been so far "no concerted effort to include Langmuir circulation (LC) into turbulence closure models". This problem is mainly related to the non-local character of Langmuir circulation which should probably be parameterised in terms of non-local closures for third moments.

4 Numerics

After the big task of deriving closed sets of mathematical equations for the physical processes under investigation is discussed in depth in chapters 2 and 3, the next task will be discussed in much less detail here: The numerical discretisation of these sets of equations in such a way that the solution of the mathematical equations is approximated with sufficient accuracy. The reason for this numerical discussion being considerably shorter is not its limited relevance but the fact that here many standard methods can be applied which are in detail presented in numerical text books such as those by *Hirsch* [1988] or *LeVeque* [1992]. This chapter focuses mainly on numerical methods which are of specific relevance for turbulence modelling in a one-dimensional water column model such as ensuring positivity of positive definite quantities (section 4.2), conservation of kinetic energy (4.3) and boundary conditions related to the law of the wall (section 4.4).

For the one-dimensional applications discussed in chapters 6 and 7, much care in discretising the equations would probably not be necessary, since sufficiently fine resolution in time and space is generally not a limiting problem. However, since one major scope of small-scale turbulence modelling must be the simulation of turbulence and mixing in three-dimensional coarse-resolution models, discretisations have to be found which guarantee sufficient accuracy also for such models. This can however not always be achieved, especially when the relevant processes are of smaller scale than typical model resolutions.

4.1 General second-order approximation

For the spatial discretisation, the water column is divided into N_i layers of not necessarily equal thickness h_i:

$$h_i = (\gamma_i - \gamma_{i-1})D, \qquad i = 1, \ldots, N_i. \tag{4.1}$$

with nondimensional interfaces γ_i with $\gamma_0 = -1$, $\gamma_{i-1} < \gamma_i$ and $\gamma_{N_i} = 0$, see *Burchard and Petersen* [1997]. A zooming of layers can be for example obtained by:

$$\gamma_i = \frac{\tanh\left((d_l + d_u)\frac{i}{N_i} - d_l\right) + \tanh(d_l)}{\tanh(d_l) + \tanh(d_u)} - 1, \qquad i = 0, \ldots, N_i \tag{4.2}$$

where D is the height of the water column, N_i the number of layers and d_l and d_u zooming parameters. For $d_u = d_l = 0$, the discretisation is equidistant, for $d_l = 0$ and $d_u > 0$, the grid is refined towards the surface and for $d_l > 0$ and $d_u = 0$, the grid is refined towards the bottom. With both $d_l > 0$ and $d_u > 0$, zooming towards surface and bed is obtained. In other cases, it might be advantageous to perform a zooming somewhere else in the water column such as in the region of the thermocline. Such a refinement could however be much more efficiently obtained by using general vertical coordinates such as isopycnal coordinates (see *Bleck and Smith* [1990]) or layer thicknesses proportional to the macro length scale (see *Baumert et al.* [2000]). Especially the latter technique requires to consider some extra grid-related vertical advection.

The discrete values for the mean flow quantities $\bar{u}$, $\bar{v}$, $\bar{T}$, and $\bar{S}$ represent interval means and are therefore located at the centres of the intervals, and the turbulent quantities k, L, ε, ν_t, ν_t', N, P, B, c_μ, and c_μ' are positioned at the interfaces of the intervals. The indexing is such, that the interface above an interval has the same index than the interval itself. This means that mean flow quantities range from $i = 1, .., N_i$ while turbulent quantities range from $i = 0, .., N_i$ (see figure 4.1). The staggering of the grid allows for a straightforward discretisation of the vertical fluxes of momentum and tracers without averaging. However, for the vertical fluxes of k, L, and ε, averaging of the eddy diffusivities is necessary. This is only problematic for the fluxes near the surface and the bottom, where viscosities at the boundaries have to be considered for the averaging. These can however be derived from the law of the wall, see section 3.2.3.

The time stepping is equidistant, based on two time levels and not limited by Courant numbers, because of the absence of advection and an implicit treatment of vertical diffusion. In the following, the discretisation of a simple diffusion equation

$$\partial_t X - \partial_z(\nu \partial_z X) = 0 \tag{4.3}$$

will be shown with the Neumann-type boundary conditions

$$\nu \partial_z X = F_s \qquad \text{for } z = \zeta, \tag{4.4}$$

and

$$\nu \partial_z X = F_b \qquad \text{for } z = -H. \tag{4.5}$$

The semi-implicit discretisation for a mean flow quantity such as momentum or tracers is of the following form[1]:

[1] Despite the fact that the layers are moving, the variable layer thickness is not considered in the discretisations of the time derivatives. In a two- or three-

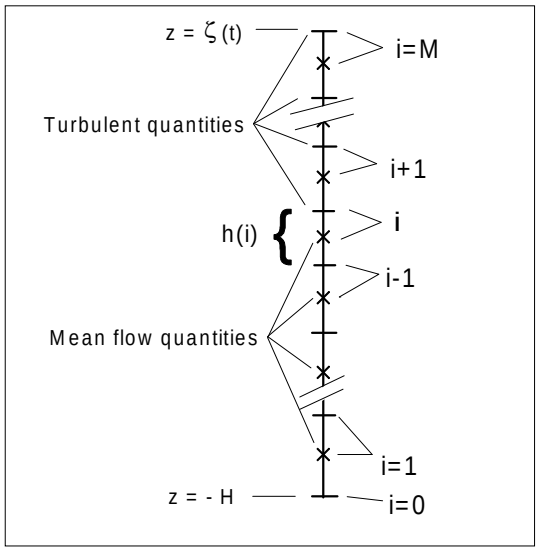

Fig. 4.1. Spatial organisation and indexing of the numerical grid.

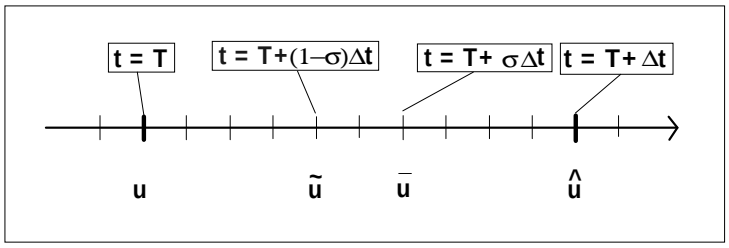

Fig. 4.2. Temporal organisation and indexing of the numerical grid. Here, a time stepping slightly more implicit than the *Crank and Nicolson* [1947] scheme with $\sigma = 0.6$ is shown.

$$\frac{X_{N_i}^{n+1} - X_{N_i}^{n}}{\Delta t} - \frac{F_s - \nu_{N_i-1}^{n} \frac{X_{N_i}^{n+\sigma} - X_{N_i-1}^{n+\sigma}}{0.5(h_{N_i}^{n+1} + h_{N_i-1}^{n+1})}}{h_{N_i}^{n+1}} = 0, \tag{4.6}$$

$$\frac{X_i^{n+1} - X_i^{n}}{\Delta t} - \frac{\nu_i^{n} \frac{X_{i+1}^{n+\sigma} - X_i^{n+\sigma}}{0.5(h_{i+1}^{n+1} + h_i^{n+1})} - \nu_{i-1}^{n} \frac{X_i^{n+\sigma} - X_{i-1}^{n+\sigma}}{0.5(h_i^{n+1} + h_{i-1}^{n+1})}}{h_i^{n+1}} = 0, \tag{4.7}$$

$$\frac{X_1^{n+1} - X_1^{n}}{\Delta t} - \frac{\nu_1^{n} \frac{X_2^{n+\sigma} - X_1^{n+\sigma}}{0.5(h_2^{n+1} + h_1^{n+1})} - F_b}{h_1^{n+1}} = 0, \tag{4.8}$$

for $1 < i < N_i$. Here, the semi-implicit time level is defined as follows:

$$X^{n+\sigma} = \sigma X^{n+1} + (1-\sigma) X^{n}. \tag{4.9}$$

Thus, for $\sigma = 0$ a fully explicit, for $\sigma = 1$ a fully implicit and for $\sigma = 0.5$ the *Crank and Nicolson* [1947] second-order in time scheme is obtained. Figure 4.2 shows an example for $\sigma = 0.6$. It should be noted that often a time stepping is preferable which is slightly more implicit than the *Crank and Nicolson* [1947] scheme in order to obtain asymptotic stability, see *Samarskij* [1984] and the discussion by *Burchard* [1995].

This semi-implicit differencing leads for each transport equation to a system of linear equations with the following tri-diagonal matrix:

$$\begin{aligned}
&-X_{N_i-1}^{n+1} \frac{\sigma \Delta t \nu_{N_i-1}^{n}}{0.5 h_{N_i}^{n+1} (h_{N_i}^{n+1} + h_{N_i-1}^{n+1})} \\
&+X_{N_i}^{n+1} \left(1 + \frac{\sigma \Delta t \nu_{N_i-1}^{n}}{0.5 h_{M_i}^{n+1} (h_{N_i}^{n+1} + h_{N_i-1}^{n+1})} \right) = \\
&\qquad X_{N_i-1}^{n} \frac{(1-\sigma) \Delta t \nu_{N_i-1}^{n}}{0.5 h_{N_i}^{n+1} (h_{N_i}^{n+1} + h_{N_i-1}^{n+1})} \\
&\qquad +X_{N_i}^{n} \left(1 - \frac{(1-\sigma) \Delta t \nu_{N_i-1}^{n}}{0.5 h_{N_i}^{n+1} (h_{N_i}^{n+1} + h_{N_i-1}^{n+1})} \right) + \frac{\Delta t}{h_{N_i}^{n+1}} F_s,
\end{aligned} \tag{4.10}$$

dimensional model this would cause non-conservation of the physical quantity to be transported because the continuity equation would be violated without using the conservative formulation of the equations. However in this one-dimensional environment, advection is not considered and thus the conservative form of the equations would be incomplete and non-conservative.

$$
\begin{aligned}
&-X_{i-1}^{n+1}\frac{\sigma\Delta t\nu_{i-1}^{n}}{0.5h_i^{n+1}(h_i^{n+1}+h_{i-1}^{n+1})}\\
&+X_i^{n+1}\left(1+\frac{\sigma\Delta t\nu_{i-1}^{n}}{0.5h_i^{n+1}(h_i^{n+1}+h_{i-1}^{n+1})}+\frac{\sigma\Delta t\nu_i^{n}}{0.5h_i^{n+1}(h_{i+1}^{n+1}+h_i^{n+1})}\right)\\
&-X_{i+1}^{n+1}\frac{\sigma\Delta t\nu_i^{n}}{0.5h_i^{n+1}(h_{i+1}^{n+1}+h_i^{n+1})}=\\
&\qquad X_{i-1}^{n}\frac{(1-\sigma)\Delta t\nu_{i-1}^{n}}{0.5h_i^{n+1}(h_i^{n+1}+h_{i-1}^{n+1})}\\
&\qquad +X_i^{n}\left(1-\frac{(1-\sigma)\Delta t\nu_{i-1}^{n}}{0.5h_i^{n+1}(h_i^{n+1}+h_{i-1}^{n+1})}-\frac{(1-\sigma)\Delta t\nu_i^{n}}{0.5h_i^{n+1}(h_{i+1}^{n+1}+h_i^{n+1})}\right)\\
&\qquad +X_{i+1}^{n}\frac{(1-\sigma)\Delta t\nu_i^{n}}{0.5h_i^{n+1}(h_{i+1}^{n+1}+h_i^{n+1})}\qquad \text{for } 1<i<N_i,
\end{aligned}
\tag{4.11}
$$

and

$$
\begin{aligned}
&X_1^{n+1}\left(1+\frac{\sigma\Delta t\nu_1^{n}}{0.5h_1^{n+1}(h_2^{n+1}+h_1^{n+1})}\right)\\
&-X_2^{n+1}\frac{\sigma\Delta t\nu_1^{n}}{0.5h_1^{n+1}(h_2^{n+1}+h_1^{n+1})}=\\
&\qquad X_1^{n}\left(1-\frac{(1-\sigma)\Delta t\nu_1^{n}}{0.5h_1^{n+1}(h_2^{n+1}+h_1^{n+1})}\right)\\
&\qquad +X_2^{n}\frac{(1-\sigma)\Delta t\nu_1^{n}}{0.5h_1^{n+1}(h_2^{n+1}+h_1^{n+1})}-\frac{\Delta t}{h_1^{n+1}}F_b,
\end{aligned}
\tag{4.12}
$$

which is solved by means of the simplified Gaussian elimination.

4.2 Positive definite quantities

Many basic turbulent quantities are non-negative by definition, such as the turbulent kinetic energy, k, the turbulent dissipation rate, ε, or the macro length scale L. Their prognostic transport equations and the boundary conditions are formulated in such a way, that the non-negativity is mathematically ensured, see *Mohammadi and Pironneau* [1994]. The same is true for marine ecosystem models in which e.g. nutrients and phytoplankton are considered as concentrations which have to be non-negative as well.

It is thus necessary that the discretised forms of the physical equations retain the principle of non-negativity. This problem will be here investigated in more detail.

A typical model problem would be the following:

$$\partial_t X = P - QX, \quad P, Q > 0 \tag{4.13}$$

with X denoting any non-negative quantity, P a non-negative source term, QX a non-negative sink term, and t denoting time. P and Q may depend on X and t. It can easily be shown that with (4.13) X remains non-negative for any non-negative initial value X_0 and limited Q. For the k-equation and the kL equation, Q would be proportional to $k^{1/2}L^{-1}$ and for the ε equation, Q would be proportional to εk^{-1}.

A straight-forward, explicit in time discretisation of (4.13) would be the following:

$$\frac{X^{n+1} - X^n}{\Delta t} = P^n - Q^n X^n \tag{4.14}$$

with the superscripts denoting the old (n) and the new ($n+1$) time level and Δt denoting the time step. In this case, the numerical solution on the new time level would be

$$X_i^{n+1} = X_i^n(1 - \Delta t Q_i^n) + \Delta t P_i^n, \tag{4.15}$$

which is negative for a negative right hand side of (4.14) and

$$\Delta t > \frac{X^n}{X^n Q^n - P^n}. \tag{4.16}$$

Since it is computationally unreasonable to restrict the time step in such a way that (4.16) is avoided, a numerical procedure first published by *Patankar* [1980] is generally applied:

$$\frac{X^{n+1} - X^n}{\Delta t} = P^n - Q^n X^{n+1}, \tag{4.17}$$

which yields the always non-negative solution for X^{n+1},

$$X^{n+1} = \frac{X^n + \Delta t P^n}{1 + \Delta t Q^n}, \tag{4.18}$$

see also *Deleersnijder et al.* [1997]. Thus, the so-called quasi-implicit formulation (4.17) by *Patankar* [1980] is a sufficient condition for positivity applied in almost all numerical turbulence models. Given this, the commenting footnote made by *Patankar* [1980] on page 145 of his book is still justified:

> For many readers, this seemingly minor topic may turn out to be most valuable information in this book. In practical computations, it is quite common to encounter erroneous results such as negative mass

fractions and negative turbulence kinetic energy. These have such a devastating effect on the rest of the calculation and on the success of the iterations that they must be prevented at all costs. Fortunately, prevention is possible and easy.

Unfortunately, the use of the *Patankar* [1980] trick has the consequence that the numerical scheme is only of first order in time. It would be desirable to construct a higher-order scheme still guaranteeing positivity.

4.3 Conservation of energy flux

As shown in equation (2.24), the loss of mean kinetic energy into turbulence equals the shear production as source for the turbulent kinetic energy, see equation (2.31). The same principle holds for the buoyancy production when a transport equation for the buoyancy b is calculated. In a recent publication, *Burchard* [2002] demonstrated how a numerical scheme can be constructed which retains this physical principle also for the discrete solutions. For doing so, a simplified system of equations is considered. When neglecting horizontal transports, pressure gradients, and rotation, the transport equation for the along-wind velocity component is of the following form:

$$\partial_t \bar{u} - \partial_z(\nu_t \partial_z \bar{u}) = 0. \tag{4.19}$$

From (4.19), the budget of mean kinetic energy, $e_{kin} = \bar{u}^2/2$, is derived:

$$\partial_t e_{kin} - \partial_z(\nu_t \partial_z e_{kin}) = -\nu_t(\partial_z \bar{u})^2 = -P \tag{4.20}$$

with $P = \nu_t(\partial_z \bar{u})^2$. The buoyancy b is calculated by means of the following dynamic equation:

$$\partial_t b - \partial_z\left(\nu_t' \partial_z b\right) = 0. \tag{4.21}$$

By multiplying (4.21) with the coordinate z, a dynamic equation for the potential energy $e_{pot} = -zb$ is obtained:

$$\partial_t e_{pot} - \partial_z\left((-z)\nu_t' \partial_z b\right) = \nu_t' \partial_z b = -B. \tag{4.22}$$

The discretisation of the momentum equation is carried out according to the *Crank and Nicolson* [1947] scheme, see equation (4.7):

$$\frac{\hat{u}_j - u_j}{\Delta t} - \frac{\nu_{j+\frac{1}{2}} \frac{\bar{u}_{j+1} - \bar{u}_j}{z_{j+1} - z_j} - \nu_{j-\frac{1}{2}} \frac{\bar{u}_j - \bar{u}_{j-1}}{z_j - z_{j-1}}}{z_{j+\frac{1}{2}} - z_{j-\frac{1}{2}}} = 0 \tag{4.23}$$

with $\bar{u} = \sigma\hat{u} + (1-\sigma)u$, where $\hat{u}$ is the velocity value on the 'new' and u the velocity value on the 'old' time level, see figure 4.2. $z_{j+\frac{1}{2}}$ and $z_{j-\frac{1}{2}}$ denote the heights of the grid interfaces on which the turbulent quantities are located, see figure 4.1.

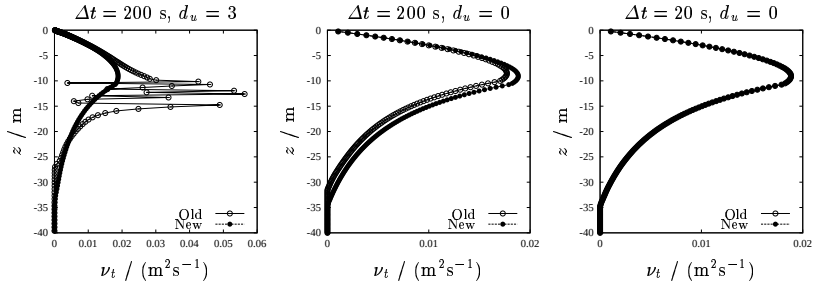

Fig. 4.3. Profiles of eddy viscosity ν_t obtained by applying the new (bullets) and the old (circles) discretisations of turbulence production terms. The three spatial and temporal discretisations 1. (left), 2. (middle) and 3. (right) have been used.

Multiplying (4.23) with $\frac{1}{2}(\hat{u}_j + u_j)$ leads to:

$$\begin{aligned}
&\frac{\hat{e}_j - e_j}{\Delta t} - \frac{\nu_{j+1/2}\frac{\bar{e}_{j+1}-\bar{e}_j}{z_{j+1}-z_j} - \nu_{j-1/2}\frac{\bar{e}_j-\bar{e}_{j-1}}{z_j-z_{j-1}}}{z_{j+1/2}-z_{j-1/2}} = \\
&\quad -\frac{1}{2}\nu_{j+1/2}\frac{\sigma(\hat{u}_{j+1}-\hat{u}_j)(\hat{u}_{j+1}-u_j)+(1-\sigma)(u_{j+1}-u_j)(u_{j+1}-\hat{u}_j)}{(z_{j+1/2}-z_{j-1/2})(z_{j+1}-z_j)} \\
&\quad -\frac{1}{2}\nu_{j-1/2}\frac{\sigma(\hat{u}_j-\hat{u}_{j-1})(\hat{u}_j-u_{j-1})+(1-\sigma)(u_j-u_{j-1})(\hat{u}_j-u_{j-1})}{(z_{j+1/2}-z_{j-1/2})(z_j-z_{j-1})} \\
&\quad =: -P^l_{j+1/2} - P^u_{j-1/2}.
\end{aligned} \tag{4.24}$$

Thus, the shear production should be discretised as follows (denoted by "New"):

$$\begin{aligned}
P_{j+1/2} &= \frac{P^l_{j+1/2}(z_{j+1/2}-z_{j-1/2}) + P^u_{j+1/2}(z_{j+3/2}-z_{j+1/2})}{z_{j+1}-z_j} \\
&= \nu_{j+1/2}\frac{(\bar{u}_{j+1}-\bar{u}_j)(\tilde{u}_{j+1}-\tilde{u}_j)}{(z_{j+1}-z_j)^2},
\end{aligned} \tag{4.25}$$

where $\tilde{u}_j = \frac{1}{2}(\hat{u}_j + u_j)$. For deriving (4.25), the discrete equation (4.24) was first multiplied with $(z_{j+1/2} - z_{j-1/2})$ in order to obtain layer-integrated discrete energy fluxes. When inserting the discrete production terms P^u_j and P^l_j into the discrete turbulent kinetic energy equation, they have to be divided by the thickness of the reference layers for turbulent kinetic energy.

In contrast to that, a "straight-forward" discretisation would be (from now on denoted as "Old"):

$$P_{j+1/2} = \nu_{j+\frac{1}{2}} \left[\frac{\hat{u}_{j+1} - \hat{u}_j}{z_{j+1} - z_j} \right]^2 . \tag{4.26}$$

An equivalent formalism can be applied to the buoyancy equation (4.21). With the formalism given above, the discretisation is of the following form:

$$\frac{\hat{b}_j - b_j}{\Delta t} - \frac{\nu_{j+1/2} \frac{\bar{b}_{j+1} - \bar{b}_j}{z_{j+1} - z_j} - \nu_{j-1/2} \frac{\bar{b}_j - \bar{b}_{j-1}}{z_j - z_{j-1}}}{z_{j+1/2} - z_{j-1/2}} = 0 \tag{4.27}$$

After multiplication with z_j and some algebraic operations, the following equation for the discrete potential energy $p_j = -z_j b_j$ is obtained:

$$\begin{aligned} &\frac{\hat{p}_j - p_j}{\Delta t} + \frac{\frac{1}{2}(z_{j+1} + z_j)\nu_{j+1/2} \frac{\bar{b}_{j+1} - \bar{b}_j}{z_{j+1} - z_j} - \frac{1}{2}(z_j + z_{j-1})\nu_{j-1/2} \frac{\bar{b}_j - \bar{b}_{j-1}}{z_j - z_{j-1}}}{z_{j+1/2} - z_{j-1/2}} = \\ &\quad \frac{1}{2}\nu_{j+1/2} \frac{\bar{b}_{j+1} - \bar{b}_j}{z_{j+1/2} - z_{j-1/2}} + \frac{1}{2}\nu_{j-1/2} \frac{\bar{b}_j - \bar{b}_{j-1}}{z_{j+1/2} - z_{j-1/2}} \\ &\quad =: -B^l_{j+1/2} - B^u_{j-1/2}, \end{aligned} \tag{4.28}$$

The terms on the right hand side are the discrete expressions for the sinks and sources of potential energy due to vertical mixing of density. In order to achieve total energy conservation, these have to be used for the discretisation of the turbulent buoyancy production. The discrete buoyancy production at $z_{j+1/2}$ would thus be of the following form:

$$B_{j+1/2} = -\nu_{j+1/2} \frac{\bar{b}_{j+1} - \bar{b}_j}{z_{j+1} - z_j}. \tag{4.29}$$

which again differs from a direct discretisation which would be formulated as:

$$B_{j+1/2} = -\nu_{j+1/2} \frac{\hat{b}_{j+1} - \hat{b}_j}{z_{j+1} - z_j}. \tag{4.30}$$

In the following the performance of these two discretisations for the shear production term will be tested with a simple wind entrainment experiment. This experiment by *Kato and Phillips* [1969] which simulates the entrainment of a turbulent surface boundary layer into stably stratified flow is described in detail in section 6.2.

In order to keep the mathematical model as simple as possible, a one-equation model is used with the TKE-equation (3.41), and an algebraic length scale equation of the following form:

$$L = \left(\frac{1}{\kappa(-z+z_0)} + \frac{1}{c\frac{k^{1/2}}{N}} \right)^{-1}, \tag{4.31}$$

where the first term is a length limitation near the surface given by the law of the wall and the second term is a length limitation due to the effect of stable stratification. The surface roughness parameter is here set to $z_0 = 0.1$ m and the von Kármán constant is given by $\kappa = 0.4$. The stability parameter c should depend on the stability functions c_μ and c'_μ and has been calibrated here to $c = 0.4$ such that it reasonably reproduces the mixed layer depth evolution for the wind entrainment experiment given by equation (6.1). This length scale parameterisation is similar to that of *Axell and Liungman* [2001] who used slightly different values for c.

The eddy viscosity is then calculated from the simple relations

$$\nu_t = c_\mu \frac{k^2}{\varepsilon}, \qquad \nu'_t = \frac{\nu_t}{P_r} \tag{4.32}$$

with $c_\mu = 0.09$ and the turbulent Prandtl number P_r from (3.109). For the numerical simulations, three different resolutions in time and space have been used:

1. A non-equidistant grid spacing with strong zooming towards the surface according to (4.1) and (4.2) with zooming coefficients $d_u = 3$ and $d_l = 0$ and the number of layers, $N_i = 200$. This results in a near-surface layer depth of $h_{N_i} = 0.008$ m and a near bed layer depth of $h_1 = 0.754$ m. The time step chosen here is $\Delta t = 200$ s.
2. An equidistant grid-spacing with $N_i = 200$ (resulting in layer thicknesses of 0.25 m) and $\Delta t = 200$ s.
3. An equidistant grid-spacing with $N_i = 200$ (resulting in layer thicknesses of 0.25 m) and $\Delta t = 20$ s.

The level of implicitness has been set to $\sigma = 0.6$ for the momentum and the buoyancy equation, a value slightly larger than the semi-implicit value 0.5 ensuring second-order accuracy in time, but which is also known for causing numerical instabilities. For the turbulent kinetic energy equation, a fully implicit time-stepping with $\sigma = 1$ has been chosen in order to further stabilise the model.

Figure 4.3 shows profiles of eddy viscosity ν_t obtained with the new energy-conserving discretisation of turbulence production terms (4.25) and (4.29) and the old not energy-conserving discretisation (4.26) and (4.30), using the three spatial and temporal resolutions 1. - 3. given above.

It is clearly seen that the old discretisation is numerically unstable in the region of maximum eddy viscosity for non-equidistant grid-spacing with long time steps of $\Delta t = 200$ s. In contrast to this, the new discretisation results in a stable and smooth solution.

For equidistant grid-spacing and large time steps of $\Delta t = 200$ s, the old method is numerically stable at the end of the run time, but significantly

underestimates the mixed layer depth obtained with high resolution. Only for equidistant grid spacing and small time steps of $\Delta t = 20$ s, the old method results in a final viscosity profile optically not distinguishable from the profile obtained with the new method.

For a more detailed discussion of the implications of this new numerical scheme, see *Burchard* [2002].

4.4 Boundary conditions

It would be a desirable property of a model to accurately reproduce relevant processes also for rather coarse vertical resolution. Only then, the integration of such a model into three-dimensional ocean models is justified. This is difficult near the boundaries, since large gradients can significantly reduce the performance of numerical models. Therefore, caution is needed when discretising the boundary conditions.

The Dirichlet-type bottom boundary condition for momentum, (3.57), is an example for a physical condition which has to be modified for the numerical discretisation, since the discrete velocity point nearest to the bottom is half a grid box away from the point where the boundary condition is defined. Furthermore, due to the logarithmic law, high velocity gradients are typical near the bed. Simply setting the discrete bottom velocity to zero, would therefore lead to large discretisation errors. Instead, a flux condition using bottom stresses is derived from the log-law discussed in section 3.2.3.

For the determination of the normalised bottom stresses

$$\frac{\tau_b^x}{\rho_0} = u_*^{bx} u_*^b, \tag{4.33}$$

$$\frac{\tau_b^y}{\rho_0} = u_*^{by} u_*^b \tag{4.34}$$

with the friction velocities $u_*^b = \sqrt{\tau_b/\rho_0}$ with $\tau_b = \sqrt{(\tau_b^x)^2 + (\tau_b^y)^2}$, assumptions about the structure of velocity inside the discrete bottom layer have to be made. We use here the logarithmic profile (3.51) derived from the law of the wall in section 3.2.3. Therefore, estimates for the velocities in the centre of the bottom layer can be achieved by:

$$u_b = \frac{u_*^{bx}}{\kappa} \ln\left(\frac{0.5h_1 + z_0^b}{z_0^b}\right), \tag{4.35}$$

$$v_b = \frac{u_*^{by}}{\kappa} \ln\left(\frac{0.5h_1 + z_0^b}{z_0^b}\right). \tag{4.36}$$

For $h_1 \to 0$, the original Dirichlet-type no-slip boundary conditions (3.57) are retained. Another possibility would be to specify the bottom velocities

u_b and v_b such that they are equal to the layer-averaged log-law velocities (see *Baumert et al.* [1989], *Baumert and Radach* [1992]). The calculation of this is however slightly more time consuming and does not lead to a higher accuracy.

For the discretisation of the turbulent quantities, the law of the wall has to be further exploited. For the k-kL model (see section 3.2.6), *Burchard and Petersen* [1999] found that it is accurate also for coarse vertical resolution, when the Dirichlet-type boundary conditions for k and L, (3.62) and (3.56), respectively, are directly discretised. In order to obtain this property also for k-ε models, the boundary conditions have to be formulated and discretised with care. This is necessary in order to cope with the asymptotical behaviour of the dissipation rate near vertical boundaries. In the following, the straightforward discretisations of the boundary conditions (3.63) and (3.66) will be discussed and their numerical performances compared to an analytical test case. The viscosities for the turbulent equations have to be averaged from ν_t values (placed at the same position as other turbulent quantities, see figure 4.1) in order to guarantee second-order accuracy for the discretisation of diffusion terms in the case of uniform grid spacing. In the standard discretisation used here, this is also applied to the surface and the bottom interval. The spatial accuracy of this standard discretisation of ε boundary conditions (3.63) and (3.66) will be tested by discretising the constant stress steady state boundary layer equations, see section 3.2.3.

The results for $\bar{u}$ are shown in figure 4.4 on a logarithmic scale. With the flux condition (3.66), the logarithmic profile of $\bar{u}$ is reproduced for all vertical resolutions, even if the boundary layer is resolved with three intervals only. With the Dirichlet-type boundary condition (3.63), an extremely fine vertical resolution is needed near the bottom in order to reproduce the analytical solution accurately. Only the bottom values for $\bar{u}$ are by definition identical with the analytical solutions, see equation (4.35). This fine resolution could only be achieved with the non-equidistant zooming (4.2) resulting in a height of the near bottom interval of only $0.003 z_0$. Such fine resolutions are not affordable in three-dimensional models. *Stelling* [1995] discussed the low accuracy of the standard discretisation of the Dirichlet-type boundary condition. He suggested to compute the first discrete eddy viscosity value for ε by $\nu_\varepsilon = u_*^4/(\sigma_\varepsilon \varepsilon)$, a relation which can be derived from the law of the wall with $P = \varepsilon$. A test computation carried out by *Burchard et al.* [1998] for the analytical test case discussed above shows the same high accuracy than achieved by the standard discretisation of the Neumann-type boundary condition (3.66). However, the *Stelling* [1995] approach does not work for stress free surface flow, because it assumes a no-flux condition for ε there. In contrast to the flux condition (3.66) this predicts unrealistically high near surface values for the eddy viscosity. Therefore, the use of the Neumann-type flux condition (3.66) seems to be preferable for k-ε model computations, see section 6.1.

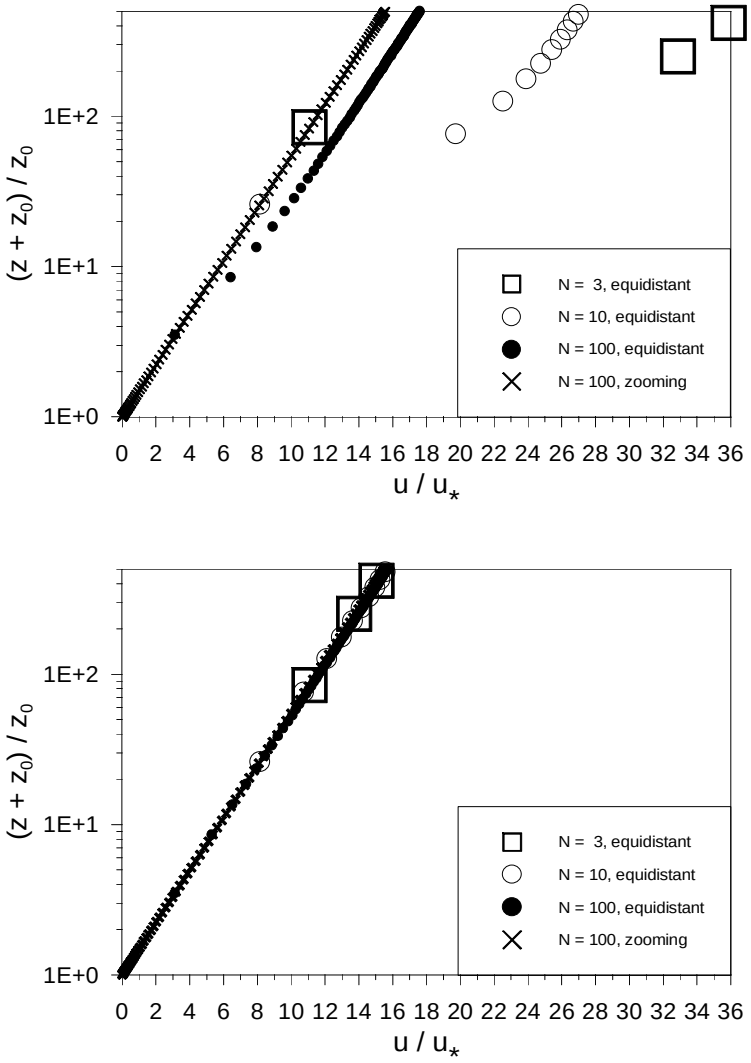

Fig. 4.4. Non-dimensional profiles of velocity for non-stratified boundary layer flow calculated with a k-ε model with different vertical resolution. Upper panel: Dirichlet-type boundary condition for ε, (3.63); Lower panel: Neumann-type boundary condition for ε, (3.66). This figure has been taken from *Burchard and Petersen* [1999].

It has been shown by *Burchard and Petersen* [1999] that with this boundary condition, the k-ε and the k-kL models are of similar accuracy also in the mixed layer (see figure 7.17).

Another approach has been suggested by *Baumert et al.* [1989] and was later used by *Burchard* [1995] and *Baumert et al.* [2000]. They averaged the log-law distribution of dissipation rate over the lowermost grid box and use this as boundary condition at $z = -H$. Since this location is half a grid box away from the centre of the lowermost grid box, this scheme can only be of first order in space.

5 The GOTM model

After presenting the mathematical equations for marine turbulence modelling in chapters 2 and 3 and their numerical discretisation in chapter 4, this all needs to be implemented in a computer code before it is of any practical use. Many of the physical and numerical features discussed in these chapters have indeed been implemented, tested and applied in recent years by the author of this book and his co-workers in the GOTM model. This model will briefly be described here in this chapter. For more information, see *Burchard et al.* [1999] or at `http://www.gotm.net` on the World Wide Web. All model simulations presented in chapters 6 and 7 have been carried out with GOTM.

Other examples for water column models which are freely available are for example PROBE (see *Svensson* [1998]) and the one-dimensional versions of the Princeton Ocean Model (POM, see *Blumberg and Mellor* [1987]) and COHERENS (see *Luyten et al.* [1999]).

5.1 General introduction

GOTM stands for *General Ocean Turbulence Model* and means that the model simulates small-scale turbulence and vertical mixing as far as possible in a general manner and without calibration to specific applications. This general character is underlined by the fact that the model is applied to scenarios in various regions, specifications and scales, such that the model is frequently verified (and unfortunately sometimes falsified as well). The model is modular such that refinements or extensions especially for the turbulence models, but also for the mean flow modelling can easily be carried out. The aim of generality is very ambitious, and there are always situations for which turbulence closures on a higher level would be required. GOTM is a one-dimensional model for the water column, which means that all horizontal gradients have to be either prognostically prescribed, parameterised or neglected. The turbulence module inside GOTM is organised such that it can be integrated into three-dimensional ocean or atmosphere models for calculating the vertical exchange coefficients. Observational data can be read in into GOTM such that – after interpolation to the temporal-spatial grid – they can be used as forcing or validation data. The model output is optionally

in ASCII or netCDF format, the latter being a binary format which can be read by various modern graphical packages.

Since April 1999, GOTM can be downloaded as FORTRAN77 or FORTRAN90/95 source code from the web site `http://www.gotm.net` on the World Wide Web, together with forcing and validation data, a report by *Burchard et al.* [1999], etc. The user group consists of more than 120 users world wide. Until May 2002, the web site had more than 10000 visitors (since June 1999). Apart from the author of the present study (`hans@gotm.net`), Karsten Bolding (`karsten@gotm.net`, Ispra), Manuel Ruiz Villarreal (`manuel@gotm.net`, Hamburg), Pierre-Phillipe Mathieu (`pp@gotm.net`, Reading), Georg Umgiesser (`georg@gotm.net`, Venice), Encho Demirov (`encho@gotm.net`, Bologna) and Lars Umlauf (`lars@gotm.net`, Lausanne) are co-authors of GOTM.

5.2 Treatment of physics

Standard transport equations for mean quantities are designed for horizontal velocity components, potential temperature, salinity and suspended matter. A general tracer algorithm is part of GOTM as well, allowing for easy implementation of biological models, if only the source and sink terms are known. Several terms which contain horizontal gradients need special treatment. The surface slopes which represent the barotropic pressure gradients can easily be determined by local observations or results from three-dimensional numerical models. It is also sufficient to prescribe a time series of near-bed velocity components for reconstructing the barotropic pressure gradient, see *Burchard* [1999]. The internal pressure gradient, which results from horizontal density gradients can be prescribed from observations or model results. Advective and horizontal diffusive terms are neglected in the velocity equations. Rotation, and vertical mixing (assuming that an eddy viscosity is known) do not pose any problems. For the active tracer equations it is especially the advective terms which are not easy to handle: There are three options: neglect (especially in the open ocean), relaxation to observations or prescription of observed horizontal gradients. In cases where the vertical velocity is known from observations or theoretical considerations, it can be used for vertical advection, see *Bolding et al.* [2000]. Standard relations derived from the law of the wall are used as surface and bottom boundary conditions, see section 3.2.3. At the sea surface, they have to be prescribed or calculated from meteorological observations with the aid of bulk formulae using the simulated or observed sea surface temperature. The suspended matter module is written so far for non-cohesive matter, but there are plans for refinements. The density is calculated by means of the UNESCO equation of state, either with the full version or linearisations of it. A somewhat exotic GOTM module simulates the interaction of sea grass canopies with turbulence and currents according to the method suggested by *Verduin and Backhaus* [2000].

In GOTM, the modelling of turbulence is carried out as described in chapters 2 and 3. It is based on the Boussinesq eddy viscosity assumption (3.19), with which the turbulent fluxes are proportional to the gradients of the transported quantities. By doing so, phenomena such as counter-gradient fluxes, which are relevant for convection scenarios, are however not reproducible. Another effect which is not considered is the direct effect of rotation on turbulent mixing, which is significant only for deep convection, see section 3.1.2. The proportionality factors between the fluxes and the gradients are the vertical exchange coefficients, which are calculated according to the Kolmogorov-Prandtl relation as product of three factors: a dimensionless stability function, a turbulent velocity scale and a turbulent macro length scale, see equation (3.24). The stability functions which are different for momentum and for tracers and which can depend on shear and stratification contain complex algebraic closures for the second moments, see section 3.1.3. For the calculation of the velocity scale and the macro length scale, various zero-, one- and two-equation models are included into GOTM. The k-ε (see section 3.2.5) and the k-kL model by *Mellor and Yamada* [1982] (see section 3.2.6) are the most well-known two-equation models inside GOTM. For these models some recent developments are considered. Furthermore, the generic two-equation model recently suggested by *Umlauf and Burchard* [2001] (see section 3.2.13) has been implemented into GOTM. Especially for the purpose of better comparison, also other types of models such as the K-profile parameterisation (KPP) model (see *Large et al.* [1994]) will be integrated into GOTM in the future.

One weakness of all turbulence models is the reproduction of internal mixing processes which are controlled by the dynamics of internal waves, see section 3.3.3. These are often produced non-locally by various complex processes not properly represented in three-dimensional models. In GOTM, we solve the problem by limiting the macro length scale by means of the buoyancy length and the turbulent kinetic energy by a constant minimum value, which acts as a tuning parameter. By doing so, background values for the eddy viscosity of the order of $10^{-5} \ldots 10^{-4}$ $\mathrm{m^2 s^{-1}}$ are obtained, see section 3.3.3.

5.3 Coupling with three-dimensional models

For the FORTRAN77- as well as for the FORTRAN90/95-version of GOTM, the turbulence modules are separated from the rest of the model such that an easy integration into three-dimensional circulation models is possible without changes in GOTM[1]. Inside the three-dimensional models, interfaces need

[1] A scale analysis by *Delhez et al.* [1999] shows that the advective terms and the horizontal diffusion terms in the TKE-equation are negligible compared to the other terms in this equation for a shelf sea simulation. This justifies the use of

to be installed which simply transfer the data structure of GOTM to that of the three-dimensional model. That might decrease the execution speed of specifically efficient three-dimensional models, but the experience with three-dimensional community models shows that this is generally no problem. Couplings between three-dimensional models and GOTM have so far been tested for MOM (Modular Ocean Model, Geophysical Fluid Dynamic Laboratory, Princeton, see *Bryan* [1969] and *Cox* [1984]), a classical Ocean General Circulation Model, with POM (Princeton Ocean Model, Princeton University, *Blumberg and Mellor* [1987]), a coastal model, with COHERENS (European Community, see *Luyten et al.* [1999]), a shelf sea model, with MOHID (Instituto Superior Técnico, Universidade Tecnica de Lisboa, Portugal, see *Martins et al.* [1998]) and with GETM (General Estuarine Transport Model, see *Burchard and Bolding* [2002]), both estuary models. These couplings are presently under further investigation.

5.4 Informatics

For obtaining the full spectrum of GOTM, a FORTRAN90/95-compiler, the program `Make` and the netCDF library are needed. GOTM runs under all UNIX and LINUX systems, but has also been used under WINDOWS-95 and later WINDOWS versions. For the documentation of the source code, the system `protex` is used, with the aid of which standard LaTeX text can be integrated into the code such that even complex mathematical formulae can be documented in a clear way. Since `protex` is a target in `Makefile`, the command `make doc` generates a LaTeX document of about 120 pages.

5.5 Applications

The most well-known GOTM application is the simulation of the mixed layer at Ocean Weather Station Papa in the Northern Pacific, see section 7.2, for which data of temperature profiles and meteorological parameters for a period of about 20 years are available. Typical shelf sea applications which include surface as well as bottom processes, are located in the Irish Sea (*Burchard et al.* [1998], see section 7.4.1) and the Northern North Sea (see *Burchard and Baumert* [1995], *Burchard and Petersen* [1999], *Bolding et al.* [2000]), see section 7.3.1, where FLEX (Fladenground-Experiment 1976) is the classical scenario. Some realistic estuarine scenarios have been simulated with GOTM as well, such as the Oosterschelde in The Netherlands and Knebel Vig in Denmark, see *Burchard et al.* [2000]. For some newer scenarios in the

one dimensional version of this equation inside a three-dimensional model. The situation could however be different in estuaries were strain-induced periodic stratification acts, see section 7.4.2.

North Sea (see section 7.3.2), the Liverpool Bay (see section 7.4.2) and lake Lago Maggiore (see section 7.5), observations of the turbulent dissipation rate have been made. Those could in principle be well reproduced by applying GOTM. For more details regarding the simulations of realistic scenarios with GOTM, see chapter 7. GOTM also contains some idealised scenarios such as the penetration of a mixed layer into a stably stratified water column by means of wind (Kato-Phillips experiment, see section 6.2) or cooling (Deardorff experiment, see section 6.3). Furthermore, GOTM is increasingly applied to estuaries, for which the idealised scenario `Estuary` with constant horizontal gradients of salinity is a helpful exercise.

5.6 User group

Without the users of GOTM, most of them working in Europe or North America, GOTM could have never become a well-tested and documented model. Through the regular contact between authors and users, the user-friendliness and the physical basis of the model could be significantly improved. Round mails are sent regularly by email to the GOTM user group (`users@gotm.net`) informing them about model innovations. Further motivation for improvements and extensions comes from the close connection between GOTM and the concerted action CARTUM (Comparative Analysis and Rationalisation of Second-Moment Turbulence Models), a brainstorming activity bringing together turbulence experts from all over the world.

6 Idealised test cases

In order to study the basic performance of boundary layer models, it is often advantageous to apply them first to idealised situations for which solutions are known from laboratory experiments or Large Eddy Simulation studies. This procedure does of course not guarantee that these models also perform sufficiently well for complex real-world problems. However, when the models already fail for such standard situations, it is almost certain that their performance in real-world situations is even worse.

Three idealised scenarios will be studied here in detail, which are open channel flow (see section 6.1), a wind-entrainment experiment motivated by the laboratory experiment by *Kato and Phillips* [1969], see section 6.2, and a convective penetration experiment motivated by laboratory experiments by *Willis and Deardorff* [1974], see section 6.3. The wind entrainment experiment in section 6.2 will be extensively used for the calibration of the buoyancy production related quantities $c_{3\varepsilon}$ for the k-ε model and E_3 for the k-kL model, see sections 6.2.1 and 6.2.2, and a stability analysis of various stability functions, see section 6.2.3. It should be noted that the wind entrainment experiment has already been used for studying the numerical stability of two different discretisations of the vertical velocity shear and the Brunt-Väisälä frequency, see section 4.3.

6.1 Channel flow

As basic comparative tests for the performance of k-ε and k-kL two-equation models, two steady state barotropic channel flow situations, including comparisons with data, have been chosen: A surface stress forced flow which induces a constant stress over the vertical (Couette flow) and a pressure gradient-driven flow (e.g., tidal or river flow). Empirical data and numerical model results are displayed in figure 6.1 in non-dimensional form. For a more extensive discussion see *Burchard et al.* [1998].

If surface stress is the only forcing for steady-state open channel flow, then a constant stress over the whole water column and a solution symmetric to mid-depth results for all models. It can be shown furthermore that $P = \varepsilon$ and $k = (u_*^b/c_\mu)^2$ hold everywhere, if molecular viscosity is neglected. The solution for the turbulent kinetic energy k implies that for a constant stability

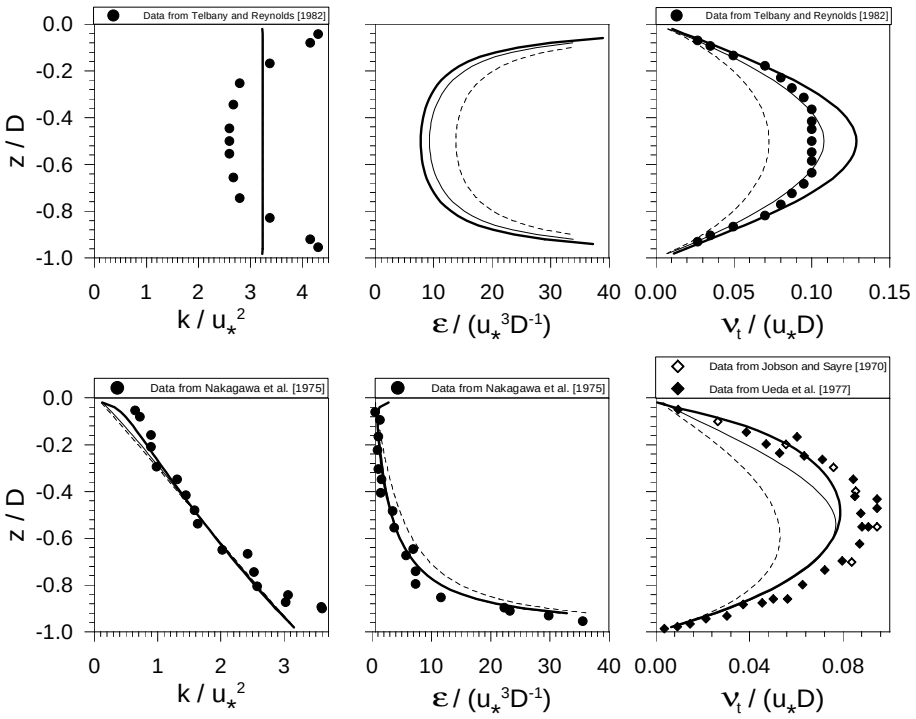

Fig. 6.1. Simulations of barotropic open channel flow with comparison against data. (top) Stress-driven Couette flow. Data from *Telbany and Reynolds* [1982] (turbulent kinetic energy and eddy viscosity). (bottom) Pressure gradient-driven flow. Data from *Nakagawa et al.* [1975] (turbulent kinetic energy and dissipation rate), *Jobson and Sayre* [1970], and *Ueda et al.* [1977] (both eddy viscosity). Bold line, k-ε model; thin line, k-kL model, triangle-shaped L_z, see equation (3.77); dashed line, Mellor-Yamada model, parabola-shaped L_z, see equation (3.76). This figure has been taken from *Burchard et al.* [1998].

function c_μ, the TKE will also be constant. In contrast to that, the empirical data in figure 6.1 strongly increase towards bottom and surface. This deficiency of the model is even given for the stability functions of *Canuto et al.* [2001] which depend on shear. This is because local equilibrium of turbulence ($P = \varepsilon$) directly implies $\alpha_M = (c_\mu^0)^3/c_\mu$, which means that α_M and c_μ are here not depending on the flow structure and are therefore constants. A solution to this problem could here be the introduction of wall proximity functions (see *Rodi* [1980]). Except at mid-depth where the measurements might not be reliable, the k-ε model result for eddy viscosity shows good agreement with the measurements. For the Mellor-Yamada model, a triangle-shaped length

scale L_z had to be prescribed rather than the usual parabolic-shaped one in order to achieve sufficient agreement between measurements and model simulations.

If the only forcing is a surface slope then a shear stress linearly decreasing from bottom to surface is resulting. As figure 6.1 shows, the models sufficiently reproduce the measured turbulent profiles with the limitations mentioned above: the increase of TKE towards the bottom is underestimated by all models. And for the Mellor-Yamada model, only a triangle-shaped L_z sufficiently reproduces the viscosity. It should be mentioned here, that a straight forward discretisation of the k-ε model with Dirichlet-type boundary conditions and an averaging of eddy viscosity for turbulent quantities would lead to an eddy viscosity profile with an unrealistic maximum near the surface (see also *Burchard et al.* [1998]). Therefore, the Neumann-type boundary conditions (equation (3.65) for k and equation (3.66) for ε) have been used here.

6.2 The Kato-Phillips experiment

In this experiment, a mixed layer induced by a constant surface stress penetrates into a stably stratified fluid with density increasing linearly down from the surface. The water depth is assumed to be infinite. *Price* [1979] suggested a solution for the evolution of the mixed-layer depth D_m based on a constant Richardson number

$$D_m(t) = 1.05 u_*^s N_0^{-1/2} t^{1/2}, \tag{6.1}$$

where u_*^s is the surface friction velocity and N_0 the constant initial Brunt-Väisälä frequency. Following several authors (see e.g. *Deleersnijder and Luyten* [1994], *Burchard et al.* [1998]) we transform this laboratory experiment to ocean dimensions with $u_*^s = 10^{-2}\ \mathrm{m\,s^{-1}}$ and $N_0 = 10^{-2}\ \mathrm{s^{-1}}$.

6.2.1 Calibration of $c_{3\varepsilon}$

First of all, the concept of the steady-state gradient Richardson number R_i^{st} can be validated by means of this entrainment experiment. The stability functions by *Canuto et al.* [2001], CA and CB, see section 3.1.3 are applied in combination with the k-ε model with values for R_i^{st} ranging from 0.2 to 0.8. Figure 6.2 shows the evolution of the entrainment depth, here defined as the distance of the lowermost point below the surface with a turbulent kinetic energy of $k > 10^{-5}\ \mathrm{J\,kg^{-1}}$. The results for the mixed layer depth are however not sensitive to the actual choice of this criterium, see also *Deleersnijder and Luyten* [1994]. It can be clearly seen that R_i^{st} determines the entrainment rate. For low values of R_i^{st}, a situation with $R_i > R_i^{st}$ in the region of the pycnocline is reached earlier with the consequence that turbulence is decaying and

the entrainment is reduced. For high values of R_i^{st}, $R_i < R_i^{st}$ holds over nearly the entire mixed layer and therefore mixing and entrainment is enhanced. It can be seen from this experiment that $R_i^{st} = 0.25$ seems to be a reasonable value for the steady-state Richardson number. With this choice, we can now fix $c_{3\varepsilon}$ for each set of stability functions (see table 6.1). Obviously, $c_{3\varepsilon}$ has the same value for equivalent non-equilibrium and quasi-equilibrium stability functions. In this framework, values of $c_{3\varepsilon}$ with a steady-state Richardson number of $R_i^{st} = 0.25$ can also be determined for the standard k-ε model with simple stability functions. If a turbulent Prandtl number according to equation (3.109) is chosen, then $c_{3\varepsilon} = -0.4$ results, which is in agreement to the findings of *Burchard et al.* [1998], who calibrated $c_{3\varepsilon}$ for an even simpler standard k-ε model with constant stability functions. The value of $R_i^{st} = 0.25$ cannot be reached by the model of *Kantha and Clayson* [1994]. We therefore use $R_i^{st} = 0.225$ for their model, which corresponds to the value for $c_{3\varepsilon}$ given in table 6.1. Negative values for $c_{3\varepsilon}$ are indeed confirmed for all sets of stability functions.

Model	c_μ^0	R_i^c	$c_{3\varepsilon}$	E_3
KC	0.094	0.235	-0.404	5.093
RH	0.121	0.615	-0.444	5.33
CA	0.077	0.847	-0.629	5.884
CB	0.094	1.02	-0.566	5.939

Table 6.1. Neutral stability function c_μ^0, critical Richardson number R_i^c, and buoyancy related parameters $c_{3\varepsilon}$ and E_3. $c_{3\varepsilon}$ is based on a steady-state gradient Richardson number of $R_i^{st} = 0.25$, only for the model KC $R_i^{st} = 0.225$ was used. E_3 is based on $R_i^{st} = 0.196$, see section 6.2.2.

As mentioned in section 3.2.11, the estimates for the steady-state Richardson number by *Shih et al.* [2000] do indeed indicate a value of $R_i^{st} \approx 0.25$ for the case of high Reynolds numbers.

Figures 6.3 and 6.4 show results for the mixed layer depth evolution and profiles of eddy viscosity and diffusivity and turbulent kinetic energy at 30 hours after the onset of surface stress. Eight different sets of stability functions have been used for these simulations, namely the models KC, RH, CA, CB and their quasi-equilibrium versions. For all simulations, the dissipation rate equation (3.67) has been used with the values for $c_{3\varepsilon}$ from table 6.1. It can be seen from figure 6.3 that the non-equilibrium version of the KC model (it should be noted that it is the quasi-equilibrium version which has been suggested by *Kantha and Clayson* [1994]) tends to strong oscillations and therefore produces useless results. This has already been reported by *Deleersnijder and Luyten* [1994] for the very similar model of *Mellor and Yamada* [1982]. In contrast to this, the quasi-equilibrium version of the KC model performs well, empirical and simulated mixed layer depth are very close to

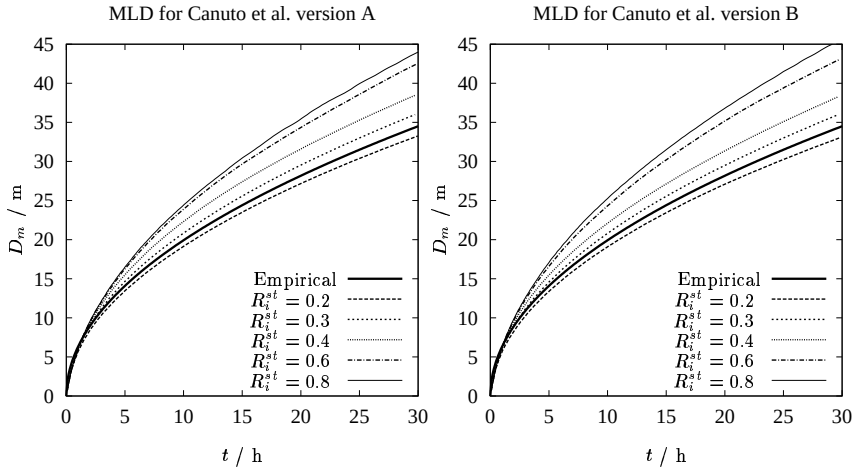

Fig. 6.2. Development of the mixed-layer depth (deepest point with $k > 10^{-5}$ J kg^{-1}) for the simulation of the Kato-Phillips experiment. Model results for the complete versions of the models A (left) and B (right) of *Canuto et al.* [2001] for various values of R_i^{st}.

each other (see figure 6.4). For a detailed investigation of this stability problem, see *Burchard and Deleersnijder* [2001] and section 6.2.3. It is however strange that the profile of turbulent kinetic energy shows a maximum in the lower part of the mixed layer. This effect has already been demonstrated by *Burchard et al.* [1998]. Turbulence measurements for this mixed layer experiment do unfortunately not exist. However, in a Large Eddy Simulation study of a similar experimental set-up (but with consideration of rotation) carried out by *Moeng and Sullivan* [1994] such a local maximum of k is not visible.

The other sets of stability functions all show (i) a perfect fit with the empirical curve of *Price* [1979], (ii) the expected monotone decrease of turbulent kinetic energy down from the surface and (iii) a numerically stable performance.

6.2.2 Calibration of E_3

As mentioned in section 3.2.11, the choice of $E_3 = 1.8$ does not allow for steady-state solutions for homogeneous shear layers, see also *Baumert and Peters* [2000] and *Burchard and Bolding* [2001]. This should have negative consequences for the performance of the k-kL model. Figure 6.5 shows the evolution of mixed layer depth D_m over 30 hours and the profile for the macro length scale L at the end of the simulation of the wind entrainment experiment calculated with the quasi-equilibrium stability functions by *Kantha and Clayson* [1994]. If no constraints to L are applied, the simulated mixed layer

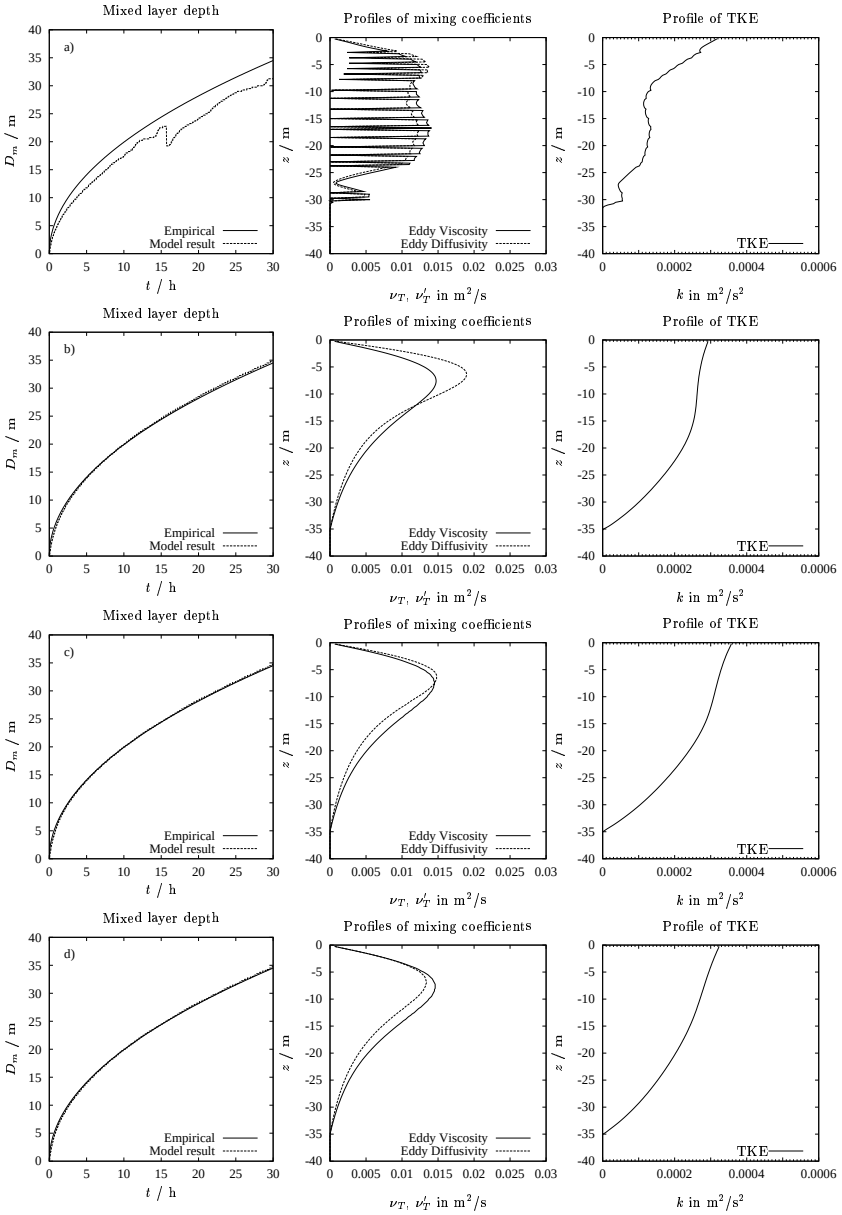

Fig. 6.3. Development of the mixed-layer depth (deepest point with $k > 10^{-5}$ J kg^{-1}) and profiles of mixing coefficients and turbulent kinetic energy after 30 hours for the simulation of the Kato-Phillips experiment. Model results for the complete versions of the a) model of *Kantha and Clayson* [1994], b) *Rodi* [1980] and *Hossain* [1980], c) model A of *Canuto et al.* [2001], and d) model B of *Canuto et al.* [2001]. For all model runs, $R_i^{st} = 0.25$ has been chosen, with the exception of the KC model, where $R_i^{st} = 0.225$ was used.

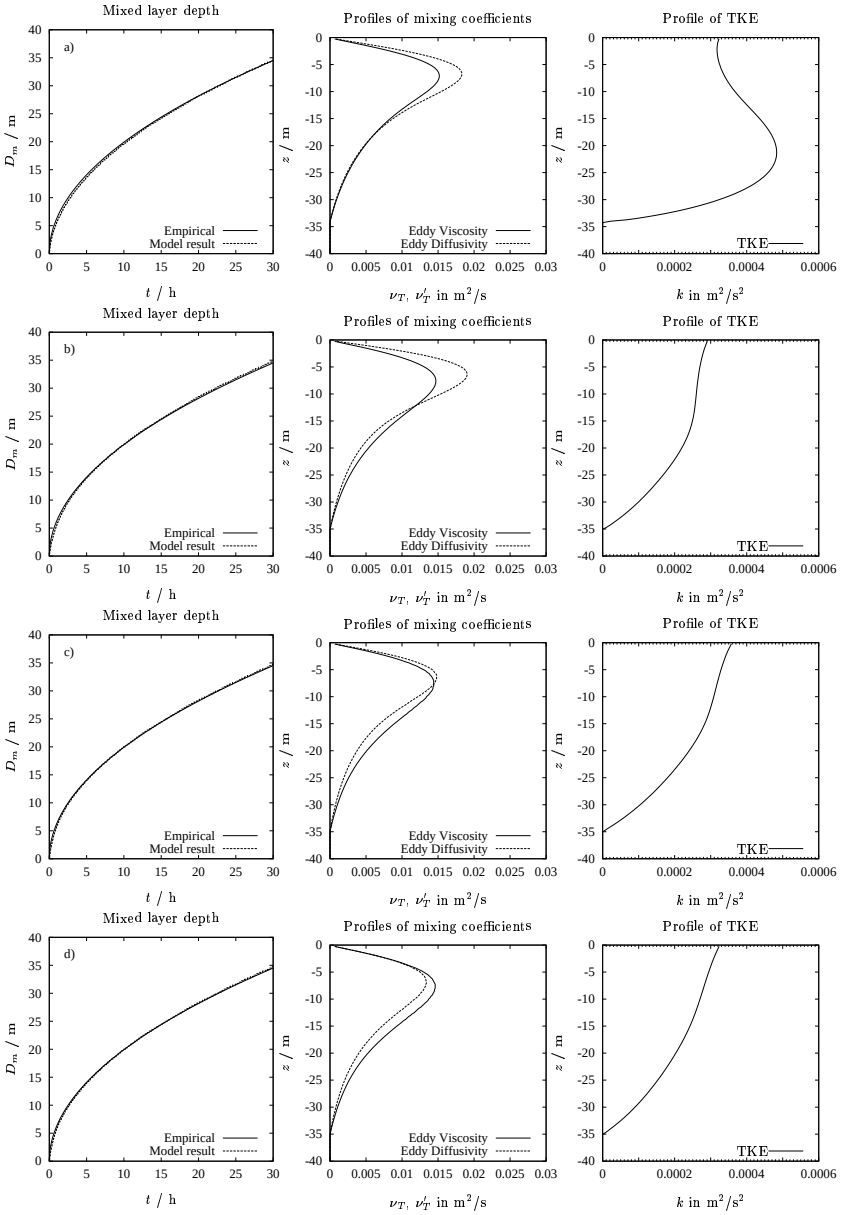

Fig. 6.4. Development of the mixed-layer depth (deepest point with $k > 10^{-5}$ J kg^{-1}) and profiles of mixing coefficients and turbulent kinetic energy after 30 hours for the simulation of the Kato-Phillips experiment. Model results for the quasi-equilibrium versions of the a) model of *Kantha and Clayson* [1994], b) *Rodi* [1980] and *Hossain* [1980], c) model A of *Canuto et al.* [2001], and d) model B of *Canuto et al.* [2001]. For all model runs, $R_i^{st} = 0.25$ has been chosen, with the exception of the KC model, where $R_i^{st} = 0.225$ was used.

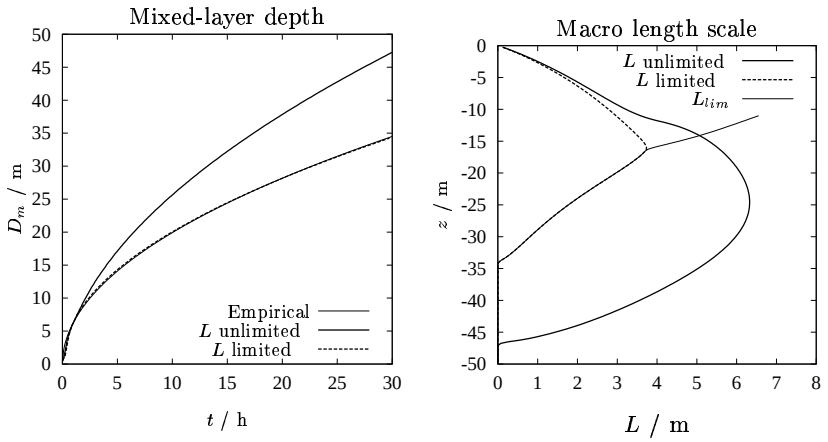

Fig. 6.5. Kato-Phillips experiment simulated with the k-kL model with and without length scale limitation (3.73). Displayed are here evolution of mixed layer depth and macro length scale L and the critical length scale L_{lim}.

depth D_m exceeds the estimate (6.1) by 38 %. It has to be concluded that this simulation result is physically unsound which is a consequence of the inadequate choice for E_3.

In the past, this problem has been circumvented by explicitly limiting the macro length scale by the constraint (3.73), see *Galperin et al.* [1988]. The resulting mixed layer depth evolution and the length scale profile are shown in figure 6.5 as well. The mixed layer depth is now nearly indistinguishable from the estimate (6.1), and, of course, the length scale has now the desired limitation due to stable stratification. However, this could only be achieved by replacing the dynamic equation for kL by the algebraic relation (3.73) in the lower half of the mixed layer.

R_i^{st}	$-B/\varepsilon$	$-G_H$	E_3	D_m
0.160	0.209	0.110	5.634	32.50 m
0.180	0.229	0.178	5.294	33.25 m
0.200	0.246	0.320	5.051	33.75 m
0.220	0.260	0.755	4.875	34.00 m
0.239	0.271	15.86	4.752	34.25 m

Table 6.2. Values of normalised buoyancy production $-B/\varepsilon$, buoyancy parameter $-G_H$, parameter E_3 and mixed layer depth D_m (in m) after 30 hour for the Kato-Phillips experiment as a function of the steady-state gradient Richardson number R_i^{st}. These values are for the *Kantha and Clayson* [1994] quasi-equilibrium stability functions.

It is expected also for the k-kL model equipped with the quasi-equilibrium stability functions of *Kantha and Clayson* [1994] that mixing increases with increasing steady-state gradient Richardson number R_i^{st} since for $R_i > R_i^{st}$ turbulence decays and vice versa. The wind entrainment experiment is performed for values of R_i^{st} ranging from 0.16 to 0.239 without the limit (3.73). Respective values for E_3 are given in table 6.2. Figure 6.6 and table 6.2 show that indeed higher values of R_i^{st} induce deeper mixing. For all choices of R_i^{st}, the mixed layer depth (defined as the uppermost position in the water column with $k < 10^{-5}\,\mathrm{J\,kg^{-1}}$) is slightly below the estimate (6.1), after 30 hours of entrainment ranging from 32.50 m ($R_i^{st} = 0.16$) to 34.25 m ($R_i^{st} = 0.24$) whereas (6.1) estimates 34.50 m. This is an indication that also for the k-kL model, $R_i^{st} = 0.25$ appears to be a suitable choice.

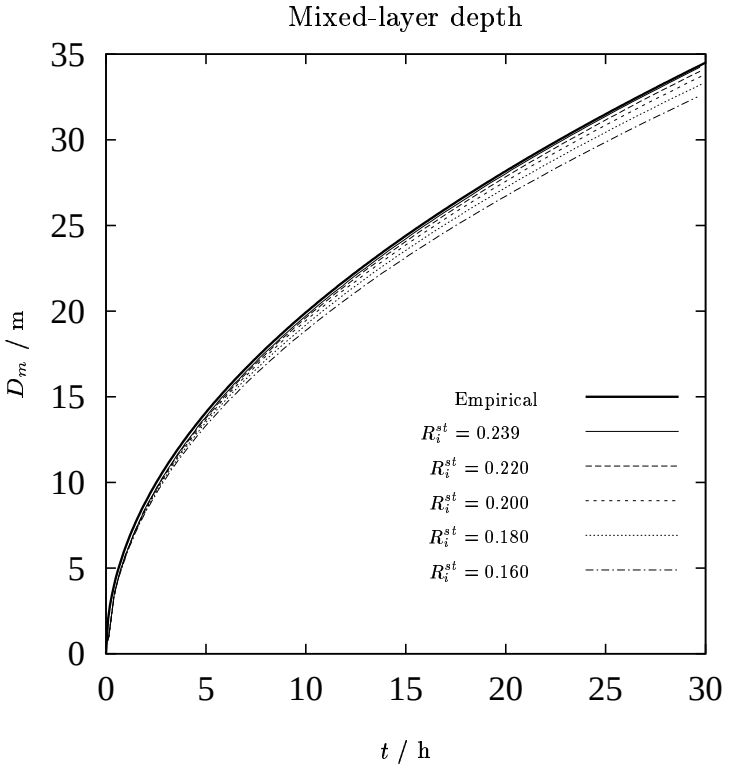

Fig. 6.6. Kato-Phillips experiment simulated with the k-kL model for various values of the steady-state gradient Richardson number R_i^{st} without limitation (3.73). Displayed is here the evolution of the mixed layer depth.

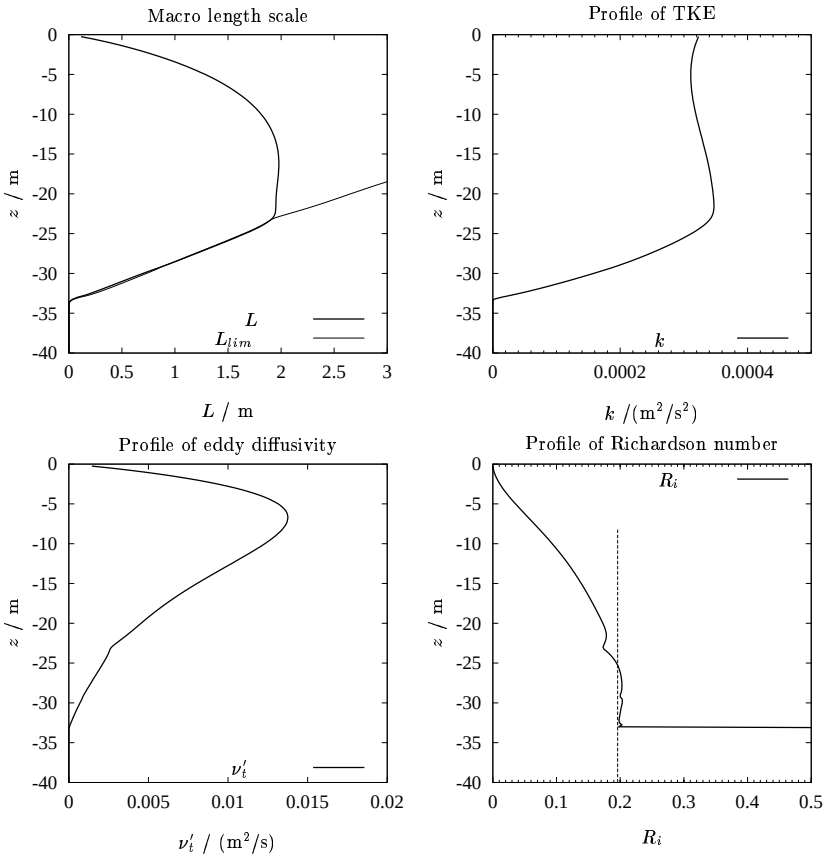

Fig. 6.7. Kato-Phillips experiment simulated with the k-kL model without length scale limitation and $R_i^{st} = 0.196$ (equivalent to $E_3 = 5.093$). Displayed are macro length scale L, turbulent kinetic energy k, eddy diffusivity ν_t' and gradient Richardson number R_i. For this simulation, the stability parameter $G_H \propto \alpha_N$ has been limited in accordance with (3.73).

Osborn [1980] actually gives an estimate of an upper bound for eddy diffusivity in the ocean pycnocline:

$$\nu_t' \leq 0.2 \frac{\varepsilon}{N^2}, \tag{6.2}$$

which may be transformed to the simple relation $P_b/\varepsilon \leq 0.2$ giving $E_3 \geq 5.8$ and is equivalent to $R_i^{st} = 0.152$ (see *Burchard* [2001a]). This low value for the steady-state Richardson number R_i^{st} might be a consequence of breaking internal waves acting as an additional source of turbulent mixing which is neglected in this study, see section 3.3.3.

For the case $R_i^{st} = 0.196$ which is equivalent to the length scale limitation under stable stratification, (3.73), some profiles will be inspected here since this leads to $G_H = G_H^{lim}$ for the steady-state solution in homogeneous shear layers being equivalent to (3.73). The E_3 values for $R_i^{st} = 0.196$ as computed from the non-equilibrium stability functions presented in section 3.1.3, are shown in table 6.1. The profile of the macro length scale L shows that this constraint is automatically fulfilled with high accuracy (see figure 6.7) although L is unconstrained. This is a consequence of the fact that the gradient Richardson number is close to the steady-state Richardson number in the entrainment region above the pycnocline. The local maximum of k in the lower half of the mixed layer is a specific effect of the *Kantha and Clayson* [1994] stability functions and has already been discussed by *Burchard et al.* [1998] for the *Galperin et al.* [1988] stability functions, see also section 6.2.1. Although the use of $R_i^{st} = 0.196$ is equivalent to the algebraic length scale limitation by *Galperin et al.* [1988], $R_i^{st} = 0.25$ might also here be the physically more correct value, see figure 6.6.

6.2.3 Stability of second-moment closures

Several authors have reported serious stability problems with the *Mellor and Yamada* [1982] stability functions, which are structurally similar to the *Kantha and Clayson* [1994] non-equilibrium stability functions as presented in section 3.1.3 (see *Deleersnijder and Luyten* [1994], *Burchard et al.* [1999] and *Villarreal* [2000]). It could be shown that the specific algebraic closure for the second moments was responsible for these instabilities, since they occurred as well, when using other length scale parameterisations such as the dissipation rate equation. A solution to the problem had already been suggested by *Galperin et al.* [1988] without discussing the stability problem: to use the so-called quasi-equilibrium version of the closure for the second moments which can be derived from the *Mellor and Yamada* [1982] model by additionally assuming local turbulence equilibrium only for the second-moment closure.

Burchard and Deleersnijder [2001] have recently further investigated this stability problem. The numerical experiments had the major purpose to test the hypothesis by *Deleersnijder and Luyten* [1994] that normalised stress u_*^2/k decreasing with increasing normalised shear α_M is responsible for the instabilities. Therefore, they conducted experiments with the original constraint on normalised shear, (3.34), and the more restrictive version (3.35). They carried out the following numerical simulations of this wind entrainment experiment[1]:

1. *Mellor and Yamada* [1982] stability functions with the old constraint (3.34) on $G_M \propto \alpha_M$ and the k-ε model.

[1] Besides the k-ε model simulations shown here, *Burchard and Deleersnijder* [2001] made equivalent simulations with the k-kL model. Apart from a slightly less stable behaviour of the k-kL model no significant differences could be observed.

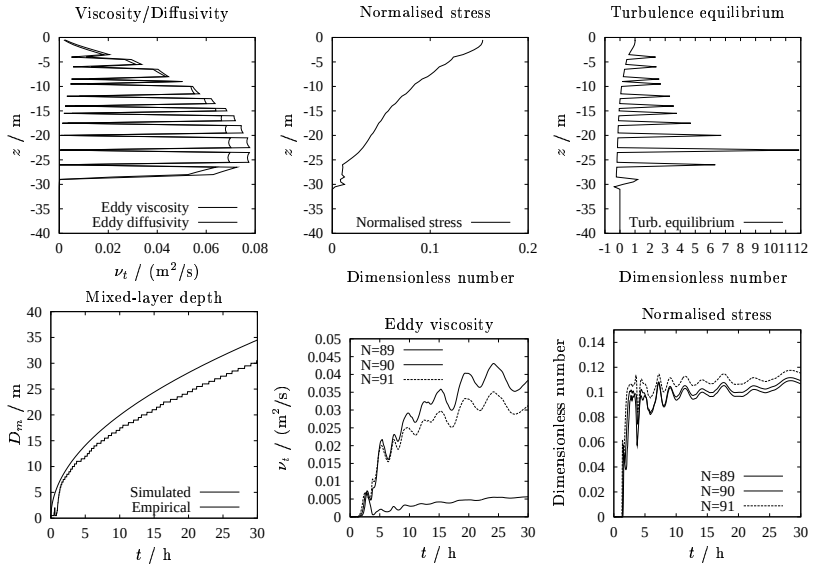

Fig. 6.8. Simulation results of run # 2 for the wind entrainment experiment by using the *Mellor and Yamada* [1982] stability functions with constraint (3.34) on $G_M \propto \alpha_M$. The turbulent length scale is here calculated with the ε-equation (3.67).

2. *Mellor and Yamada* [1982] stability functions with the new constraint (3.35) on $G_M \propto \alpha_M$ and the k-ε model.

The time step is $\Delta t = 100$ s, and the vertical spacing is 0.5 m. For both model runs, profiles after 30 h for eddy viscosity and diffusivity, normalised stresses and local turbulence equilibrium $(P+B)/\varepsilon$, and time series of mixed layer depth, eddy viscosity ν_t and normalised stress $0.5u_*^2/k$ are shown in figures 6.8 – 6.9. For the latter two time series, the values at discrete indices $N = 89$, $N = 90$ and $N = 91$ corresponding to 5.5, 5 and 4.5 m below the surface, respectively, have been recorded.

The stability functions by *Mellor and Yamada* [1982] with the original constraint on $G_M \propto \alpha_M$, see equation (3.34), show significant spikes in the eddy viscosity and diffusivity profiles, see figures 6.8 and 6.8. This has already been shown by *Deleersnijder and Luyten* [1994] for the k-kL model. Similar spikes are visible for the local turbulence equilibrium profiles. It is striking that except for the boundaries of the mixed layer, the expected value of $(P + B)/\varepsilon = 1$ is never close to unity. In contrast to that, the profiles of normalised stresses are rather smooth, with small spikes only. The same can be observed for the turbulent kinetic energy k and the shear stress u_*^2. This means that two solutions for the viscosity (and the shear) lead to the same shear stress, both of which are physically irrelevant, since they are far from the local turbulence equilibrium. The time series of viscosity at three adjacent

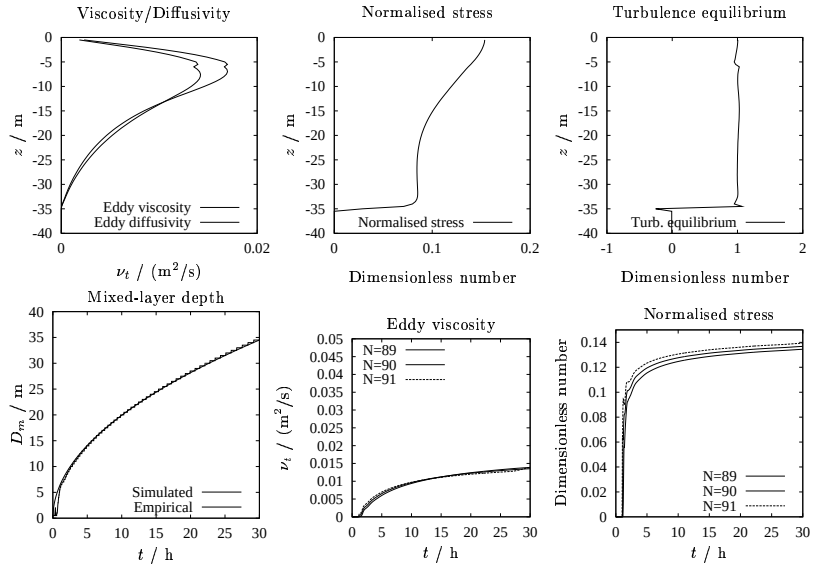

Fig. 6.9. Simulation results of run # 4 for the wind entrainment experiment by using the *Mellor and Yamada* [1982] stability functions with constraint (3.35) on $G_M \propto \alpha_M$. The turbulent length scale is here calculated with the ε-equation (3.67).

grid points about 5 m below the surface show that there are some oscillations in time with a period of the order of hours, much longer than the time step. The solution seems to be smooth in the beginning, but at a certain point, a bifurcation for the viscosities sets on (after about 3 hours).

When using the new constraint (3.35) instead of the original constraint (3.34), the bifurcation problem does not arise any more, and consequently, all profiles are rather smooth, see figure 6.9. Only a small spike remains for the viscosity/diffusivity profiles which can be removed by further decreasing the upper limit for $G_M \propto \alpha_M$. Since turbulence is close to local equilibrium over the whole mixed layer, it is not the original stability functions which are used here, but only the constraint (3.35). The k-ε model shows now a good agreement with the empirical mixed layer depth.

This confirms what has been discussed in section 3.1.5: that shear stress decreasing with increasing shear in the region of local turbulence equilibrium probably causes instabilities. It is shown here that this problem problem can be avoided by tightening up the constraint on $G_M \propto \alpha_M$. It can be seen from figure 6.3 that these problems do not arise for the RH, CA and CB stability functions, which also depend on stratification and shear. This physically correct behaviour can be explained by the fact that the local turbulence equilibrium is in a region where shear stress increases with shear, see figure 3.5. The use of the alternative constraint (3.35) is however not an adequate means for improving the performance of the *Mellor and Yamada* [1982] stability func-

tions, since they are simply replaced by a simple algebraic condition. Two alternatives should be considered instead: either using the quasi-equilibrium version of the *Mellor and Yamada* [1982] stability functions (which are identical with the *Galperin et al.* [1988] stability functions) or using physically more complete stability functions like those of *Canuto et al.* [2001] or also the *Rodi* [1980] and *Hossain* [1980] stability functions.

A third alternative had been applied to older versions of the Princeton Ocean Model and the Modular Ocean Model (pers. comm. George Mellor), which is to numerically filter $G_M \propto \alpha_M$ before using it for the calculation of the stability functions $S_M \propto c_\mu$ and $S_H \propto c'_\mu$:

$$G_M(i) \to 0.25 G_M(i-1) + 0.5 G_M(i) + 0.25 G_M(i+1). \tag{6.3}$$

Experiments with the implementation of this filter conducted by the author of this book did however not sufficiently remove these instabilities. Furthermore, the use of such a numerical filter is simply hiding the physical problems with this type of stability function and can therefore not be recommended.

6.3 The Willis-Deardorff experiment

Although strong convective events occur in the ocean only in a few areas, they are important for the ocean circulation and it is therefore desirable that they are sufficiently reproduced by turbulence closure models. A free convection simulation similar to the laboratory experiment carried out by *Willis and Deardorff* [1974], will be presented here. The scenario simulated here is the same as used by *Large et al.* [1994]. By means of a constant negative surface heat flux of 100 $\mathrm{W\,m^{-2}}$, a convective boundary layer is entrained into a stably stratified ocean with a surface temperature of 22^oC and a temperature gradient of 1^oC per 10 m. Shear and rotation are not present. For this free convection simulation recent Large Eddy Simulation (LES) data are available from *Mironov et al.* [2000].

Model	Entrainment depth
k-ε model, KC	12.5
k-ε model, RH	11.9
k-ε model, CA	12.2
k-ε model, CB	12.4
KPP	13.0
Convective adjustment	11.2

Table 6.3. Entrainment depth D_m in m for various mixed-layer models after three days of constant cooling with 100 $\mathrm{W\,m^{-2}}$, with an initially stable temperature gradient of 0.1 $\mathrm{K\,m^{-1}}$ and a constant salinity of 35 psu.

In table 6.3, the entrainment depth (position of minimum normalised turbulent heat flux) for all experiments after three days of cooling is given. Comparison is made to a simple scheme with convective adjustment (see *Bryan* [1969], the depth is here the height of the homogenised layer) and the K-profile parameterisation (KPP) model (see *Large et al.* [1994], the value has been estimated from their figure 1). As expected, all depths for the models presented here are between the latter two depths. The least deepening (11.2 m) is provided by the convective adjustment scheme which does not perform any active entrainment in terms of steepening the buoyancy gradient below the convective boundary layer.

Similarly to the wind entrainment experiment, see equation (6.1), also here a formula for the depth of the convective boundary layer D_m can be derived from simple energy conservation considerations, see *Turner* [1973]:

$$D_m = \left(\frac{2B_0}{N_0^2}t\right)^{1/2}, \tag{6.4}$$

which is based on convective deepening without entrainment. For a more general theory including entrainment, see *Zilitinkevich* [1991]. With the surface heat flux and the initial temperature structure given above, a surface buoyancy flux[2] of $B_0 \approx 0.52 \cdot 10^{-7}$ W kg^{-1} and a background stratification of $N_0^2 \approx 2 \cdot 10^{-4}$ s^{-2} result, leading with (6.4) to $D_m \approx 11.6$ m, which is close to the numerical value for convective adjustment given in table 6.3.

The turbulence models presented here mix deeper (11.9 m - 12.5 m) due to their capability of reproducing active entrainment. The fully empirical, non-local KPP model provides further deepening (13.0 m) of the convective boundary layer.

Furthermore, after 3 days of cooling profiles of various quantities are shown, normalised by the Deardorff convective velocity scale,

$$w_* = (B_0 D_m)^{1/3}, \tag{6.5}$$

the temperature scale,

$$T_* = (\nu_t' \partial_z T)|_{z=0} / w_*, \tag{6.6}$$

and the surface buoyancy flux B_0 versus z/D_m. Here D_m is the depth of the entrainment layer the base of which is defined as the height with the minimum heat flux.

The results for mean temperature, heat flux, dissipation rate and the variances $\langle\tilde{u}^2\rangle$, $\langle\tilde{w}^2\rangle$ and $\langle\tilde{T}^2\rangle$ (see equations (3.30) - (3.33)) and the respective results from the *Mironov et al.* [2000] LES study are shown in figure 6.10. In contrast to the idealised view of a mixed layer, the temperature profile in the

[2] The buoyancy flux varies slightly with time and the initial Brunt-Väisälä frequency varies slightly with depth because of the non-linearity of the equation of state.

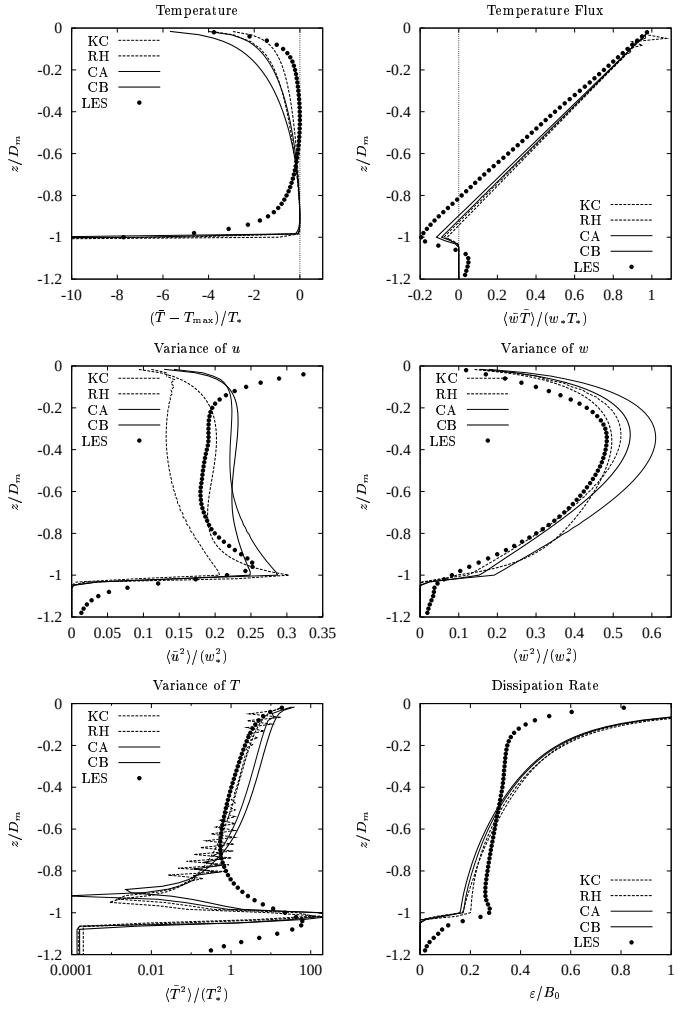

Fig. 6.10. Free convection experiment of *Willis and Deardorff* [1974]. Profiles of the normalised temperature profile $(\bar{T} - T_{\max})/T_*$, normalised temperature flux $\langle \tilde{w}\tilde{T} \rangle / w_* T_*$, and the normalised autocorrelations $\langle \tilde{u}^2 \rangle / w_*^2$, $\langle \tilde{w}^2 \rangle / w_*^2$, and $\langle \tilde{T}^2 \rangle / T_*^2$ and dissipation rate ε / B_0 calculated by using different models for the stability functions: *Kantha and Clayson* [1994] (KC), *Rodi* [1980] and *Hossain* [1980] (RH), *Canuto et al.* [2001] version A (CA), and *Canuto et al.* [2001] version B (CB). The model simulations are compared to LES simulations by *Mironov et al.* [2000].

convective boundary layer (CBL) resulting from the LES study has an almost symmetric structure with a super-adiabatic dense layer near the surface and a stably stratified layer at the base. A comparison with the temperature flux from the LES study shows that counter-gradient fluxes occur over a large portion (roughly $-0.8 \leq z/D_m \leq -0.4$) of the convective boundary layer. The counter-gradient fluxes can be explained by the structure of the vertical velocity fluctuations. Strong but narrow downdrafts transport cold near-surface water down, causing compensating weak updrafts bringing warmer water up (see e.g. *Zilitinkevich et al.* [1999]). In a recent study of convective turbulence in a small Swiss lake, *Jonas et al.* [2002] concluded that the cold water at the base of the CBL is not entrained from the underlying thermocline, but supplied by the strong downdrafts from the super-adiabatic surface layer. This view is further supported by the fact that the cold stratified layer at the base of the CBL vanishes in the presence of a mean shear which might destroy the structure of up- and downdrafts (see *Jonas et al.* [2002]).

From figure 6.10, three shortcomings of the two-equation models are obvious:

1. Counter-gradient fluxes are not included in the model because of its inherent down-gradient approximation. Therefore, temperature profiles of LES and turbulence closures are principally different. This suggests that non-local processes are important here.
2. The height of the active entrainment layer is underestimated by the turbulence closure models. This can best be seen in the profiles of $\langle \tilde{w}\tilde{T} \rangle$ and $\langle \tilde{T}^2 \rangle$. Potential reasons could here be the down-gradient approximation for the turbulent kinetic energy flux and the fact that turbulent transport of $\langle \tilde{w}\tilde{T} \rangle$ and $\langle \tilde{T}^2 \rangle$ is neglected. It can be seen from figure 6.11 that the TKE-diffusion term is qualitatively reproduced by the model (here CA), but underestimated by a factor of approximately 2.
3. The profile of $\langle \tilde{u}^2 \rangle$ near the surface suggests that the turbulent transport of this quantity should not be neglected here. Otherwise, the positive flux of $\langle \tilde{u}^2 \rangle$ through the surface as suggested by the LES simulations cannot be properly prescribed. Similarly, the temperature variance $\langle \tilde{T}^2 \rangle$ lacks vertical diffusion at the base of the convective mixed layer where the profile from the present closures tend to zero when the mean temperature gradient vanishes.

Despite these problems, numerical simulations of convective turbulence with two-equation models including the down-gradient approximation result in generally good agreement with field data, see the study by *Stips et al.* [2001] and the discussion in section 7.5.

It should be noted that *Canuto et al.* [1994] obtained a good agreement between LES data and simulation results for a free convection experiment with a full Reynolds closure model using dynamic transport equations for $\langle \tilde{w}\tilde{T} \rangle$, $\langle \tilde{T}^2 \rangle$, $\langle \tilde{w}^2 \rangle$, $\langle \tilde{u}^2 \rangle$ and ε including complex algebraic closure schemes for all relevant third moments. It should be the aim of future work to find a

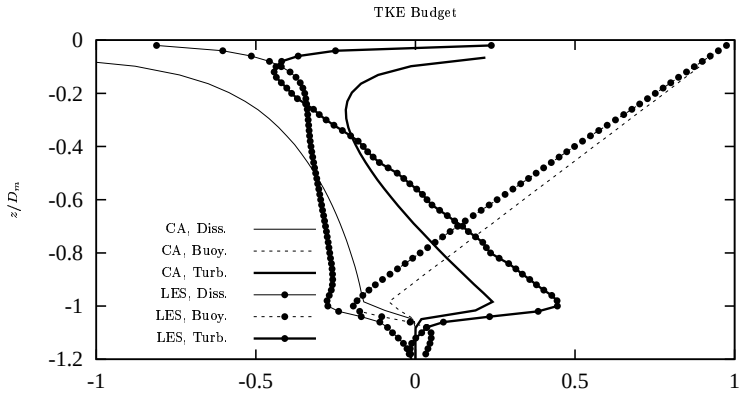

Fig. 6.11. Budget of the TKE equation calculated from the CA model compared to LES data from *Mironov et al.* [2000]. Diss: turbulent dissipation rate; Buoy: buoyancy production; Turb: turbulent transport. For the LES data, turbulent and pressure transport are added together here. All terms are normalised with the surface buoyancy flux B_0, the height z is normalised with the entrainment layer depth D_m.

reasonable compromise between this complex model by *Canuto et al.* [1994] and the two-equation models presented here, in terms of both, efficiency and predictability.

7 Oceanic and limnic applications

7.1 Introduction

In this chapter, the turbulence closure schemes developed and discussed in chapters 2 - 6 are finally applied for simulating real world scenarios observed by means of in-situ measurements. All these simulations have been described in more detail in journal publications of which the author of this book is a co-author. In the framework of this study it is not possible to describe all interesting details of the field campaigns and the model simulations. The most important features are shown here, but for details, the reader is referred to the original publications.

For most model simulations in this chapter, one certain model has been used. It is the k-ε model as described in section 3.2.5 in combination with the algebraic second-moment closure by *Canuto et al.* [2001]. A steady-state Richardson number of $R_i^{st} = 0.25$ is used, for a discussion, see section 6.2.1. As simple internal mixing parameterisation a limitation of k and ε according to equations (3.73) and (3.134) has been chosen as discussed in section 3.3.3.

There are a lot of calculations to be made outside the actual water column model. The surface fluxes have to be derived from meteorological observations by means of bulk formulae. Here, the formulae of *Kondo* [1975] are mainly in use. Due to the uncertainties of the meteorological observations and the bulk formulae, it is however always difficult to determine which portion of the heat content in the water column is due to surface fluxes and which is due to lateral advection. When bed friction is important, the bed roughness has to be determined. This can most accurately be done by fitting near-bed high resolution Acoustic Doppler Current Profilers (ADCP) to a logarithmic velocity profile, see equation (3.51) such that thus friction velocity and bed roughness are estimated.

According to *Paulson and Simpson* [1977] the radiation I in the upper water column may be parameterised by

$$I(z) = I_0 \left(a e^{-\eta_1 z} + (1-a) e^{-\eta_2 z} \right) . \tag{7.1}$$

Here, I_0 is the albedo corrected radiation normal to the sea surface. The weighting parameter a and the attenuation lengths for the longer and the shorter fraction of the short-wave radiation, η_1 and η_2, respectively, depend

on the turbidity of the water. *Jerlov* [1968] defined 6 different classes of water from which *Paulson and Simpson* [1977] calculated the weighting parameter a and the attenuation coefficients η_1 and η_2. It should however be noted that these classes are idealisations. Natural waters have attenuation coefficients which are highly variable in time and space due to phytoplankton and suspended matter concentrations.

During some of the field campaigns simulated below, observations of turbulent dissipation rate have been carried out. In contrast to measurements of mean flow properties such as flow velocity, temperature and salinity, turbulence observations are not yet standard. Therefore, the basic principle of such dissipation rate measurements as they have been introduced into oceanography by *Osborn* [1974] is briefly discussed here. The technique which has been used in the field studies presented below is based on small-scale vertical shear measurements by means of a shear probe mounted on a freely rising or freely falling profiler. The shear probe itself consists of an axially symmetric airfoil of revolution mounted at the end of a cylindrical shaft. The operation principle of the airfoil shear probe has been described in detail by *Prandke and Stips* [1998]:

> The mean velocity due to the profiling speed is aligned with the axis of revolution. While the probe is not sensitive to axial forces, the cross-stream (transverse) components of turbulent velocity produce a lifting force at the airfoil. A piezoceramic beam embedded within the airfoil made of rubber material senses the lift force. The output of the piezoceramic element is a voltage proportional to the instantaneous cross-stream component of the velocity field.

When the small-scale shear $\partial_z \tilde{u}$ is estimated from the voltage output, the dissipation rate ε can be calculated according to its definition, see equation (2.32). Since only one component of the vertical shear is observed with shear probes, the local isotropy assumption for the dissipative scales has to be made in order to extrapolate to the complete dissipation rate:

$$\varepsilon = 7.5\,\nu \left\langle (\partial_z \tilde{u})^2 \right\rangle . \tag{7.2}$$

The ensemble averaging procedure needed for calculating ε is replaced by spatial and temporal filtering. This is justified by making the ergodic assumption.

Two types of shear probes are used in the field studies discussed below, the FLY shear probe operated by the School of Ocean Sciences in Bangor, Wales and the MST shear probe operated by the Joint Research Centre in Ispra, Italy and the ISW Wassermeßtechnik Dr. Hartmut Prandke in Petersorf, Germany. They are different in many details, the major difference being the bigger size of the FLY shear probe and the profiler on which it is mounted. This bigger size makes the FLY shear probe on one hand more robust against disturbances from surface waves, cable oscillations and ship movements, but

also results in a more difficult resolution of the smallest dissipative eddies when the level of turbulence is high. For a detailed discussion of these different instruments, see *Prandke and Stips* [1998] and *Dewey et al.* [1987].

All simulations discussed below are carried out with the water column model GOTM (General Ocean Turbulence Model). The scenarios including all data are available from the address `http://www.gotm.net`. For details concerning the GOTM model, see chapter 5.

Two classical scenarios without micro-structure observations will be simulated in the following and four more recent scenarios with observations of the turbulent dissipation rate obtained with FLY or MST shear probes. The classical scenarios are Ocean Weather Station Papa in the Northern Pacific Ocean (see section 7.2), a mixed layer scenario with observations of temperature profiles in the upper 250 m during more than 20 years[1], and the Fladenground Experiment 1976 in the Northern North Sea (see section 7.3.1), with observations of temperature profiles for the full water column during spring warming. These two scenarios have been used by several authors for the validation of various mixed layer models. They demonstrate how the temperature structure in the water column reacts on turbulent mixing, but do not validate the turbulence models directly. Therefore, the scenarios with turbulence micro-structure measurements are investigated here as well. The oldest is the 1993, 24-hour stratified and tidally forced scenario in the Western Irish Sea (see section 7.4.1), which has already been used by some authors for model validations. The other three scenarios have only been simulated once (with the GOTM model) so far: the Northern North Sea 1998 PROVESS scenario with tidally induced turbulence in the bottom boundary layer and wind induced turbulence in the surface boundary layer during autumn cooling (see section 7.3.2), the Liverpool Bay 1999 scenario with turbulence generated by strain-induced periodic stratification (see section 7.4.2) and (adding some more generality to the title of this book) the 1995 Lake Lago Maggiore scenario with convective turbulence mainly generated by surface cooling (see section 7.5).

7.2 Northern Pacific Ocean

For the Northern Pacific, long term observations of meteorological parameters and temperature profiles are available. The station Papa at 145°W, 50°N has the advantage that it is situated in a region where the horizontal advection of heat and salt is assumed to be small. Various authors used these data for validating turbulence closure schemes (*Denman* [1973], *Martin* [1985], *Gaspar et al.* [1990], *Large et al.* [1994], *Kantha and Clayson* [1994], *D'Alessio et al.* [1998], *Burchard et al.* [1999], *Villarreal* [2000], *Axell and Liungman* [2001]). As for any realistic oceanic test case, also other factors than the choice of

[1] Simulations during one year will be shown here only.

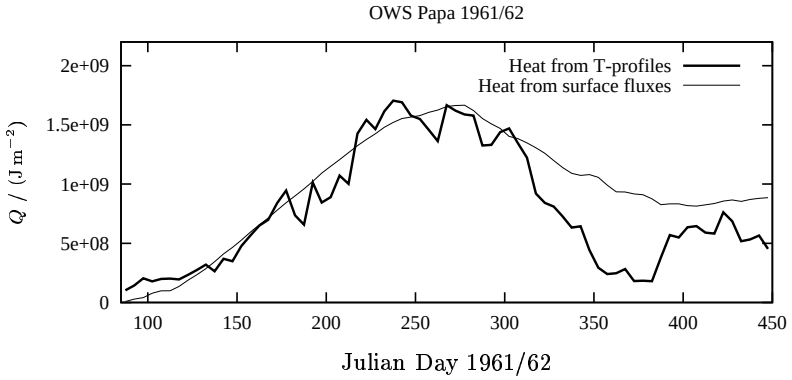

Fig. 7.1. Relative heat content Q of the water column at OWS Papa from March 1961 to March 1962. Bold line: 5 day means of heat content as calculated from measured temperature profiles. Thin line: 5 day means of heat content as calculated from surface heat fluxes.

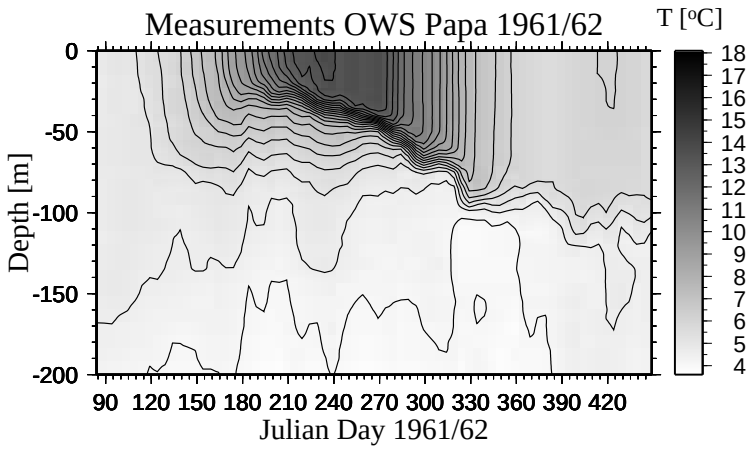

Fig. 7.2. Temperature evolution for OWS Papa in the Northern Pacific Ocean from March 1961 to March 1962 from CTD measurements.

the mixed layer model play an important role for the agreement between the model results and the measurements. First of all, the momentum and heat fluxes at the sea surface are never available as direct observations, but are calculated using bulk formulae. Measurements such as fractional cloud cover are never exact. Furthermore, horizontal advection of heat and salt, which is neglected in one-dimensional water column models, can strongly influence the measured profiles of temperature and salinity. And, maybe the

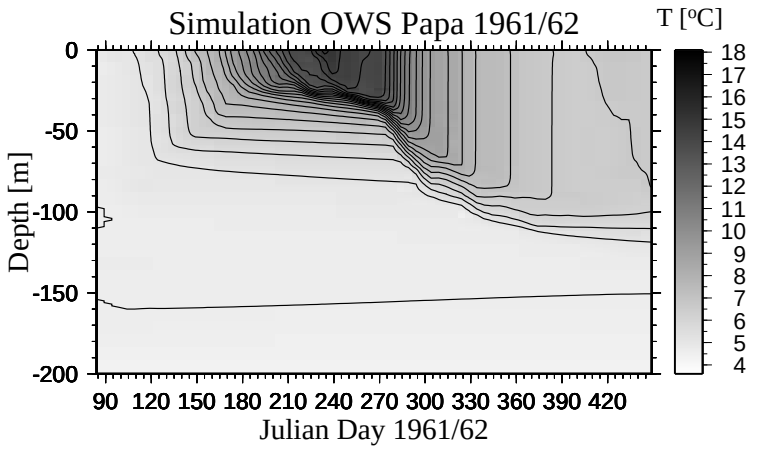

Fig. 7.3. Temperature evolution for OWS Papa in the Northern Pacific Ocean from March 1961 to March 1962. Results of the simulation with the version A of the *Kantha and Clayson* [1994] model with the stationary gradient Richardson number set to $R_i^{st} = 0.225$.

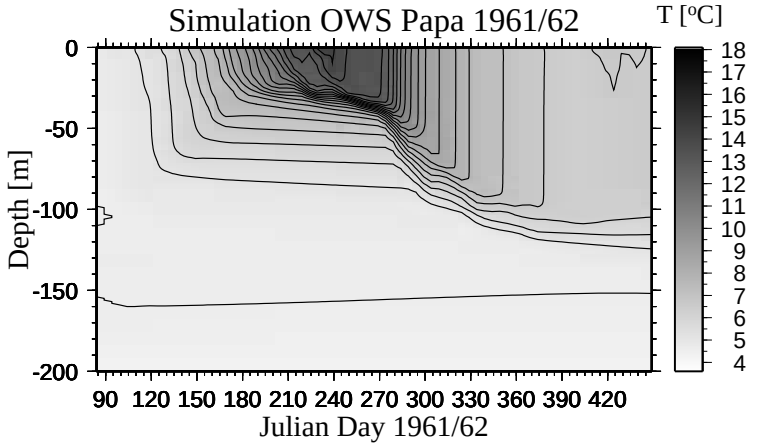

Fig. 7.4. Temperature evolution for OWS Papa in the Northern Pacific Ocean from March 1961 to March 1962. Results of the simulation with the version A of the *Canuto et al.* [2001] model with the stationary gradient Richardson number set to $R_i^{st} = 0.25$.

most important, the bulk formulae for the parameterisation of cross surface fluxes of momentum, heat and fresh water are strictly empirical.

The way how bulk formulae for the surface momentum and heat fluxes (see equations (3.59) and (3.60)) have been used here is discussed in detail in *Burchard et al.* [1999]. The relative heat content of the upper 250 m of the water column from temperature profiles and surface heat fluxes between March 1961 and March 1962 is shown in figure 7.1. Until beginning of November 1961 (around day 310), the agreement between the curves is sufficient enough for allowing for a one-dimensional simulation. Afterwards, cold water is horizontally advected, a process described in detail by *Large et al.* [1994].

For mixing below the thermocline, an internal wave and shear instability parameterisation as suggested by *Large et al.* [1994] has been used.

Figures 7.3 and 7.4 show results of the model simulations with the stability functions of *Kantha and Clayson* [1994] and *Canuto et al.* [2001], respectively, in comparison to measured temperature profiles (figure 7.2). The overall temperature evolution is well simulated by both models. A more detailed comparison between measurements and the two different model simulations of temperature profiles is shown in figure 7.5. Until day 210, the agreement between both simulations and the observations is fairly good. Then, around day 240, the models predict a too shallow mixed layer, obviously due to wrong surface fluxes or strong advective events such as downwelling, see figure 7.1, where a mismatch between the heat content of the water column and the accumulated surface heat fluxes is evident around day 240. It can be seen as well that the *Kantha and Clayson* [1994] model predicts a slightly shallower mixed layer than the *Canuto et al.* [2001] model. This has the consequence that the *Kantha and Clayson* [1994] model overpredicts the SST during summer (days 210 - 280 see figure 7.6). Until day 280, the r.m.s. error for SST between both simulations and the observations is rather small, 0.36 K for the *Canuto et al.* [2000] and 0.33 K for the *Kantha and Clayson* [1994] model. However, the SST evolution strongly depends on the internal wave parameterisation, and thus these r.m.s. errors are not discriminative for the quality of the turbulence models. It should be noted that exactly the parameters of *Large et al.* [1994] have been used for this, other than by *Kantha and Clayson* [1994] who had (while applying a kL instead of an ε equation) to use a background diffusivity 5 times higher in order to predict the SST realistically. This leads however to a thermocline too diffusive compared to measured temperature profiles (see *Burchard et al.* [1999]).

As a final comparison, the standard k-ε model with simple stability functions from equations (3.108) and (3.109) is applied to the OWS Papa scenario. As discussed in section 6.2.1, a value of $c_{3\varepsilon} = -0.4$ has been chosen in order to reach a steady-state Richardson number of $R_i^{st} = 0.25$. Here, only the SST evolution is shown in relation to observations (see figure 7.7). It can be seen that this standard k-ε model performs similarly to the other two, more com-

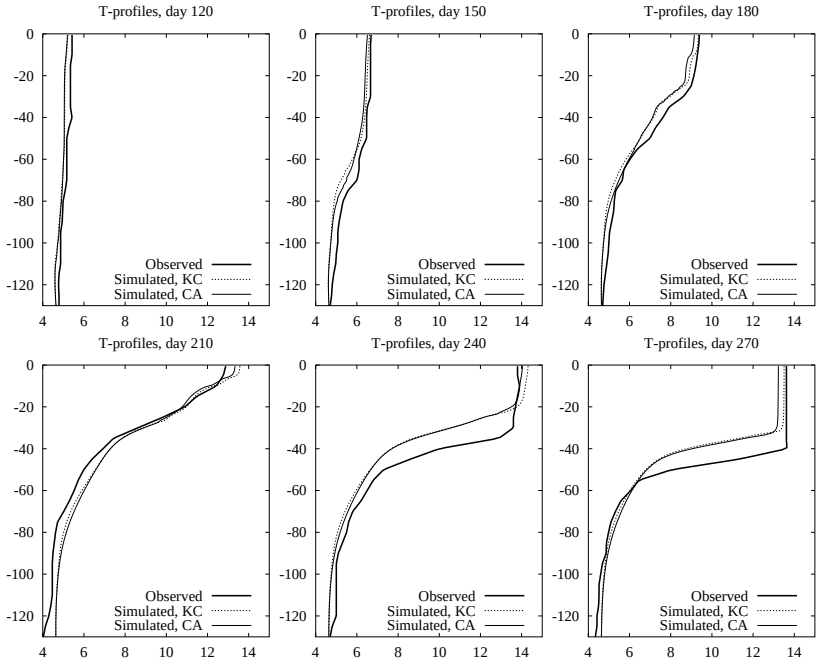

Fig. 7.5. Measured and simulated temperature profile at station OWS Papa during spring and summer 1961. The simulations were carried out with the quasi-equilibrium version of the *Kantha and Clayson* [1994] model with the stationary gradient Richardson number set to $R_i^{st} = 0.225$ and the version A of the *Canuto et al.* [2001] model with the stationary gradient Richardson number set to $R_i^{st} = 0.25$.

plex models. The agreement between measured and simulated SST is even better for this model.

Altogether, three models have been finally used for simulations of the Ocean Weather Station Papa observations: the quasi-equilibrium version of the *Kantha and Clayson* [1994], the full version of the *Canuto et al.* [2001] model, and the empirical second-moment closure provided by the standard k-ε model. The result is that the *Canuto et al.* [2001] model mixes slightly deeper than the *Kantha and Clayson* [1994] model, maybe due to the smaller steady-state gradient Richardson number which had to be chosen for the latter model. Too shallow mixed layers computed by so-called differential mixed layer models (defined in contrast to bulk models which average over the entire mixed layer) have been reported by *Martin* [1985] who used among others the OWS Papa data for comparing various models. He made too small critical Richardson numbers responsible for this phenomenon and could obtain acceptable model results at OWS Papa for increasing the critical Richardson number to $R_i^c = 0.3$.

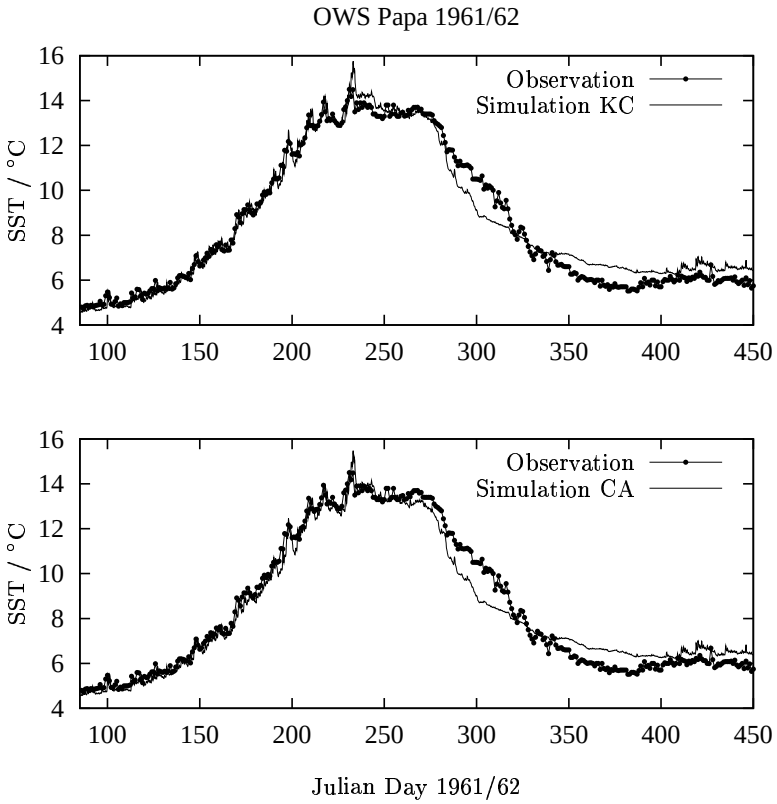

Fig. 7.6. Sea surface temperature at OWS Papa from March 1961 to March 1962. Upper panel: Measured SST and SST simulated with the quasi-equilibrium version of the *Kantha and Clayson* [1994] model with the stationary gradient Richardson number set to $R_i^{st} = 0.225$. Lower panel: Measured SST and SST simulated with the version A of the *Canuto et al.* [2001] model with the stationary gradient Richardson number set to $R_i^{st} = 0.25$.

It should however be noted here that it is mainly the steady-state Richardson number which determines the growth or decay of turbulence rather than the critical Richardson number which just sets an upper limit to the gradient Richardson number.

It is not surprising that the simple but widely used standard k-ε model with a constant stability function for momentum fully fits into our concept of the steady-state Richardson number, and produces results for the mixed layer test cases which are compatible with those computed by the complex algebraic Reynolds stress closure model under consideration here, the *Canuto et al.* [2001] model. It should be reminded that such standard k-ε models were able to accurately approximate length scale ratios observed in the laboratory

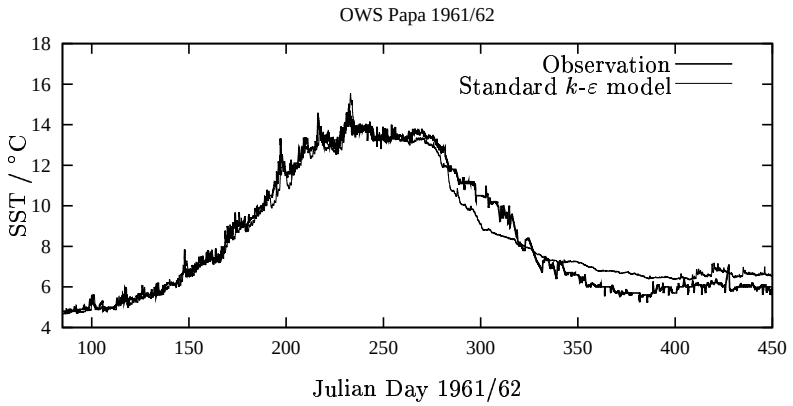

Fig. 7.7. Sea surface temperature at OWS Papa from March 1961 to March 1962. Bold line: Measured SST, thin line: SST simulated with the standard k-ε model with the stationary gradient Richardson number set to $R_i^{st} = 0.25$.

under structural equilibrium conditions, see *Baumert and Peters* [2000] and also figure 3.14.

In terms of mixed-layer modelling, this investigation can thus not discriminate between the quality of performances between the fully empirical stability functions (standard k-ε model), the *Kantha and Clayson* [1994] and the advanced *Canuto et al.* [2001] stability functions.

7.3 Northern North Sea

Due to its ecological and economic importance, the North Sea is probably the shelf sea area in the world which has been most intensively investigated. Two major oceanographic campaigns have been carried out in the Northern North Sea in order to better understand the impact of physical processes on biogeochemical parameters: the Fladenground Experiment 1976 (FLEX'76) and the Northern North Sea campaign 1998 (NNS'98)[2], see figure 7.8 for the locations. One argument for choosing the Northern North Sea for these investigations is the fact that horizontal advection is not dominant there due to the long distance from coasts and lateral fresh water inflow. However, many investigations have indeed shown, that even here advective effects are present with high spatial and temporal variability, see e.g. the comprehensive work by *Becker* [1981] and also the discussion by *Bolding et al.* [2000]. This

[2] The Northern North Sea campaign 1998 has been carried out as part of PROVESS (Processes of Vertical Exchange in Shelf Seas), a still ongoing project funded by the European Commissions MAST-III program under the number MAS3-CT97-0025.

lateral advection of temperature and salinity needs to be considered with care when the physical and biogeochemical processes in the Northern North Sea are investigated.

In the following, the observations during FLEX'76 (see section 7.3.1) and NNS'98 (see section 7.3.2) are simulated with a water column model in combination with various turbulence closure schemes discussed in chapter 3.

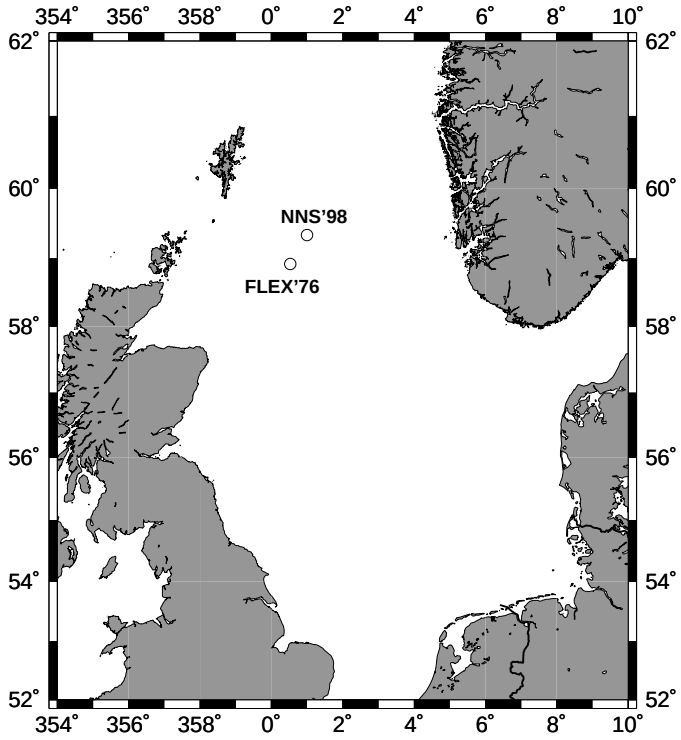

Fig. 7.8. Positions of the Fladenground Experiment 1976 (FLEX'76), see section 7.3.1 and the Northern North Sea Experiment 1998 (NNS'98), see section 7.3.2 in the Northern North Sea.

7.3.1 Fladenground Experiment 1976

A data set which has been used throughout the last 20 years as a calibration for mixing parameterisations has been collected during the measurements of the Fladenground Experiment 1976 (FLEX'76) campaign. These measurements of meteorological forcing and temperature profiles were carried out

in spring 1976 in the northern North Sea at a water depth of about 145 m and a geographical position at 58°55'N and 0°32'E, see figure 7.8. Turbulent quantities have not been measured. For further details concerning the measurements, see *Soetje and Huber* [1980] and *Brockmann et al.* [1984]. This FLEX'76 data set has been used by several authors in order to test different mixing schemes (see e.g. *Friedrich* [1983], *Frey* [1991], *Burchard and Baumert* [1995], *Pohlmann* [1997], *Burchard and Petersen* [1999], *Mellor* [2001a]).

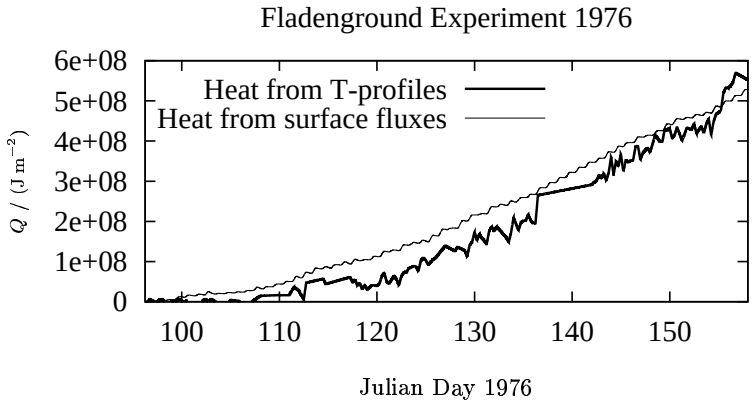

Fig. 7.9. Relative heat content of the water column during the Fladenground Experiment 1976. Bold line: heat content as calculated from measured temperature profiles. Thin line: heat content as calculated from surface heat fluxes.

In figure 7.9, the relative heat budget for the FLEX'76 site calculated from measured temperature profiles and from surface heat fluxes computed by means of standard bulk formulae (for details, see *Burchard and Petersen* [1999]) are shown. Differences between the two curves are mainly due to horizontal advection of different water masses. Figures 7.11 and 7.12 demonstrate that both models under consideration correctly simulate the basic evolution of measured temperature profiles (given in figure 7.10). This temperature evolution is characterised by homogeneous vertical temperature distribution in the beginning (until day 110) and subsequent stabilisation of the water column due to increasingly positive surface heat fluxes. Around day 133, a storm homogenises the upper 50 m. This storm is investigated in more detail below. It can however be seen that the *Canuto et al.* [2001] model produces thermoclines which are deeper than those predicted by the *Kantha and Clayson* [1994] model. This has the consequence that from day 125 on the sea surface temperature is clearly lower for the *Canuto et al.* [2001] than for the *Kantha and Clayson* [1994] model. Up to day 145 the model SST is closer to the measured SST. Afterwards, the *Kantha and Clayson* [1994] model shows better agreement between measured and simulated SST.

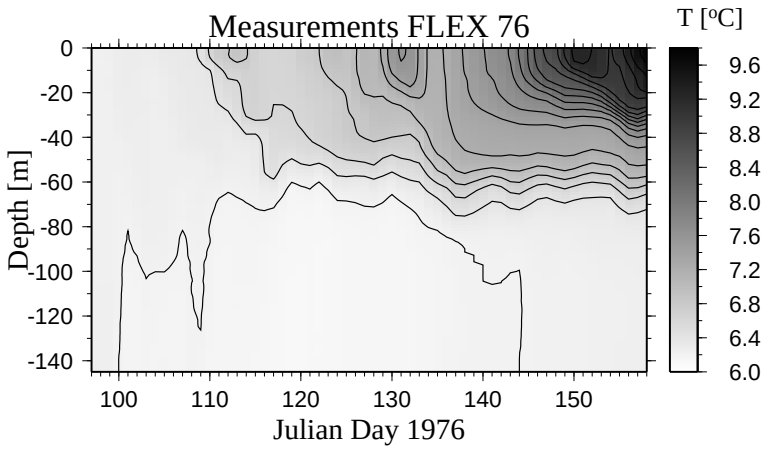

Fig. 7.10. Temperature evolution for the FLEX'76 site in the northern North Sea from CTD measurements.

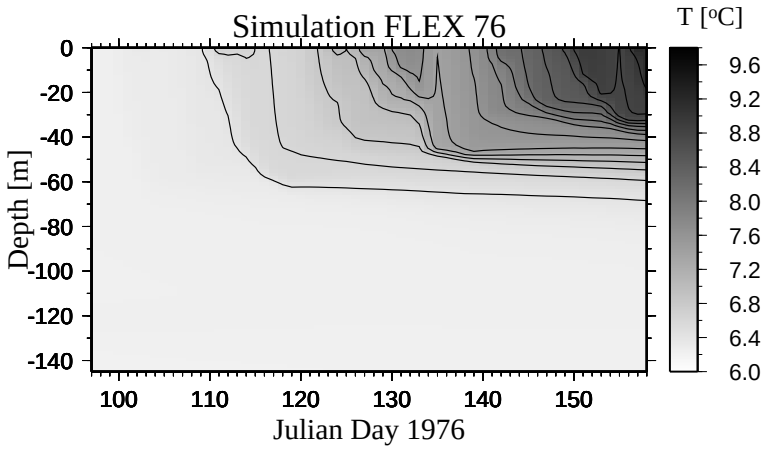

Fig. 7.11. Temperature evolution for the FLEX'76 site in the northern North Sea. Results of the simulation with the quasi-equilibrium version of the *Kantha and Clayson* [1994] model with the stationary gradient Richardson number set to $R_i^{st} = 0.225$.

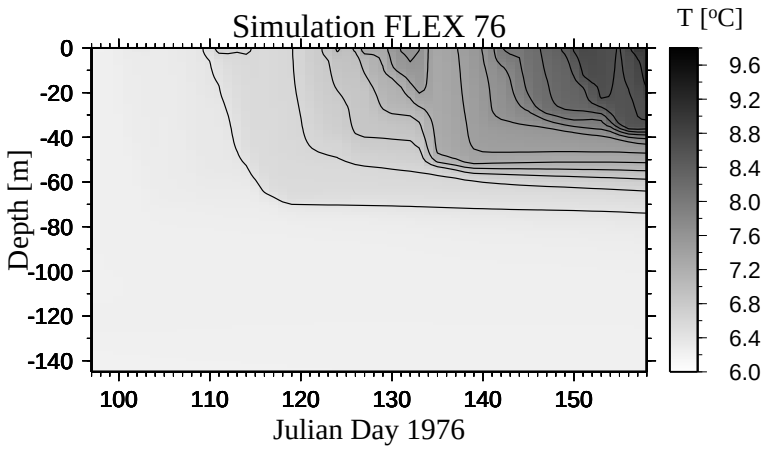

Fig. 7.12. Temperature evolution for the FLEX'76 site in the northern North Sea. Results of the simulation with the version A of the *Canuto et al.* [2001] model with the stationary gradient Richardson number set to $R_i^{st} = 0.25$.

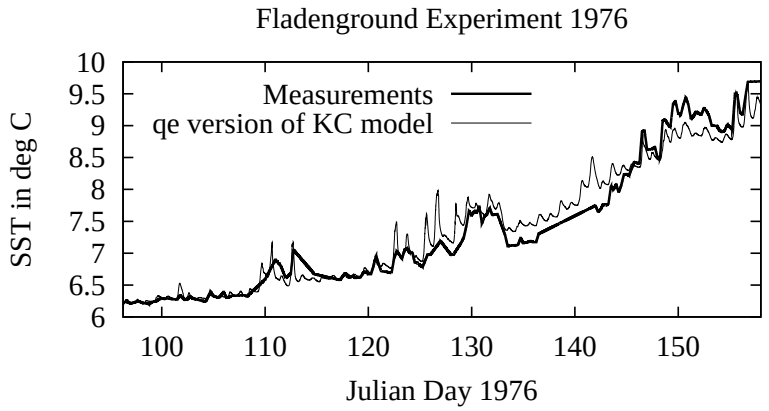

Fig. 7.13. Sea surface temperature during the Fladenground Experiment 1976. Bold line: Measured SST, thin line: SST simulated with the quasi-equilibrium version of the *Kantha and Clayson* [1994] model with the stationary gradient Richardson number set to $R_i^{st} = 0.225$.

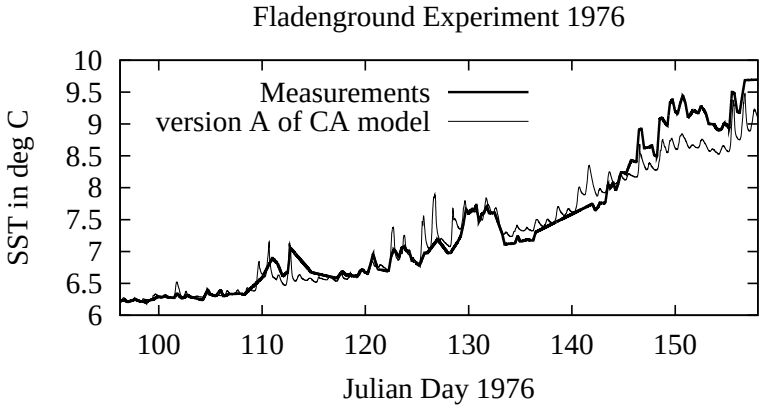

Fig. 7.14. Sea surface temperature during the Fladenground Experiment 1976. Bold line: Measured SST, thin line: SST simulated with the version A of the *Canuto et al.* [2001] model with the stationary gradient Richardson number set to $R_i^{st} = 0.25$.

In the following, the most predominant physical feature of the FLEX'76 campaign is discussed: the storm during day 133 and its consequences for the vertical temperature distribution. The impact of the surface wave breaking parameterisation by *Craig and Banner* [1994], see also section 3.3.2, and the related modifications to the k-ε model by *Burchard* [2001b] are investigated here as well. The forcing during four days before, during and after the storm and the resulting surface roughness length calculated by means of the *Charnok* [1955] formula (3.44) (which has here been limited by a lower bound of 0.02 m) and simulated sea surface temperature are shown in figure 7.15. The simulated sea surface temperatures, which are here represented by the value of the uppermost grid box, are nearly identical, with ($c_w = 100$) and without ($c_w = 0$) wave breaking parameterisation. This is caused by the fact that the near-surface temperature gradients are weak and therefore do not create increased vertical fluxes due to higher eddy viscosities (see figure 7.16). It does therefore not matter here at which height near the surface the sea surface temperature is defined in order to be compared with the observed bulk sea surface temperature. The observations are in principle reproduced by the model. Deviations may be explained by wrong estimates of air-sea fluxes, horizontal advection or inaccurate measurements.

A closer inspection of the simulated current speed profiles before and during the storm (see figure 7.16) reveals that the model indeed predicts a wave-enhanced layer. During the storm this wave-enhanced layer can be clearly seen in the near-surface current speed, which is due to increased vertical mixing significantly smaller with wave-breaking parameterisation. The vertical mean transport is of course the same with and without wave break-

ing, since the boundary condition for momentum is not affected by the wave-breaking parameterisation - other than the logarithmic representation of the vertical axis would suggest. In contrast to that, the current speed profiles are hardly affected by wave breaking during calm wind conditions.

For all wind conditions, the wave-enhanced layer can be clearly seen in the profiles of eddy diffusivity, turbulent kinetic energy and turbulent dissipation rate. The height of the wave-enhanced layer strongly depends on the surface roughness as a function of surface friction velocity. It should be noted that the shape of the turbulent quantities near the surface appear slightly different here in comparison to the idealised experiments discussed in section 3.3.2. This is merely due to the different scaling of the vertical axis. Here, the distance from the lower end of the unresolved surface layer of height z_0^s is shown in contrast to the previous plots, where the distance from the surface has been used.

It should be noted that a fine vertical resolution near the surface had to be used in order to resolve the wave-enhanced layer also during weak-wind phases with a small surface roughness length. In order to resolve the minimum roughness length of $z_0^s = 0.02$ m, $N_i = 200$ vertical layers with a surface zooming parameter of $d_u = 3.5$ had to be used, see equation (4.2). This resulted in a height of the surface layer of less than 0.01 m such that according to the study performed in section 4.4 a sufficient resolution was reached. In spite of the fine vertical resolution numerically stable results could be produced with relatively large time steps of $\Delta t = 120s$.

Finally, figure 7.17 shows profiles of temperature for the k-ε and the k-kL model (in combination with the *Galperin et al.* [1988] quasi-equilibrium stability functions, see *Burchard and Petersen* [1999]) with different vertical resolutions before and after the storm, without the *Craig and Banner* [1994] wave breaking parameterisation. It is demonstrated that the models are discretised such that even for a coarse resolution of about 10 m ($N_i = 14$ layers), the effect of the storm is well reproduced, although the mixed layer before the storm is not resolved. As already discussed in section 4.4, only a careful numerical treatment of the k-ε model near the surface allows for this good performance (see also *Burchard and Petersen* [1999]).

7.3.2 PROVESS-NNS 1998 Experiment

The data used here were collected as a subset of the overall PROVESS Northern North Sea (NNS) experiment, which lasted from September 1998 until November 1998. During the PROVESS NNS experiment in autumn 1998, microstructure measurements were taken from R/V DANA from October 16 until October 25 with an MST shear probe (see *Prandke and Stips* [1998] and also *Stips et al.* [2000]) and from R/V PELAGIA from October 21 until October 28 with a FLY shear probe (see *Dewey et al.* [1987]). There was furthermore a 20 hour period of intensive joint measurements from October 22 to 23 when both ships were cruising against wind and waves at a distance of

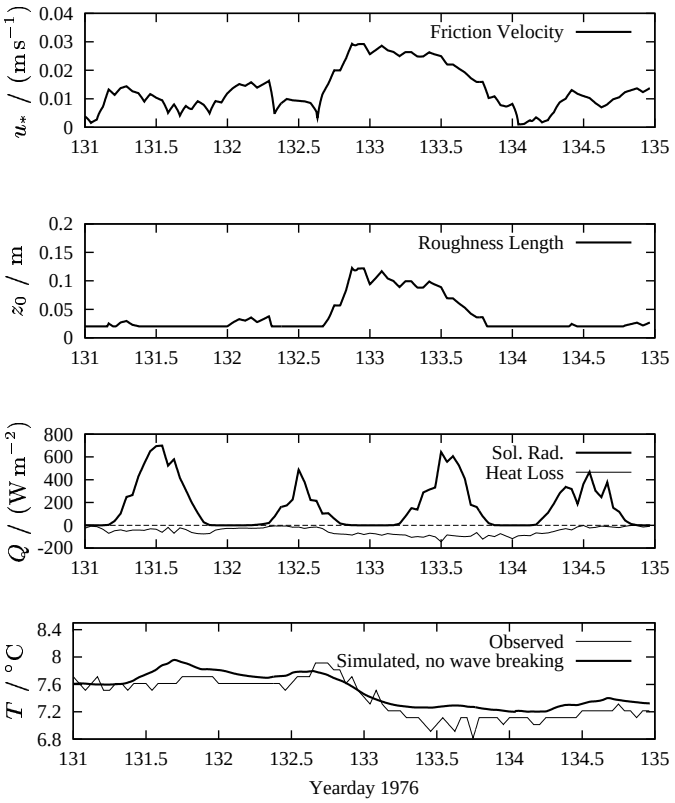

Fig. 7.15. Time series of surface friction velocity, surface roughness length, solar radiation and surface heat loss, and simulated and observed sea surface temperature before, during and after a storm at the FLEX'76 central station.

about one nautical mile, see *Prandke et al.* [2000]. During this period, 65 casts were made with the MST profiler and 72 casts with the FLY profiler. The central location was at 59°20' N and 1° E, at a mean water depth of about 110 m. In addition to the microstructure measurements, concurrent observations of current velocity from a moored ADCP were available. The bottom mounted ADCP was operated by the Proudman Oceanographic Laboratory (POL). Further the temperature field was measured with a thermistor chain from the Netherlands Oceanographic Institute (NIOZ). Meteorological data were sampled by the ship's weather station.

For a better understanding of the underlying physical processes at the station NNS in the Northern North Sea, three simulations are carried out, an annual for the whole year 1998, a seasonal for September and October 1998 and an episodical during the period of the observations of turbulent

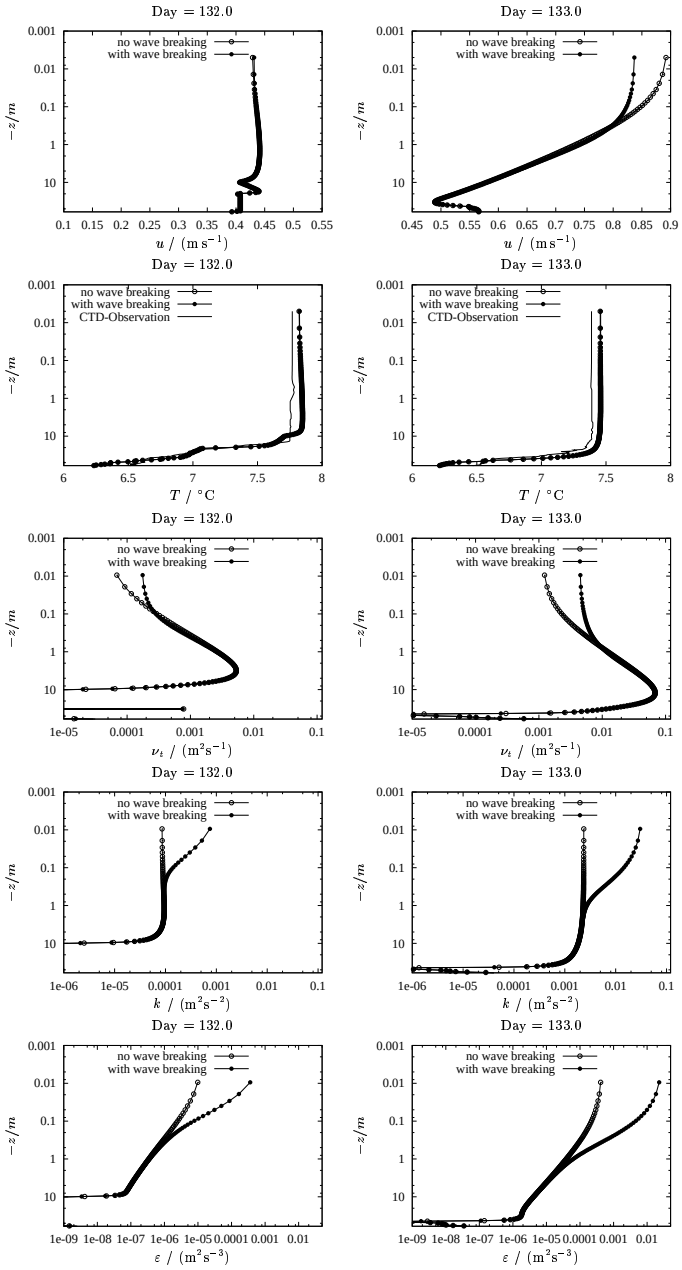

Fig. 7.16. Profiles of simulated current speed, simulated and observed temperature, and simulated eddy diffusivity, turbulent kinetic energy and turbulent dissipation rate before (left) and during (middle) a storm at the FLEX'76 central station. The simulations have been carried out with and without wave breaking parameterisation. The vertical axis is logarithmic and for the turbulent quantities the horizontal axis as well.

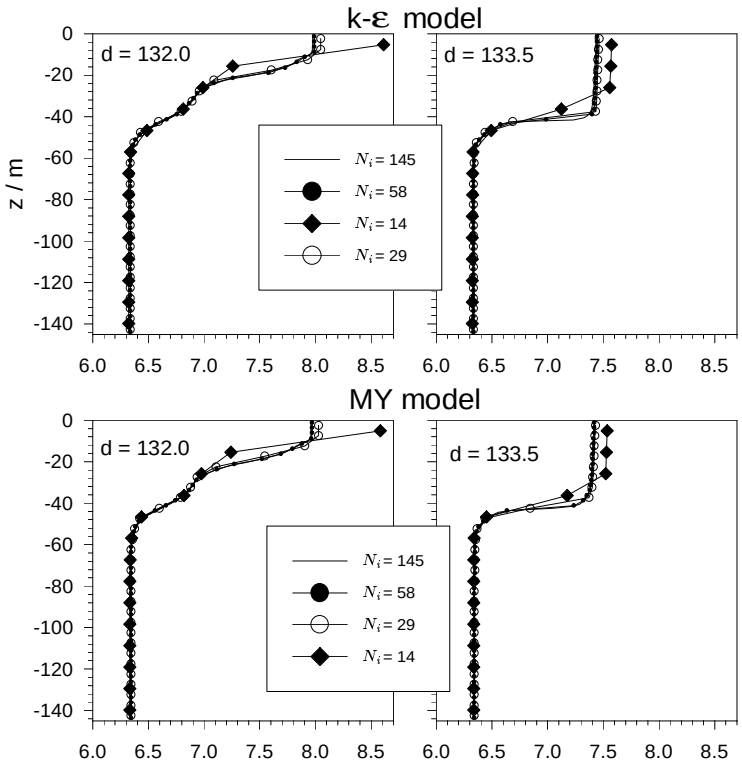

Fig. 7.17. Profiles of modelled temperature for different vertical resolutions. Results are shown for strong near surface stratification before a storm (d=132) and for a well-mixed situation after a subsequent storm (d=133.5). The upper panels show k-ε model results, the lower panels k-kL model results. This figure has been taken from *Burchard and Petersen* [1999].

dissipation with the MST and the FLY shear probes. This period is characterised by strongly variable winds and high surface waves. For all model simulations carried out here, the k-ε model in combination with the *Canuto et al.* [2001] second moment closure as described in chapter 3 is applied. As simple internal mixing parameterisation, the length scale limitation (3.133) and a minimum turbulent kinetic energy of $k_{\min} = 10^{-6}\ \mathrm{J\,kg^{-1}}$ has been applied, see also section 3.3.3 and the discussion by *Bolding et al.* [2000]. For all model simulations, the time step was $\Delta t = 100$ s and the vertical layer height $\Delta z = 1$ m.

For the annual simulation, time series of surface slopes $\partial_x \zeta$ and $\partial_y \zeta$ were extrapolated from observations during autumn 1998 based on four partial

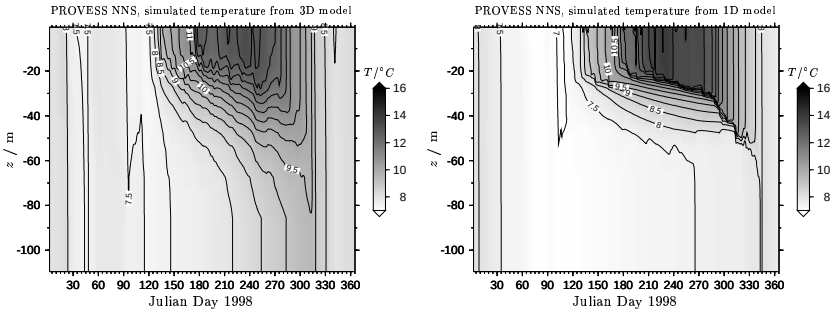

Fig. 7.18. Temperature evolution at station NNS during 1998 simulated with a three-dimensional (left panel) and a one-dimensional (right panel) model. For the one-dimensional simulations, a k-ε model in combination with the *Canuto et al.* [2001] second-moment closure has been applied.

tides by means of harmonic analysis. All necessary meteorological data are from the UK Meteorological Office Model. For calculating the resulting surface fluxes, the bulk formulae from *Kondo* [1975] were used. Since no observations for the sea surface temperature (SST) are available for the whole year 1998 at station NNS, the simulated SST is used as input into the bulk formulae. For the evolution of the vertical salinity profile, which is known to stabilise stratification during summer months, a relaxation to results obtained with a prognostic three-dimensional model of the North Sea by *Pohlmann* [1996a] was carried out. By doing so, the horizontal advection, which is the dominant process for salinity dynamics in the Northern North Sea, is parameterised. The resulting temperature evolution for this annual simulation is shown in figure 7.18 in comparison to the results of the three-dimensional model of *Pohlmann* [1996a] which is forced by weekly observed sea surface temperature and which uses the fully algebraic turbulence model by *Kochergin* [1987]. For both, the one-dimensional and the three-dimensional model, stratification starts to establish in the beginning of May. The three-dimensional model however is much more diffusive which might be either due to a too high background diffusivity or due to numerical diffusion caused by vertical advection. As a consequence of this, the three-dimensional model destratifies earlier, already around November 10, in contrast to the one-dimensional model, which remains stratified until December 5.

Figure 7.19 shows semi-diurnal oscillations of T and S in the region of the pycnocline during the period of the seasonal simulation in September and October 1998. A major period of about 3 days is visible which can most likely be interpreted as the synoptical meteorological scale. These semidiurnal and synoptic oscillations are here interpreted as internal waves and not as mixing events. One argument for this is that the oscillations only occur in the

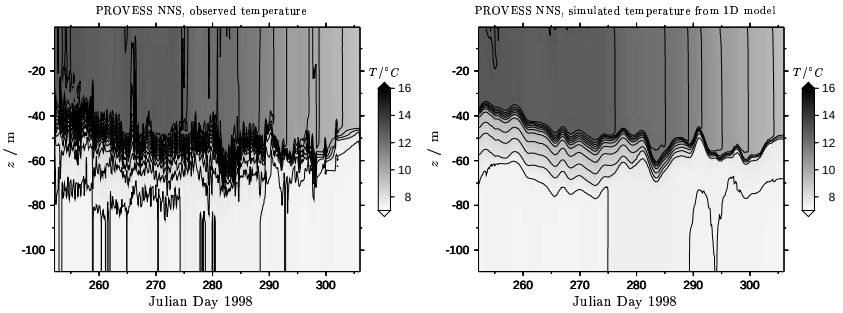

Fig. 7.19. Observed (left panel) and simulated (right panel) temperature at station NNS during autumn 1998. The simulations have been carried out with relaxation of temperature and salinity to observed values in the top and bottom 20 m and application of observed vertical motion of the pycnocline. For the simulations, a k-ε model in combination with the *Canuto et al.* [2001] second-moment closure has been applied.

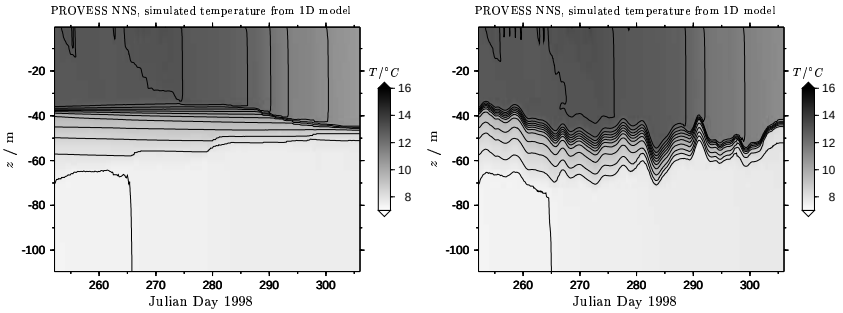

Fig. 7.20. Simulated temperature at station NNS during autumn 1998. The simulations in the left panel has been carried out without relaxation of temperature and salinity to observed values and without vertical advection. For the simulations, a k-ε model in combination with the *Canuto et al.* [2001] second-moment closure has been applied. The results shown in the right panel are obtained without relaxation, but with application of vertical advection.

strongly stratified region of the pycnocline, and not in the surface or bottom mixed layers as would be expected for mixing events, see figure 7.19.

In order to consider this vertical advection in the model simulation, the observed (from thermistor chains) and low-pass filtered vertical pycnocline motion are applied as spatially constant advective velocity to temperature and salinity in the whole water column. It is assumed that water of the same temperature and salinity is flowing in at the surface boundary (during negative vertical velocity) and at the bottom boundary (during positive vertical velocity). This is admissible due to the two-layered structure of the water col-

umn with well-mixed surface and bottom boundary layers. We assume that the current velocity and the turbulence quickly adapt to the new pycnocline height and therefore do not apply vertical advection to the respective dynamical equations. In figure 7.20 two seasonal simulations are compared, one with vertical advection and one without. In the simulation without vertical advection, the pycnocline basically stays at about 40 m below the surface and is only slightly mixed down during the storms during end of October. Since both simulations are driven with the same surface heat fluxes (due to the use of observed SST for calculating these fluxes), the surface layer is heated up less when vertical advection is applied.

In order to achieve good agreement between model results and observations, a relaxation of simulated profiles to observations of temperature and salinity is carried out in the upper 20 m of the water column with a relaxation time scale of $\tau_R = 24$ h, see *Burchard et al.* [1999]. The resulting temperature evolution is shown in figure 7.19. It is no surprise that the agreement between observations and simulation results is good now after all these manipulations. Such a realistic stratification is however needed for successfully simulating observations of velocity and turbulence, as carried out in the following episodic simulations.

The main purpose of this episodic simulation is to intercompare observations and simulations of turbulent dissipation rate under these stormy conditions. The most relevant forcing is thus shown in figure 7.21. The meteorological forcing is characterised by strong cooling with weak positive heat flux due to solar radiation only during few hours on some days. The strongest heat loss of about 300 $\mathrm{W\,m^{-2}}$ during the night from October 20 to 21 is driven by a storm with wind speeds of up to 20.5 $\mathrm{m\,s^{-1}}$. For the hours during maximum wind speed, dissipation rate observations were not made due to danger for staff and material.

The upper two panels in figure 7.22 give an overview over the dissipation rate measurements carried out in October 1998 from two ships during this campaign in the Northern North Sea. The dependence of dissipation rates from surface and bed stress can roughly be seen, and also the expected decrease of the dissipation rates with increasing distance from the surface and bottom, respectively.

The measurements of dissipation rate made from October 22 to 23 during the period of intense parallel observations with the two profilers are reproduced in the upper two panels of figure 7.23. They have been compared in detail by *Prandke et al.* [2000], state that the overall structure of the two measured temporal-spatial fields agrees well. Due to the high surface stress, high dissipation rates of above 10^{-7} $\mathrm{W\,kg^{-1}}$ are confined to the upper 20 m most of the time. Also the temporal structure of the surface stress is clearly visible in the dissipation rate observations: high near-surface dissipation rates dominate until about 17 h of October 22, and the wind stress minimum in the early morning of October 23 is present in both observational data sets

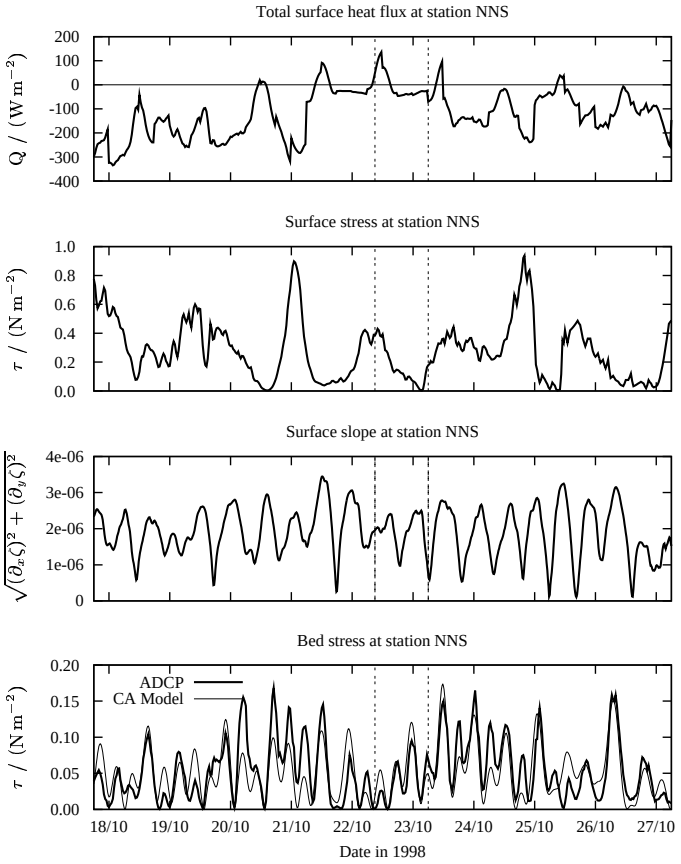

Fig. 7.21. Atmospheric and tidal forcing at station NNS from October 16 to October 27. Upper panel: Total surface heat flux in $\mathrm{W\,m^{-2}}$ as calculated from bulk formulae and cloud cover; second panel: Surface stress in $\mathrm{N\,m^{-2}}$ as calculated from bulk formulae; third panel: absolute value of observed surface slopes; bottom panel: Bed stress in $\mathrm{N\,m^{-2}}$ as estimated from ADCP and calculated from the CA model. The period of intense parallel observations is marked by the two vertical dashed lines.

as well. In contrast to the upper layer, the dissipation rate in the lower layer is increasing with time due to periodically increasing bottom stresses. Furthermore, the thermocline with enhanced dissipation rates is present in both measurements at a height of about -60 m. *Prandke et al.* [2000] thus concluded that "fair agreement" between both observations was obtained, significantly improving the credibility of dissipation rate measurements.

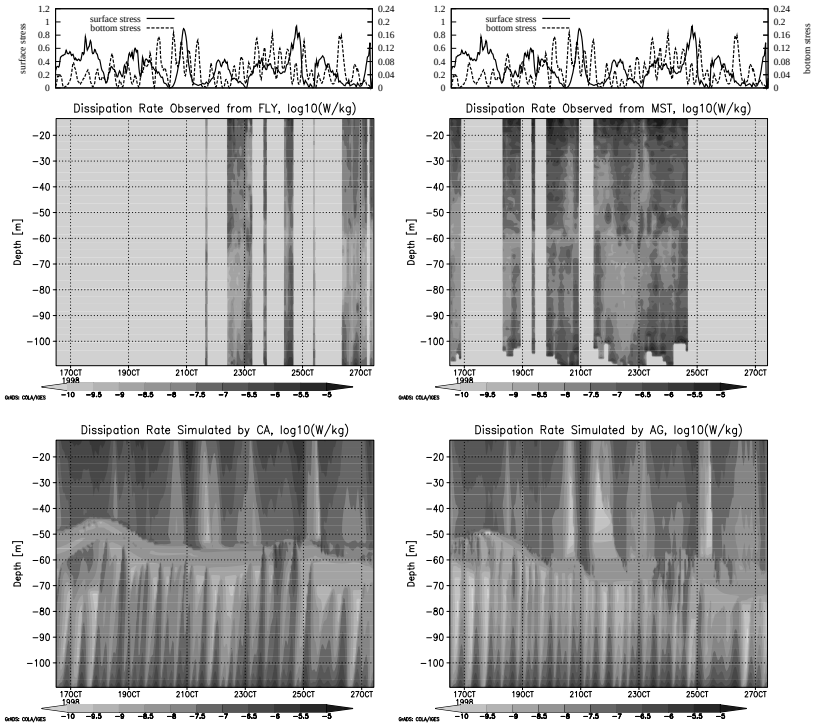

Fig. 7.22. Observed (top two panel) and simulated (lower two panels) turbulent dissipation rates ε in $\mathrm{W\,kg^{-1}}$ during During one week in October 1998. Upper left panel: FLY observations; upper right panel: MST-observations; lower left panel: model with second-moment closure from *Canuto et al.* [2001] (CA); lower right panel: k-model with an algebraic length scale from *Robert and Ouellet* [1987] (AG). The small top panels show surface and bottom stress in $\mathrm{N\,m^{-2}}$.

Results for observed and simulated dissipation rates are shown in $\mathrm{W\,kg^{-1}}$ in figures 7.22 and 7.23. The upper 12 m are not shown because there the observations are clearly contaminated by the influence of the research vessels.

The general comparison between the observed and simulated dissipation rates is difficult during the whole period of measurements (October 17 to 27) due to the sparseness of observations, see the upper two panels of figure 7.22. For the six day period from October 19 to 24, a comparative study between observations with the MST shear probe and CA model results has been carried out by *Bolding et al.* [2000]. Most of the observed features could be reproduced and thus explained by the model. Differences occurred mainly due to intermittency with randomly distributed levels of high turbulence not reproduced by the model. Further discrepancies were due to wrong model

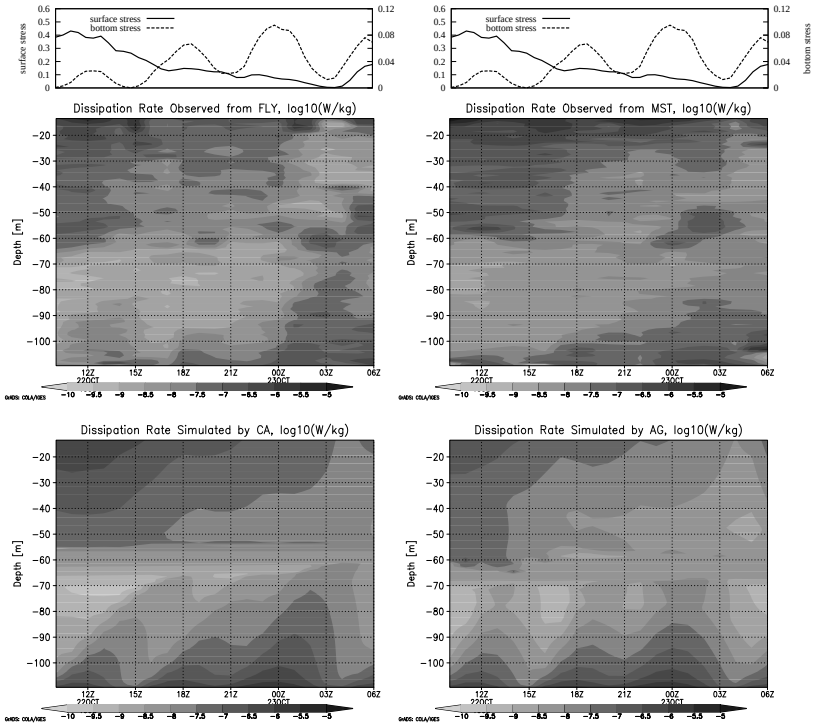

Fig. 7.23. Observed (top two panel) and simulated (lower two panels) turbulent dissipation rates ε in $\mathrm{W\,kg^{-1}}$ during the 20-hour period of intensive parallel observations. Upper left panel: FLY observations; upper right panel: MST-observations; lower left panel: model with second-moment closure from *Canuto et al.* [2001] (CA); lower right panel: k-model with length scale from *Robert and Ouellet* [1987] (AG). The small top panels show surface and bottom stress in $\mathrm{N\,m^{-2}}$.

forcing and simplified model assumptions such as the eddy diffusivity assumption and simple parameterisation of internal wave mixing.

The lower panel of figure 7.22 shows model results for the whole period obtained with the k-ε model with second-moment closure by *Canuto et al.* [2001] (CA) and the one-equation model with the algebraic macro length scale by *Robert and Ouellet* [1987] (AG). They do of course basically agree well with each other, since they are identical except for the turbulence closure models. The simple model AG shows significantly less time lag of dissipation rate with distance from surface and bottom. From figure 7.23, the upward propagation speed of the near-bed dissipation rate maximum generated at about midnight from October 22 to 23 can be estimated as approximately $4 \cdot 10^{-3}\ \mathrm{m\,s^{-1}}$ for the CA model and $9 \cdot 10^{-3}\ \mathrm{m\,s^{-1}}$ for the AG model. From

analysing time series of simulated dissipation rates at 30 m above the bed, *Burchard et al.* [2001] estimated time lag behind the logarithmic law of about 3 1/2 hours for the CA model and about 1 1/2 hours for the AG model. This results in a propagation speed of about $2.4 \cdot 10^{-3}$ m s^{-1} for the CA model and of about $5.5 \cdot 10^{-3}$ m s^{-1} for the AG model. Analysing this time lag from the observations is rather difficult. As a rough estimate one could say that both profilers show a time lag of about half an hour less than the two-equation models. Similar phase lags have been observed by *Simpson et al.* [2000] for a stratified site in the Irish Sea, see section 7.4.1.

Figure 7.23 shows model results for this period of intense parallel observations. In the surface mixed layer, the CA model results agree better with the MST observations, which have been assumed by *Prandke et al.* [2000] to be more realistic near the surface at high wind speeds than the FLY observations.

In the bottom boundary layer, the observations and model results basically agree with respect to the tendency of turbulence growing with time. It should be noted that the first peak in dissipation rate is probably overpredicted by the models, since the bed stress is overpredicted, see figure 7.21. A better agreement between simulations and observations would have been achieved by forcing the model directly with observed bed stresses instead of surface slopes, a method introduced in detail by *Burchard* [1999].

It can be concluded from this comparative study for the Northern North Sea that the turbulence in the bottom and surface boundary layer can be successfully reproduced by two-equation turbulence model. The reliability of such models seems to lie within the uncertainties of the measurements as demonstrated here by comparing two independent observations. In the region of stable stratification, good estimates for the dissipation rate cannot be given. The instruments measure too scarcely for obtaining a statistical basis for determining the dissipation rate with some confidence in this highly intermittent region (see also the discussion by *Baker and Gibson* [1987]). The models contain tuning parameters such as the lower limit of turbulent kinetic energy used here, see equation (3.133).

One further conclusion is that the one-equation model AG used here does underestimate time lag effects of turbulence, probably due to wrong representation of turbulent time scales. In contrast to this, two-equation models have been carefully calibrated by laboratory experiments of freely decaying turbulence. It should be investigated in future model studies whether this is a general feature of one-equation models or if more complex algebraic length scale parameterisations such as the one by *Gaspar et al.* [1990] solve this problem.

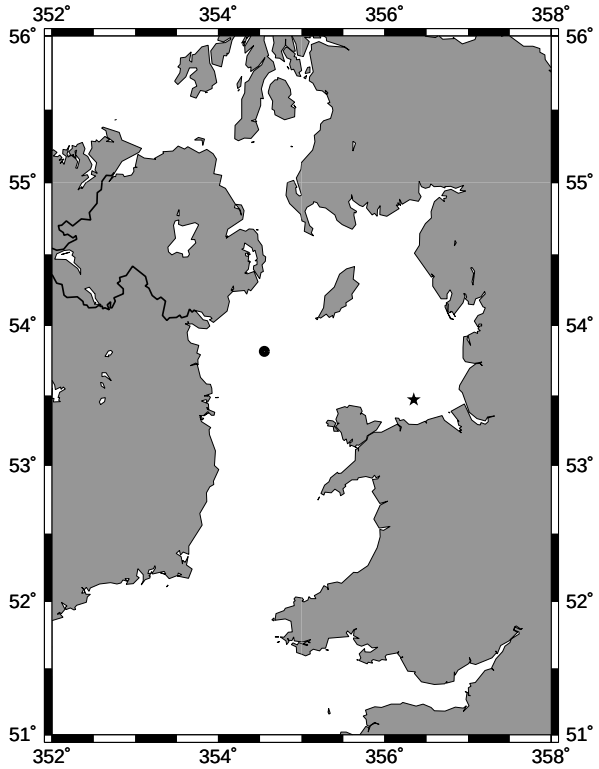

Fig. 7.24. Map of the Irish Sea with the locations of the seasonally stratified campaign in the Western Irish Sea (bullet) and the tidally induced stratification campaign in the Liverpool Bay (star).

7.4 Irish Sea

7.4.1 Seasonally stratified

In this section, dissipation rate measurements carried out by *Simpson et al.* [1996] in the Western Irish Sea with the FLY shear probe are simulated, see also *Burchard et al.* [1998]. The measurements were made over a 24 hour period in July 1993 at a site with water depth of 90 m and position 53°49'N, 5°27'W, see figure 7.24. The site has rectilinear tidal currents, and the tidal current amplitude at the time of the measurements was 0.45 m s^{-1}. During the observational period the water column was thermally stratified with near surface temperature of 14°C and temperatures of 10°C below the thermocline, which was situated 75 m above the sea-bed. In addition to hourly conductivity-temperature-depth profiles and moored current meter measure-

ments, turbulent dissipation was measured using a FLY free-fall shear probe. Six profiles were made per hour, and these were averaged together to give hourly means. Measurements made in the top 10 m of the water column have been excluded as the probe may still be accelerating, and the signal may be contaminated by the ships wake.

The forcing data for the model is provided by a time series of current measurements taken 12 m above the bed, from which a sea surface slope is calculated such that the model exactly reproduces the observed flow (see *Burchard* [1999]). Cross-surface heat exchange is calculated from dew point temperature, wind speed, and direct solar radiation observed at a nearby meteorological station. Cross-surface momentum exchange is calculated from the observed wind speed and direction (following *Simpson et al.* [1996]).

Figure 7.25 shows isopleth diagrams of measured and modelled dissipation rate. The model results are shown for the stability functions by *Galperin et al.* [1988] and the simple internal wave model by *Luyten et al.* [1996b], see also section 3.3.3, and reproduce the observed M_4 period oscillations in the bottom layer (caused by the flooding and ebbing of the predominant semi-diurnal M_2 tide).

The phase lag between dissipation rate and bottom friction, which is increasing with distance from the bottom, can be clearly seen in the measurements (figure 7.25). This is in principle well reproduced by the simulations with both of the models, although the k-ε model seems to stronger and thus more realistically simulate this time lag. This faster response of the k-kL model could have two reasons: (i) the inclusion of the diagnostic length scale L_z in the kL equation or (ii) the higher values of diffusivity for turbulent quantities in the k-kL model, see equation (3.71). In a recent analysis, *Simpson et al.* [2000] estimated the phase lag across the bottom boundary layer to be approximately four hours. They argue that this phase lag is not due to diffusion of turbulent kinetic energy up from the bottom boundary but due to the phase lag in vertical shear, which in turn defines the turbulence production.

However, the variability of the dissipation rate in the stratified core region of the flow cannot be resolved by the simple internal wave model included, see figure 7.26. Here, the effect of the simple internal mixing parameterisation suggested by *Luyten et al.* [1996b] can be clearly seen. Without the limitations (3.133) and (3.134), the dissipation rate would tend to values several orders of magnitude smaller than the observations[3]. It should however be kept in mind that here the minimum value for k, $k_{\min} = 7.6 \cdot 10^{-6}\ \mathrm{J\,kg^{-1}}$, has been tuned to these observations.

The similarity between the k-ε and the k-kL model, which is demonstrated in figure 7.25, has been extensively discussed by *Burchard et al.* [1998], where further details of this simulation are given. Earlier model simulations of the

[3] It should be noted that the dissipation rate in the thermocline might be below the detection limit of the shear probes due to collapse of turbulence.

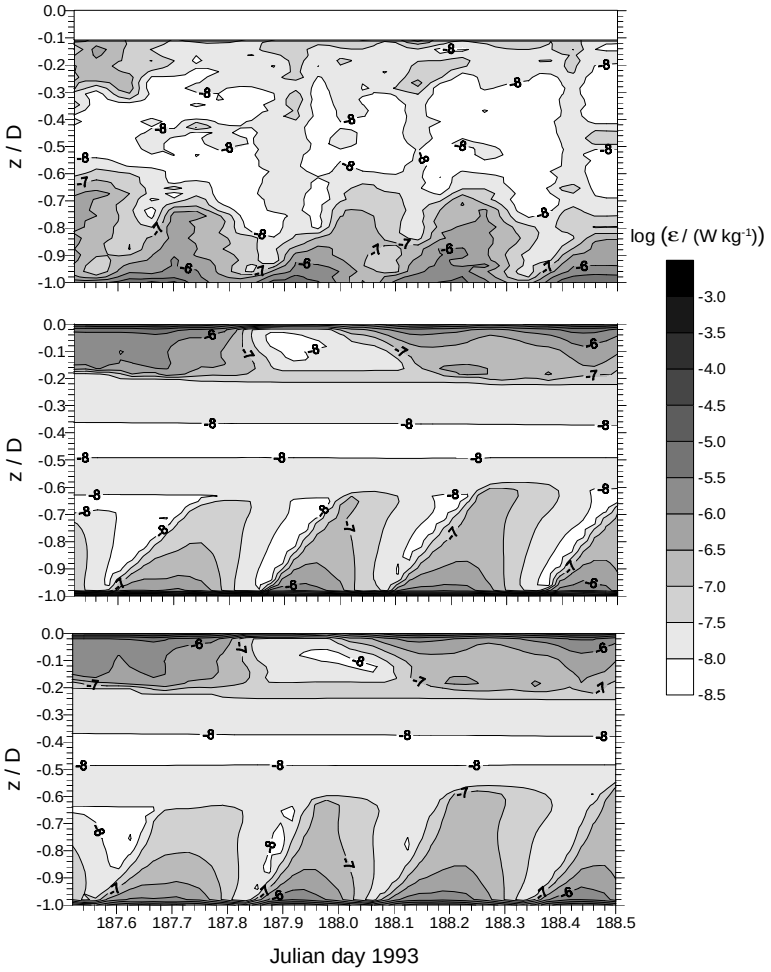

Fig. 7.25. Irish Sea simulation: Isopleth diagrams showing the development of dissipation rate during 24 hours in summer 1993. (top) Observations by *Simpson et al.* [1996], (middle) k-ε model result, (bottom) k-kL model result. For both model simulations, the *Galperin et al.* [1988] stability functions and the simple internal wave model by *Luyten et al.* [1996b] have been used. This figure has been taken from *Burchard et al.* [1998].

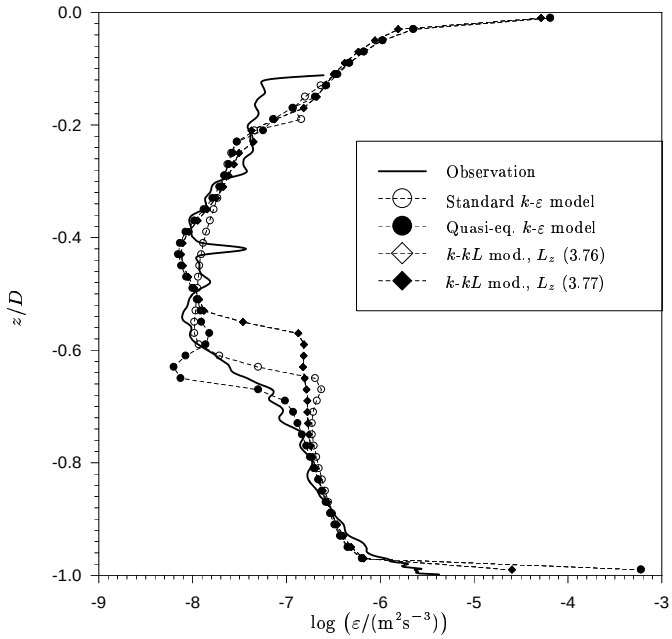

Fig. 7.26. Irish Sea simulation: Mean profiles of turbulent dissipation rate ε from observations by *Simpson et al.* [1996] and model simulations. This figure has been adapted from *Burchard et al.* [1998].

Irish Sea measurements have been carried out by *Simpson et al.* [1996] and *Luyten et al.* [1996b]. In these two papers, measurements at a well-mixed site in the Irish Sea have been successfully simulated as well. Recently, these dissipation rate measurements have also successfully been reproduced by *Axell and Liungman* [2001] who used a one-equation model with a simple algebraic length scale parameterisation.

7.4.2 Periodically stratified

In coastal areas with lateral freshwater inflow from rivers, the physical dynamics are even more complex than in seasonally stratified regions as discussed in sections 7.3.1, 7.3.2 and 7.4.1. In such so-called regions of freshwater inflow (ROFI), the assumption of horizontal homogeneity, which is often made for seasonally stratified regions, is definitely wrong. ROFIs are characterised by horizontal gradients of salinity and temperature which establish a dynamically relevant horizontal density gradient. Generally, the riverine wa-

ter is warmer and less saline than the marine water off-shore, such that the density increases with distance from the estuary[4].

In the presence of tides, a characteristic cycle of stratification and destratification is established. During flood, i.e. flow in the direction of decreasing density, denser water is stratified above less denser water by means of vertical current shear, thus building up an unstable stratification. This causes in turn intense vertical mixing leading to a homogenised water column at the end of the flood. In contrast to that, less denser water is moved over denser water during ebb tide, leading to a dampening of turbulent mixing and strong stratification of the water column at the end of the ebb tide. This mechanism of strain-induced tidal stratification (SIPS) has been analysed in detail by *Simpson et al.* [1990] on the basis of observations in Liverpool Bay.

Two mechanisms associated with horizontal density gradients establish a residual flow in such a way that the long-term mean currents are directed towards the coast (or freshwater source) near the bed and towards the sea near the surface. One mechanism for this estuarine circulation known for long is the direct consequence of the internal pressure gradient due to horizontal density gradients, see equations (3.4) and (3.5). For this so-called gravitational circulation, the presence of tides is not necessary. The second mechanism is the tidal velocity asymmetry: During flood near-bed velocity profiles are vertically homogenised due too enhanced vertical mixing and during ebb they are stretched due to damped turbulent mixing. In the tidal average, this leads to tidal mean flood-dominated near-bed currents. This mechanism has been analysed in detail by *Jay and Musiak* [1994] as a major driving force for estuarine turbidity maxima. In a two-dimensional modelling study of an idealised estuary, *Burchard and Baumert* [1998] could show that this tidal velocity asymmetry is even more important for the trapping of particles in meso-tidal estuaries than the gravitational circulation. Detailed observations of mean flow and turbulence parameters in the Hudson River presented by *Peters* [1997], *Peters* [1999], *Peters and Bokhorst* [2000] and *Peters and Bokhorst* [2001] clearly show the dependence of this mechanism on external parameters such as the spring-neap cycle and river run-off.

Various authors have carried out numerical simulations of circulation in ROFIs with one-dimensional water column models. *Luyten et al.* [1996a] used observations in the Rhine outflow area off the Dutch coast for the intercomparison of several turbulence closure models. *Simpson and Sharples* [1992] and *Sharples and Simpson* [1995] applied a water column model to the Liverpool Bay ROFI established by the freshwater run-off of the rivers Ribble, Mersey and Dee.

Simpson et al. [2001] present for the first time numerical simulations of turbulence dissipation measurements in a ROFI. These will be discussed here

[4] It should be noted that this is not true for all estuaries. In arid regions with strong evaporation, estuaries might be saltier than the coastal ocean, such that the estuary is inverse, see e.g. *Nunes Vaz et al.* [1990].

in detail. The major question of this numerical model study is whether boundary layer models as presented in chapter 3 are capable of qualitatively and also quantitatively reproducing the asymmetric cycle of turbulence in a ROFI. This is not clear a priori, since one characteristic feature of the underlying SIPS mechanism is strong convective mixing, which is difficult to quantify with local turbulence closure models in the absence of shear, see section 6.3. Another difficulty is the correct quantification of density forcing which is difficult to observe, since it is believed to vary in time and space, see *Simpson et al.* [1990].

The observations have been carried out by *Rippeth et al.* [2001] in the Liverpool Bay ROFI on July 5 and 6, 1999 at a position of 53°28.4'N, 3°39.2'W, see figure 7.24. This period is about three days after spring tide, with calm weather and clear sky. The dissipation rate measurements were carried out with a FLY shear probe mounted on a free-falling profiler. Sensors for temperature and conductivity attached to the profiler give detailed information on the vertical density distribution during each cast. Nearby, an ADCP was mounted on the bottom, giving information on the vertical velocity structure. Some accompanying CTD casts were made in order to achieve estimates for the horizontal gradients of temperature and salinity. For further details concerning the observations, see *Rippeth et al.* [2001].

Similarly to the simulations of OWS Papa (see section 7.2) and NNS'98 (see section 7.3.2), also here a k-ε model in combination with the second-moment closure by *Canuto et al.* [2001] is applied with a steady-state Richardson number of $R_i^{st} = 0.25$. For the reproduction of these observations by means of a numerical water column model, some further parameters have to be estimated. The surface fluxes are based on ship observations and from a nearby meteorological station at Hawarden. From the ship, wind speed and direction at 10 m above the sea surface and air pressure have been taken. From Hawarden station, observations of dry air, wet bulb and dew point temperature are used. Since the surface fluxes are calculated externally by means of bulk formulae of *Kondo* [1975], the sea surface temperature from measurements (FLY profiler) has been used. The bed roughness has been estimated from near-bed ADCP measurements as $z_0^b \approx 0.0025$ m by means of fits to the law of the wall, see section 3.2.3. The external pressure gradient due to surface slopes is estimated according to a method suggested by *Burchard* [1999] by means of adjustment to near bed velocity observations. The CTD casts carried out during the campaign did only allow for rough estimates of the horizontal density gradient. The horizontal salinity and temperature gradients for a typical summer situation have been estimated by *Sharples* [1992] to $\partial_s S = 0.0425$ psu km^{-1} and $\partial_s T = -0.0575$ K km^{-1}, respectively. Here, s is the gradient into the direction $\alpha = 78°$ rotated anti-clockwise from North. However, good agreement between observed and simulated salinity and temperature could here only be obtained after multiplying these estimated values with the factor of 2. This discrepancy might be due to the neglect of temporal

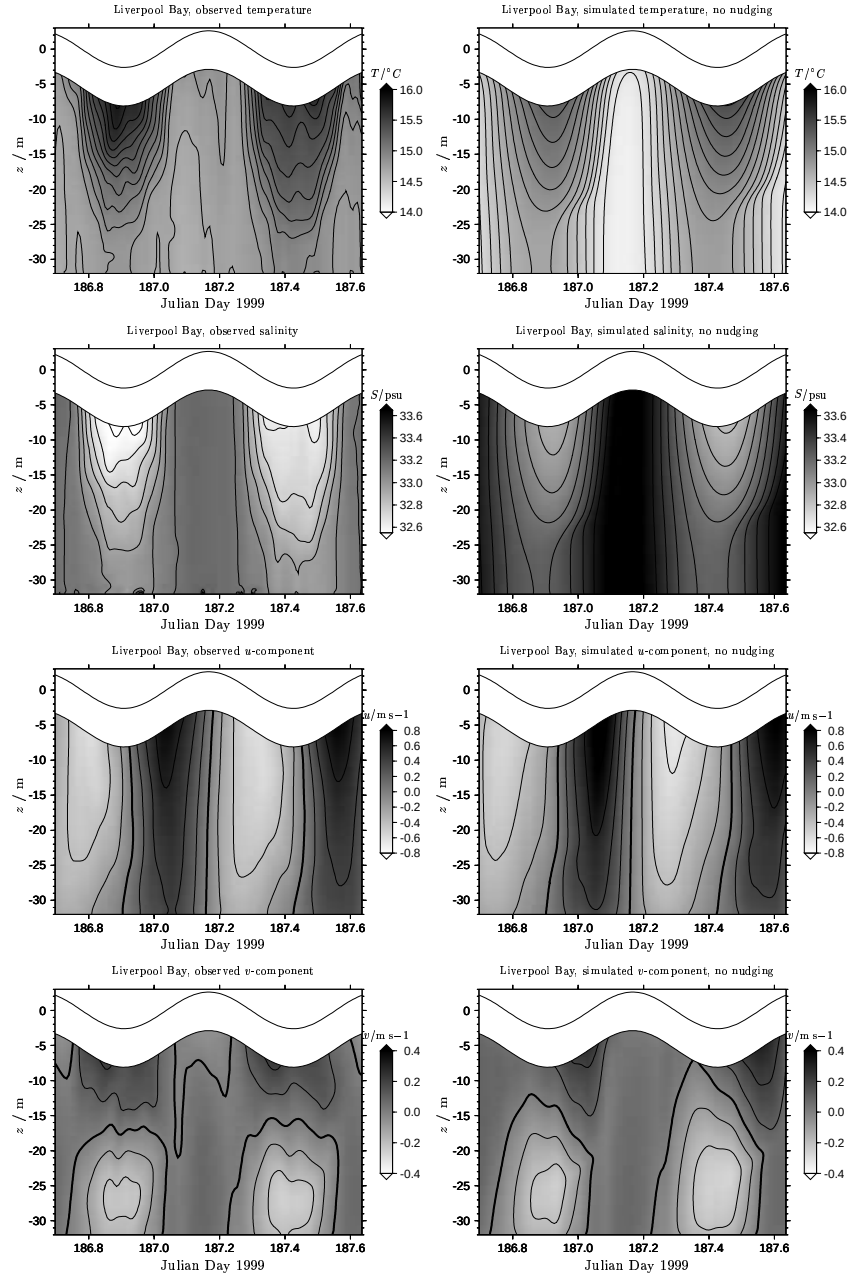

Fig. 7.27. Strain-induced Periodical Stratification (SIPS) in Liverpool Bay: Temperature $\bar{T}$, salinity $\bar{S}$ and velocity components $\bar{u}$ and $\bar{v}$ from observations by *Rippeth et al.* [2001] and simulations without nudging to observed $\bar{T}$ and $\bar{S}$ for two tidal cycles.

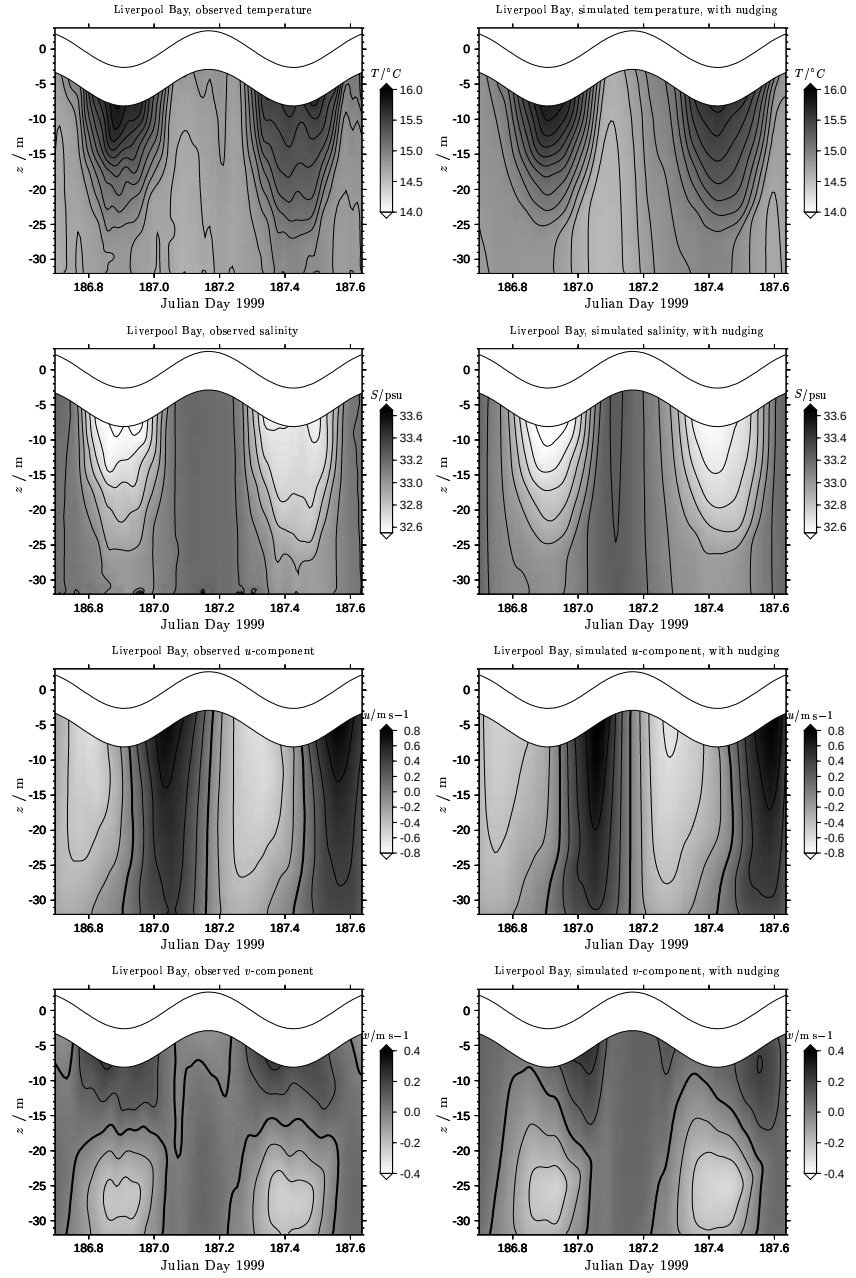

Fig. 7.28. Strain-induced Periodical Stratification (SIPS) in Liverpool Bay: Temperature $\bar{T}$, salinity $\bar{S}$ and velocity components $\bar{u}$ and $\bar{v}$ from observations by *Rippeth et al.* [2001] and simulations with nudging to observed $\bar{T}$ and $\bar{S}$ for two tidal cycles.

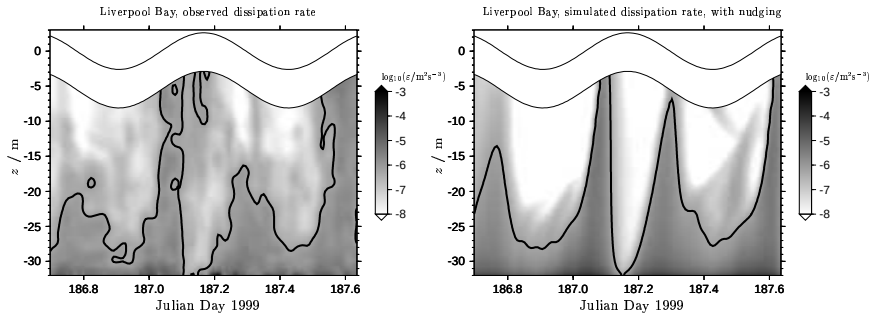

Fig. 7.29. Strain-induced Periodical Stratification (SIPS) in Liverpool Bay: Turbulent dissipation rate ε in $\mathrm{W\,kg^{-1}}$ from observations by *Rippeth et al.* [2001] and simulations with nudging to observed $\bar{T}$ and $\bar{S}$ for two tidal cycles. For better interpretation, the -6.2 isoline is drawn as a bold line.

and spatial variability of real horizontal gradients. From these gradients of salinity and temperature, gradients of buoyancy, $\partial_x b$ and $\partial_y b$ as they occur on the right hand sides of equations (3.4) and (3.5) are calculated by means of the equation of state.

Figure 7.27 shows simulated temperature $\bar{T}$, salinity $\bar{S}$, and horizontal velocity components $\bar{u}$ and $\bar{v}$ in comparison to observations. With the above mentioned increased horizontal $\bar{T}$ and $\bar{S}$ gradients, the observed tidal cycle is basically well reproduced. The typical SIPS cycle is clearly visible in both, observations and model results with a well-mixed water column after flood (day numbers 187.1 and 187.6) and strong stratification after ebb (day numbers 186.9 and 187.4). This comparison demonstrates the general capability of the model to quantitatively and qualitatively reproduce the SIPS mechanism.

However, a closer inspection of figure 7.27 reveals some differences between observations and model results which lead to significant deviations between observed and simulated turbulent dissipation rate ε (not shown here). In contrast to the observations, $\bar{T}$ and $\bar{S}$ exhibit an increasing phase shift during stratified periods with increasing distance from the bed. This is also visible in the $\bar{v}$ component of the velocity. This phase shift might be due to the simplifying assumption of the $\bar{T}$ and $\bar{S}$ gradients being constant in time and space.

In order to avoid this mean flow error for the simulation of the turbulent dissipation rate, a relaxation of simulated profiles of $\bar{T}$ and $\bar{S}$ profiles towards observations with a time scale of $\tau_R = 3$ hours is applied. The resulting mean flow and stratification is shown in figure 7.28. It is no surprise that now the phase shift observed before is vanished. But now, also the simulated velocity is better in phase with the observations.

For this improved mean flow situation, observed and simulated profiles of turbulent dissipation rate ε are compared in figure 7.29. The basic tidal cycle

of observed dissipation rate is well reproduced by the model simulations. The dissipation rate peaks with the M_4 tidal period at day numbers 186.8 (full ebb), 187.1 (full flood), 187.3 (full ebb) and 187.6 (full flood). The tidal asymmetry is clearly pronounced, with increased dissipation rates reaching only to about 15 m above the bed during ebb and reaching the surface during flood. Due to the calm weather conditions, near-surface turbulence is weak during ebb tides, when strong stratification isolates the surface from the bottom. During mixing events, the simulated dissipation rates do also quantitatively agree well with the observations.

It seems however that more detailed and controlled observations of mean flow properties would be needed for further investigating these details. This model study presented by *Simpson et al.* [2001] shows that the basic features of strain-induced periodic stratification and the underlying turbulence dynamics can be properly represented by boundary layer models. This has the implication that three-dimensional hydrostatic models are indeed an appropriate tool for studying estuarine dynamics and associated estuarine turbidity maxima.

7.5 Free convection in Lago Maggiore

The aim of this final study is to simulate convection observed in natural waters with the turbulence closure models discussed in chapter 3. The difficulties of such local models with simulating convective turbulence have been discussed in detail in section 6.3 where turbulence profiles for free convection are compared to LES results. Oceanic observations of free convection without shear are however difficult to obtain, for one example in the Pacific Ocean, see *Brainerd and Gregg* [1993a] for observations and *Brainerd and Gregg* [1993b] for model simulations. In lakes however free convection is a characteristic feature. In this section, the work carried out by *Stips et al.* [2001] on observing and simulating nearly shear-free in a pre-alpine lake is presented.

As study site Lago Maggiore (45°54'N, 8° 36' E) in northern Italy[5] was selected, see figure 7.30. The mean depth of the lake is 176 m with a maximum depth of 370 m. In the northern part the shore is steep. The length is 66 km, the mean breadth only 3.9 km. The lake has a surface area of 212.5 km^2 and a volume of 37.5 km^3. The river inflow has a mean of about 9 km^3 per year, resulting in a theoretical water renewal time of about 4 years. Lago Maggiore is a mesotrophic lake with tendency towards oligotrophy, see *Mosello* [1989]. For the light attenuation, Jerlov Type IIIb water (*Jerlov* [1968]) should be principally a good approximation. The original coefficients ($a = 0.78$, $\eta_1 = 1.4$ m^{-1} and $\eta_2 = 7.9$ m^{-1}, see equation (7.1)) do however not describe the attenuation near the surface well. Especially the predicted relative irradiance between 1.0 m depth and the surface is much higher than the clear water

[5] The northern end of the lake is situated in Switzerland.

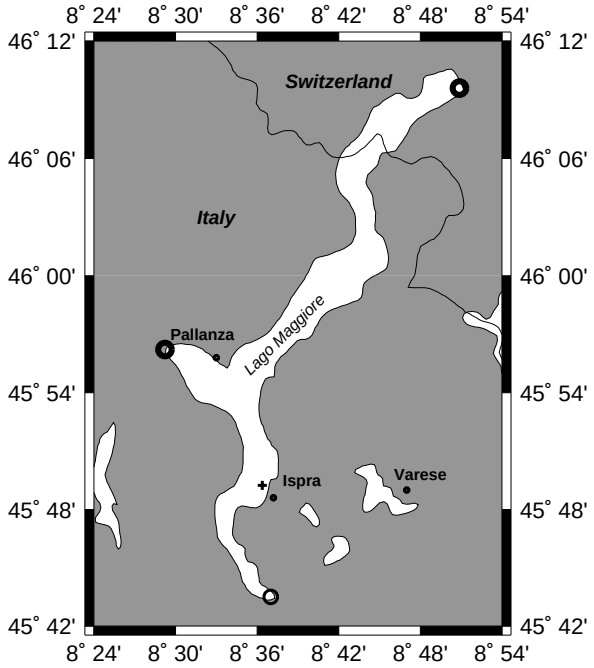

Fig. 7.30. Map of Lago Maggiore and surroundings in northern Italy and Switzerland. The cross marks the measurement site near Ispra. The bold circles in the north and the west are major inflows from rivers, the thin circle in the south is the outflow of the lake.

values from *Hasse* [1971]. This is unrealistic such that the simulations would result in wrong near-surface temperatures. The coefficients were recalculated in order to fit the observed temperature distribution as $a = 0.7$, $\eta_1 = 0.4$ m^{-1} and $\eta_2 = 8.0$ m^{-1}.

The measurements were made during three days in winter 1995 (December 18-21) at the shore of Ispra (45° 49,244'N, 8° 36,377'E), see figure 7.30. The measurements were carried out with an uprising profiler located 150 m from the shore at a water depth of 42 m. Such the sampled depth interval ranged from 30 m up to the surface. On the profiler, an MST shear probe, a fast temperature sensor and temperature and conductivity probes were mounted such that profiles of turbulent dissipation rate ε, temperature variance ε_T, mean temperature $\bar{T}$ and mean salinity $\bar{S}$ could be derived. For a detailed description of the data analysis, see *Stips et al.* [2001].

Wind speed was measured from a small buoy about 30 m away from the probe location with an anemometer at a height of 95 cm above the water

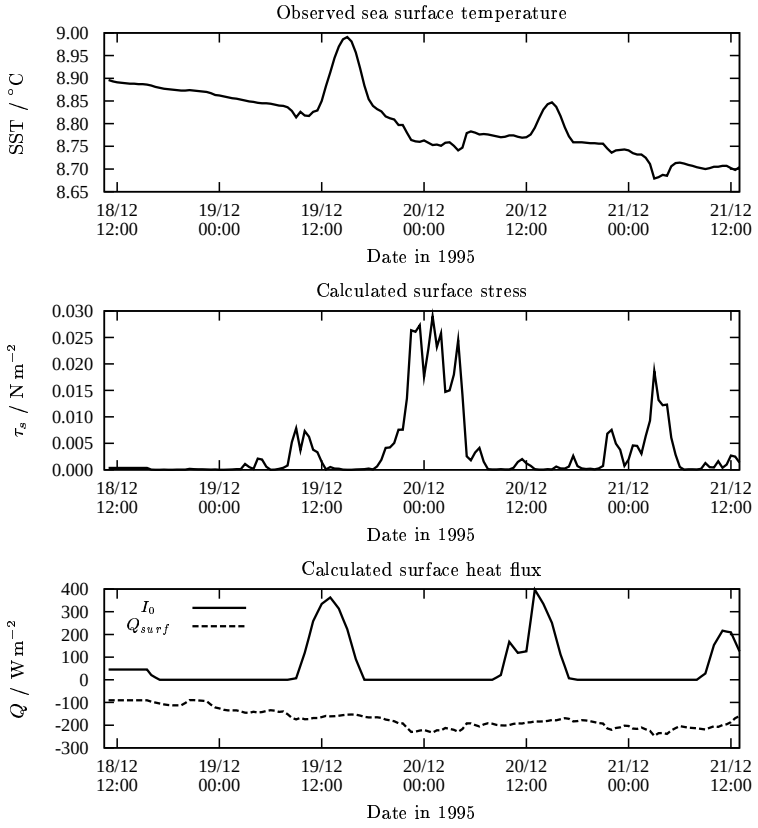

Fig. 7.31. Observed sea surface temperature (upper panel), calculated surface stress (middle panel) and solar radiation and surface heat fluxes $Q_{surf} = Q_s + Q_l + Q_b$ (lower panel) during three winter days over Lago Maggiore, northern Italy.

surface. The accuracy is ± 0.1 m s^{-1}. Air temperature and relative humidity were recorded at the measurement location on shore at a height of 10 m above lake surface. The cloud cover has been estimated every hour. Incident solar radiation was measured at the meteorological station in Pallanza, in a distance of about 10 km from the measuring site. An analysis of heat fluxes obtained by various bulk formulae showed however a significant deviation between the heat content of the water column and accumulation of these heat fluxes. This could be due to the fact that these bulk formulae are designed for oceanic conditions such that they are not valid for a lake with weak wind conditions. Thus, instead of using the calculated surface heat fluxes from bulk

formulae, they were calculated from the heat gain of the water column under consideration of the solar radiation[6].

The surface forcing derived from these measurements is shown in figure 7.31, for a detailed discussion of the derivation see *Stips et al.* [2001]. During these three days, the surface temperature has been sinking by 0.2 K with local maxima in the afternoons of December 19 and 20 and local minima during increased night time convection, when cold water was mixed up. The wind was mainly weak with only one small peak with a speed of about 4 $\mathrm{m\,s^{-1}}$ during the night from December 19 to 20. The solar radiation during the day with maxima up to 400 $\mathrm{W\,m^{-2}}$ could not compensate the surface heat loss due to latent and sensible heat flux such that the overall heat loss was about $3.1 \cdot 10^7$ $\mathrm{J\,m^{-2}}$ which corresponds to an average heat loss for the water of about 115 $\mathrm{W\,m^{-2}}$.

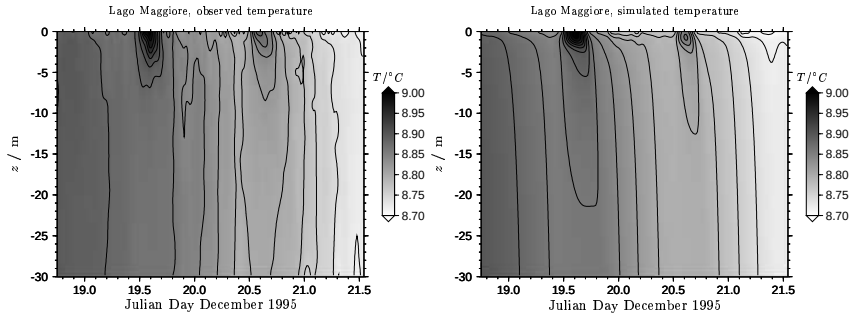

Fig. 7.32. Observed and simulated temperature $\bar{T}$ in Lago Maggiore during three days in December 1995.

For the simulation of these observations in Lago Maggiore, the same numerical model is used as for the Liverpool Bay simulation discussed in section 7.4.2, i.e. a k-ε model in combination with the second-moment closure by *Canuto et al.* [2001] with a steady-state Richardson number of $R_i^{st} = 0.25$. Figure 7.32 shows that the temperature evolution during the three days of campaign is basically well reproduced by the model. During the afternoons of December 19 and 20, a near-surface stable stratification is built up due to solar radiation. This warmer water is however quickly mixed down after sunset due to surface cooling. Despite of these two heating events, temperature is generally decreasing. One significant difference between observed and simulated temperature evolution is visible: The observed isotherms are mostly vertically oriented below 3 m whereas the simulations predict unstable stratification almost everywhere. This phenomenon has already been discussed in

[6] The reason for this discrepancy could of course also be due to lateral advection caused by differential cooling. For a detailed discussion, see *Stips et al.* [2001].

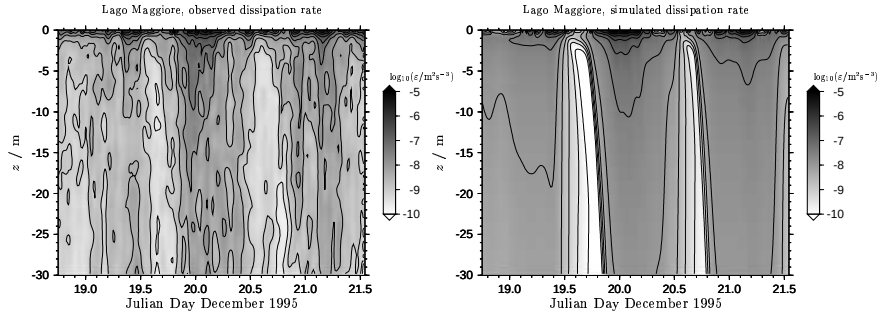

Fig. 7.33. Observed and simulated turbulent dissipation rate ε in Lago Maggiore during three days in December 1995.

section 6.3 when an idealised free convection scenario was simulated. All models based on the eddy viscosity assumption (as the model used here) can only transport heat upwards by means of turbulent transport when the vertical temperature gradient is unstable, i.e. temperature is decreasing with height. However, as seen in figure 6.10, the turbulent transport can also be against the gradient in the bulk of the convective boundary layer. Such counter-gradient transport processes seem to act also here in Lago Maggiore and cause efficient vertical mixing. Stable stratification under convective conditions can also be seen in figure 7.34, where temperature profiles have been averaged over periods of 12 hours. For obtaining better agreement between these observations and model results, parameterisation of non-local transports would be necessary.

It is interesting to see now, how good the observed turbulence is reproduced for this convective scenario. Figure 7.33 compares observed and simulated turbulent dissipation rates. The first impression is of course again that the observations are noisy and the model results are not. This is due to the statistical character of turbulence which is always calculated from too small samples when in-situ measurements are made. Undersampling[7] is a problem in field studies of turbulence even under relatively calm conditions like in Lago Maggiore. Apart from the noise level of the observations, some agreement can be seen between observations and model results in figure 7.33. During the two short heating periods, turbulent dissipation is decreasing by several orders of magnitude below the stratified region. During nighttime, in contrast, high dissipation rates penetrate down. However, similarly to the simulated temperature, a time lag can be detected in the model results which has not been observed. Moreover, vertical gradients of dissipation rate seem

[7] The number of casts per time is limited in calm regions with little lateral advection since the profiler itself generates turbulence which needs to be dissipated until the next cast at the same location.

to be overestimated by the numerical model. Again, this phenomenon has already been discussed for simulations of the free convection laboratory study, see figure 6.10. A closer inspection of turbulent dissipation rate profiles as obtained from 12 hour averaging shows that the shape of observed profiles is much more variable than the shape of simulated profiles, see figure 7.35. A consistent conclusion is difficult to draw from this figure. One significant feature is that the best agreement is obtained during the night from December 19 to 20, a phase of wind forcing with wind speeds up to 4 $\mathrm{m\,s^{-1}}$. The good agreement between observations and model simulations of dissipation rate for boundary layer shear flow has already been demonstrated in sections 7.3 and 7.4 for tidal bottom boundary layers. Apart from the significantly better agreement during this wind event, it is impossible for the other periods to determine which of the deviations are due to model deficiencies and which are due to general model simplifications such as neglect of lateral advection. The comparative idealised free convection study in section 6.3 has clearly shown the shortcomings of the model. It is one satisfying result of this field study simulation that the basic turbulence dynamics under free convection are basically well reproduced. This is also true for a quantity which is even more difficult to simulate, the dissipation rate ε_T of temperature variance $\langle \tilde{T}2 \rangle$ (see equation (2.28)), which is shown in figure 7.36. As the turbulent dissipation rate ε, the temperature dissipation ε_T can be detected from instantaneous vertical gradients (of temperature) measured by means of a fast temperature sensor. As for ε, the basic shape and size of ε_T is quantified by the model simulations, although the slopes seem to be overestimated. This could also be due to some near-bed processes such as slope convection which are not reproduced by this one-dimensional model. It should be kept in mind that the model parameterisation for the temperature dissipation ε_T, see equation (2.41), is based on highly simplifying assumptions, just as the transport equation (3.67) for ε.

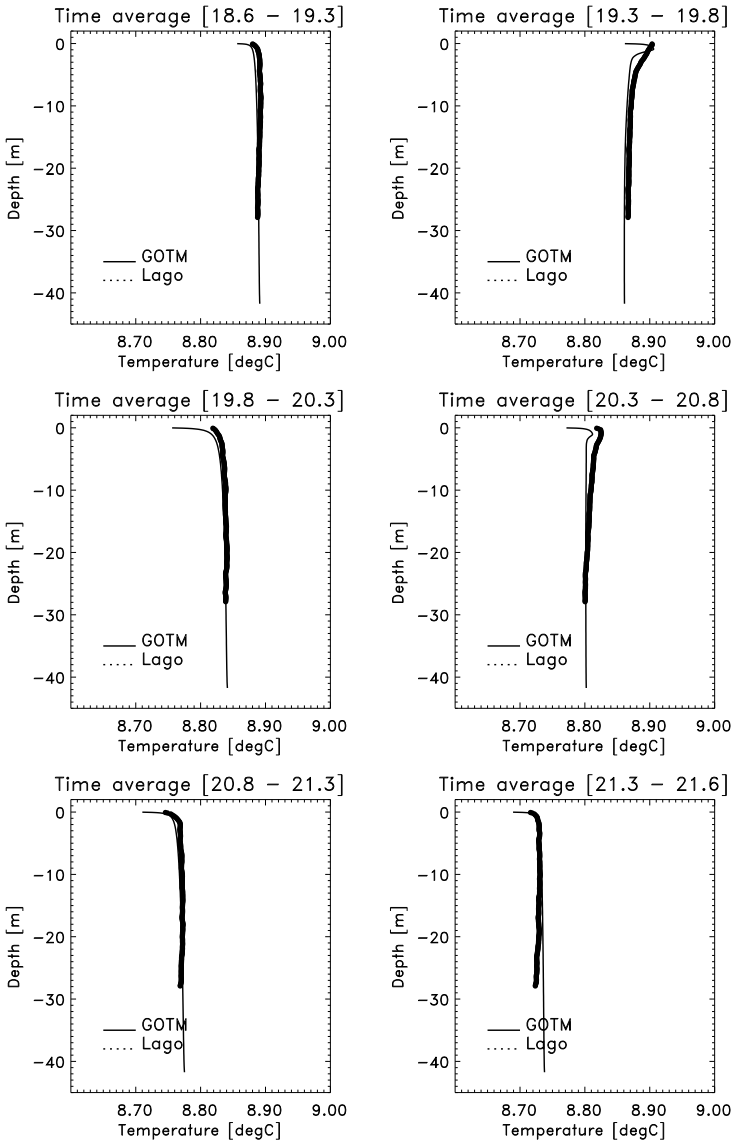

Fig. 7.34. Observed and simulated profiles of temperature $\bar{T}$ in Lago Maggiore during three days in December 1995. The Observations and the model results have been averaged over periods of 12 hours.

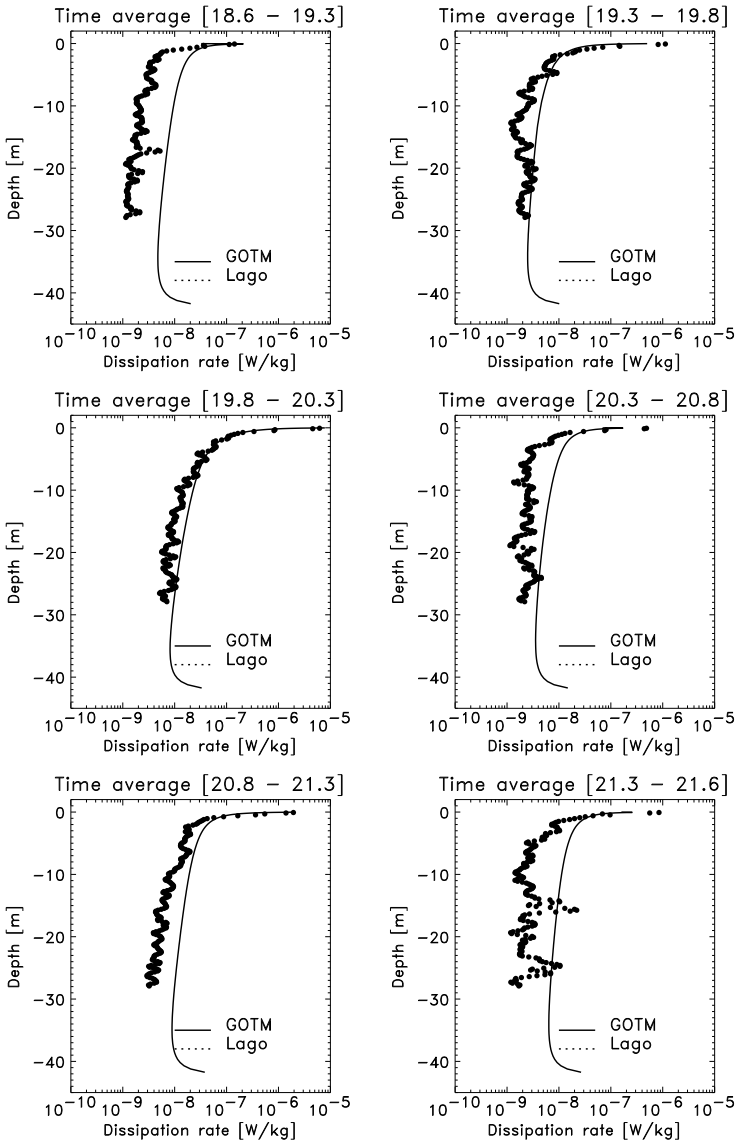

Fig. 7.35. Observed and simulated profiles of turbulent dissipation rate ε in Lago Maggiore during three days in December 1995. The Observations and the model results have been averaged over periods of 12 hours.

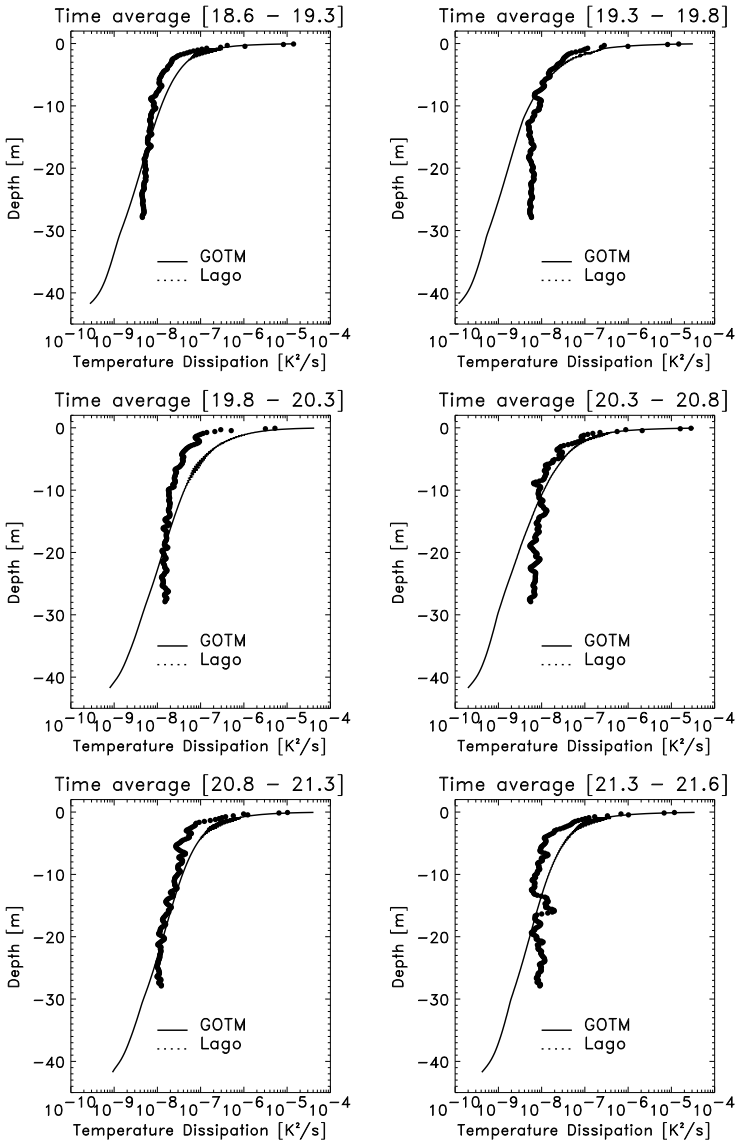

Fig. 7.36. Observed and simulated profiles of temperature variance dissipation rate ε_T in Lago Maggiore during three days in December 1995. The Observations and the model results have been averaged over periods of 12 hours.

8 Future Perspectives

The present study probably rises more questions than it answers. Rather than summarising the achievements discussed in the previous chapters, ten of these open problems are listed and briefly discussed below. They can be used as a guideline for further research. First of all, this list is far from being complete, there are many other problems to be solved as well in the field of marine turbulence modelling. But these future tasks discussed below seem to be – seen from the perspective of the author – the major fields in which further research is needed. However, these open problems have not been intuitively formulated by the author alone. This view is strongly influenced by the discussion with colleagues, mainly during meetings of the CARTUM project, a concerted action on advanced turbulence modelling funded by the European Community.

The first four points are closely related to each other and can probably not be dealt with separately: parameterisations of third-order fluxes, non-local features, internal waves and Langmuir circulation. For these four research fields, substantial contributions from Large Eddy Simulation and Direct Numerical Simulation studies have been made and and can be expected in the future. The determination of surface roughness is a unsolved problem which got more attention during recent years in connection with the parameterisations of the effect of breaking surface waves on near-surface turbulence. The recently presented generic model is based on an old idea which might have a much stronger potential than all other two-equation models. The numerical stability of turbulence models would deserve some more strict mathematical analysis. Due to increasing computer resources, advanced turbulence closure schemes could be more and more used within three-dimensional circulation models. This coupling needs further attention as well. Finally, two observational challenges are mentioned: Improved observations of turbulent kinetic energy by high resolution acoustic profilers and the design of refined field campaigns for better investigating the interaction between turbulence and density gradients in regions of freshwater inflow.

1. **Third-order fluxes:** Third-order fluxes occur in two types of Reynold's averaged equations for second-order fluxes, in the equations for Reynolds stresses, temperature fluxes and salt fluxes and in the equations for turbulent kinetic energy and its dissipation rate. They are of different im-

portance for two-equation models with algebraic second-moment closure, since for the latter quantities, transport equations are solved and for the former not. In the applications discussed in this study, the down-gradient approximation for the vertical turbulent fluxes of turbulent kinetic energy and its dissipation rate has been used, which has been shown to significantly underestimate the physical values, see also figure 6.11. Various physically more sound parameterisations for these third-order fluxes have been suggested in the literature, ranging from non-local relations to complex algebraic closures as the one suggested by *Canuto et al.* [1994] and *Canuto et al.* [2001]. What is missing up to now is a comprehensive comparative study of these different formulations on the basis of which their quality in terms of accuracy and computational costs can be estimated.

2. **Non-locality:** The most striking consequence of neglecting non-local features in the algebraic second-moment closures is the failure in reproducing counter-gradient fluxes which are clearly evident in free convection studies, see figure 6.10 and also the simulations in Lago Maggiore, section 7.5. But also in basic tidal flow, counter-gradient fluxes occur during the flow reversal when the shear production can be negative. The neglect of non-locality by most differential turbulence closure models has given rise to empirical non-local models such as the K-Profile Parameterisation (KPP) model by *Large et al.* [1994]. The non-locality of differential turbulence closure models is a direct consequence of applying the local equilibrium assumption for second-moments and thus neglecting third-order moments. For consideration of non-local features in such models, see e.g. *Zilitinkevich et al.* [1999].
3. **Internal waves:** As discussed in section 3.3.3 of this study, the treatment of internal wave dynamics in turbulence closure models is generally treated on a low level of sophistication, and the present study is no exception to this rule. The reason is the yet poor understanding of these processes due to their complexity. Furthermore, the internal waves and turbulence are difficult to separate, the wave-turbulence transition has only recently been investigated in detail, see *D'Asaro and Lien* [2000]. It is postulated by recent studies that internal waves are the major mechanism for causing third-order transports in stably stratified flows, see *Zilitinkevich* [2002]. The key for explaining why differential models do often underestimate mixing in stably stratified flow might be found here. The recently suggested model modifications by *Axell* [2002] and by *Baumert and Peters* [2002] might be guidelines to solve this problem.
4. **Langmuir circulation:** This mechanism in the surface mixing layer in the ocean caused by the interaction between breaking surface waves and Stokes drift is often treated as a niche in oceanography. Only recent Large Eddy Simulation studies by *Skyllingstad and Denbo* [1995] and *McWilliams et al.* [1997] revealed the important role of Langmuir

circulation for transport and mixing in the mixed layer. The difficulty in understanding Langmuir circulation is that it significantly deviates from the idealistic view of counter-rotating vortices in the ocean mixed layer leaving the characteristic streaky patterns at the surface as evidence. Like internal waves, Langmuir circulation overlaps with turbulent motions which led to the expression *Langmuir turbulence* (pers. comm. Eric Skyllingstad). Further LES and DNS studies are expected to help better understanding the role of this Langmuir turbulence for non-local transports in the oceanic mixed layer.

5. **Surface roughness:** Breaking of surface waves is a complicated physical mechanism which can not even be fully reproduced by the Navier-Stokes equations due to the neglect of surface tension. Thus, parameterisations are needed on any level of modelling, even in DNS studies. In models, which use bulk formulations for the fluxes of momentum, heat, freshwater and gases through the sea surface (most models do that), a surface roughness length has to be specified for reproducing near surface statistical properties of the flow. It is evident that this is much more complicated than estimating the bed roughness with the aid of velocity profile observations. In the literature, no agreement is found whether and how the surface roughness scales with the significant wave height. *Craig* [1996] concludes his study of extending the theory of interaction between breaking surface waves and turbulence with the remark that the theory cannot be considered as a functional predictive tool without solving the problem of determinating the surface roughness length.
6. **Generic Model:** The expression *Generic Model* is here taken from *Baumert et al.* [2000] who used it for introducing a general notation for the length scale equation. When structurally comparing the k-ε, the k-kL and the k-ω^2 model, *Launder and Spalding* [1974] concluded that the k-ε model is the only physically sound model, since only for this model the turbulent Schmidt number resulting after fitting to the law of the wall is of the order of unity. The first results of the Generic Model as recently published by *Umlauf and Burchard* [2001] show however, that certain realisations are more convincing than any of the conventional models. This is possible due to the fact that the Generic Model can be adapted to a greater variety of problems. Still, the full potential of this model is not yet exploited, a task which should be investigated in the near future.
7. **Numerical stability:** Various types of turbulence models tend to show numerical instabilities at even relatively short time steps. Examples for this are usually fully algebraic models which need to be non-linearly iterated in order to stabilise them, see e.g. *Frey* [1991]. But also higher-order turbulence closures like the k-ε model or the k-kL model tend to generate instabilities when they are used in combination with certain stability functions, see *Deleersnijder and Luyten* [1994] and *Burchard and Deleersnijder* [2001] and also section section 6.2.3. Although a physical

explanation for the latter problem has been found, a strict mathematical analysis of such instabilities is missing so far.

8. **Three-dimensional models:** The integration of complex turbulence closure models into three-dimensional circulation models is becoming more and more realistic with increasing computer resources. Suitable turbulence models must be numerically robust (i.e. providing good approximations for large time steps and coarse spatial resolution) and computationally efficient. Numerical problems do often occur near the bed with geopotential coordinates and in horizontally staggered grids due to necessary spatial averaging of shear production terms. Often, water column models are directly implemented into three-dimensional models without consideration of turbulence advection. For the ocean, this might be justified (see *Delhez et al.* [1999]), but for tidal estuaries with fronts this might be an inaccuracy with significant consequences. This problem of turbulence advection and also the general numerical problems occurring when implementing a water column turbulence model into three-dimensional models surely deserve further attention in the future.
9. **Observations of TKE:** Technically, observations of small-scale shear and small scale temperature gradients and thus dissipation of turbulent kinetic energy and temperature variance are easier to observe than the variances of velocity (turbulent kinetic energy) and temperature itself. Acoustic profiling techniques generally have too coarse resolution for observing all energy-containing scales relevant for the determination of turbulent kinetic energy. However, with the aid of high-resolution Acoustic-Doppler Current Profilers (ADCP) Reynolds stresses, shear production and to a certain degree also turbulent kinetic energy can be estimated, see *Stacey et al.* [1999]. There are currently several research activities evaluating the quality of such measurements when applied to resolve near bed turbulence in tidal boundary layers (pers. comm. Tom Rippeth, Ralph Cheng) and for the surface mixed layer (pers. comm. Uli Lass). Joint observations of turbulent dissipation rate as micro-scale parameter and turbulent kinetic energy as integral scale parameter could help to better understanding marine turbulence and its simulation by means of turbulence models.
10. **New SIPS field study:** The one-dimensional model simulation of strain-induced periodic stratification in Liverpool Bay (see section 7.4.2) clearly demonstrates that the characteristic asymmetries of velocity, stratification and turbulence can in principle be reproduced with turbulence models. However, the assumption of constant temperature and salinity gradients seem to be a serious simplification which leads to time lags between observed and simulated profiles. Also, the neglect of momentum advection could have serious consequences. Thus, there is a need for further field studies in regions of freshwater run-off near the coast or also inside estuaries. Such a study should account for the spring-neap

cycle and a variable freshwater source in order to observe the sensitivity of the system of variations of forcing. Time and space variations of horizontal momentum, temperature and salinity gradients should be measured. It should be attempted to simulated these observations with one-dimensional, but also with three-dimensional models in order to explain these variations. Such a comprehensive study could help to better understand estuarine circulation and the transport phenomena (such as estuarine turbidity maxima) associated with it.

9 Appendix

9.1 Notation

9.1.1 General comments

Since many complex partial differential equations are contained in this book, a compact way of denoting partial derivatives has been chosen here:

$$\partial_t = \frac{\partial}{\partial t}, \quad \partial_x = \frac{\partial}{\partial x}, \tag{9.1}$$

and

$$\partial_i = \frac{\partial}{\partial x_i}. \tag{9.2}$$

For simplicity, the summation convention of Einstein is extensively used in this manuscript. This means that summation is applied to repeated indices:

$$\partial_j v_j = \partial_1 v_1 + \partial_2 v_2 + \partial_3 v_3. \tag{9.3}$$

Furthermore, the following symbols are used:

$$\delta_{ij} = \begin{cases} 1 \text{ for } i = j, \\ 0 \text{ for } i \neq j, \end{cases} \tag{9.4}$$

and

$$\varepsilon_{ijl} = \begin{cases} 1 & \text{for cyclic order of indices,} \\ -1 & \text{for anticyclic order of indices,} \\ 0 & \text{for two or more identical indices} \end{cases} \tag{9.5}$$

which are the Kronecker symbol and the alternating tensor, respectively.

9.1.2 Turbulence models

Different notations have always been a major threshold for comparing different turbulence parameterisations. For calculating the eddy viscosity ν_t and eddy diffusivity ν_t', we use the following form (see section 3.1.2):

$$\nu_t = c_\mu \frac{k^2}{\varepsilon}, \qquad \nu_t' = c_\mu' \frac{k^2}{\varepsilon}, \tag{9.6}$$

which automatically results from the algebraic Reynolds stress closure. In other models such as *Mellor and Yamada* [1974] and *Mellor and Yamada* [1982], an alternative formulation is used:

$$K_M = S_M q L, \qquad K_H = S_H q L \tag{9.7}$$

with $q^2 = 2k$ and K_M and K_H being other notations for the eddy viscosity and diffusivity ν_t and ν_t', respectively. S_M and S_H correspond to the stability functions c_μ and c_μ' with the conversion

$$S_M = \frac{c_\mu}{\sqrt{2} c_L}, \quad S_H = \frac{c_\mu'}{\sqrt{2} c_L} \tag{9.8}$$

with c_L from (3.25).

The non-dimensional shear and buoyancy numbers on which the stability functions depend are here consequently expressed as

$$\alpha_M = \frac{k^2}{\varepsilon^2} M^2, \qquad \alpha_N = \frac{k^2}{\varepsilon^2} N^2. \tag{9.9}$$

With the *Mellor and Yamada* [1974] and *Mellor and Yamada* [1982] notation for these non-dimensional parameters,

$$G_M = \frac{L^2}{q^2} M^2, \qquad G_H = \frac{L^2}{q^2} N^2, \tag{9.10}$$

the conversion between α_M, α_N and G_M and G_H is of the following form:

$$G_M = \frac{c_L^2}{2} \alpha_M, \qquad G_H = \frac{c_L^2}{2} \alpha_N. \tag{9.11}$$

By means of (9.8) and (9.11), the sets of stability functions presented in section 3.1.3 may be transformed to the other notation.

It should be noted that further definitions of stability functions are often used such as $\nu_t = c_\mu \sqrt{k} L$ (see *Burchard et al.* [1998]) and $\nu_t = 2 c_\mu k^2 / \varepsilon$ (see *Canuto et al.* [2001]).

Another reason for confusion is often the different use of the parameter $c_{3\varepsilon}$ in the dissipation rate equation (3.67). In this paper, the right hand side of that equation reads as $(\varepsilon/k)(c_{1\varepsilon} P + c_{3\varepsilon} B - c_{2\varepsilon} \varepsilon)$, but often the form $(\varepsilon/k)(c_{1\varepsilon}(P + c_{3\varepsilon} B) - c_{2\varepsilon} \varepsilon)$ (*Rodi* [1980], *Burchard and Baumert* [1995]) is used. This, of course will lead to different values for $c_{3\varepsilon}$.

9.2 List of symbols

Param.	Physical meaning	Unit/Value	Ref.
α	aspect ratio	–	p. 30
α_C	parameter in Charnok formula	1400	(3.44)
α_k	spatial decay rate of k	–	(3.116)
α_m	exponent	–	(3.119)
α_M	shear parameter	–	(3.26)
α_N	buoyancy parameter	–	(3.26)
β_S	haline expansion coefficient	$\mathrm{kg\,m^{-3}psu^{-1}}$	(2.8)
β_T	thermal expansion coefficient	$\mathrm{kg\,m^{-3}K^{-1}}$	(2.8)
γ_i	relative vertical coordinate	–	(4.1)
δ_{ij}	Kronecker symbol	–	(9.4)
Δt	time step	s	(4.6)
Δz	vertical grid size	m	p. 152
ε	dissipation of TKE	$\mathrm{W\,kg^{-1}}$	(2.31)
ε_0	initial values for dissipation	$\mathrm{m^2s^{-3}}$	(3.91)
ε_ε	dissipation of dissipation	$\mathrm{m^2s^{-4}}$	(2.33)
ε_{ij}	dissipation of $\langle\tilde{u}_i\tilde{u}_j\rangle$	$\mathrm{m^2s^{-3}}$	(2.25)
ε_{ijl}	alternating tensor	–	(9.5)
ε_{iT}	dissipation of heat flux	$\mathrm{m\,K\,s^{-2}}$	(2.26)
$\varepsilon_{\min}$	limiting value for dissipation	$\mathrm{W\,kg^{-1}}$	(3.133)
ε_T	dissipation of T variance	$\mathrm{K^2s^{-1}}$	(2.28)
ε_{TS}	dissipation of T-S correlator	$\mathrm{K\,psu\,s^{-1}}$	(2.29)
ζ	sea surface elevation	m	(3.4)
η_1	attenuation coefficient	$\mathrm{m^{-1}}$	(7.1)
κ	von Kármán constant	0.4	(3.37)
$\tilde{\kappa}$	slope of L for $S = N = 0$	≈ 0.2	(3.116)
λ	Kolmogorov micro scale	m	(3.40)
μ	dynamic viscosity	$1.3 \cdot 10^{-3}$ $\mathrm{kg\,m^{-1}s^{-1}}$	(2.1)
ν	kinematic viscosity	$1.3 \cdot 10^{-6}$ $\mathrm{m^2s^{-1}}$	(2.2)
ν'	thermal diffusivity	$1.38 \cdot 10^{-7}$ $\mathrm{m^2s^{-1}}$	(2.5)
ν''	haline diffusivity	$1.1 \cdot 10^{-9}$ $\mathrm{m^2s^{-1}}$	(2.6)
ν_t	eddy viscosity for momentum	$\mathrm{m^2s^{-1}}$	(3.24)
$(\nu_t)^{IW}$	backgr. viscosity, internal waves	$\mathrm{m^2s^{-1}}$	(3.132)
$(\nu_t)^{SI}$	backgr viscosity, shear instability	$\mathrm{m^2s^{-1}}$	(3.131)
ν_t'	eddy difusivity for tracers	$\mathrm{m^2s^{-1}}$	(3.24)
$(\nu_t')^{IW}$	backgr diffusivity, internal waves	$\mathrm{m^2s^{-1}}$	(3.132)
$(\nu_t')^{SI}$	backgr diffusivity, shear instability	$\mathrm{m^2s^{-1}}$	(3.131)
ξ	non-dim distance from surface	–	(3.38)
Π_{ij}	pressure-strain corr. of $\langle\tilde{u}_i\tilde{u}_j\rangle$	$\mathrm{m^2s^{-3}}$	(2.25)

Param.	Physical meaning	Unit/Value	Ref.
Π_{iT}	pressure-strain corr. of heat flux	$\mathrm{m\,K\,s^{-2}}$	(2.26)
ρ	potential density	$\mathrm{kg\,m^{-3}}$	(2.4)
ρ_0	reference density	$\mathrm{kg\,m^{-3}}$	(2.4)
σ	Crank-Nicolson parameter	–	(4.6)
σ_ε	Schmidt no. for ε	–	(3.66)
$\sigma_{\varepsilon 0}$	Schmidt no. for ε, wave breaking	–	(3.123)
σ_ω	Schmidt no. for ω	–	(3.78)
$\sigma_{\varepsilon 1}$	Schmidt no. for ε, log-law	–	(3.70)
σ_{nm}	Schmidt no. for generic equation	–	(3.111)
τ	turbulent time scale	s	(3.79)
τ_1	time scale for analytical solution	s	(3.89)
τ_ε	turbulent time scale for ε-equation	s	(3.80)
τ_k	turbulent time scale for k-equation	s	(3.79)
τ_m	time scale for analytical solution	s	(3.90)
τ_b	absolute value of bottom stress	$\mathrm{N\,m^{-2}}$	(4.33)
τ_b^x	bottom stress in x-direction	$\mathrm{N\,m^{-2}}$	(4.33)
τ_b^y	bottom stress in y-direction	$\mathrm{N\,m^{-2}}$	(4.34)
τ_R	relaxation time scale	s	p. 155
τ_s	absolute value of surface stress	$\mathrm{N\,m^{-2}}$	fig. 7.21
τ_s^x	surface stress in x-direction	$\mathrm{N\,m^{-2}}$	(3.59)
τ_s^y	surface stress in y-direction	$\mathrm{N\,m^{-2}}$	(3.59)
τ_∞	asymptotic turbulent time scale	s	(3.84)
Φ	latitude	–	(2.4)
Φ_H	Monin-Obukhov param. (heat)	–	(3.37)
Φ_M	Monin-Obukhov param. (mom.)	–	(3.37)
ω	turbulence frequency	$\mathrm{s^{-1}}$	(3.78)
ω_i	comp. of total vorticity	$\mathrm{s^{-1}}$	(3.138)
Ω	earth angular vel.	$7.3 \cdot 10^{-5}\ \mathrm{s^{-1}}$	(2.4)
Ω_i	comp. of earth rotation vector	$\mathrm{s^{-1}}$	(2.4)
Ω_{ij}	redistribution of $\langle \tilde{u}_i \tilde{u}_j \rangle$	$\mathrm{m^2 s^{-3}}$	(2.25)
Ω_{iT}	redistribution of heat flux	$\mathrm{m\,K\,s^{-2}}$	(2.26)
a	parameter being between 0 and 1	–	(3.126)
b	buoyancy	$\mathrm{m\,s^{-2}}$	(3.4)
B	buoyancy production of TKE	$\mathrm{m^2 s^{-3}}$	(2.31)
B_0	surface buoyancy flux	$\mathrm{m^2 s^{-3}}$	(6.5)
B_1	emp. parameter for k-kL model	–	(3.71)
B_ε	buoyancy production of ε	$\mathrm{m^2 s^{-4}}$	(2.33)
B_{ij}	buoyancy production of $\langle \tilde{u}_i \tilde{u}_j \rangle$	$\mathrm{m^2 s^{-3}}$	(2.25)
B_{iT}	buoyancy production of heat flux	$\mathrm{m\,K\,s^{-2}}$	(2.26)
c	speed of sound	$\mathrm{m\,s^{-1}}$	p. 33

Param.	Physical meaning	Unit/Value	Ref.
$c_1, \ldots, c_5$	emp. coefficients for Π_{ij}	–	(2.34)
$c_{1T}, \ldots, c_{4T}$	emp. coefficients for Π_{iT}	–	(2.37)
$c_{1\varepsilon}, \ldots, c_{3\varepsilon}$	emp. coefficients for ε-equation	–	(3.67)
$c_{1\omega}, \ldots, c_{3\omega}$	emp. coefficients for ω-equation	–	(3.78)
$c_{1nm}, \ldots, c_{3nm}$	emp. coefficients for generic eq.	–	(3.111)
c_T	emp. coefficient for ε_T	–	(2.41)
c_μ	stab. funct. for mom.	–	(3.19)
c_μ^0	neutral stab. funct. for mom.	–	p. 37
c_μ'	stab. funct. for tracers	–	(3.21)
c_L	parameter for macro length scale	–	(3.25)
c^{LC}	coeff. for Langmuir downwelling vel.	–	(3.141)
c_p'	specific heat capacity of water	$3980\,\mathrm{J kg^{-1} K^{-1}}$	(2.5)
c_w	coeff. for TKE flux, wave-breaking	100	(3.117)
C	param. in anal. sol. of k-ε system	–	(3.89)
C_t	parameter for Thorpe scale	1.4	(3.103)
D	water depth	m	(3.46)
D_{ij}	anisotropic shear prod. of $\langle \tilde{u}_i \tilde{u}_j \rangle$	$\mathrm{m^2 s^{-3}}$	(2.34)
D_m	mixed layer depth	m	(3.142)
d_b	distance from bottom	m	(3.76)
d_l	bottom grid zooming parameter	–	(4.2)
d_s	distance from surface	m	(3.76)
d_u	surface grid zooming parameter	–	(4.2)
$e_1, \ldots, e_4$	emp. parameters for variances	–	(3.30)
e	mean kinetic energy	$\mathrm{m^2 s^{-2}}$	(2.23)
$E(k_w)$	energy spectrum	$\mathrm{m^3 s^{-2}}$	(2.9)
$E_1, \ldots, E_3$	emp. parameters for kL equation	–	(3.71)
f	Coriolis parameter	$\mathrm{s^{-1}}$	(3.4)
$\mathcal{F}_i$	frictional force	$\mathrm{kg\,m^{-2} s^{-2}}$	(2.1)
g	gravitational acceleration	$9.81\ \mathrm{m\,s^{-2}}$	(2.4)
g_i	comp. of grav. acc. vector	$\mathrm{m\,s^{-2}}$	(2.4)
G_H	buoyancy parameter	–	(9.10)
G_M	shear parameter	–	(9.10)
h_0^b	height of bott. roughness elements	m	(3.43)
$\mathcal{H}$	vertical length scale in the ocean	m	(3.1)
h_i	discrete layer depth	m	(4.1)
H	mean water depth	m	(3.46)
H_s	significant wave height	m	p. 88
i	index or exponent	–	(2.4)
I	solar radiation in water column	$\mathrm{W\,m^{-2}}$	(2.5)
I_0	solar radiation at surface	$\mathrm{W\,m^{-2}}$	(7.1)

Param.	Physical meaning	Unit/Value	Ref.
j	index or exponent	–	(2.4)
k	turbulent kinetic energy (TKE)	$\mathrm{J\,kg^{-1}}$	(2.30)
k_0	initial value for TKE	$\mathrm{J\,kg^{-1}}$	(3.90)
$k_{\min}$	background value for TKE	$\mathrm{J\,kg^{-1}}$	(3.134)
k_w	wave no.	$\mathrm{m^{-1}}$	(2.9)
l	index or exponent	–	(2.4)
L	integral-scale macro length	m	(2.10)
L_0	surface value of macro length	m	fig. 3.20
$\mathcal{L}$	length scale	m	(2.2)
L_b	buoyancy length scale	m	(3.99)
L_E	Ellison length scale	m	(3.102)
L_{lim}	limit for macro length scale	m	(3.73)
L_M	Monin-Obukhov length	m	(3.37)
L_O	Ozmidov length	m	(3.98)
L_{Th}	Thorpe scale	m	(3.103)
L_w	surface wave length	m	(3.137)
L_z	progn. length scale for kL eq.	m	(3.71)
m	index or exponent	–	(2.25)
M	shear frequency	$\mathrm{s^{-1}}$	(3.26)
n	index	–	(2.13)
N	Brunt-Väisälä frequency	$\mathrm{s^{-1}}$	(3.26)
N_0	initial Brunt-Väisälä frequency	$\mathrm{s^{-1}}$	(6.1)
N_i	no. of discrete layers	–	(4.1)
p	pressure	$\mathrm{N\,m^{-2}}$	(2.4)
p_0	hydrostatic reference pressure	$\mathrm{N\,m^{-2}}$	(3.3)
P	shear production of TKE	$\mathrm{m^2 s^{-3}}$	(2.31)
P_ε	shear prod. of dissipation	$\mathrm{m^2 s^{-4}}$	(2.33)
P_{ij}	shear prod. of $\langle \tilde{u}_i \tilde{u}_j \rangle$	$\mathrm{m^2 s^{-3}}$	(2.25)
P_r	turbulent Prandtl no.	–	p. 46
P_r^0	neutral turbulent Prandtl no.	0.74	(3.109)
P_{iT}	mean gradient prod. of heat flux	$\mathrm{m\,K\,s^{-2}}$	(2.26)
P_T	mean gradient prod. of T variance	$\mathrm{K^2 s^{-1}}$	(2.28)
P_{TS}	mean gradient prod. of T-S corr.	$\mathrm{K\,psu\,s^{-1}}$	(2.29)
q	rms vel. fluctuations	$\mathrm{m\,s^{-1}}$	(2.10)
Q	Heat content	$\mathrm{J\,m^{-2}}$	fig. 7.1
Q_b	long-wave back radiation at surface	$\mathrm{W\,m^{-2}}$	(3.60)
Q_E	evaporation	$\mathrm{kg\,m^{-2} s^{-1}}$	(3.61)
Q_l	latent surface heat flux	$\mathrm{W\,m^{-2}}$	(3.60)
Q_P	precipitation	$\mathrm{kg\,m^{-2} s^{-1}}$	(3.61)
Q_s	sensitive surface heat flux	$\mathrm{W\,m^{-2}}$	(3.60)

Param.	Physical meaning	Unit/Value	Ref.
Q_{tot}	total surface heat flux	$\mathrm{W\,m^{-2}}$	fig. 7.21
R_e	integral-scale Reynolds no.	–	(2.10)
R_i	gradient Richardson no.	–	p. 45
R_i^c	critical gradient Richardson no.	–	p. 46
R_i^{st}	steady-state gradient Richardson no.	–	(3.96)
R_i^∞	R_i for Miles-Howard theory	0.25	(3.109)
R_o	turbulent Rossby no.	–	p. 36
S	salinity	psu	(2.6)
S_0	reference salinity	psu	(2.8)
S_{ij}	shear tensor	$\mathrm{s^{-1}}$	(2.34)
S_H	stab. funct. for tracers	–	(9.8)
S_l	stab. funct. for kL	–	(3.71)
S_M	stab. funct. for momentum	–	(9.8)
S_q	stab. funct. for k in k-kL model	–	(3.72)
t	time	s	(2.4)
T	potential temperature	K	(2.5)
T_*	Deardorff temperature scale	K	(6.6)
T_0	reference temperature	K	(2.8)
$\mathcal{T}$	time scale	s	(2.2)
u	vel. comp. in x direction	$\mathrm{m\,s^{-1}}$	(3.1)
u_*	friction vel.	$\mathrm{m\,s^{-1}}$	(3.35)
u_*^b	bottom friction vel.	$\mathrm{m\,s^{-1}}$	(3.43)
u_*^{bx}	x-comp. of bottom friction vel.	$\mathrm{m\,s^{-1}}$	(4.33)
u_*^{by}	y-comp. of bottom friction vel.	$\mathrm{m\,s^{-1}}$	(4.34)
u_*^s	surface friction vel.	$\mathrm{m\,s^{-1}}$	(3.44)
u_*^{sx}	x-comp. of surface friction vel.	$\mathrm{m\,s^{-1}}$	(3.59)
u_*^{sy}	y-comp. of surface friction vel.	$\mathrm{m\,s^{-1}}$	(3.59)
$\mathcal{U}$	vel. scale	$\mathrm{m\,s^{-1}}$	(2.2)
$\mathcal{U}_*$	turbulent vel. scale	$\mathrm{m\,s^{-1}}$	(3.1)
U_{10}	x-comp. of 10 m wind speed vector	$\mathrm{m\,s^{-1}}$	(3.137)
u_b	x-comp. near-bed discrete vel.	$\mathrm{m\,s^{-1}}$	(4.35)
U_s	x-comp. of Stokes drift vel.	$\mathrm{m\,s^{-1}}$	(3.137)
v_i	vel. comp. in x_i-direction	$\mathrm{m\,s^{-1}}$	(2.3)
v	vel. comp. in y direction	$\mathrm{m\,s^{-1}}$	(3.1)
V_{10}	y-comp. of 10 m wind speed vector	$\mathrm{m\,s^{-1}}$	(3.137)
v_b	y-comp. near-bed discrete vel.	$\mathrm{m\,s^{-1}}$	(4.36)
V_{ij}	vorticity tensor	$\mathrm{s^{-1}}$	(2.38)
V_s	y-comp. of Stokes drift vel.	$\mathrm{m\,s^{-1}}$	(3.137)
w	vel. comp. in z direction	$\mathrm{m\,s^{-1}}$	(3.1)
w_*	Deardorff vel. scale	$\mathrm{m\,s^{-1}}$	(6.5)

Param.	Physical meaning	Unit/Value	Ref.
w_*^{LC}	Langmuir circulation downwelling vel.	$\mathrm{m\,s^{-1}}$	(3.141)
x	northward coordinate	m	(2.4)
y	eastward coordinate	m	(2.4)
z	upward coordinate	m	(2.4)
z'	distance from surface or bottom	m	(3.3)
z_0^b	bottom roughness length	m	(3.43)

References

Abdella, K., and N. A. McFarlane, A new second-oder turbulence closure scheme for the planetary boundary layer, *Journal of Atmospheric Sciences*, *54*, 1850–1867, 1997.

Aikman, F., G. L. Mellor, T. Ezer, D. Shenin, P. Chen, L. Breaker, K. Bosley, and D. B. Rao, Toward an east coast operational nowcast/forecast system, in *Modern Approaches to Data Assimilation in Ocean Modeling*, edited by P. Malanotte-Rizzoli, pp. 347–376, Elsevier Sci., New York, 1996.

Andre, J. C., P. Lacarrere, and K. Traore, Pressure effects on triple correlations in turbulent convective flows, in *Turbulent shear flow*, vol. 3, pp. 243–252, Springer, 1982.

Anis, A., and J. N. Moum, Surface wave-turbulence interactions: Scaling $\varepsilon(z)$ near the sea surface, *J. Phys. Oceanogr.*, *25*, 2025–2045, 1995.

Axell, L., Wind-driven internal waves and Langmuir circulations in a numerical ocean model of the southern Baltic Sea, *J. Geophys. Res.*, 2002, in print.

Axell, L., and O. Liungman, A one-equation turbulence model for geophysical applications: Comparison with data and the k-epsilon model, *Environmental Fluid Mechanics*, *1*, 71–106, 2001.

Ayotte, K. W., et al., An evaluation of neutral and convective planetary boundary-layer parameterizations relative to Large Eddy Simulations, *Bound. Layer Meteor.*, *79*, 131–175, 1996.

Baker, M. A., and C. H. Gibson, Sampling turbulence in the stratified ocean: Statistical consequences of strong intermittency, *J. Phys. Oceanogr.*, *17*, 1817–1836, 1987.

Batchelor, G. K., *An introduction to fluid mechanics*, Cambridge University Press, Cambridge, 1967.

Baum, E., and E. A. Caponi, Modeling of the effects of buoyancy on the evolution of geophysical boundary layers, *J. Geophys. Res.*, *97*, 15,513–15,527, 1992.

Baumert, H., Dreidimensionale hydrodynamisch-numerische Simulation geschichteter Wassermassen bei Anströmung eines Hindernisses, *Tech. rep.*, Zentrum für Meeres- und Klimaforschung, Universität Hamburg, Institut für Meereskunde, Hamburg, Germany, 1992.

Baumert, H., and H. Peters, Second-moment closures and length scales for weakly stratified turbulent shear flows, *J. Geophys. Res.*, *105*, 6453–6468, 2000.

Baumert, H., and H. Peters, Toward a two-equation turbulence closure without adjustable parameters, 2002, poster presented at the Ocean Sciences Meeting, Honululu, Hawaii, February 2002.

Baumert, H., and G. Radach, Hysteresis of turbulent kinetic energy in nonrotational tidal flows: A model study, *J. Geophys. Res.*, *97*, 3669–3677, 1992.

Baumert, H., G. Bruckner, E. Kleine, R. Kluge, and W. Müller, Abschlußbericht zur G_4-verteidigung, *Tech. rep.*, Karl-Weierstraß-Institut für Mathematik, Akademie der Wissenschaften der DDR, Berlin, 1989.

Baumert, H., G. Chapalain, H. Smaoui, J. P. McManus, H. Yagi, M. Regener, J. Sündermann, and B. Szilagy, Modelling and numerical simulation of turbulence, waves and suspended sediments for pre-operational use in coastal seas, *Coastal Engineering*, *41*, 63–93, 2000.

Becker, G. A., Beiträge zur Hydrographie und Wärmebilanz der Nordsee, *Dt. Hydrogr. Z.*, *34*, 167–262, 1981.

Beckers, J.-M., La mediterranée occidentale: de la modélisation mathématique à la simulation numérique, Ph.D. thesis, Université de Liège, Belgium, 1995, collection des publications de la Faculté des Sciences Appliquées No. 136.

Beckers, J.-M., H. Burchard, J.-M. Campin, E. Deleersnijder, and P.-P. Mathieu, Another reason why simple discretizations of rotated diffusion operators cause problems in ocean models. Comments on the paper *isoneutral diffusion in a z-coordinate ocean model* by Griffies et al., *J. Phys. Oceanogr.*, *28*, 1552–1559, 1998.

Bertuccioli, L., G. I. Roth, J. K. T. R., and Osborn, Turbulence measurements in the bottom boundary layer using Particle Image Velocimetry, *J. Atmos. Ocean. Technol.*, *16*, 1635–1646, 1999.

Blackadar, A. K., The vertical distribution of wind and turbulent exchange in neutral atmosphere, *J. Geophys. Res.*, *67*, 3095–3102, 1962.

Blanke, B., and P. Delecluse, Variability of the tropical Atlantic Ocean simulated by a general circulation model with two different mixed-layer physics, *J. Phys. Oceanogr.*, *23*, 1363–1388, 1993.

Bleck, R., and L. T. Smith, A wind-driven isopycnic coordinate model of the North and Equatorial Atlantic Ocean. 1. Model development and supporting experiments, *J. Geophys. Res.*, *95*, 3273–3285, 1990.

Blumberg, A. F., and G. L. Mellor, A description of a coastal ocean circulation model, in *Three dimensional ocean models*, edited by N. S. Heaps, pp. 1–16, American Geophysical Union, Washington, D.C., 1987.

Bolding, K., H. Burchard, T. Pohlmann, and A. Stips, Turbulent mixing in the Northern North Sea: a numerical model study, *Cont. Shelf Res.*, 2000, submitted.

Bradshaw, P., *An introduction to turbulence and its measurements*, Pergamon, 1975.

Brainerd, K. E., and M. C. Gregg, Diurnal stratification and turbulence in the oceanic surface mixed layer. 1. Observations, *J. Geophys. Res.*, *98*, 22,645–22,656, 1993a.

Brainerd, K. E., and M. C. Gregg, Diurnal stratification and turbulence in the oceanic surface mixed layer. 2. Modeling, *J. Geophys. Res.*, *98*, 22,645–22,656, 1993b.

Briggs, D. A., J. H. Ferziger, J. R. Koseff, and S. G. Monismith, Entrainment in a shear-free turbulent mixing layer, *J. Fluid Mech.*, *310*, 215–241, 1996.

Brockmann, U. H., K. Eberlein, K. Huber, H.-J. Neubert, G. Radach, and K. Schulze (Eds.), *JONSDAP '76: FLEX/INOUT Atlas, Vol. 1*, no. 63 in ICES Oceanographic Data Lists and Inventories, Conseil International pour l'Exploration de la Mer, Copenhagen, Denmark, 1984.

Bryan, K., A numerical model for the study of the world ocean, *J. Computat. Phys.*, *4*, 347–376, 1969.

Burchard, H., Turbulenzmodellierung mit Anwendungen auf thermische Deckschichten im Meer und Strömungen in Wattengebieten, Ph.D. thesis, Institut für Meereskunde, Universität Hamburg, 1995, published as: Report 95/E/30, GKSS Research Centre.

Burchard, H., Recalculation of surface slopes as forcing for numerical water column models of tidal flow, *App. Math. Modelling*, *23*, 737–755, 1999.

Burchard, H., Note on the q^2l equation by Mellor and Yamada [1982], *J. Phys. Oceanogr.*, *31*, 1377–1387, 2001a.

Burchard, H., Simulating the wave-enhanced layer under breaking surface waves with two-equation turbulence models, *J. Phys. Oceanogr.*, *31*, 3133–3145, 2001b.

Burchard, H., Energy-conserving discretisation of turbulent shear and buoyancy production, *Ocean Modelling*, *4*, 347–361, 2002.

Burchard, H., and H. Baumert, On the performance of a mixed-layer model based on the k-ε turbulence closure, *J. Geophys. Res.*, *100*, 8523–8540, 1995.

Burchard, H., and H. Baumert, The formation of estuarine turbidity maxima due to density effects in the salt wedge. A hydrodynamic process study, *J. Phys. Oceanogr.*, *28*, 309–321, 1998.

Burchard, H., and K. Bolding, Comparative analysis of four second-moment turbulence closure models for the oceanic mixed layer, *J. Phys. Oceanogr.*, *31*, 1943–1968, 2001.

Burchard, H., and K. Bolding, GETM – a general estuarine transport model. Scientific documentation, *Tech. Rep. EUR 20253 EN*, European Commission, 2002.

Burchard, H., and E. Deleersnijder, Stability of algebraic non-equilibrium second-order closure models, *Ocean Modelling*, *3*, 33–50, 2001.

Burchard, H., and O. Petersen, Hybridisation between σ and z coordinates for improving the internal pressure gradient calculation in marine models with steep bottom slopes, *Int. J. Numer. Meth. Fluids*, *25*, 1003–1023, 1997.

Burchard, H., and O. Petersen, Models of turbulence in the marine environment – A comparative study of two-equation turbulence models, *J. Mar. Sys.*, *21*, 29–53, 1999.

Burchard, H., O. Petersen, and T. P. Rippeth, Comparing the performance of the Mellor-Yamada and the k-ε two-equation turbulence models, *J. Geophys. Res.*, *103*, 10,543–10,554, 1998.

Burchard, H., K. Bolding, and M. R. Villarreal, GOTM – a general ocean turbulence model. Theory, applications and test cases, *Tech. Rep. EUR 18745 EN*, European Commission, 1999.

Burchard, H., A. Stips, W. Eifler, K. Bolding, and M. R. Villarreal, Numerical simulation of dissipation measurements in non-stratified and strongly stratified estuaries, in *Interactions between estuaries, coastal seas and shelf seas*, edited by T. Yanagi, pp. 1–18, Terra Scientific Publishing, Tokyo, 2000.

Burchard, H., K. Bolding, T. P. Rippeth, A. Stips, J. H. Simpson, and J. Sündermann, Microstructure of turbulence in the Northern North Sea: A comparative study of observations and model simulations, *Journal of Sea Research*, 2001, in print.

Businger, J. A., J. C. Wyngaard, Y. Izumi, and E. F. Bradley, Flux profile relationships in the atmospheric surface layer, *Journal of Atmospheric Sciences*, *28*, 181–189, 1971.

Canuto, V. M., Turbulent convection with overshooting: Reynolds stress approach, *Journal of Astrophysics*, *392*, 218–232, 1992.

Canuto, V. M., Large eddy simulation of turbulence: a subgrid model including shear, vorticity, rotation and buoyancy, *Journal of Astrophysics*, *428*, 729–752, 1994.

Canuto, V. M., Compressible turbulence, *Journal of Astrophysics*, *482*, 827–851, 1997.

Canuto, V. M., and M. Dubovikov, A dynamical model for turbulence. IV. Buoyancy driven flows, *Physics of Fluids*, *9*, 2118–2131, 1997a.

Canuto, V. M., and M. Dubovikov, A dynamical model for turbulence. V. The effect of rotation, *Physics of Fluids*, *9*, 2132–2140, 1997b.

Canuto, V. M., F. Minotti, C. Ronchi, M. Ypma, and O. Zeman, Second-order closure PBL model with new third-order moments: Comparison with LES data, *Journal of Atmospheric Sciences*, *51*, 1605–1618, 1994.

Canuto, V. M., A. Howard, Y. Cheng, and M. S. Dubovikov, Ocean turbulence. Part I: One-point closure model. Momentum and heat vertical diffusivities, *J. Phys. Oceanogr.*, *31*, 1413–1426, 2001.

Canuto, V. M., A. Howard, Y. Cheng, and M. S. Dubovikov, Ocean turbulence. Part II: Vertical diffusivities of momentum, heat, salt, mass, and passive scalars, *J. Phys. Oceanogr.*, *32*, 240–264, 2002.

Charnok, H., Wind stress on a water surface, *Q. J. R. Meteorol. Soc.*, *81*, 639–640, 1955.

Chen, C. T., and F. J. Millero, Precise thermodynamic properties of natural waters covering only the limnological range, *Limnol. Oceanogr.*, *31*, 657–662, 1986.

Cheng, N.-S., and A. W.-K. Law, Measurements of turbulence generated by oscillating grid, *J. Hydr. Eng.*, *127*, 201–208, 2001.

Chorin, A., and J. Marsden, *An introduction to fluid mechanics*, Springer Universitext, 1979.

Chou, P. Y., On an extension of reynolds method of finding apparent stresses and the nature of turbulence, *Chinese J. Phys.*, *4*, 1–33, 1940.

Chou, P. Y., On velocity correlations and the solutions of the equations of the turbulent fluctuations, *Quart. Applied Math.*, *3*, 38–54, 1945.

Clayson, C. A., and L. H. Kantha, Turbulent kinetic energy and its dissipation rate in the equatorial mixed layer, *J. Phys. Oceanogr.*, *29*, 2146–2166, 1999.

Cox, M. D., A primitive equation, 3-dimensional model for the ocean, *Tech. Rep. 1*, Geophysical Fluid Dynamics Laboratory, University of Princeton, Princeton, N. J., 1984, 75 pp.

Craig, P. D., Velocity profiles and surface roughness under breaking waves, *J. Geophys. Res.*, *101*, 1265–1277, 1996.

Craig, P. D., and M. L. Banner, Modelling wave-enhanced turbulence in the ocean surface layer, *J. Phys. Oceanogr.*, *24*, 2546–2559, 1994.

Craik, A. D. D., and S. Leibovich, A rational model for Langmuir circulation, *J. Fluid Mech.*, *73*, 401–426, 1976.

Crank, J., and P. Nicolson, A practical method for numerical evaluation of solutions of partial differential equations of the heat-conduction type, *Proc. Cambridge Philos. Soc.*, *43*, 50–67, 1947, re-published in: John Crank 80th birthday special issue *Adv. Comput. Math.* **6** (1997) 207-226.

D'Alessio, S. D. J., K. Abdella, and N. A. McFarlane, A new second-order turbulence closure scheme for modeling the oceanic mixed layer, *J. Phys. Oceanogr.*, *28*, 1624–1641, 1998.

Daly, B. J., and F. H. Harlow, Transport equations of turbulence, *Physics of Fluids*, *13*, 2634–2649, 1970.

D'Asaro, E. A., and R.-C. Lien, The wave-turbulence transition for stratified flows, *J. Phys. Oceanogr.*, *30*, 1669–1678, 2000.

Deleersnijder, E., and P. Luyten, On the practical advantages of the quasi-equilibrium version of the Mellor and Yamada level 2.5 turbulence closure applied to marine modelling, *App. Math. Modelling*, *18*, 281–287, 1994.

Deleersnijder, E., J.-M. Beckers, J.-M. Campin, M. El Mohajir, T. Fichefet, and P. Luyten, Some mathematical problems associated with the development and use of marine models, in *The mathematics of models for clima-*

tology and environment, edited by J. I. Diaz, vol. 48 of *NATO ASI Series*, pp. 41–86, Springer, Berlin, Heidelberg, 1997.

Delhez, E. J. M., M. Grégoire, J. C. J. Nihoul, and J.-M. Beckers, Dissection of the GHER turbulence closure scheme, *J. Mar. Sys.*, *21*, 379–397, 1999.

Demirov, E., and N. Pinardi, The Mediterranean circulation from 1979 to 1993 model simulations. Part I: Interannual variability, *J. Mar. Sys.*, 2001, in print.

Demirov, E., W. Eifler, M. Ouberdous, and N. Hibma, ISPRAMIX – a three-dimensional free surface model for coastal ocean simulations and satellite data assimilation on parallel computers, *Tech. Rep. EUR 18129 EN*, European Commission, 1998.

Denbo, D. W., and E. D. Skyllingstad, An open ocean Large Eddy Simulation model with application to deep convection in the Greenland Sea, *J. Geophys. Res.*, *101*, 1095–1110, 1996.

Denman, K. L., A time-dependent model of the upper ocean, *J. Phys. Oceanogr.*, *3*, 173–184, 1973.

deSilva, I. P. D., and H. J. S. Fernando, Some aspects of mixing in a stratified turbulent patch, *J. Fluid Mech.*, *240*, 601–625, 1992.

Dewey, R. K., W. R. Crawford, A. E. Gargett, and N. S. Oakey, A microstructure instrument for profiling oceanic turbulence in coastal bottom boundary layers, *Journal of Atmospheric and Oceanic Technology*, *4*, 288–297, 1987.

Dickey, T. D., and G. L. Mellor, Decaying turbulence in neutral and stratified fluids, *J. Fluid Mech.*, *99*, 13–31, 1980.

Domaradzki, J. A., and G. L. Mellor, A simple turbulence closure hypothesis for the triple velocity correlation functions in homogeneous isotropic turbulence, *J. Fluid Mech.*, *140*, 45–61, 1984.

Drennan, W. M., A. A. Donelan, E. A. Terray, and K. B. Katsaros, Oceanic turbulence dissipation rate measurements in SWADE, *J. Phys. Oceanogr.*, *26*, 808–815, 1996.

Eifler, W., and W. Schrimpf, ISPRAMIX, a hydrodynamic program for computing regional sea circulation patterns and transfer processes, *Tech. Rep. EUR 14856 EN*, European Commission, 1992.

Ezer, T., Decadal variabilities of the upper layers of the subtropical North Atlantic: An ocean model study, *J. Phys. Oceanogr.*, *29*, 3111–3124, 1999.

Ezer, T., On the seasonal mixed layer simulated by a basin-scale ocean model and the Mellor-Yamada turbulence scheme, *J. Geophys. Res.*, *105*, 16,843–16,855, 2000.

Ezer, T., and G. L. Mellor, A numerical study on the variability and the separation of the Gulf Stream induced by surface atmospheric forcing and lateral boundary flows, *J. Phys. Oceanogr.*, *22*, 660–682, 1992.

Ezer, T., and G. L. Mellor, Simulations of the Atlantic Ocean with a free surface sigma coordinate system, *J. Geophys. Res.*, *102*, 15,647–15,657, 1997.

Fefferman, C. L., Existence & smoothness of the Navier-Stokes equation, 2000, manuscript. Available from: Clay Mathematics Institute, 1770 Massachusetts Avenue, # 331, Cambridge, Massachusetts 02140, U.S.A. See also World Wide Web at `http://www.claymath.org/prize_problems/index.htm`.

Ferziger, J. H., Large eddy simulation, in *Simulation and modeling of turbulent flows*, edited by M. Y. Hussaini and T. Gatski, Cambridge University Press, New York, 1995.

Ferziger, J. H., and M. Perić, *Computational methods for fluid mechanics*, Springer, Berlin, Heidelberg, New York, 1999.

Frey, H., A three-dimensional, baroclinic shelf sea circulation model – 1. The turbulence closure scheme and the one-dimensional test model, *Cont. Shelf Res.*, *11*, 365–395, 1991.

Friedrich, H., Simulation of the thermal stratification at the FLEX central station with a one-dimensional integral model, in *North Sea Dynamics*, edited by J. Sündermann and W. Lenz, pp. 396–411, Springer, 1983.

Frisch, U., *Turbulence: the legacy of A. N. Kolmogorov*, Cambridge University Press, 1995.

Galperin, B., and L. H. Kantha, Turbulence model for rotating flow, *AIAA Journal*, *27*, 750–757, 1989.

Galperin, B., L. H. Kantha, S. Hassid, and A. Rosati, A quasi-equilibrium turbulent energy model for geophysical flows, *Journal of Atmospheric Sciences*, *45*, 55–62, 1988.

Galperin, B., A. Rosati, L. H. Kantha, and G. L. Mellor, Modeling rotating stratified turbulent flows with applications to oceanic mixed layers, *J. Phys. Oceanogr.*, *19*, 901–916, 1989.

Gargett, A. E., and G. Holloway, Dissipation and diffusion by internal wave breaking, *J. Mar. Res.*, *42*, 15–27, 1984.

Garrett, C. J., and W. Munk, Space-time scales of internal waves, *Geophys. Astrophys. Fluid Dyn.*, *2*, 255–264, 1972.

Garrett, C. J., and W. Munk, Space-time scales of internal waves: A progress report, *J. Geophys. Res.*, *80*, 291–297, 1975.

Gaspar, P., Y. Gregoris, and J. Lefevre, A simple eddy kinetic energy model for simulations of the oceanic vertical mixing: Tests at station Papa and long-term upper ocean study site, *J. Geophys. Res.*, *95*, 16,179–16,193, 1990.

Gemmrich, J. R., and D. M. Farmer, Near-surface turbulence and thermal structure in a wind-driven sea, *J. Phys. Oceanogr.*, *29*, 480–499, 1999.

Gent, P. R., and J. C. McWilliams, Isopycnal mixing in ocean circulation models, *J. Phys. Oceanogr.*, *20*, 150–155, 1990.

Gerz, T., U. Schumann, and S. E. Elghobashi, Direct numerical simulation of stratified homogeneous turbulent shear flows, *J. Fluid Mech.*, *200*, 563–594, 1989.

Gibson, M. M., and B. E. Launder, Ground effects on pressure fluctuations in the atmospheric boundary layer, *J. Fluid Mech.*, *86*, 491–511, 1978.

Gill, A. E., *Atmosphere–ocean dynamics*, vol. 30 of *International Geophysics Series*, Academic Press, 1982.

Goosse, H., E. Deleersnijder, T. Fichefet, and M. H. England, Sensitivity of a global coupled ocean-sea ice model to the parameterisation of vertical mixing, *J. Geophys. Res.*, *104*, 13,681–13,695, 1999.

Grant, W. D., and O. S. Madsen, Combined wave and current interaction with a rough bottom, *J. Geophys. Res.*, *84*, 1797–1808, 1979.

Grassl, H., The dependance of the measured cool skin of the ocean on wind stress and total hear flux, *Bound. Layer Meteor.*, *10*, 465–474, 1976.

Gregg, M. C., Diapycnical mixing in the thermocline: A review, *J. Geophys. Res.*, *92*, 5249–5286, 1987.

Gregg, M. C., and T. B. Sanford, The dependance of turbulent dissipation on stratification in a diffusively stable thermocline, *J. Geophys. Res.*, *93*, 12,381–12,392, 1988.

Griffies, S. M., A. Gnanadesikan, R. C. Pacanowski, V. D. Larichev, J. K. Dukowicz, and R. D. Smith, Isoneutral diffusion in a z-coordinate ocean model, *J. Phys. Oceanogr.*, *28*, 805–830, 1998.

Haidvogel, D. B., and A. Beckmann, *Numerical Ocean Circulation Modelling*, vol. 2 of *Series on Environmental Science and Management*, Imperial College Press, London, 1999.

Hanjalic, K., and B. E. Launder, A Reynolds stress model of turbulence and its application to thin shear flows, *J. Fluid Mech.*, *52*, 609–638, 1972.

Hannoun, I. A., H. J. S. Fernando, and E. J. List, Turbulence structure near a sharp density interface, *J. Fluid Mech.*, *189*, 189–209, 1988.

Hasse, L., The dependence of the measured cool skin of the ocean on wind stress and total heat flux, *Bound. Layer Meteor.*, *10*, 465–474, 1971.

Hassid, S., and B. Galperin, A turbulent energy model for geophysical flows, *Bound. Layer Meteor.*, *26*, 397–412, 1983.

Hassid, S., and B. Galperin, Modeling rotating flows with neutral and unstable stratification, *J. Geophys. Res.*, *99*, 12,533–12,548, 1994.

Hinze, J. O., *Turbulence*, 2 ed., McGraw-Hill, 1975.

Hirsch, C., *Numerical computation of internal and external flows. Vol. 1: Fundamentals of numerical discretisation*, Wiley Series in Numerical Methods in Engineering, Wiley, Chichester, 1988.

Holt, S. E., J. R. Koseff, and J. H. Ferziger, A numerical study of the evolution and structure of homogeneous stably stratified sheared turbulence, *J. Fluid Mech.*, *237*, 499–539, 1992.

Hopfinger, E. J., and J. A. Toly, Spatially decaying turbulence and its relation to mixing across density interfaces, *J. Fluid Mech.*, *78*, 155–175, 1976.

Hossain, M. S., Mathematische Modellierung von turbulenten Auftriebsströmungen, Ph.D. thesis, Universität Karlsruhe, 1980.

Jay, D. A., and J. D. Musiak, Particle trapping in estuarine tidal flows, *J. Geophys. Res.*, *99*, 445–461, 1994.

Jerlov, N. G., *Optical oceanography*, Elsevier, 1968.

Jobson, H. E., and W. W. Sayre, Vertical mass transfer in open channel flow, *J. Hydraul. Div. Am. Soc. Civ. Eng.*, *96*, 703–724, 1970.

Jonas, T., A. Wüest, A. Stips, and W. Eugster, Observations of a quasi shear-free lacustrine convective boundary layer: Stratification and its implications on turbulence, *J. Geophys. Res.*, 2002, submitted.

Jones, H., and J. Marshall, Convection with rotation in a neutral ocean, *J. Phys. Oceanogr.*, *23*, 1009–1039, 1993.

Jungclaus, J. H., and G. L. Mellor, A three-dimensional model study of the Mediterranean outflow, *J. Mar. Sys.*, *24*, 41–66, 2000.

Jungclaus, J. H., and M. Vanicek, Frictionally modified flow in a deep ocean channel: Application to the Vema Channel, *J. Geophys. Res.*, *104*, 21,123–21,136, 1999.

Kagan, B. A., *Ocean-atmosphere interaction and climate modelling*, Cambridge University Press, Cambridge, 1995.

Kämpf, J., and J. O. Backhaus, Ice-ocean interactions during shallow convection under conditions of steady winds: Three-dimensional numerical studies, *Deep-Sea Research II*, *46*, 1335–1355, 1999.

Kantha, L. H., On some aspects and applications of second-moment closure, *Tech. rep.*, Athmospheric and Oceanic Sciences Program, Princeton University, 1988, unpublished manuscript.

Kantha, L. H., and C. A. Clayson, An improved mixed layer model for geophysical applications, *J. Geophys. Res.*, *99*, 25,235–25,266, 1994.

Kantha, L. H., and C. A. Clayson, *Small-scale processes in geophysical fluid flows*, vol. 67 of *International Geophysics Series*, Academic Press, 2000.

Kato, H., and O. M. Phillips, On the penetration of a turbulent layer into stratified fluid, *J. Fluid Mech.*, *37*, 643–655, 1969.

Ke, X., M. B. Collins, and S. E. Poulos, Velocity structure and sea bed roughness associated with intertidal (sand and mud) flats and saltmarshes of the Wash. U.K., *Journal of Coastal Research*, *10*, 702–715, 1994.

Keller, L., and A. Friedmann, Differentialgleichungen für die turbulente Bewegung einer kompressiblen Füssigkeit, in *Proceedings of the First International Congress on Applied Mechanics*, pp. 395–405, Delft, 1924.

Kevorkian, J., and J. D. Cole, *Multiple scale and singular perturbation methods*, vol. 114 of *Appl. Math. Sci.*, Springer, New York, Berlin, Heidelberg, 1996.

Kitaigorodskii, S. A., M. A. Donelan, J. L. Lumley, and E. A. Terray, Wave turbulence interactions in the upper ocean. Part II: Statistical characteristics of wave and turbulent components of the random velocity field in the marine surface layer, *J. Phys. Oceanogr.*, *13*, 1988–1999, 1983.

Klein, R., Semi-implicit extension of a Gudunov-type scheme based on low Mach number asymptotics I: One-dimensional flow, *J. Computat. Phys.*, *121*, 213–237, 1995.

Kochergin, V. P., Three-dimensional prognostic models, in *Three dimensional ocean models*, edited by N. S. Heaps, pp. 201–208, American Geophysical Union, Washington, D.C., 1987.

Kochergin, V. P., and S. N. Sklyar, Semianalytical version of approximation of system of equations in the 'b-ε' turbulence model, *Russ. J. Numer. Anal. Math. Modell.*, *7*, 405–418, 1992.

Kolmogorov, A. N., The local structure of turbulence in incompressible viscous fluid for very large reynolds numbers, *Dokl. Akad. Nauk SSSR*, *30*, 301–305, 1941, reprinted in: *Proc. R. Soc. Lond.* A **434**, 9-13 (1991).

Kolmogorov, A. N., The equations of turbulent motion on an incompressible fluid, *Izv. Akad. Nauk SSSR, Seria fizicheska, VI (1-2)*, 56–58, 1942, english translation: Imperial College, *Mech. Eng. Dept. Rept. ON/6*, 1968.

Kondo, J., Air-sea bulk transfer coefficients in diabatic conditions, *Bound. Layer Meteor.*, *9*, 91–112, 1975.

Langmuir, I., Surface motion of water induced by wind, *Science*, *87*, 119–123, 1938.

Large, W. G., and P. R. Gent, Validation of vertical mixing in an equatorial ocean model using Large Eddy Simulations and observations, *J. Phys. Oceanogr.*, *29*, 449–464, 1999.

Large, W. G., J. C. McWilliams, and S. C. Doney, Oceanic vertical mixing : a review and a model with nonlocal boundary layer parameterisation, *Rev. Geophys.*, *32*, 363–403, 1994.

Launder, B. E., On the effect of a gravitational field on the turbulent transport of heat and momentum, *J. Fluid Mech.*, *67*, 569–581, 1975a.

Launder, B. E., Progress in the modelling of turbulent transport, 1975b, Lecture Series No. 76, von Kármán Institute, Belgium, 139 pp.

Launder, B. E., turbulence modelling for the nineties: Second-moment closure ..... and beyond ?, in *International Conference on Numerical Methods in Fluid Mechanics*, edited by K. W. Morton, pp. 1–18, Springer, New York, 1990.

Launder, B. E., and D. B. Spalding, *Mathematical models of turbulence*, Academic Press, New York, 1972.

Launder, B. E., and D. B. Spalding, The numerical computation of turbulent flow, *Computer Methods in Applied Mechanics and Engineering*, *3*, 269–289, 1974.

Launder, B. E., G. J. Reece, and W. Rodi, Progress in the development of a reynolds-stress turbulence closure, *J. Fluid Mech.*, *68*, 537–566, 1975.

Ledwell, J. R., A. J. Watson, and C. S. Law, Evidence of slow mixing across the pycnocline from an open-ocean tracer-release experiment, *Nature*, *364*, 701–703, 1993.

Leibovich, S., On the evolution of the system of the wind drift currents and Langmuir circulations in the ocean. Part I: Theory and averaged current, *J. Fluid Mech.*, *79*, 715–743, 1977.

Leibovich, S., The form and dynamics of Langmuir circulations, *Ann. Rev. Fluid Mech.*, *15*, 391–427, 1983.

Lesieur, M., *Turbulence in fluids*, vol. 40 of *Fluid mechanics and its applications*, 3 ed., Kluwer Academic Publ., Dordrecht, 1997.

LeVeque, R. J., *Numerical methods for conservation laws*, Birkhäuser, Basel, Boston, Berlin, 1992.

Li, M., and C. Garrett, Cell merging and the jet/downwelling ratio in Langmuir circulation, *J. Mar. Res.*, *51*, 737–769, 1993.

Luyten, P. J., E. Deleersnijder, J. Ozer, and K. G. Ruddick, Presentation of a family of turbulence closure models for stratified shallow water flows and preliminary application to the Rhine outflow region, *Cont. Shelf Res.*, *16*, 101–130, 1996a.

Luyten, P. J., J. H. Simpson, and T. P. Rippeth, Comparison of turbulence models for homogeneous and stratified flows with turbulence measurements in the Irish Sea, 1996b, paper presented at the MAST Workshop on Turbulence Modelling, Bergen, Norway.

Luyten, P. J., J. E. Jones, R. Proctor, A. Tabor, P. Tett, and K. Wild-Allen, COHERENS – A coupled hydrodynamical-ecological model for regional and shelf seas: User documentation, *Tech. rep.*, Management Unit of the Mathematical Models of the North Sea, Brussels, 1999, 914 pp.

Marchuk, G. I., V. P. Kochergin, V. I. Klimok, and V. A. Sukhorukov, On the dynamics of the ocean surface mixed layer, *J. Phys. Oceanogr.*, *7*, 865–875, 1977.

Marshall, J., and F. Schott, Open-ocean convection: Observations, theory and models, *Rev. Geophys.*, *37*, 1–64, 1999.

Martin, P. J., Simulation of the mixed layer at OWS November and Papa with several models, *J. Geophys. Res.*, *90*, 903–916, 1985.

Martin, P. J., Testing and comparison of several mixed-layer models, *Tech. Rep. 143*, Naval Oceanographic Research and Development Agency (NORDA), Stennis Space Center, Mississippi, 1986.

Martins, F., R. Neves, and P. Leitão, A three-dimensional hydrodynamic model with generic vertical coordinate, in *Hydroinformatics '98*, edited by V. Babovic and L. C. Larsen, pp. 1403–1410, Balkema, Rotterdam, 1998, Proceedings of the third International Conference on Hydroinformatics, Copenhagen, Denmark, 24-26 August 1998.

McWilliams, J. C., P. P. Sullivan, and C.-H. Moeng, Langmuir turbulence in the ocean, *J. Fluid Mech.*, *334*, 1–30, 1997.

Meier, H. E. M., Embedding a k-ε turbulence model into a three-dimensional model of the western Baltic Sea, 1997, manuscript presented at the 1$^{\text{st}}$ BASYS annual science meeting, 29.09.-01.10.1997, Warnemünde, Germany, 13 pp.

Meier, H. E. M., The use of the k-ε turbulence model within the Rossby Centre regional ocean climate model: parameterisation, development and results, *Tech. Rep. RO 28*, Swedish Meteorological and Hydrological Institute, Norrköping, Sweden, 2000.

Meier, H. E. M., On the parameterisation of mixing in three-dimensional Baltic Sea models, *J. Geophys. Res.*, pp. 30,997–31,016, 2001.

Meister, A., Asymptotic single and multiple scale expansions in the low Mach number limit, *SIAM J. Appl. Math.*, pp. 256–271, 1999.

Mellor, G. L., Ensemble average, turbulence closure, *Advances in Geophysics*, *28B*, 345–358, 1985.

Mellor, G. L., Retrospect on oceanic boundary layer modelling and second moment closure, in *Parameterization of Small-Scale Processes; Proceedings of the Aha Hulikoa Hawaiian Winter Workshop*, edited by P. Müller and D. Henderson, pp. 251–271, Univ. of Hawaii at Manoa, Honolulu, 1989.

Mellor, G. L., One-dimensional, ocean surface layer modeling, a problem and a solution, *J. Phys. Oceanogr.*, *31*, 790–803, 2001a.

Mellor, G. L., Oscillating bottom boundary layer, *J. Geophys. Res.*, 2001b, submitted.

Mellor, G. L., and T. Yamada, A hierarchy of turbulence closure models for planetary boundary layers, *Journal of Atmospheric Sciences*, *31*, 1791–1806, 1974.

Mellor, G. L., and T. Yamada, Development of a turbulence closure model for geophysical fluid problems, *Rev. Geophys.*, *20*, 851–875, 1982.

Mironov, D. V., V. M. Gryanik, V. N. Lykossov, and S. S. Zilitinkevich, Comments on "A new second-order turbulence closure model for the planetary boundary layer", *Journal of Atmospheric Sciences*, *56*, 3478–3483, 1999.

Mironov, D. V., V. M. Gryanik, C.-H. Moeng, D. J. Olbers, and T. H. Warncke, Vertical turbulence structure and second-moment budgets in convection with rotation: A Large-Eddy Simulation study, *Q. J. R. Meteorol. Soc.*, *126*, 477–515, 2000.

Moeng, C.-H., and P. P. Sullivan, A comparison of shear and buoyancy-driven planetary boundary layer flow, *Journal of Atmospheric Sciences*, *51*, 999–1022, 1994.

Moeng, C.-H., and J. C. Wyngaard, Evaluation of turbulent transport and dissipation closures in second-order modeling, *Journal of Atmospheric Sciences*, *46*, 2311–2330, 1989.

Mohamed, M. S., and J. C. Laure, The decay power law in grid-generated turbulence, *J. Fluid Mech.*, *219*, 195–214, 1990.

Mohammadi, B., and O. Pironneau, *Analysis of the k-epsilon turbulence model*, vol. 31 of *Research in Applied Mathematics*, Wiley - Masson, 1994.

Monin, A. S., and A. M. Obukhov, Basic laws of turbulent mixing in the ground layer of the atmosphere, *Akad. Nauk SSSR Geofiz. Inst. Tr.*, *151*, 163–187, 1954.

Mosello, R., The trophic evolution of lake Maggiore as indicated by its water chemistry and nutrient loads, *Mem. Ist. Ital. Idrobiol*, *46*, 69–87, 1989.

Moum, J. N., The quest for k_ρ – Preliminary results from direct measurements of turbulent fluxes in the ocean, *J. Phys. Oceanogr.*, *20*, 1980–1984, 1990.

Müller, P., G. Holloway, F. Henyey, and N. Pomphrey, Nonlinear interactions among internal gravity waves, *Rev. Geophys.*, *24*, 493–536, 1986.

Munk, W. H., and E. R. Anderson, Notes on the theory of the thermocline, *J. Mar. Res.*, *3*, 276–295, 1948.

Nakagawa, H., I. Nezu, and H. Ueda, Turbulence in open channel flow over smooth and rough beds, *Proc Jpn. Soc. Civ. Eng.*, *241*, 155–168, 1975.

Navier, L. M. H., Mémoire sur le loi du mouvement des fluides, *Mémoire de l'Académie des Sciences de l'Institut de France*, *6*, 389–440, 1822, annee 1823, publ. 1827.

Nezu, I., and H. Nakagawa, *Turbulence in open channel flows*, Balkema, Rotterdam, Brookfield, 1993.

Ng, K. H., and D. B. Spalding, Some applications of a model of turbulence to boundary layers near walls, *Physics of Fluids*, *15*, 20–30, 1972.

Nihoul, J. C. J., E. Deleersnijder, and S. Djenidi, Modelling the general circulation of shelf seas by 3D k-ε models, *Earth-Science Reviews*, *26*, 163–189, 1989.

Noh, Y., and H. J. Kim, Simulations of temperature and turbulence structure of the oceanic boundary layer with the improved near-surface process, *J. Geophys. Res.*, *104*, 15,621–15,634, 1999.

Nokes, R. I., On the entrainment rate across a density interface, *J. Fluid Mech.*, *188*, 185–204, 1988.

Nunes Vaz, R. A., G. W. Lennon, and D. G. Bowers, Physical behaviour of a large negative or inverse estuary, *Cont. Shelf Res.*, *3*, 277–309, 1990.

Olbers, D. J., Models of the oceanic internal wave field, *Rev. Geophys. Space Phys.*, *21*, 1567–1606, 1983.

Omstedt, A., A coupled one-dimensional sea ice-ocean model applied to a semi-enclosed basin, *Tellus*, *42A*, 568–582, 1990.

Omstedt, A., J. Sahlberg, and U. Svensson, Measured and numerically simulated autumn cooling in the Bay of Bothnia, *Tellus*, *35A*, 231–240, 1983.

Orszak, S. A., Statistical theory of turbulence, in *Fluid dynamics 1973*, edited by R. Balian and J. L. Peube, pp. 237–374, Gordon and Breach, Les Houches Summer School of Theoretical Physics, 1977.

Osborn, T. R., Vertical profiling of velocity microstructure, *J. Phys. Oceanogr.*, *1*, 109–115, 1974.

Osborn, T. R., Estimates of the local rate of vertical diffusion from dissipation measurements, *J. Phys. Oceanogr.*, *10*, 83–89, 1980.

Osborn, T. R., D. M. Farmer, S. Vagle, S. A. Thorpe, and M. Cure, Measurements of bubble plumes and turbulence from a submarine, *Atmos.-Ocean*, *30*, 419–440, 1992.

Patankar, S. V., *Numerical Heat Transfer and Fluid Flow*, McGraw-Hill, New York, 1980.

Paulson, C. A., and J. J. Simpson, Irradiance measurements in the upper ocean, *J. Phys. Oceanogr.*, *7*, 952–956, 1977.

Peters, H., Observations of stratified turbulent mixing in an estuary. Neap-to-spring variations during high river flow, *Estuarine, Coastal and Shelf Science*, *45*, 69–88, 1997.

Peters, H., Spatial and temporal variability of turbulent mixing in an estuary, *J. Mar. Res.*, *57*, 805–845, 1999.

Peters, H., and R. Bokhorst, Microstructure observations of turbulent mixing in a partially mixed estuary. Part I: Dissipation rate, *J. Phys. Oceanogr.*, *30*, 1232–1244, 2000.

Peters, H., and R. Bokhorst, Microstructure observations of turbulent mixing in a partially mixed estuary. Part II: Salt flux and stress, *J. Phys. Oceanogr.*, *31*, 1105–1119, 2001.

Peters, H., M. C. Gregg, and T. B. Sanford, Detail and scaling of turbulent overturns in the Pacific Equatorial Undercurrent, *J. Geophys. Res.*, *100*, 18,349–18,368, 1995.

Piccorillo, P. S., and C. W. van Atta, The evolution of a uniformly sheared thermally stratified turbulent flow, *J. Fluid Mech.*, *334*, 61–86, 1997.

Pietrzak, J., J. B. Jacobson, H. Burchard, H. J. Vested, and O. Petersen, A three-dimensional hydrostatic model for coastal and ocean modelling using a generalised topography following co-ordinate system, *Ocean Modelling*, *4*, 173–205, 2002.

Pohlmann, T., Untersuchung hydro- und thermodynamischer Prozesse in der Nordsee mit einem dreidimensionalen numerischen Modell, Ph.D. thesis, Universität Hamburg, 1991, published in: Berichte aus dem Zentrum für Meeres- und Klimaforschung der Universität Hamburg, 23.

Pohlmann, T., Predicting the thermocline in a circulation model of the North Sea – Part I: Model description, calibration and verification, *Cont. Shelf Res.*, *16*, 131–146, 1996a.

Pohlmann, T., Calculating the annual cycle of vertical eddy viscosity in the North Sea with a three-dimensional circulation model, *Cont. Shelf Res.*, *16*, 147–161, 1996b.

Pohlmann, T., Estimating the influence of advection during FLEX'76 by means of a three-dimensional shelf sea circulation model, *Dt. Hydrogr. Z.*, *49*, 215–226, 1997.

Pollard, R. T., Observations and theories of Langmuir circulations and their role in near surface mixing, in *A Voyage of Discovery: George Deacon 70th Anniversary Volume*, edited by M. Angel, pp. 235–251, Pergamon, 1977.

Polzin, K., K. Speer, J. Toole, and R. Schmitt, Intense mixing of Antarctic bottom water in the equatorial Atlantic, *Nature*, *380*, 54–57, 1996.

Prandke, H., and A. Stips, Test measurements with an operational microstructure-turbulence profiler: Detection limits of dissipation rates, *Aquatic Sciences*, *60*, 191–209, 1998.

Prandke, H., K. Holtsch, and A. Stips, MITEC technology development: The microstructure/turbulence measuring system mss, *Tech. Rep. EUR 19733 EN*, European Commission, Joint Research Centre, Ispra, Italy, 2000.

Prandtl, L., Über ein neues Formelsystem für die ausgebildete Turbulenz, *Nachr. Akad. Wiss. Göttingen, Math.-Phys. Klasse*, p. 6, 1945.

Price, J. F., On the scaling of stress-driven entrainment experiments, *J. Fluid Mech.*, *90*, 509–529, 1979.

Reynolds, O., On the dynamical theory of incompressible viscous fluids and the determination of the criterion, *Phil. Trans. R. Soc. Lond. A*, *186*, 123–164, 1895.

Richardson, L. F., *Weather prediction by numerical process*, Cambridge University Press, 1922.

Rippeth, T. P., N. Fisher, and J. H. Simpson, The semi-diurnal cycle of turbulent dissipation in the presence of tidal straining, *J. Phys. Oceanogr.*, *31*, 2458–2471, 2001.

Robert, J. L., and Y. Ouellet, A three-dimensional finite-element model for the study of steady and non-steady natural flows, in *Three-dimensional models of marine and estuarine dynamics*, edited by J. C. J. Nihoul and B. M. Jamart, vol. 45 of *Elsevier Oceanography Series*, pp. 359–372, 1987.

Rodi, W., A new algebraic relation for calculating the reynolds stresses, *Z. Angew. Math. Mech.*, *56*, T219–T221, 1976.

Rodi, W., Turbulence models and their application in hydraulics, *Tech. rep.*, Int. Assoc. for Hydraul. Res., Delft, The Netherlands, 1980.

Rodi, W., Examples of calculation methods for flow and mixing in stratified flows, *J. Geophys. Res.*, *92*, 5305–5328, 1987.

Rogallo, R. S., Numerical experiments in homogeneous turbulence, 1981, NASA Tech. Memo. 81315.

Rohr, J. J., An experimental study of evolving turbulence in uniform mean shear flow with and without stable stratification, Ph.D. thesis, University of San Diego, 1985, available from Department of Appl. Mech. and Engrg. Sci., Univ. of Calif., San Diego, La Jolla, CA 92093.

Rohr, J. J., E. C. Itsweire, K. N. Helland, and C. W. van Atta, Growth and decay of turbulence in a stably stratified shear flow, *J. Fluid Mech.*, *195*, 77–111, 1988.

Rosati, A., and K. Miyakoda, A general circulation model for upper ocean simulation, *J. Phys. Oceanogr.*, *18*, 1601–1626, 1988.

Rotta, J. C., Statistische Theorie nichthomogener Turbulenz, *Z. Physik*, *129*, 547–572, 1951.

Rotta, J. C., Über eine Methode zur Berechnung turbulenter Scherströmungen, *Tech. Rep. 69 A 14*, Aerodynamische Versuchsanstalt Göttingen, Göttingen, Germany, 1968.

Ruddick, K. G., E. Deleersnijder, P. J. Luyten, and J. Ozer, Haline stratification in the Rhine-Meuse freshwater plume: a three-dimensional model sensitivity analysis, *Cont. Shelf Res.*, *15*, 1597–1630, 1995.

Samarskij, A. A., *Theorie der Differenzenverfahren*, Akademische Verlagsgesellschaft Geest and Portig, Leipzig, 1984.

Sander, J., Dynamic equations and turbulent closures in geophysics, *Continuum Mech. Thermodyn.*, *10*, 1–28, 1998.

Sander, J., D. Wolf-Gladrow, and D. Olbers, Numerical studies of open ocean deep convection, *J. Geophys. Res.*, *100*, 20,579–20,600, 1995.

Schott, F., M. Visbeck, and U. Send, Open ocean deep convection, Mediterranean and Greenland Seas, in *Ocean Processes in Climate Dynamics: Global and Mediterranean Examples*, edited by P. Malanotte-Rizzoli and A. R. Robinson, pp. 203–225, Kluwer Academic Publishers, 1994.

Schumann, U., Correlations in homogeneous stratified shear turbulence, *Acta Mechanica*, *2*, 105–111, 1994.

Schumann, U., and T. Gerz, Turbulent mixing in stably stratified shear flows, *J. Appl. Meteorol.*, *34*, 33–48, 1995.

Send, U., and J. Marshall, Integral effects of deep convection, *J. Phys. Oceanogr.*, *25*, 855–872, 1995.

Sharples, J., Time-dependent stratification in regions of large horizontal density gradient, Ph.D. thesis, School of Ocean Sciences, University of Wales, Bangor, 1992.

Sharples, J., and J. H. Simpson, Semi-diurnal and longer period stability cycles in the Liverpool Bay region of freshwater influence, *Cont. Shelf Res.*, *15*, 295–313, 1995.

Sheng, Y. P., and C. Villaret, Modelling the effect of suspended sediment stratification on bottom exchange processes, *J. Geophys. Res.*, *94*, 14,429–14,444, 1989.

Shih, L. H., J. R. Koseff, J. H. Ferziger, and C. R. Rehmann, Scaling and parameterisation of stratified homogeneous turbulent shear flow, *J. Fluid Mech.*, *412*, 1–20, 2000.

Shih, T. S., and A. Shabbir, Advances in modeling the pressure correlation terms in the second moment equations, in *Studies in Turbulence*, edited by T. B. Gatsky, S. Sarkar, and C. G. Speziale, pp. 91 – 128, Springer, New York, 1992.

Simpson, J. H., and J. Sharples, Dynamically active models in the prediction of estuarine circulation, in *Dynamics and exchanges in estuaries and the coastal zone*, edited by D. Prandle, vol. 40 of *Coastal and Estuarine Studies*, pp. 101–113, American Geophysical Union, Washington, 1992.

Simpson, J. H., J. Brown, J. Matthews, and G. Allen, Tidal straining, density currents, and stirring in the control of estuarine stratification, *Estuaries*, *26*, 1579–1590, 1990.

Simpson, J. H., W. R. Crawford, T. P. Rippeth, A. R. Campbell, and J. V. S. Cheok, The vertical structure of turbulent dissipation in shelf seas, *J. Phys. Oceanogr.*, *26*, 1579–1590, 1996.

Simpson, J. H., T. P. Rippeth, and A. R. Campbell, The phase lag of turbulent dissipation in tidal flow, in *Interactions between estuaries, coastal seas and shelf seas*, edited by T. Yanagi, pp. 57–67, Terra Scientific Publishing, Tokyo, 2000.

Simpson, J. H., H. Burchard, N. R. Fisher, and T. P. Rippeth, Modelling the cycle of tidal dissipation in a region of tidal straining, *Cont. Shelf Res.*, 2001, accepted for publication.

Skyllingstad, E. D., and D. W. Denbo, An ocean large-eddy simulation of Langmuir circulation in the surface mixed layer, *J. Geophys. Res.*, *100*, 8501–8522, 1995.

Skyllingstad, E. D., W. D. Smyth, J. N. Moum, and H. Wijesekera, Upper-ocean turbulence during a westerly wind burst: A comparison of Large-Eddy Simulation results and microstructure measurements, *J. Phys. Oceanogr.*, *29*, 5–28, 1999.

Smagorinsky, J., General circulation experiments with the primitive equations, *Monthly Weather Review*, *91*, 99–164, 1963.

Smith, J. D., and S. R. McLean, Spatially averaged flow over a wavy surface, *J. Geophys. Res.*, *82*, 1735–1746, 1977.

Smyth, W. D., Dissipation range geometry and scalar spectra in sheared, stratified turbulence, *J. Fluid Mech.*, *401*, 209–242, 1999.

Smyth, W. D., and J. N. Moum, Length scales of turbulence in stably stratified mixing layers, *Physics of Fluids*, *12*, 1327–1342, 2000a.

Smyth, W. D., and J. N. Moum, Anisotropy of turbulence in stably stratified mixing layers, *Physics of Fluids*, *12*, 1343–1362, 2000b.

Smyth, W. D., J. N. Moum, and D. R. Caldwell, The efficiency of mixing in turbulent patches: inferences from direct simulations and microstructure observations, *J. Phys. Oceanogr.*, *31*, 1969–1992, 2001.

Soetje, K. C., and K. Huber, A compilation of data on the thermal stratification at the central station in the northern North Sea during FLEX'76, *"Meteor"-Forsch.-Ergebnisse, Reihe A*, *22*, 69–77, 1980.

Speziale, C. G., R. Abid, and E. C. Anderson, A critical evaluation of two-equation models for near-wall turbulence, 1990, AIAA Paper 90-1481, Seattle, WA.

Stacey, M. T., S. G. Monismith, and J. R. Burau, Measurements of Reynolds stress profiles in unstratified tidal flow, *J. Geophys. Res.*, *104*, 10,933–10,949, 1999.

Stacey, M. W., Simulation of the wind-forced near-surface circulation in Knight Inlet: A parameterisation of the roughness length, *J. Phys. Oceanogr.*, *29*, 1363–1367, 1999.

Stacey, M. W., and S. Pond, On the Mellor-Yamada turbulence closure scheme: The surface boundary condition for q^2, *J. Phys. Oceanogr.*, *27*, 2081–2086, 1997.

Stelling, G. S., Compact differencing for stratified free surface flow, *Advances in Hydro-Science and -Engineering*, *2*, 378–386, 1995.

Stips, A., H. Prandke, and U. Tschesche, Report on microstructure data processing and presentation of the results from the PROVESS-1098 campaign, *Tech. Rep. I.00.128*, European Commission, Joint Research Centre, Ispra, Italy, 2000.

Stips, A., H. Burchard, K. Bolding, and W. Eifler, Measurements and modelling of convective turbulence in Lake Lago Maggiore, Italy, *Ocean Dynamics*, 2001, submitted.

Stokes, G. G., On the theories of the internal friction of fluids in motion, and of the equilibrium and motion of elastic solids, *Trans. Cambridge Phil. Soc.*, *8*, 287–305, 1845, reprinted in: Mathematical and Physical Papers (1880) 1: 75-129, Cambridge, University Press.

Sullivan, P. P., C.-H. Moeng, B. Stevens, D. H. Lenschow, and S. D. Mayor, Structure of the entrainment zone capping the convective atmospheric boundary layer, *Journal of Atmospheric Sciences*, *55*, 3042–3064, 1998.

Svensson, U., Mathematical model of the seasonal thermocline, *Tech. Rep. 1001*, University of Lund, Dept. of Water Resources, Lund, Sweden, 1978.

Svensson, U., The structure of the turbulent Ekman layer, *Tellus*, *31*, 340–350, 1979.

Svensson, U., PROBE, program for boundary layers in the environment. System description and manual, *Tech. Rep. 24*, Swedish Meteorological and Hydrological Institute, Norrköping, Sweden, 1998.

Svensson, U., and A. Omstedt, A mathematical model of the ocean boundary layer under drifting melting ice, *J. Phys. Oceanogr.*, *20*, 161–171, 1990.

Taylor, G. I., Statistical theory of turbulence, *Proc. Trans. R. Soc. Lond. A*, *151*, 421–478, 1935.

Telbany, M. M. M. E., and A. J. Reynolds, The structure of turbulent plane Couette flow, *J. Fluids Eng.*, *104*, 367–372, 1982.

Tennekes, H., Two- and three-dimensional turbulence: Predictability and other problems, in *Lecture Notes on Turbulence – Lecture Notes from the NCAR-GTP Summer School June 1987*, edited by J. R. Herring and J. C. McWilliams, pp. 20–35, World Scientific, Singapore, 1989.

Terray, E. A., M. A. Donelan, Y. C. Agrawal, W. M. Drennan, K. K. Kahma, A. J. Williams III, P. A. Hwang, and S. A. Kitaigorodskii, Estimates of kinetic energy dissipation under breaking waves, *J. Phys. Oceanogr.*, *26*, 792–807, 1996.

Terray, E. A., W. M. Drennan, and M. A. Donelan, The vertical structure of shear and dissipation in the ocean surface layer, in *The wind-driven air-sea interface-electromagnetic and acoustic sensing, wave dynamics and turbulent fluxes*, edited by M. L. Banner, pp. 239–245, 1999.

Therry, G., and P. Lacarrère, Improving the eddy kinetic energy model for planetary boundary layer description, *Bound. Layer Meteor.*, *17*, 63–88, 1983.

Thompson, S. M., and J. S. Turner, Mixing across an interface due to turbulence generated by an oscillating grid, *J. Fluid Mech.*, *67*, 349–368, 1975.

Thorpe, S. A., Turbulence and mixing in a Scottish loch, *Phil. Trans. R. Soc. Lond. A*, *286*, 125–181, 1977.

Thorpe, S. A., On the shape and breaking of finite amplitude internal gravity waves in a shear flow, *J. Fluid Mech.*, *85*, 7–31, 1979.

Thorpe, S. A., On the determination of K_v in the near-surface ocean from acoustic measurements of bubbles, *J. Phys. Oceanogr.*, *14*, 855–863, 1984a.

Thorpe, S. A., The effect of Langmuir circulation on the distribution of submerged bubbles caused by breaking wind waves, *J. Fluid Mech.*, *142*, 151–170, 1984b.

Thorpe, S. A., The breakup of Langmuir circulation and the instability of an array of vortices, *J. Phys. Oceanogr.*, *16*, 1462–1478, 1992.

Thorpe, S. A., T. R. Osborn, J. F. E. Jackson, A. J. Hall, and R. G. Lueck, Measurements of turbulence in the upper ocean mixing layer using Autosub, *J. Phys. Oceanogr.*, 2002, accepted for publication.

Townsend, A. A., *The structure of turbulent shear flow*, Cambridge University Press, 1976.

Turner, J. S., *Buoyancy effects in fluids*, Cambridge University Press, 1973.

Ueda, H., R. Möller, S. Komori, and T. Mizushina, Eddy diffusivity near the free surface of open channel flow, *Int. J. Heat Mass Transfer*, *20*, 1127–1136, 1977.

Uittenbogaard, R. E., The importance of internal waves for mixing in a stratified eastuarine tidal flow, Ph.D. thesis, University of Delft, 1995.

Umlauf, L., Turbulence parameterisation in hydrobiological models for natural waters, Ph.D. thesis, Technical University of Darmstadt, Germany, 2001, published in: Darmstädter Dissertationen, no. D 17.

Umlauf, L., and H. Burchard, A generic length-scale equation for geophysical turbulence models, *J. Phys. Oceanogr.*, 2001, submitted.

Umlauf, L., H. Burchard, and K. Hutter, The performance of an extended k-ω turbulence model for geophysical flows, *Ocean Modelling*, 2001, submitted.

van Haren, H., Properties of vertical current shear across stratification in the North Sea, *J. Mar. Sys.*, *58*, 465–491, 2000.

Verduin, J. J., and J. O. Backhaus, Dynamics of plant-flow interactions for the seagrass *amphibolis antarctica*: Field observations and model simulations, *Estuarine, Coastal and Shelf Science*, *50*, 185–204, 2000.

Villarreal, M. R., Parameterisation of turbulence in the ocean and application of a 3D baroclinic model to the Ria de Pontevedra, Ph.D. thesis, Departamento de Fisica da Materia Condensada, Grupo de Fisica Non-Lineal, Universidade de Santiago de Compostela, 2000, available from the World Wide Web at `http://www.gotm.net`.

von Storch, H., and F. W. Zwiers, *Statistical analysis in climate research*, Cambridge University Press, 1999.

Wang, D., J. C. McWilliams, and W. G. Large, Large-eddy simulation of the diurnal cycle of deep equatorial turbulence, *J. Phys. Oceanogr.*, *28*, 129–148, 1998.

Weller, R. A., and J. F. Price, Langmuir circulation within the oceanic mixed layer, *Deep-Sea Research*, *35*, 711–747, 1988.

Wilcox, D. C., Reassessment of the scale-determining equation for advanced turbulence models, *AIAA Journal*, *26*, 1299–1310, 1988.

Wilcox, D. C., *Turbulence Modeling for CFD*, 2 ed., DCW Industries, 1998.

Willis, G. E., and J. W. Deardorff, A laboratory model of the unstable planetary boundary layer, *Journal of Atmospheric Sciences*, *31*, 1297–1307, 1974.

Winterwerp, H., On the dynamics of high-concentrated mud suspensions, Ph.D. thesis, Delft University of Technology, 1999, Vol. 99.3 of Communications on Hydraulic and Geotechnical Engineering, Delft University of Technology.

Yamada, T., Simulations of nocturnal drainage flows by a q^2l turbulence closure model, *Journal of Atmospheric Sciences*, *40*, 91–106, 1983.

Zeierman, S., and M. Wolfshtein, Turbulent time scale for turbulent flow calculations, *AIAA Journal*, *24*, 1606–1610, 1986.

Zeman, O., and H. Tennekes, A self-contained model for the pressure terms in the turbulent stress equations of the neutral atmospheric boundary layer, *Journal of Atmospheric Sciences*, *32*, 1808–1813, 1975.

Zilitinkevich, S. S., *Turbulent penetrative convection*, Avebury Technical, 1991.

Zilitinkevich, S. S., Third-order transport due to internal waves and non-local turbulence in the stably stratified surface layer, *Q. J. R. Meteorol. Soc.*, *128*, 913–926, 2002.

Zilitinkevich, S. S., V. M. Gryanik, V. N. Lykossov, and D. V. Mironov, Third-order transport and nonlocal turbulence closures for convective boundary layers, *Journal of Atmospheric Sciences*, *56*, 3463–3477, 1999.

Index